

Systematic coarse-graining procedures for molecular systems

vorgelegt von

Diplom-Physiker

Thomas Heinemann

aus Magdeburg

Von der Fakultät II - Mathematik und Naturwissenschaften

der Technischen Universität Berlin

zur Erlangung des akademischen Grades

Doktor der Naturwissenschaften

Dr. rer. nat.

genehmigte Dissertation

Promotionsausschuss:

Vorsitzender: Prof. Dr. Mario Dähne

1. Gutachterin: Prof. Dr. Sabine H. L. Klapp

2. Gutachter: Prof. Dr. Christos N. Likos

Tag der wissenschaftlichen Aussprache: 2. März 2016

Berlin 2016

Publications

The main ideas and figures of this work have appeared previously in the following publications:

- Thomas Heinemann, Karol Palczynski, Joachim Dzubiella, and Sabine H. L. Klapp. *Angle-resolved effective potentials for disk-shaped molecules*. J. Chem. Phys. **141**, 214110 (2014).
<http://dx.doi.org/10.1063/1.4902824>
- Thomas Heinemann, Karol Palczynski, Joachim Dzubiella, and Sabine H. L. Klapp. *Coarse-grained electrostatic interactions of coronene: Towards the crystalline phase*. J. Chem. Phys. **143**, 174110 (2015).
<http://dx.doi.org/10.1063/1.4935063>
- Thomas Heinemann, Moritz Antlanger, Martial Mazars, Sabine H. L. Klapp, and Gerhard Kahl. *Equilibrium structures of anisometric, quadrupolar particles confined to a monolayer*. J. Chem. Phys. **144**, 074504 (2016).
<http://dx.doi.org/10.1063/1.4941585>

Abstract

In this thesis, we present two fundamental strategies to model systems comprising many molecules in a more abstract or coarse-grained manner. The goal is to reduce the number of the degrees of freedom for computing many-particle simulations of large systems over long time scales.

A challenging feature of coarse-grained systems is implicitly including the dynamics of the microscopic degrees of freedom characterized by small length- and time-scales. In particular, the typical time scale of electronic wave functions is in the order of attoseconds, while for large molecules it is several femtoseconds.

The first strategy illustrates the systematic abstraction of the atomic level of detail of a system consisting of two coronene molecules, which possess a discotic shape. We force a coarse-grained configuration in an equilibrium ensemble to occur equally frequently, regardless of the level of detail. This frequency directly leads to the effective potential between these molecules. For phase-space sampling at the atomic level, we use *Langevin dynamics* results with modifications based on *umbrella sampling* or *steered dynamics* techniques. We treat the complex electrostatics of these molecules - which is essential for the molecular orientation in the crystalline phase - separately from the main coarse-graining procedure. To fit our temperature and angle-dependent effective molecule-molecule potential, we use several models with a different number of parameters. We additionally investigate the applicability of these models through *molecular dynamics* simulations in systems with constant temperature and mostly constant pressure. We also consider the structure and melting behavior of the system in the isotropic and condensed phases. We conclude that a model with an extended charge distribution is required, particularly to reproduce the correct temperature.

In our second strategy, we introduce a model for the interaction in two dimensions, where the electrostatics is approximated through a linear point quadrupole. For this purpose, we consider monodisperse systems of purely repulsive ellipses with different aspect ratios and an embedded linear point quadrupole along one main axis. Using molecular dynamics simulations, we examine the partly quite complex structure of the systems and their melting temperatures at a constant pressure. We deduce that the crystalline phases of the molecules with high eccentricity melt at higher temperatures than crystalline phases of more isotropically-shaped molecules. We also discuss the applicability of our results to systems with different parameter settings.

In principle, both strategies presented here can be applied at various orders of magnitude. Further possible fields of application are colloidal systems or even cosmic objects, provided relativistic effects are considered.

Zusammenfassung

In dieser Arbeit führen wir zwei grundlegende Strategien ein, um Systeme aus vielen Molekülen auf abstrakter Ebene zu modellieren, sodass Vielteilchensimulationen von großen Systemen und Zeiträumen numerisch realisierbar werden.

Einen schwierigen Aspekt stellt hierbei die Abstraktion der Dynamik mikroskopischer Freiheitsgrade dar, welche auf kleineren Längen- und Zeitskalen abläuft. Anzuführen sei, dass die typische Zeitskala von elektronischen Wellenfunktionen im Bereich von Attosekunden liegt; bei größeren Molekülen liegt sie hingegen bei einigen Femtosekunden.

Die erste Strategie zeigt beispielhaft eine systematische Abstraktion der atomistischen Details eines Systems aus zwei Coronenmolekülen, die eine scheibenförmige Geometrie aufweisen. Die jeweilige Häufigkeit einer abstrakten Konfiguration in einem Gleichgewichtsensemble, welche die Grundlage zur Berechnung des effektiven Potentials zwischen den Molekülen bildet, forcieren wir als Erhaltungsgröße beim Wechsel der Details. Für das Phasenraum-Sampling auf atomistischer Detailsbene nutzen wir *Langevin-Dynamics*-Resultate, wobei Modifizierungen, basierend auf *Umbrella-Sampling*- und *Steered-Dynamics*-Techniken, benutzt wurden. Die relativ komplexe Elektrostatik dieser Moleküle, die für die Orientierung der Moleküle in der kristallinen Phase notwendig ist, behandeln wir indessen gesondert. An das temperatur- und winkelabhängige effektive Molekül-Molekül-Potential nähern wir mehrere Modelle mit verschieden großer Anzahl an Parametern an. Die Anwendbarkeit unserer Modelle untersuchen wir mit Hilfe von *Molekulardynamik*-Simulationen bei konstanter Temperatur und gegebenenfalls konstantem Druck. Dabei betrachten wir das System in isotroper als auch kondensierter Phase hinsichtlich Struktur und Schmelzverhalten. Insbesondere für die Reproduktion der Schmelztemperatur schlussfolgern wir, dass ein Modell mit ausgedehnter Ladungsverteilung erforderlich ist.

In der zweiten Strategie führen wir ein abstraktes Modell für die Wechselwirkung von anisotropen Molekülen in zwei Dimensionen ein, deren Elektrostatik näherungsweise durch einen linearen Quadrupol beschrieben werden kann. Dazu betrachten wir einkomponentige Systeme aus rein repulsiven Ellipsen mit unterschiedlichen Seitenverhältnissen und festem eingebetteten linearen Quadrupol entlang einer Hauptachse. Mittels Molekulardynamik-Simulationen analysieren wir für verschiedene Temperaturen bei konstantem Druck die teils sehr vielfältige Struktur der Systeme sowie das Schmelzverhalten. Die kristallinen Phasen aus Molekülen mit hoher Exzentrizität zeigen demnach bei einer Temperaturerhöhung gegenüber isotrop-geformten Molekülen gleicher Größe ein stark retardiertes Schmelzverhalten. Des Weiteren diskutieren wir die Anwendbarkeit dieser Resultate auf Systeme mit anderen Parametersätzen.

Prinzipiell können diese Strategien auf beliebige Größenordnungen (wie zum Beispiel kolloidale Systeme) angewandt werden. Unter Berücksichtigung relativistischer Effekte ist bedingt sogar eine Anwendung auf kosmische Objekte möglich.

Contents

1	Introduction	1
1.1	Overview	1
1.2	Coarse-graining	1
1.3	Coarse-grained molecular dynamics	5
1.4	Monolayer study	6
1.5	Structure of this thesis	9
2	Fundamentals in statistical mechanics	10
2.1	Preface	10
2.2	Ensemble theory	11
2.2.1	Canonical (NVT) ensemble	11
2.2.2	Isobaric-isothermal (NPT) ensemble	13
2.2.3	Grand canonical (μ VT) ensemble	15
2.3	Virial expansion	15
2.3.1	Thermal equation of state	15
2.3.2	Virial expansion coefficients	17
2.4	Maxwell-Boltzmann distribution	18
2.5	Phase transitions	20
2.6	Ergodicity	24
2.7	Structural properties	24
2.7.1	Pair distribution functions	24
2.7.2	2D order parameters	27
2.7.3	3D order parameters	29
3	Simulation methods	30
3.1	Preface	30
3.2	Langevin dynamics (LD)	31
3.3	Berendsen weak-coupling scheme	31
3.3.1	Translation	32
3.3.2	Rotation	33
3.3.3	Solving the Berendsen equations of motion	34
3.3.4	Speed probability distribution	36
3.4	Canonical velocity rescaling scheme	36

3.5	Periodic boundary conditions	38
3.5.1	Adjust positions	38
3.5.2	Adjust relative positions	38
3.6	Random configurations	39
3.7	Treatment of interactions	39
3.7.1	Short-range treatment	39
3.7.2	Long-range treatment	39
3.7.2.1	Coulomb interactions	40
3.7.2.2	Quadrupole-quadrupole interactions	42
3.8	Speed-up techniques	44
3.8.1	Neighbor lists	44
3.8.1.1	2D-quadratic simulation box	45
3.8.1.2	Parallelogram / Triclinic simulation box	46
3.8.2	Time step variation	47
4	From microscopic to coarse-grained systems	48
4.1	Preface	48
4.2	Microscopic description	49
4.2.1	Atomistically-resolved model	49
4.2.2	Electronic density functional theory	50
4.2.3	Electrostatic potential fit	52
4.3	Coarse-grained (CG) description	52
4.3.1	Coronene dimer	53
4.3.2	Mapping functions	54
4.4	Histogram function	55
4.4.1	Definition	55
4.4.2	Umbrella sampling	56
4.4.3	Thermodynamic integration	57
4.4.4	Non-equilibrium sampling – steered dynamics	58
4.5	Definition of the effective pair potential	60
4.5.1	Kirkwood’s potential of mean force	60
4.5.2	Pure distance-dependent effective potential in a molecular dimer	63
4.5.3	Distance and orientation dependent effective potential in a molec- ular dimer	64
4.5.4	Configurational entropy	65
4.5.4.1	Pure distance dependence	65
4.5.4.2	Distance and orientation dependence	66
5	Effective pair potential for coronene molecules	68
5.1	Preface	68
5.2	Van der Waals interaction	69
5.2.1	Numerical details	69
5.2.2	Angle-averaged effective potentials	70
5.2.3	Angle-resolved effective potentials	71

5.3	Fitting the effective potential	72
5.3.1	Hard ellipsoid (HE) potential	74
5.3.2	Kabadi potential	74
5.3.3	Modified Gay-Berne (mGB) potential	75
5.3.4	Spherical model (S)	76
5.3.5	Parametrized curves	76
5.4	Coarse-grained electrostatics	77
5.4.1	Including electrostatics via a direct sum	79
5.4.2	Multipole expansion	80
5.4.3	Point quadrupole approach	81
5.4.4	Charged-ring approach	82
5.4.5	Ground state curves	85
5.4.6	Temperature dependent curves	86
6	Molecular bulk system of coronene molecules	89
6.1	Preface	89
6.2	Van der Waals coronene	90
6.2.1	Isotropic regime	90
6.2.2	Columnar hexagonal nematic regime	93
6.2.3	Performance of the van der Waals models	95
6.3	Coronene with electrostatics	97
6.3.1	Bulk crystal at room temperature	98
6.3.2	Melting of the bulk crystal	99
6.3.3	Performance of the models with electrostatics	100
7	2D monolayer	102
7.1	Preface	102
7.2	Model	103
7.3	Results	106
7.4	Consequences of the Melting behavior	112
8	Conclusion and outlook	114
	Appendices	119
A.1	Continuous phase transition	120
A.2	First derivatives	121
A.2.1	Modified Gay-Berne (mGB) interaction	121
A.2.2	Linear quadrupole-quadrupole (QQ) interaction	122
A.2.3	Soft repulsive ellipse interaction	122
A.3	Parametrizations	123
A.4	Enthalpy and order parameter curves for the monolayer system at ground state	126
A.5	Reduction of parameter space for hard particles	128

A.5.1	Ground state	128
A.5.2	Finite temperatures	128
A.6	Applicability of parameter scaling for non-hard particles at ground state	129
A.7	Annealing results for the monolayer system	130

Bibliography

Abbreviations

CG	coarse-grained
MD	molecular dynamics
SD	steered dynamics
US	umbrella sampling
FEP	free energy perturbation method
HIOS	hybrid inorganic/organic systems
FF	face-face
PD	parallel displaced
D	dimension of the system
BOOP	bond-orientational order parameter
PMF	potential of mean force
DFT	density functional theory
GS	ground state
vdW	van der Waals
GB	Gay-Berne
mGB	modified Gay-Berne
pq	point quadrupole
HE	hard-ellipse
QHE	quadrupolar hard-ellipse

Chapter 1

Introduction

1.1 Overview

In this thesis we provide insight into a thorough bottom-up investigation of the physical behavior in equilibrium many-particle systems for long length- and time scales. This constitutes a serious computational problem that should be tackled in many-particle simulations in order to trace the behavior of such systems for long durations and long length scales. An efficient method to counter such problems is by effectively reducing the huge number of degrees of freedom via implementing the so-called *coarse-graining* methods. Taking advantage of this method makes it possible to explore length and time scales in the order of micrometers and nanoseconds and beyond. Nonetheless, the evaluation of the interactions between the coarse-grained interaction site prototypes in this coarser level of resolution is not straight-forward. This work provides a cohesive method to determine these kind of effective interactions where each interaction site represents one discotic molecule. As an exemplary case, we have considered “coronene” which is a discotic, conjugated organic molecule. Moreover, its high axial and top-down symmetry leads to a well justified assumption of uniaxiality. In addition to the coarse-graining of coronene, an investigation of the applicability of the underlying method towards different dimensions and molecular symmetries is carried out. We further scrutinize the quality of coarse-graining for coronene at different levels of detail using different types of molecular dynamics (MD) simulations. Finally, a parameter study of a rather simple coarse-grained model of anisotropic molecules with electrostatics in a monolayer is presented. In the following, we introduce the relevant topics.

1.2 Coarse-graining

An important goal in statistical and computational physics is to describe atomistically-detailed many-particle systems in a coarse-grained level of detail. After constructing a coarse-graining prototype it is straight forward to perform many-particle simulations of larger system sizes and longer time scales. In this work, we consider the transition from the atomistic detail towards the molecular detail in a system composed of many molecules in two and three spatial dimensions. In order to describe the molecular arrangement of these systems, one typically considers a large variety of interactions, even on the atomistic level (such as covalent, Coulomb or Lennard-Jones interactions,

or even higher particle interactions due to bending or torsion of a molecule; see, e.g., Ref. 208). It is often revealed that a treatment on the atomistic level is insufficient for a proper description of the particle arrangements; even atomic point charges [151] or atomic electrostatic multipoles [155] in benzene (a small discotic organic molecule) do not reproduce the correct charge distribution in a benzene dimer, i.e., quantum chemical theories are required for the whole system composed of electrons and nuclei. At this time, this level of detail is computationally as well as theoretically far too challenging, especially for finite temperature simulations. As a consequence, the description of the underlying system in a coarse-grained, and at the same time in a sufficient manner using effective interactions, is essential. These effective interactions depend on fewer variables, called coarse-grained variables.

So far, there has been a large amount of work devoted to coarse-graining procedures. In particular, there is a plethora of relevant studies in which effective molecule-molecule interactions are implemented by considering the solvent particles explicitly [62, 96, 212] or implicitly [15, 39, 65, 65, 66, 71, 90, 158, 170, 198, 207, 212]. Some studies scrutinized effective interactions of certain molecular species, such as liquid hydrocarbons [91], alkanes [139] or polycyclic aromatic hydrocarbons (PAH) [205]. Other works, designated to biophysics, incorporated studies of DNA [131, 132, 140], phospholipids [85], polymers [9, 112], ring-polymers [18, 153], proteins [44], lipids [16], polymer chains [41], aminoacid side chains [121], amphiphilic peptides [49] or biomolecules such as protein-DNA complexes [203]. A further interesting application for coarse-graining are fluids, where the molecules can be grouped into united interacting units [52, 210] thus allowing a semi-explicit treatment of solvent particles. Of particular concern are also micrometer-sized particles or colloids, e.g., red blood cells [152] or clay mineral particles [192].

The fundamental coarse-graining theory on which this work is based, stems from Kirkwood who introduced in Ref. 98 the potential of mean force (PMF) (see Sec. 4.5). In the same article, Kirkwood defined the pair distribution function (see Sec. 2.7.1) and the method of thermodynamic integration (see Sec. 4.4.3), both of which are also substantial in the present work. The PMF is the potential that corresponds to the mean force acting between two particles. It is a free energy profile as a function of the coarse-grained variables and depends on temperature. The free energy profiles can be created using atomistic simulation trajectory data both in equilibrium [23, 40, 89, 182] and in non-equilibrium [87, 109, 148]. Alternatively to computer simulations, one might use experimental data [28] for the sampling method as well.

Most studies involving pure spherical symmetric coarse-grained sites, i.e., effective interactions between these sites (normally groups of atoms) solely depend on distance. More specifically, there are studies involving one [18, 90, 111, 158, 212] or more [64, 85] coarse-grained sites per molecule. A typical example for pure distance-based coarse-graining are star-shaped polymers [111] whose distance-dependent pair interactions are rather soft even at moderate temperatures. With regard to solid phases, the pure distance-dependent coarse-graining between strongly anisotropic molecules is obviously insufficient. Representing, on the contrary, each molecule through an angle- and position dependent coarse-grained site may thereby lead to improved descriptions of real systems. For the sake of completeness, there are also studies investigating the PMF as a function of angles inside molecules [105, 162].

There are a variety of coarse-graining methods such as force matching [51, 84, 114], reverse Monte Carlo [124], iterative Boltzmann inversion scheme [193, 194] or integral equation schemes [110] based on structural properties. In the force matching method, a functional involving the difference of forces on the coarse-grained sites and the reference forces is minimized with respect to the coarse-grained variables. The reverse Monte Carlo is a technique capable of reproducing the pair distribution function of a measured, or reference, system with a model system by rearranging the model particles. This kind of approach has been further developed towards the iterative Boltzmann inversion scheme [193, 194] where the coarse-grained interaction potential is refined after each simulation run using the coarse-grained and the reference pair distribution function. A coarse-graining method that is based on a new force-field is proposed by Martini *et al.* [115, 206] who use chemical building blocks as their coarse-grained sites. This is a promising approach for flexible molecules such as, e.g., polymers. A more recent and interesting approach is given through neural-network-potentials (for reviews see Refs. [14, 74]). Besides those pure coarse-graining methods, also hybrid techniques which obtained a compromise between atomistic and coarse-grained detail can be achieved by adaptive-resolution techniques [154]. The coarse-grained resolution depends here on the distance, i.e., at short distances, the interaction potential is atomistic while largely separated particles interact via coarse-grained potentials.

In this thesis, a two-step procedure concerning the coarse-graining of coronene is performed. As presented here, the original Kirkwood route is extended towards a two-particle system with distance and angle dependence. In the first step, a systematic coarse-graining of coronene, involving energy contributions from covalent and van der Waals interactions as well as bending and torsional contributions between 3 and 4 atoms, is performed. The molecular shape is mainly determined through the Pauli repulsion. Each coarse-grained molecule is characterized through a position and an axial orientation vector. The coarse-grained molecule is thus axially symmetric in its interaction as depicted in Fig. 1.1. In a second step, electrostatic contributions are added on top of the coarse-grained potential.

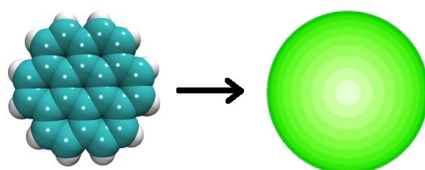


FIGURE 1.1: Transition from the atomistically-resolved coronene molecule to the coarse-grained representation. The atomistic coronene image was provided by Karol Palczynski [1]. Carbon atoms are blue and hydrogen atoms white.

The calculation of the PMF between two molecules in the absence of other molecules requires trajectory data from atomistically-resolved two-molecule simulations. For the underlying atomistic simulations that were performed by Karol Palczynski (Helmholtz Zentrum Berlin), we used Langevin dynamics (see Sec. 3.2) and the generalized Amber force-field [208] for the atomic interactions. In these simulations, histograms of the coarse-grained variables (see Sec. 4.4) are recorded. In order to improve the sampling

in rare sampled regions (e.g., at large inter-molecule separations), we used two fundamental, though different, techniques. On the one hand, we used bias potentials in a so-called umbrella sampling setup [188, 189] (see Sec. 4.4.2). In this way, the unbiased histogram function can be determined using the weighted histogram analysis method (WHAM). On the other hand, steered dynamics simulations [83, 134] (see Sec. 4.4.4) were performed and both methods qualitatively compared. In the latter method, two molecules are simulated at constraint distance. At large time scales, the distance is pulled apart very slowly. During this procedure, which is a quasi-static process, the constraint force is integrated to a work applied on this system, which leads to an effective pair potential. This kind of method is analogous to experiments where a molecule is stretched and its rupture force is measured [70, 72, 83, 113].

The effective potentials resulting from both methods are in good qualitative agreement (see Sec. 5.2) and reveal that the molecules strongly attract each other in face-to-face-like configurations. Astoundingly, these configurations are also found to be strongly temperature dependent due to bending modes affecting the variance in the inter-atomic distances between the molecules (see Sec. 5.2.3).

One should acknowledge that the latter effective potentials do not incorporate electrostatic contributions. Nonetheless, electrostatics in molecules is often essential for understanding the phase behavior. Molecules that are uncharged but bear an electrostatic potential not only have the possibility to attract and repel but also to influence the alignment towards each other. For coronene the tilted stacking [160] is found to be an artefact of the electrostatic interactions. Therefore, coronene acts as a benchmark-system to investigate electrostatics in discotics. In principle, our coarse-graining procedure could be extended straightforwardly and applied to coronene molecules with electrostatic contributions using ab-initio simulations. Though, ab-initio simulations are, from a computational prospective, very time-consuming. A total simulation time of 275 ns for two coronene molecules is too challenging presently. A less time-consuming alternative is possible through static partial charges distributed among the atoms. For this purpose, a coarse-graining study for perylene (a flat but non-discotic molecule) with static partial charges was done by Babadi *et al.* [7] using constrained steered dynamics (with additional constraints satisfying a constant molecular orientation). However, it is known that also for coronene static partial charges differ when comparing the atomic charge distribution of a monomer with those of a molecule in a bulk crystal [57] (except for selected configurations such as a parallel displaced one [213]). We have avoided using any kind of point charge electrostatic implementations in the models, since point charge patterns overestimate the charge localization, are long-ranged, and do not fulfill our symmetry requirements.

The smeared electrostatic potential of coronene around its symmetry axis is shown in Fig. 1.2(a). In order to augment our effective potential for coronene with electrostatics, we utilized two different approaches. For both approaches we used an additive composition of the van der Waals and the electrostatics interaction part. The first approach aims to represent the electrostatics at large molecule separations, while the second approach can sufficiently reproduce the electrostatic potential at narrow distances. In the first approach, we use a linear point quadrupole representation of the electrostatics [see Fig. 1.2(b)]. This kind of approach was already applied for

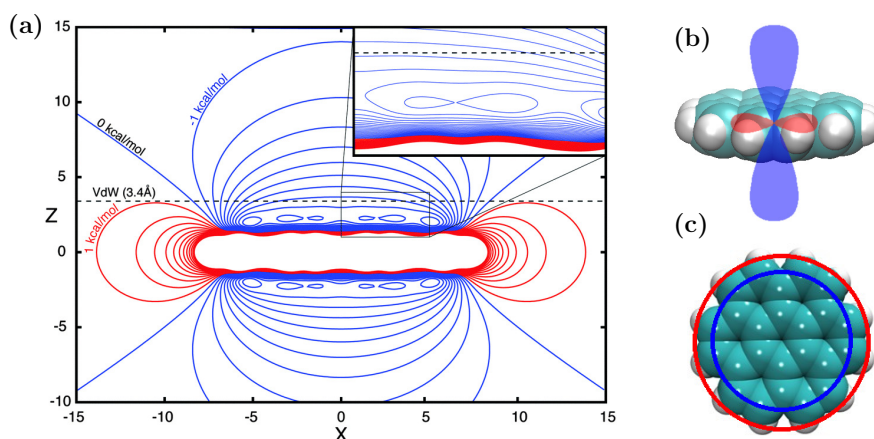


FIGURE 1.2: (a) Side view of the electrostatic potential of coronene. Reproduced from Ref. 101 with permission of the PCCP Owner Societies. (b) Side view of coronene [1] augmented with an electric quadrupole (c) top view of coronene [1] where the electrostatics is implemented through a charged-ring approach [143]. The electrostatics concentric charged rings along the hydrogen atoms (red ring - positive charge) and their neighboring carbon atoms (blue ring - negative charge).

coronene [128] where an overestimation of the interaction strength for planar configurations was observed. We address this point later in our work and investigate this issue in more detail. Nonetheless, this approach was successfully applied to benzene molecules [65] in the liquid phase with an additional dampening field for closed distances. Similar ideas are also used to model the interaction of clay particles [45, 192], which exhibit an electric double layer. In the second approach, we effectively include an extended charge distribution of coronene into our model. Obolensky *et al.* [143] showed that the entire electrostatics can be simplified mainly through two concentric charged rings as depicted in Fig. 1.2(c). This approach already has the desired symmetries, namely uniaxiality and head-to-tail symmetry. A drawback of this elaborate electrostatics model is that the evaluation of the interaction potential is numerically quite time-consuming, because for each pair interaction numerical integrations have to be performed. The value for the point quadrupole as well as those values for the ring charges are suggested in Ref. 143 developed through electronic density functional theory (see Sec. 4.2.2). Both of the present approaches allow a better representation of the $\pi - \pi$ stacking [82, 195] which is also observed in similar aromatic molecules, e.g. benzene dimers [195, 196] and hexabenzocoronene crystals [159].

1.3 Coarse-grained molecular dynamics

We have performed extensive coarse-grained and atomistic molecular dynamics (MD) simulations to explore the phase behavior and structure of bulk coronene systems presented in Chapter 5. Using MD simulations in different length scales provides the possibility to test and verify the application of coarse-graining procedures. The atomistic MD simulations were performed by Karol Palczynski and the corresponding results were used as reference data.

In MD simulations the evaluation of forces and torques is required. Since our determined effective potential (whose derivatives lead to forces and torques) is quite noisy for both biased sampling methods, it is possible that even the pair force has the wrong sign. Monte Carlo simulations, on the contrary, where only the potentials are required, are not suitable since trajectory data for the effective potential might stem from sparsely sampled phase space regions (even with bias simulations). Therefore, we follow the idea of fitting the complex coarse-grained interactions onto rather simple interaction models for coronene and perform MD simulations in different ensembles for all our many-molecule systems. The corresponding models should stabilize the coronene bulk crystal and have to reproduce the phase-transition temperature at the melting point sufficiently. At this point we want to mention that the whole coarse-graining procedure and modeling is representative for similar organic molecules in three dimensions, such as benzene or hexabenzocoronene.

With regard to the literature there have been several attempts at creating a coarse-grained model of coronene [7, 128, 143, 205]. Miller *et al.* [128] proposed a Lennard-Jones model for coronene where the interaction strength parameter is related to the contact distance. For the electrostatics they used a linear point quadrupole approach which we also investigated, as previously mentioned. Another model is given by Lilienfeld and Andrienko [205] who only focused on the face-to-face configuration. A fully more elaborate coarse-grained model is proposed by Babadi *et al.* [7] who described coronene as a biaxial soft disc potential [55]. It is developed by fitting the potential energy for fixed atomistic configurations (with static partial charges) and for various distances and configurations. However, this model is not temperature dependent.

For our approach to model the pair potentials we used an ellipsoidal contact function (see Sec. 5.3) based on the Gay-Berne (GB) potential [63] with minor modifications. With this, each molecule is modeled through one interaction site since the coronene molecule does not exhibit pronounced conformational changes in contrast to polymers or proteins, where more GB-sites [123, 209] are used. As expected, the model with the most fitting parameters performed best in our simulations.

In Fig. 1.3 we present different levels of coarse-grained models for van der Waals coronene in the isotropic phase. Specifically, the atomistic model, a coarse-grained model (our best fit), and a pure distance-dependent model are shown. The latter simple model is not in thermal equilibrium because the entire system condenses (droplet formation). This series of images represent the fact that the choice of coarse-grained variables is crucial and too few coarse-grained variables [such as in the pure-distant model shown in Fig. 1.3(c)] do not represent the original system sufficiently.

1.4 Monolayer study

The coarse-graining strategies introduced so far focusing, to a large extent, on the reproduction of the pair interaction of molecules while keeping the number of degrees of freedom to a manageable amount. The applicability of this bottom-up process is investigated in bulk systems of coronene as described before. A further interesting aspect is to include a surface into the system. In particular, we are interested in the alignment of conjugated organic molecules on inorganic surfaces. These so-called

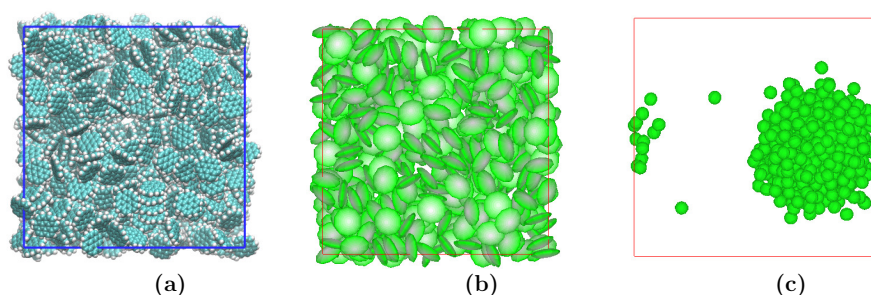


FIGURE 1.3: Snapshots of coronene in the isotropic phase with different levels of coarse-graining. Each molecule is characterized by (a) all its atomic positions [1] (b) center of mass position and axial orientation (c) center of mass position only.

hybrid inorganic/organic systems (HIOS) form a rather new field of application in optoelectronics [21, 22, 46, 167]. Two different experimentally observed structures [116], where coronene (as a conjugated and organic molecule) was grown on the inorganic germanium (001) (with half and full monolayer packing), are shown in Fig. 1.4. In this

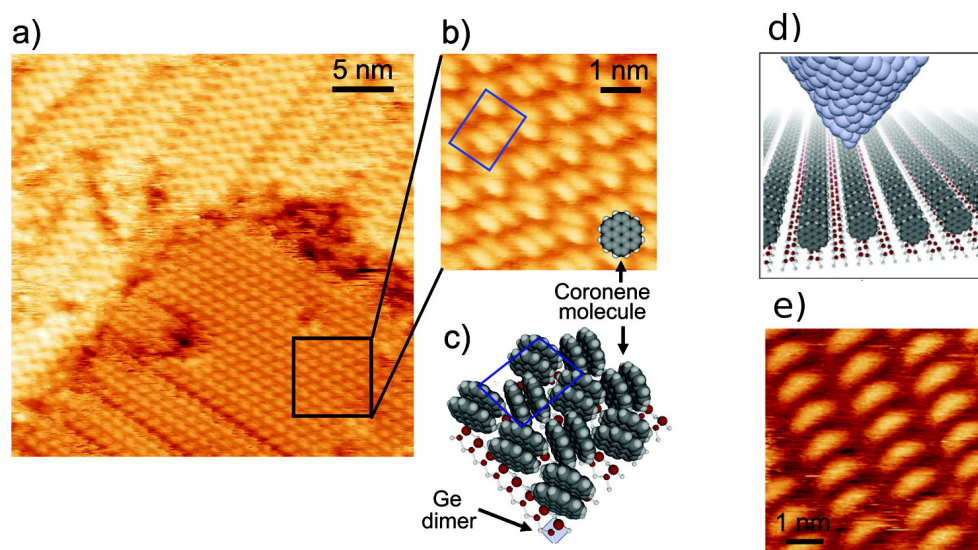


FIGURE 1.4: Steered force microscopy snapshots showing different alignment of coronene deposited on germanium (001). (a)-(c) compact structure (d)-(e) columnar structure. Reprinted with permission from Ref. 116. Copyright 2012 American Chemical Society.

example, column and herringbone-like patterns of coronene are shown. By investigating the morphologies observed in these monolayers it seems possible to tune a HIOS structure towards a higher efficiency in the charge transfer. To calculate the effective interactions, one could apply the same strategy by calculating effective molecule surface potentials additionally to the molecule-molecule potentials. However, pair-wise additivity might be an important issue in these systems since molecule and surface polarization might be rather strong.

At this point we decided to perform a top-down approach. Specifically, we studied a rather simple model for molecules attached to a surface and focused on the phase behavior. The particles are designed to mimic the shape of organic molecules that are bound to a surface. Concerning the shape of the molecules, we defined a purely repulsive but rather hard inter-molecular pair potential that foos on the ellipse-like contact distance of Berne and Pechukas [19]. The utmost reason for confining ourselves to rather hard particles lies in the reduction of the parameter space and the idea of keeping the system as simple as possible in the present study. Strictly speaking, the analytical form of the pair potential is not a hard potential. Specifically, it resembles an anisotropic soft-sphere potential with a higher exponent [165]. Its non-hard character was introduced to account for small inter-molecular overlaps. Furthermore, the numerical simplicity allowed for ground state calculations and MD simulations without specific modifications. Each of our coarse-grained molecule was only allowed to rotate inside the monolayer. In the molecules' center, which marks the only inter-molecular interaction site, lies a linear point quadrupole that is oriented along one ellipsoidal axis, i.e., its symmetry axis is parallel to the surface plane. We employed this constraint because the charge distribution in many organic molecules is approximately that of a linear quadrupole. This quadrupole represents the entire molecular electrostatics. Examples for molecules sharing this kind of symmetry are F4TCNQ, poly(para-phenylene) (e.g., benzene or biphenyl). It is worth mentioning that we did not consider any kind of interaction of the molecules with the surface. In addition, we employed in all our simulations a constant (2D) pressure. The overall goal was to obtain first insights into resulting structures appearing as ground states and at finite temperatures in these type of systems. The ground state structures were calculated by Moritz Antlanger, who used evolutionary algorithms [77]. These structures served as an input for finite temperature simulations. The temperature range covered values from 0K on, up to temperatures where the system shows disorder. An exemplary melting sequence is shown in Fig. 1.5. In this respect, we try to understand complex

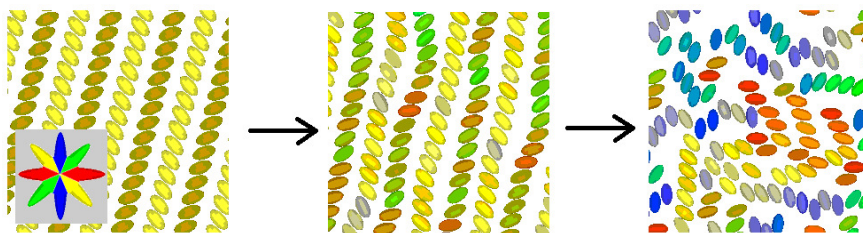


FIGURE 1.5: Exemplary melting sequence of a herringbone packed monolayer of ellipses in two dimensions from the ground state to the disordered phase. A linear quadrupole is attached at the geometric center along the long axis (in the example). Colors denote the particles' orientation.

phase behavior for different temperatures with this simple model. Taken altogether, our model seems quite “tight” since even the inter-molecular van der Waals interaction is neglected. However, using these assumptions, we can transfer our results concerning the equilibrium structures through later introduced relations between the system parameters (see Appendix A.5 and A.6). A further reason to focus on these model

systems lies in the potential applicability to specially manufactured colloidal patchy particles in a confined geometry [133, 144, 177]. We also note that Langmuir monolayers, that describe 2D films of molecules constrained to a liquid-gas interface, form another field of application. Previous Langmuir monolayer studies [93, 94] showed that the arrangement of molecules on a surface can be quite complex. In this respect, two-dimensional liquids with simultaneous orientational and translational ordering were already examined in a density functional study by Kaganer and Osipov [95]. The authors further calculate in their article the order-disorder transition temperature of an herringbone ordered system of hard discs with quadrupole-quadrupole interaction.

Other simulation studies in two dimensions involve hard ellipses [12, 34, 35, 125, 202], rectangles [117] or hard spherocylinders [10] and Janus discs [191]. In contrast to three-dimensional systems, where there is much pioneering work for quadrupolar particles at finite temperature [11, 26, 135, 136, 201] and also at ground state [129], we confined ourselves to this simple system with the purpose to investigate the structure for a large variety of particle aspect ratios and thereby also investigate symmetries in the system parameters.

We found that the phase transitions from order to disorder were of the first kind and spontaneously exhibited both a loss in translational and orientational ordering. In comparison, the melting transition for hard ellipses (density-driven) [34] was found to be of first order for all aspect ratios while the order of the phase transition between isotropic and nematic (parallel alignment of particles) phase in the hard-ellipse system proved to be of first or second order depending on the aspect ratio.

1.5 Structure of this thesis

This thesis is organized as follows: some fundamentals in statistical physics are presented in Chapter 2. Specifically, we describe the considered statistical ensembles with a constant temperature and explain the corresponding velocity distribution. Later on, we introduce the theory of phase transitions that is particularly relevant for the melting of molecular bulk crystals. As for the calculation of structural properties, e.g. order parameters and correlation functions, we present the ergodic hypothesis permitting calculations of ensemble averages within MD simulations. The underlying simulation methods including their computational implementation for the coarse-grained simulations are presented in Chapter 3. The fundamental principle of the transition from the atomistic to a more coarse-grained level of detail are outlined in Chapter 4. In the same chapter, we also define the effective or coarse-grained pair potential. Results for the effective potentials of coronene are presented in Chapter 5. We further demonstrate in Chapter 6 the applicability of our developed effective potentials in many-particle systems of molecules with MD simulations. The last important aspect of this thesis deals with a monolayer system of rather hard quadrupolar ellipses in two dimensions in Chapter 7. Finally, we sum up our findings in Chapter 8 where we also present ideas for future work.

Chapter 2

Fundamentals in statistical mechanics

2.1 Preface

In this chapter, the fundamental principles in statistical mechanics that are essential in this work are introduced. One major challenge in simulating equilibrium many-particle systems of our coarse-grained (CG) coronene molecules (see Chapter 4) or the two-dimensional monolayer-particles (see Chapter 7) is the choice of the correct statistical ensemble. In this respect, we start with the ensemble theory in Sec. 2.2 and introduce the later-used canonical and isobaric-isothermal ensemble. The canonical ensemble (mainly used to develop CG-potentials as described in Chapter 4) describes a coupling with the constant system parameters temperature, particle number and volume. In turn, the isobaric-isothermal ensemble is characterized through a constant pressure, temperature and particle number. We used the latter ensemble for studying crystalline order. In addition, we briefly present the grand canonical ensemble, which we need to derive the virial expansion in Sec. 2.3. This is an expansion of the thermal equation of state in terms of powers of density and its coefficients provide information about the non-ideal gas part for fluids at low densities. We thus calculate the second virial coefficient - which marks the first non-ideal gas coefficient - to investigate the performance of our coarse-graining and modeling (see Sec. 6.2.1). Subsequently, in Sec. 2.4 we investigate the speed distribution from the latter ensembles, which obeys the Maxwell-Boltzmann distribution. A verification of this distribution using our equations of motion is later provided in Chapter 3.3. Thereafter, in Sec. 2.5 we present basic concepts of phase transitions with special regard to solid and fluid phases. Furthermore, the ergodicity assumption is introduced in Sec. 2.6, which allows calculations of ensemble averages based upon trajectory data. Finally, in Sec. 2.7 we present our quantities used for the structural investigations (i.e. correlation functions and order parameters). These topics form the fundament for the next chapters, which build upon it. Concerning the dimensionality, separate expressions are only provided if necessary, since two- and three-dimensional many-particle systems are considered in this work.

2.2 Ensemble theory

In the following, the statistical ensembles that we employed for our calculations in the Chapters 5–7 are presented and analyzed from a statistical and thermodynamic perspective. We hereby present the canonical, the isobaric-isothermal and the grand canonical ensemble. These ensembles comprise coupled systems, where a coupling to a heat bath, pressure bath or particle bath is taken into account. We consider a canonical ensemble in Chapter 5 to obtain histogram functions (Sec. 4.4) of CG coordinates (Sec. 4.3) in a system of two coronene molecules (using Langevin dynamics described in Sec. 3.2). We further consider this type of ensemble in Sec. 6.2.1 [using a Berendsen weak coupling method (Sec. 3.3)] to explore an isotropic phase of coronene molecules. Another important ensemble in our work is the isobaric-isothermal ensemble, which we consider for simulating systems of our coronene models in Chapter 6 and for all our simulations of the monolayer system in Chapter 7. Additionally, we present the grand canonical ensemble to derive the virial expansion in Sec. 2.3, where the second virial coefficient will be used to characterize our coarse-graining procedures in the isotropic phase.

2.2.1 Canonical (NVT) ensemble

In the canonical ensemble the system of interest - i.e. system 1 - is coupled with a much larger system (heat bath), denoted as system 2 (see Fig. 2.1), whereas the overall system is completely isolated. This means that the total energy is fixed. The interaction between both systems is considered as small. System 1 has a fixed number

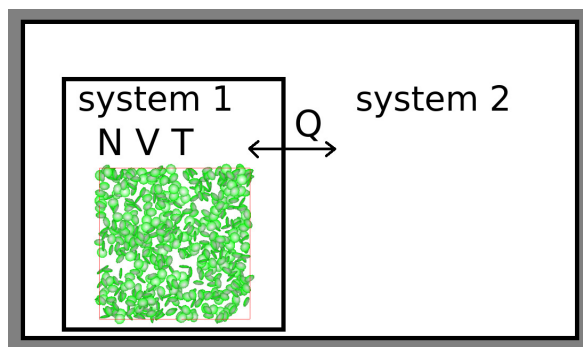


FIGURE 2.1: Illustration of a canonical ensemble. System 1 marks the system of interest and has a fixed volume V as well as particle number N . It is embedded in the much larger system 2. Both systems have the same temperature and only exchange heat. A snapshot for system 1 from our later investigation using a canonical ensemble in Sec. 6.2.1 is included and shows coronene molecules in the isotropic phase.

of particles N in a constant volume V . In contrast to an isolated system, the energy in system 1 is not constant. Furthermore, each microscopic state Γ in system 1 is defined in the present work through the particle positions $\mathbf{r}^N = \{\mathbf{r}_1, \dots, \mathbf{r}_N\}$, momenta \mathbf{p}^N , orientations $\hat{\mathbf{u}}^N$ and angular momenta \mathbf{I}^N . Following Ref. 173, it follows for the

probability density of system 1 being in state Γ with corresponding energy $E(\Gamma)$ is

$$\rho(\Gamma) \approx \frac{e^{-\frac{E(\Gamma)}{kT}}}{Z}, \quad (2.1)$$

where Z is the partition function acting as a normalization constant and the energy kT is a characteristic energy length scale incorporating the most likely energy \tilde{E}_1 in system 1. T is called temperature while k (Boltzmann constant) corrects the dimension and scales the temperature to exhibit step lengths in Kelvin or degree Celsius.

The temperature is a quantity that can be defined in both both sub-systems, yielding

$$T_1 = \left(\frac{\partial}{\partial E_1} S_1 \right)^{-1} \Bigg|_{E_1 = \tilde{E}_1}, \quad \text{with } S_1(E_1) = k \ln \Omega_1(E_1) \quad (2.2a)$$

$$T_2 = \left(\frac{\partial}{\partial E_2} S_2 \right)^{-1} \Bigg|_{E_2 = E - \tilde{E}_1}, \quad \text{with } S_2(E_2) = k \ln \Omega_2(E_2). \quad (2.2b)$$

The symbol S_1 (S_2) is called entropy of system 1 (2) as a function of the energy in system 1 (2). The quantity $\Omega_{1(2)}$ characterizes the number of states of system 1 (2) with a specific energy. The energy \tilde{E}_1 also agrees well with the energy stemming from the following condition

$$\mathcal{S}(E_1) = S_1(E_1) + S_2(E - E_1) = \max \quad (2.3)$$

for a large number of degrees of freedom (> 100) (see Ref. 60). The latter equation can thus be interpreted as an equilibrium condition. This finally leads to the well-known equilibrium condition

$$T_1 = T_2 \equiv T. \quad (2.4)$$

The canonical partition function $Z = Z(N, V, T)$ in Eq. (2.1) subsequently normalizes ρ in Eq. (2.1) according to

$$\begin{aligned} Z(N, V, T) &= \int_{\Omega} d\Gamma \rho(\Gamma) \\ &= \frac{1}{C} \int_{\Pi^{DN}} d\mathbf{p}^N \int_{V^N} d\mathbf{r}^N \int_{\Lambda^{DN}} d\mathbf{l}^N \int_{(S^{D-1})^N} d\hat{\mathbf{u}}^N \exp(-\beta E(\mathbf{p}^N, \mathbf{r}^N, \mathbf{l}^N, \hat{\mathbf{u}}^N)), \end{aligned} \quad (2.5)$$

with $C = C(N)$ being chosen to make Z dimensionless. The total D -dimensional momentum space for each particle is denoted with Π^D , while those for the angular momenta is denoted with Λ^D . The orientations $\hat{\mathbf{u}}_i$ for each particle i are integrated over all possible orientations described through the unit sphere S^{D-1} . Having defined the probability density ρ for each state Γ , it is thus possible to define the expectation value of an observable X as

$$\langle X \rangle_{\text{can}} = \int_{\Omega} d\Gamma X(\Gamma) \rho(\Gamma). \quad (2.6)$$

The equilibrium state of system 1 is characterized via the canonical partition function $Z(N, V, T)$. The free energy marks the transition from statistical mechanics to thermodynamics and is defined by

$$F(N, V, T) = -kT \ln [Z(N, V, T)]. \quad (2.7)$$

This quantity incorporates the whole thermodynamics for these kind of systems and is thus called thermodynamic potential. For given particle number N , volume V and temperature T , the free energy can be written as

$$F(N, V, T) = U_{\text{can}} - T S_{\text{can}}, \quad (2.8)$$

with internal energy $U_{\text{can}} = \langle E \rangle_{\text{can}}$ and canonical entropy $S_{\text{can}} = -k \langle \ln \rho \rangle_{\text{can}}$. Moreover, the equilibrium condition for the canonical ensemble is that $E + k \ln \rho$ is minimized. The free energy thus minimizes the latter expression with the canonical average $\langle \dots \rangle_{\text{can}}$. Since F is a thermodynamic potential U_{can} and S_{can} can also be derived from it. Specifically, we obtain

$$U_{\text{can}} = -T^2 \frac{\partial}{\partial T} \left(\frac{F(N, V, T)}{T} \right) \quad (2.9a)$$

$$S_{\text{can}} = -\frac{\partial}{\partial T} F(N, V, T). \quad (2.9b)$$

It is further interesting to characterize the kind of exchange between system 1 and 2 in a thermodynamic way. The infinitesimal change of entropy of system 1 can be assigned with the second law of thermodynamics to an infinitesimal change in heat, according to

$$\delta Q = T dS_1.$$

The “ δ ” refers to an imperfect differential, indicating that the heat is a path function. However since the temperature is fixed, δQ reduces to dQ . To sum up system 1 can only exchange heat by changing its entropy.

2.2.2 Isobaric-isothermal (NPT) ensemble

In the isobaric-isothermal ensemble, the system is kept at constant pressure P , temperature T and particle number N (see Fig. 2.2). Hereby, not only the energy E but also the volume V is allowed to change. We consider this ensemble for the CG coronene models in Chapter 6 as well as for all our simulations of the monolayer system in Chapter 7. The new partition function Δ can be written in terms of the previously-introduced canonical partition function $Z(N, V, T)$ according to

$$\Delta(N, P, T) = \frac{1}{\mathfrak{e}} \int_{\mathbb{R}^D} Z(N, V, T) e^{-\frac{PV}{kT}} dV, \quad (2.10)$$

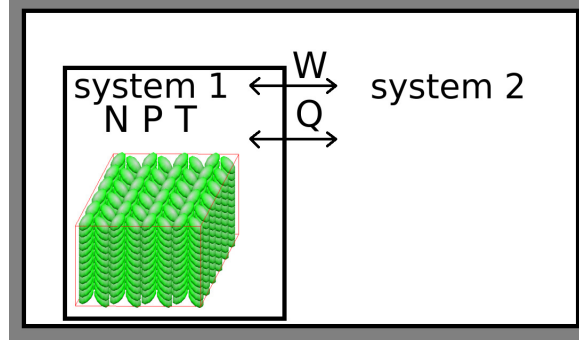


FIGURE 2.2: Illustration of an isobaric-isothermal ensemble. System 1 marks the system of interest and has a fixed particle number N . It is embedded in the much larger system 2. Both systems have the same temperature and pressure. The systems exchange heat Q and work W . A snapshot for system 1 from our later investigation using an isobaric-isothermal ensemble in Sec. 6.3 is included showing coronene molecules in the crystalline phase.

with $\mathfrak{C} = \mathfrak{C}(N)$ being chosen to make Δ dimensionless. The probability density of a certain state Γ with volume V is

$$\rho(\Gamma) \approx \frac{e^{-\frac{E(\Gamma)+PV}{kT}}}{\Delta}. \quad (2.11)$$

The free enthalpy G is the thermodynamic potential for the present ensemble and is defined by

$$G(N, P, T) = -kT \ln [\Delta(N, P, T)] \quad (2.12)$$

as a function of its natural variables N , P , T . The free enthalpy can be further decomposed into

$$G(N, P, T) = U_{(ii)} - TS_{(ii)} + PV_{(ii)}, \quad (2.13)$$

with internal energy $U_{(ii)} = \langle E \rangle_{(ii)}$ and entropy $S_{(ii)} = -k \langle \ln \rho \rangle_{(ii)}$ and volume $V_{(ii)} = \langle V \rangle_{(ii)}$. Moreover, the equilibrium condition for the isobaric-isothermal ensemble is that $E + k \ln \rho + PV$ is minimized. The free enthalpy minimizes the latter expression with the corresponding average $\langle \dots \rangle_{(ii)}$. In analogy to the canonical ensemble, the quantities can be fully determined using the thermodynamic potential alone, i.e.

$$U_{(ii)} = -T^2 \frac{\partial}{\partial T} \left(\frac{G(N, P, T)}{T} \right) + P \frac{\partial G}{\partial P}(N, P, T) \quad (2.14a)$$

$$S_{(ii)} = -\frac{\partial}{\partial T} G(N, P, T) \quad (2.14b)$$

$$V_{(ii)} = \frac{\partial G}{\partial P}. \quad (2.14c)$$

The infinitesimal change of the volume of system 1 can be assigned with the second law of thermodynamics to an infinitesimal change in the mechanical work, according

to

$$\delta W = -P dV_1 \xrightarrow{P=\text{const}} dW.$$

To sum up, system 1 can exchange heat and work by changing entropy (see canonical ensemble) and volume.

2.2.3 Grand canonical (μVT) ensemble

For further investigation (see virial expansion in Sec. 2.3.1), we also briefly consider the grand canonical ensemble, where the temperature T , the volume V and the chemical potential μ is fixed. The probability density of a certain state Γ with particle number N is

$$\rho(\Gamma) \approx \frac{e^{-\frac{E(\Gamma) - \mu N}{kT}}}{Z_{GC}}, \quad (2.15)$$

where Z_{GC} denotes the corresponding grand canonical partition function. The corresponding thermodynamic potential is denoted with

$$\Phi = F - \mu N \quad (2.16)$$

and called grand canonical potential. Furthermore, other standard ensembles exist that allow or forbid exchanges of mechanical work, heat or chemical work.

2.3 Virial expansion

In this section, we present the virial expansion in which the thermal equation of state at low densities is expressed in terms of a generalized ideal gas law. The corresponding non-ideal gas contribution is expressed in higher powers of the density. By comparing the coefficients in this series, it is possible to quantify our method of coarse-graining as performed for coronene (without electrostatic contributions) in the gas phase using the second virial coefficient in Sec. 6.2.1.

2.3.1 Thermal equation of state

The thermal equation of state ($P = P(V, T)$) in the grand canonical ensemble with the natural variables: volume V , temperature T and chemical potential $\mu = -\frac{\partial \Phi}{\partial N}$ is given according to

$$PV = -\Phi = kT \ln(Z_{GC}(\mu, V, T)), \quad (2.17)$$

with the grand canonical partition function Z_{GC} , which is expressed in terms of the canonical partition functions $Z(i, V, T)$ with $z(\mu, T) = e^{\mu/(kT)}$ being the fugacity.

$$Z_{GC}(\mu, V, T) = \sum_{i=0}^{\infty} z^i Z(i, V, T) \quad (2.18)$$

The canonical partition function for a system of i indistinguishable particles is defined as

$$Z(i, V, T) = \frac{1}{i!} \frac{1}{C^{D \cdot i}} \int_{S^{D-1}} d\hat{\mathbf{u}}_1 \int_V d\mathbf{R}_1 \cdots \int_{S^{D-1}} d\hat{\mathbf{u}}_i \int_V d\mathbf{R}_i e^{-\frac{1}{kT} E_{\text{pot}}(\hat{\mathbf{u}}_1, \dots, \hat{\mathbf{u}}_i, \mathbf{R}_1, \dots, \mathbf{R}_i)}, \quad (2.19)$$

with $\frac{1}{i!} \frac{1}{C^{D \cdot i}}$ being a factor that makes $Z(i, V, T)$ dimensionless. Specifically, for $i = 1$ and $i = 2$ we obtain

$$Z(1, V, T) = \frac{\|S^{D-1}\| V}{C^D}, \quad (2.20a)$$

$$\begin{aligned} Z(2, V, T) &= \frac{1}{2} \frac{1}{C^{2D}} \int_{S^{D-1}} d\hat{\mathbf{u}}_1 \int_V d\mathbf{R}_1 \int_{S^{D-1}} d\hat{\mathbf{u}}_2 \int_V d\mathbf{R}_2 e^{-\beta E(\hat{\mathbf{u}}_1, \hat{\mathbf{u}}_2, \mathbf{R}_1, \mathbf{R}_2)} \\ &= \frac{\|S^{D-1}\|^2 V}{C^{2D}} \int_0^\infty dR \int_0^{\pi/2} d\theta_1 \int_0^{\pi/2} d\theta_2 \int_0^\pi d\psi \sin\theta_1 \sin\theta_2 e^{-\beta E(R, \theta_1, \theta_2, \psi)}. \end{aligned} \quad (2.20b)$$

To motivate the virial expansion, Eq. (2.17) will be reformulated for the case of an ideal gas, i.e.

$$\frac{1}{kT} P = \frac{1}{V} \ln(Z_{\text{GC}}^{\text{ideal gas}}(\mu, V, T)), \quad (2.21)$$

with the grand canonical partition function of the ideal gas

$$Z_{\text{GC}}^{\text{ideal gas}}(\mu, V, T) = \sum_N z(\mu, T)^N \frac{Z(1, V, T)^N}{N!} = \exp(z(\mu, T) Z(1, V, T)).$$

Hereby, the canonical partition function of N -particles is represented as a multiplication of one-particle partition functions Z_1 , whose particles are indistinguishable (therefore factor $1/N!$). The logarithm of the grand canonical partition function reduces to

$$\ln(Z_{\text{GC}}^{\text{ideal gas}}(\mu, V, T)) = z(\mu, T) Z(1, V, T).$$

When considering the partial derivative of the upper expression with respect to μ/kT the outcome is identical, i.e.

$$\frac{\partial}{\partial \mu/kT} \ln[Z_{\text{GC}}^{\text{ideal gas}}(\mu, V, T)] = \langle N \rangle = z(\mu, T) Z(1, V, T). \quad (2.22)$$

Moreover, it matches per definition the average particle number $\langle N \rangle$. We thus yield the ideal gas law, which can be written without $\langle \dots \rangle$ in the thermodynamic limit (system size tends to infinity in a way that the surface-volume ratio tends to zero), where all equilibrium ensembles are equal.

$$\frac{1}{kT} P = \frac{\langle N \rangle}{V} \xrightarrow{\text{thermodynamic limit}} \frac{1}{kT} P = \frac{N}{V} \quad (2.23)$$

This expression further motivates the virial expansion for fluids bearing interactions.

2.3.2 Virial expansion coefficients

The virial expansion describes the thermal equation of state for a many-particle system, written as an expansion in terms of density. The first term comprising interactions of particles in this series is called the second virial coefficient B_2 , for which we deliver an explicit expression as necessary in Sec. 6.2.1 to examine the quality of coarse-graining and modeling. The virial expansion is given through

$$\frac{P}{kT} = \frac{N}{V} + B_2(T) \left(\frac{N}{V}\right)^2 + B_3(T) \left(\frac{N}{V}\right)^3 + \dots \quad (2.24)$$

It can be used to describe systems at small densities. Next the explicit expressions for the virial coefficients are motivated. The exact equation of state is given through Eq. (2.17) and can be reformulated with Eq. (2.18) as

$$PV = kT \ln(Z_{\text{GC}}(\mu, V, T)) = kT \ln\left(1 + \sum_{j=1}^{\infty} z(\mu, T)^j Z(j, V, T)\right), \quad (2.25)$$

where $z(\mu, T) = e^{\mu/kT}$ is the fugacity. We next introduce $x = Z_{\text{GC}} - 1$, i.e.

$$x = \sum_{j=1}^{\infty} z^j Z_j = Z_1 \cdot z + Z_2 \cdot z^2 + \dots,$$

where we identify $Z_j = Z(j, V, T)$. For the case of small densities N/V the fugacity and thus x are small. For $0 < 1 + x \leq 2$, the Taylor series of the logarithm developed at point 1 can be written as

$$\ln(1 + x) = x - \frac{x^2}{2} + \frac{x^3}{3} - \frac{x^4}{4} + \dots$$

Therefore, Eq. (2.25) can be reformulated in powers of z , yielding

$$PV = kT \left[(Z_1 \cdot z + Z_2 \cdot z^2 + \dots) - \frac{1}{2} (Z_1 \cdot z + Z_2 \cdot z^2 + \dots)^2 \dots \right] \quad (2.26a)$$

$$= kT \frac{\|S^{D-1}\| V}{C^D} (b_1(T) z + b_2(T) z^2 + \dots). \quad (2.26b)$$

The first two coefficients in the latter formula that do not depend on z , are defined through

$$b_1(T) = \frac{C^D}{\|S^{D-1}\| V} Z_1(T) = 1, \quad (2.27a)$$

$$b_2(T) = \frac{C^D}{\|S^{D-1}\| V} (Z_2(T) - 0.5 \cdot Z_1(T)^2). \quad (2.27b)$$

We next expand z in terms of density to express Eq. (2.26b) as an expansion in terms of density. In this respect, the particle number can be related to z , with the following

thermodynamic relation, yielding

$$N = -\frac{\partial\Phi}{\partial\mu} = \frac{\|S^{D-1}\| V}{C^D} (b_1(T) z + 2b_2(T) z^2 + \dots) \quad (2.28a)$$

$$\frac{N}{V} = \frac{\|S^{D-1}\|}{C^D} (z + 2b_2(T) z^2 + \dots). \quad (2.28b)$$

The latter equation can be approximated (since z is small) through

$$z \approx \frac{N C^D}{V \|S^{D-1}\|} - 2b_2(T) z^2 \quad (2.29a)$$

$$= \frac{N C^D}{V \|S^{D-1}\|} - 2b_2(T) \left(\frac{N C^D}{V \|S^{D-1}\|} - 2b_2(T) z^2 \right)^2. \quad (2.29b)$$

In this expansion [Eq. (2.29b)], we only consider terms up to $(N/V)^2$, i.e.

$$z = \frac{N C^D}{V \|S^{D-1}\|} - 2b_2(T) \left(\frac{N C^D}{V \|S^{D-1}\|} \right)^2. \quad (2.30)$$

With the fugacity expanded in powers of density, Eq. (2.26b) is now rewritten in the fashion of Eq. (2.24), according to

$$\frac{P}{kT} = \frac{N}{V} - b_2(T) \frac{C^D}{\|S^{D-1}\|} \frac{N^2}{V^2} + \dots \quad (2.31)$$

The corresponding second virial coefficient is thus

$$B_2(T) = -b_2(T) \frac{C^D}{\|S^{D-1}\|} = \frac{1}{V} \left(\frac{C^D}{\|S^{D-1}\|} \right)^2 (0.5 \cdot Z_1(T)^2 - Z_2(T)) = \frac{V}{2} - \frac{Z_2}{V} \left(\frac{C^D}{S^{D-1}} \right)^2. \quad (2.32)$$

2.4 Maxwell-Boltzmann distribution

The Maxwell-Boltzmann distribution describes the molecular speed distribution in an equilibrium system at constant temperature and can also be extended to rotations. In the current section, we derive corresponding expressions for two- and three-dimensional systems (denoted by $D = 3$ and $D = 2$) of particles with uniaxial orientation (referring to Chapter 6 and Chapter 7, respectively). This allows us to compare our determined distributions from our simulations with these expressions to verify our implemented dynamics (for the comparison see Sec. 3.3.4).

To proceed, we first focus on the ensemble average of the kinetic energy, which is separated into the translational and rotational part. Specifically, we have

$$\langle E_{\text{kin}} \rangle = \langle E_{\text{trans}} \rangle + \langle E_{\text{rot}} \rangle = \left\langle \sum_i \frac{\mathbf{p}_i^2}{2m_i} \right\rangle + \left\langle \sum_i \frac{\mathbf{l}_i^2}{2I_i} \right\rangle = \left\langle \sum_i \frac{p_i^2}{2m_i} \right\rangle + \left\langle \sum_i \frac{l_i^2}{2I_i} \right\rangle, \quad (2.33)$$

where the \mathbf{p}_i and \mathbf{l}_i denote the momentum and the angular momentum of particle

i , respectively. We next consider a “dummy function” f that solely depends on the absolute of the velocity of one particle, say particle 1, i.e. $f = f(v_1)$ with $v_1 = \|\mathbf{v}_1\| = \|\frac{\mathbf{p}_1}{m}\|$. The expectation value of f is thus written as

$$\langle f(\|\mathbf{v}_1\|) \rangle = \left\langle f\left(\frac{\|\mathbf{p}_1\|}{m_1}\right) \right\rangle \quad (2.34a)$$

$$= \frac{1}{C} \int_{\Pi^{DN}} d\mathbf{p}^N \int_{V^N} d\mathbf{r}^N \int_{\Lambda^{DN}} d\mathbf{l}^N \int_{(S^D)^N} d\hat{\mathbf{u}}^N f\left(\frac{\|\mathbf{p}_1\|}{m_1}\right) \frac{\exp\left(-\frac{1}{kT}(E_{\text{kin}}(\mathbf{p}^N, \mathbf{l}^N) + E_{\text{pot}}(\mathbf{r}^N, \hat{\mathbf{u}}^N))\right)}{\mathcal{Z}} \quad (2.34b)$$

$$= \int_{\Pi^D} d\mathbf{v}_1 f(\|\mathbf{v}_1\|) \frac{\exp\left(-\frac{1}{kT}E_{\text{trans}}(m_1 v_1)\right)}{\mathcal{Z}}, \quad (2.34c)$$

with the new normalization factor

$$\frac{1}{\mathcal{Z}} = \int_{\Pi^{D(N-1)}} d\mathbf{p}_2 \dots d\mathbf{p}_N \int_{V^N} d\mathbf{r}^N \frac{\exp\left(-\frac{1}{kT}(E_{\text{kin}}(p_2 \dots p_N, \mathbf{l}^N) + E_{\text{pot}}(\mathbf{r}^N, \hat{\mathbf{u}}^N))\right)}{\mathcal{Z}}. \quad (2.35)$$

Since the function f as well as the translational kinetic energy for particle 1 in Eq. (2.34c) only depend on the absolute of \mathbf{v}_1 , we can further derive the Maxwell-Boltzmann distribution $\rho(v_1)$ by considering only the integration of the speed v_1 as follows

$$\langle f(\|\mathbf{v}_1\|) \rangle = \int_{\Pi^D} d\mathbf{v}_1 f(\|\mathbf{v}_1\|) \frac{\exp\left(-\frac{1}{kT}\left(\frac{m_1}{2}v_1^2\right)\right)}{\mathcal{Z}} \quad (2.36a)$$

$$= \int_{\Pi_+} dv_1 \rho(v_1) f(v_1), \quad (2.36b)$$

where Π_+ denotes the positive one-dimensional momentum space. For three dimensions ($D = 3$), the resulting Maxwell-Boltzmann distribution and the corresponding kinetic energy distribution are

$$\rho_{3D}^{\text{trans}}(v_1) = 4\pi v_1^2 \frac{\exp\left(-\frac{m_1 v_1^2}{2k_B T}\right)}{\mathcal{Z}_{3d}}, \quad \rho_{\text{kin}}(E_{\text{kin},1}^{\text{trans}}) = \frac{\rho_{3D}^{\text{trans}}\left(\sqrt{\frac{2E_{\text{kin},1}^{\text{trans}}}{m_1}}\right)}{\sqrt{mE_{\text{kin},1}/2}}, \quad (2.37)$$

whereas for two dimensions the following holds

$$\rho_{2D}^{\text{trans}}(v_1) = 2\pi v_1 \frac{\exp\left(-\frac{m_1 v_1^2}{2k_B T}\right)}{\mathcal{Z}_{2d}}, \quad \rho_{\text{kin}}(E_{\text{kin},1}^{\text{trans}}) = \frac{\rho_{2D}^{\text{trans}}\left(\sqrt{\frac{2E_{\text{kin},1}^{\text{trans}}}{m_1}}\right)}{\sqrt{mE_{\text{kin},1}/2}}. \quad (2.38)$$

The symbols \mathcal{Z}_{2d} and \mathcal{Z}_{3d} denote constants, which normalize the distribution function ρ . The translational part of the kinetic energy due to the velocity of particle 1 is thus

$$\left\langle \frac{m_1}{2} v_1^2 \right\rangle = \begin{cases} 3 \frac{kT}{2} & , D = 3 \\ 2 \frac{kT}{2} & , D = 2 \end{cases}. \quad (2.39)$$

For three dimensions ($D = 3$), with uniaxial particles, i.e. $\boldsymbol{\omega}_1 \perp \hat{\mathbf{u}}_1$, the resulting Maxwell-Boltzmann distribution and the corresponding kinetic energy distribution read

$$\rho_{3D}^{\text{rot}}(\omega_1) = 2\pi\omega_1 \frac{\exp\left(-\frac{I_1\omega_1^2}{2k_B T}\right)}{\mathcal{Z}_{3d}}, \quad \rho_{\text{kin}}(E_{\text{kin},1}^{\text{rot}}) = \frac{\rho_{3D}^{\text{rot}}\left(\sqrt{\frac{2E_{\text{kin},1}^{\text{rot}}}{m_1}}\right)}{\sqrt{mE_{\text{kin},1}/2}}, \quad (2.40)$$

whereas for two dimensions the following holds

$$\rho_{2D}^{\text{rot}}(\omega_1) = \frac{\exp\left(-\frac{I_1\omega_1^2}{2k_B T}\right)}{\mathcal{Z}_{2d}}, \quad \rho_{\text{kin}}(E_{\text{kin},1}^{\text{rot}}) = \frac{\rho_{2D}^{\text{rot}}\left(\sqrt{\frac{2E_{\text{kin},1}^{\text{rot}}}{m_1}}\right)}{\sqrt{mE_{\text{kin},1}/2}}. \quad (2.41)$$

The rotational part of the kinetic energy due to rotations of particle 1 can be defined in analogy to the translational part, albeit with the difference that the rotational degrees of freedom correspond the translational degrees of freedom minus 1 (for uniaxial particles). Specifically, we have

$$\left\langle \frac{I_1}{2} \omega_1^2 \right\rangle = \begin{cases} kT & , D = 3 \\ \frac{kT}{2} & , D = 2 \end{cases}. \quad (2.42)$$

To end up, for the kinetic energies for all particles in a D -dimensional system, it follows

$$\langle E_{\text{trans}} \rangle = DN \frac{kT}{2}, \quad \langle E_{\text{rot}} \rangle = (D-1)N \frac{kT}{2}. \quad (2.43)$$

2.5 Phase transitions

Matter may exhibit in various phases that differ in symmetry. A typical phase diagram is illustrated in Fig. 2.3, showing exemplary snapshots of our simulation systems as developed in Chapter 6 for coronene and Chapter 7 for our monolayer systems. By changing the natural variables or (if present) an external field, the system might undergo a phase transition. Ehrenfest introduced a classification of phase transitions. A phase transition of n -th order is given if at least one of the n -th derivative of the Gibbs free enthalpy G (or a suitable thermodynamic potential) is not continuous while lower derivatives are all continuous. The Gibbs free enthalpy can be expressed in terms of the chemical potential μ according to

$$G(N, P, T) = -N \cdot \mu(P, T) = -N \cdot \min \{\mu_1, \dots, \mu_x\}. \quad (2.44)$$

The chemical potential is given through the minimum of all chemical potentials $\mu_i(P, T)$ corresponding to phase i . The number of phases x is given through the Gibbs' phase rule. First-order phase transitions hold most interest in the present work. The first derivatives volume $V = -\left(\frac{\partial G}{\partial P}\right)_T$ and entropy $S = \left(\frac{\partial G}{\partial T}\right)_P$ describe the gradient of G in P and T direction. In Fig. 2.3, a typical phase diagram in the P - T -space of a one component system (of atoms or molecules) is shown (different crystalline phases due to different orientations or bond order are neglected). All phases are separated by lines

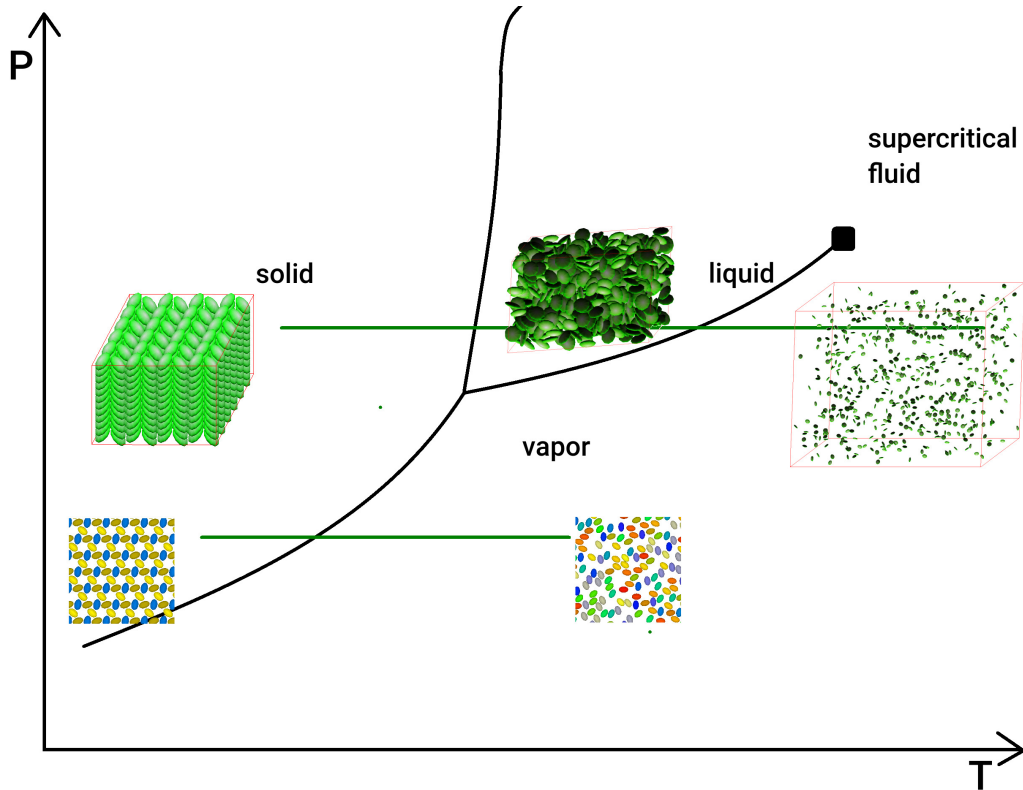


FIGURE 2.3: Exemplary phase diagram of a many-particle system is shown and augmented with snapshots of a coronene model system (using the later-introduced “implicit electrostatics model”; see Chapter 5) and a monolayer system (particles have an aspect ratio of $\kappa = 2.1$; see Chapter 7) in equilibrium. First-order phase transitions are separated by a black solid line. The critical point is denoted with a large dot at the end of the liquid-gas coexistence line. The green lines mark isobaric paths that are investigated later in this work.

describing first-order phase transitions. The green lines in Fig 2.3 illustrate isobaric paths with representative snapshots of our later investigated systems in Chapter 6 and 7. The characteristic behavior of the free enthalpy and its natural variables is shown in Fig. 2.4. The free enthalpy G is concave in all its natural variables. This follows from the positive compressibility condition [173]. Nonetheless, it has kinks at the transition. The first derivatives V and S each reveal a jump at the transition.

For further work, the transitions of the average volume and potential energy along the temperature present major concern. The average potential energy - which is a rather simple quantity to calculate during a simulation - can be reformulated in terms of

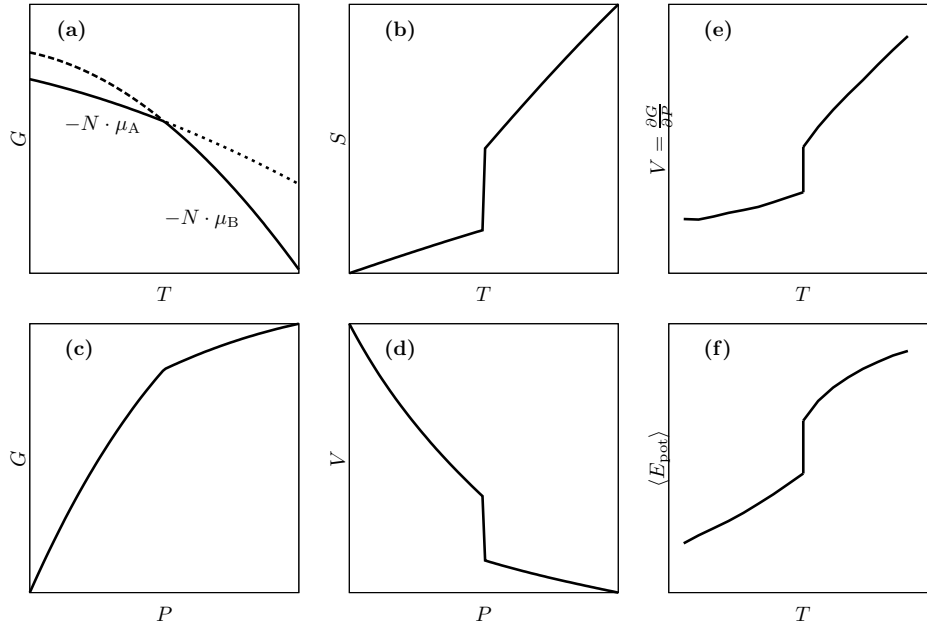


FIGURE 2.4: First-order phase transition shown by means of (a) the free enthalpy G and (b) entropy S as a function of the temperature as well as (c) G and (d) the volume V as a function of the pressure. (e) and (f) show the volume V and the potential energy $\langle E_{\text{pot}} \rangle$ as a function of the temperature.

entropy and volume which exhibit a jump discontinuity at the transition temperature. Specifically, we obtain

$$\langle E_{\text{pot}} \rangle = U - \langle E_{\text{kin}} \rangle = U - f \cdot \frac{kT}{2} \quad (2.45)$$

$$= G(T) + T S(T) - P V(T) - f \cdot \frac{kT}{2}. \quad (2.46)$$

Hereby, f represents the number of degrees of freedom. An interesting feature of first-order phase transitions is the occurrence of hysteresis of an order parameter as a function of the natural variables. For further investigation, the free enthalpy as a function of the volume V can be defined through a volume histogram $\rho(V)$, sampled in the isobaric-isothermal ensemble [168], i.e.

$$G(V) = -kT \ln(\rho(V)) + G_0, \quad \rho(V) = \langle \delta(V - \tilde{V}) \rangle. \quad (2.47)$$

As an example, we consider a temperature-driven phase transition with T_0 being the transition temperature. For this purpose, the free enthalpy reveals a double minimum structure for $T_0^- < T < T_0^+$ as shown in Fig. 2.5(a) for the temperature $T = T_0$. T_0 represents the temperature where both minima of the free enthalpy function are equal, meaning that phase A is as likely as phase B. For simplicity, we say that phase A represents a liquid phase and phase B a vapor phase (vapor is a gas where the temperature is below the critical temperature), since we observe this phase transition for coronene at normal pressure (see Chapter 6). Figs. 2.5(b) and (c) show the extremal

cases (i.e. $T = T_0^-$ and $T = T_0^+$) where the free enthalpy has a minimum and a saddle point. For temperatures lower than T_0 , the system is most likely in phase A, and vice versa. When the system in the liquid phase is heated, it remains longer in the liquid

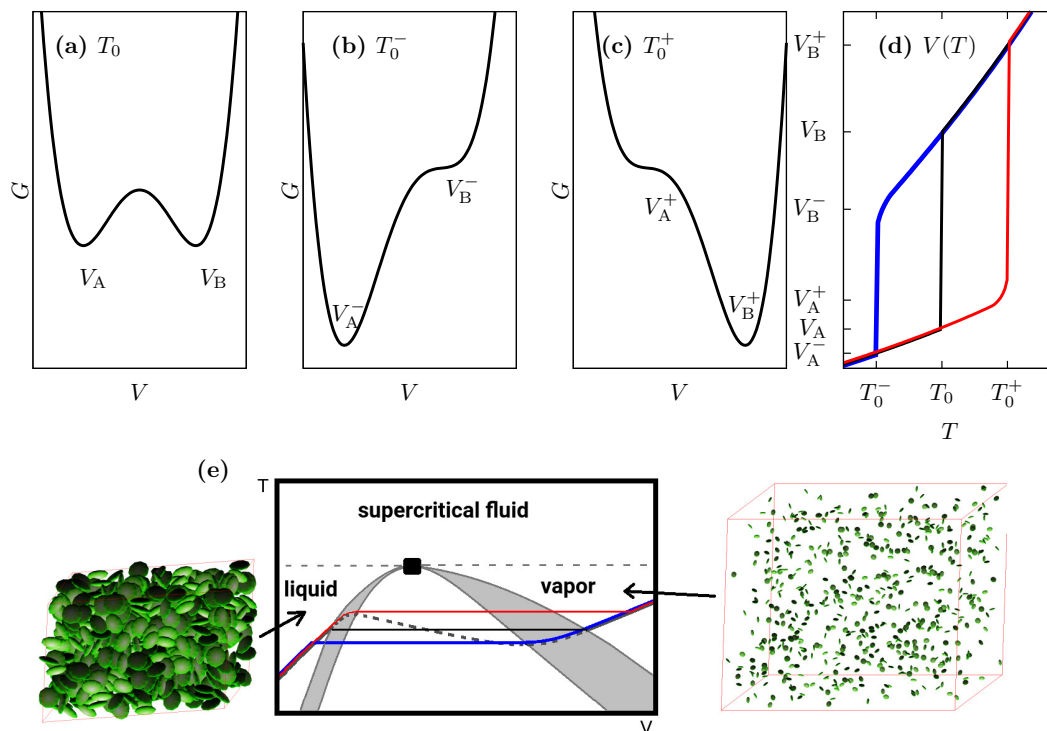


FIGURE 2.5: (a)-(c) Sketch of the free enthalpy near the A-B (e.g. liquid-vapor) phase transition temperature T_0 as a function of the volume for (a) $T = T_0$, (b) $T = T_0^-$, (c) $T = T_0^+$. (d) Volume as a function of temperature for a heating (red) as well as a cooling (blue) procedure and for a minimal free enthalpy (black). (e) Scheme of the phase diagram of coronene near the critical point.

phase up to a temperature T_0^+ , as depicted through the red curves in Figs. 2.5(d) and (e). When cooling the gas, the opposite phenomenon occurs. Accordingly, the liquid phase is reached at a temperature of T_0^- , as indicated by the blue curves. This stems from the fact that the system remains in a local minimum in the transition region (or at least for extremely long times).

Another type of phase transitions are those of second-order or continuous phase transitions. The latter also involves those of higher order. Nowadays, both kind of transitions are no longer distinguished and they are called continuous phase transitions. For example, they occur when the path in the phase diagram goes through the critical point, which we denoted as a black dot in the schematic phase diagram in Fig. 2.3. The free enthalpy and its partial derivatives along P and T through the critical temperature or pressure are shown in Fig. A.2 in Appendix A.1. In principle, one expects kinks in the S - T and V - P curves and thus jump discontinuities in the second derivatives (red curves in Fig. A.2). This is observed in the entropy for superconducting metals. Moreover, many phase transitions of second order reveal an inflexion point where the slope goes to infinity (black curves). Corresponding second derivatives exhibit

singularities at the critical point. The liquid-vapor phase transition at the critical point is an example of this type of second-order phase transition.

An important aspect of phase transitions as a whole is that they can occur in systems only in the thermodynamic limit. This is - roughly speaking - when the system size tends to infinity in a way that the surface-volume ratio tends to zero. Nonetheless, this limit is “practically” reached fast even for relatively small systems. Closer examination reveals that singularities in the n -th derivative of G are realized through very large peaks and step discontinuities are also smoothed [60].

2.6 Ergodicity

An important issue throughout our work is to calculate ensemble averages of many-particle systems in equilibrium out of trajectory data. The ergodicity hypothesis introduced by Boltzmann states that an arbitrary trajectory $\Gamma(t)$ with energy E covers all points in phase space $\Omega(E)$ [60]. This means that the phase space also comprises one phase space trajectory since trajectories are not allowed to cross. In an ergodic system, the following holds

$$\overline{f[\Gamma]} = \lim_{t \rightarrow \infty} \frac{1}{t} \int_0^t f(\Gamma(t')) dt' \stackrel{!}{=} \int_{\Omega(E)} d\Gamma' f(\Gamma') = \langle f \rangle. \quad (2.48)$$

The symbol \overline{f} represents the time average of f [which is a functional of trajectory $\Gamma(t) \in \Omega(E)$] and $\langle f \rangle$ the ensemble average of f . It is thus equivalent when measuring time averages or ensemble averages of observables when the considered time interval tends to infinity.

2.7 Structural properties

In the following, we first introduce pair distribution functions that characterize the structure and further define order parameters for two- and three-dimensional systems. We define the pair distribution functions in the canonical ensemble (see Sec. 2.2.1), and assume the thermodynamic limit (where all ensembles are equal) when using in the isobaric-isothermal ensemble. These functions and parameters are utilized later in Chapter 6 to characterize the structure in coronene bulk systems, as well as in Chapter 7 to investigate the structure of a 2D monolayer system during melting.

2.7.1 Pair distribution functions

In order to introduce the distribution functions, the density operators for the positions \mathbf{r}_i and orientations $\hat{\mathbf{u}}_i$ are given through (for pure position dependence see Ref. 75)

$$\hat{\rho}^{(1)}(\mathbf{r}', \hat{\mathbf{u}}') = \sum_i \delta(\mathbf{r}' - \mathbf{r}_i) \delta(\hat{\mathbf{u}}' - \hat{\mathbf{u}}_i) \quad (2.49)$$

$$\hat{\rho}^{(2)}(\mathbf{r}', \mathbf{r}'', \hat{\mathbf{u}}', \hat{\mathbf{u}}'') = \sum_{i, j \neq i} \delta(\mathbf{r}' - \mathbf{r}_i) \delta(\mathbf{r}'' - \mathbf{r}_j) \delta(\hat{\mathbf{u}}' - \hat{\mathbf{u}}_i) \delta(\hat{\mathbf{u}}'' - \hat{\mathbf{u}}_j). \quad (2.50)$$

The pair distribution function (or pair correlation function) g , describing the correlations between particle positions and orientations, is defined through

$$g(\mathbf{r}', \mathbf{r}'', \hat{\mathbf{u}}', \hat{\mathbf{u}}'') = \frac{\langle \hat{\rho}^{(2)}(\mathbf{r}', \mathbf{r}'', \hat{\mathbf{u}}', \hat{\mathbf{u}}'') \rangle}{\langle \hat{\rho}^{(1)}(\mathbf{r}', \hat{\mathbf{u}}') \rangle \cdot \langle \hat{\rho}^{(1)}(\mathbf{r}'', \hat{\mathbf{u}}'') \rangle}. \quad (2.51)$$

It is equivalent to the relative likelihood that there is a particle at \mathbf{r}' with orientation $\hat{\mathbf{u}}'$ and a second particle at \mathbf{r}'' with orientation $\hat{\mathbf{u}}''$ in comparison to the isotropic phase. By assuming translational invariance, we arrive at the following simplifications for the one particle densities

$$\langle \hat{\rho}^{(1)}(\mathbf{r}', \hat{\mathbf{u}}') \rangle, \langle \hat{\rho}^{(1)}(\mathbf{r}'', \hat{\mathbf{u}}'') \rangle \rightarrow \frac{N}{V} = \rho, \quad (2.52)$$

and the two-particle densities

$$\langle \hat{\rho}^{(2)}(\mathbf{r}', \mathbf{r}'', \hat{\mathbf{u}}', \hat{\mathbf{u}}'') \rangle = \left\langle \hat{\rho}^{(2)}(\mathbf{0}, \underbrace{\mathbf{r}'' - \mathbf{r}'}_{\mathbf{r}}, \hat{\mathbf{u}}', \hat{\mathbf{u}}'') \right\rangle \rightarrow \langle \hat{\rho}^{(2)}(\mathbf{r}, \hat{\mathbf{u}}', \hat{\mathbf{u}}'') \rangle, \quad (2.53)$$

with the vector $\mathbf{r} = \mathbf{r}'' - \mathbf{r}'$ and the modified two-particle density operator

$$\hat{\rho}^{(2)}(\mathbf{r}, \hat{\mathbf{u}}', \hat{\mathbf{u}}'') = \left\langle \sum_{i,j \neq i} \delta(\mathbf{r}_i) \delta(\mathbf{r} - \mathbf{r}_j) \delta(\hat{\mathbf{u}}' - \hat{\mathbf{u}}_i) \delta(\hat{\mathbf{u}}'' - \hat{\mathbf{u}}_j) \right\rangle \quad (2.54)$$

$$= \frac{1}{V} \left\langle \sum_{i,j \neq i} \delta(\mathbf{r} - (\mathbf{r}_j - \mathbf{r}_i)) \delta(\hat{\mathbf{u}}' - \hat{\mathbf{u}}_i) \delta(\hat{\mathbf{u}}'' - \hat{\mathbf{u}}_j) \right\rangle. \quad (2.55)$$

This invariance leads to the pair distribution function around a given particle, namely

$$g(\mathbf{r}, \hat{\mathbf{u}}', \hat{\mathbf{u}}'') = \frac{\langle \hat{\rho}^{(2)}(\mathbf{r}, \hat{\mathbf{u}}', \hat{\mathbf{u}}'') \rangle}{\rho^2}. \quad (2.56)$$

The vector \mathbf{r} represents in the upper equation the connecting vector between the given particle and a second particle.

Further analysis is conducted with the rotational invariant but distance-dependent coefficients of the pair distribution function, denoted with $G^{l_1, l_2, l}(r)$. The decomposition of g is defined as

$$g(\mathbf{r}, \hat{\mathbf{u}}', \hat{\mathbf{u}}'') = \sum_{l_1, l_2, l} G^{l_1, l_2, l}(r) \psi^{l_1, l_2, l}(\hat{\mathbf{r}}, \hat{\mathbf{u}}', \hat{\mathbf{u}}''). \quad (2.57)$$

The coefficients of g are defined in terms of the rotational invariants $\psi^{l_1, l_2, l}$ according to

$$G^{l_1 l_2 l}(r) = \left\langle \frac{1}{V \rho^2 A(r)} \sum_{i,j \neq i} \psi^{l_1 l_2 l}(\hat{\mathbf{r}}_{ij}, \hat{\mathbf{u}}_i, \hat{\mathbf{u}}_j) \delta(|\mathbf{r}_{ij}| - r) \right\rangle, \quad (2.58)$$

where we introduced the vector $\mathbf{r}_{ij} = \mathbf{r}_j - \mathbf{r}_i$ and $A(r) = \begin{cases} 4\pi r^2, & D = 3 \\ 2\pi r, & D = 2 \end{cases}$. In the canonical

ensemble it is also useful to replace ρ^2 by $N(N-1)/V^2$ to satisfy $g \xrightarrow{r \rightarrow \infty} 1$ rather than $1 - 1/N$ [75]. In three dimensions the invariants from Eq. (2.58) are defined as [68]

$$\psi^{l_1, l_2, l}(\hat{\mathbf{r}}_{ij}, \hat{\mathbf{u}}_i, \hat{\mathbf{u}}_j) = f^{l_1, l_2, l} \sum_{m_1, m_2, m} \text{Cg}_{m_1, m_2, m}^{l_1, l_2, l} Y_{l_1, m_1}(\theta_i, \phi_i) Y_{l_2, m_2}(\theta_j, \phi_j) Y_{l, m}^*(\theta, \phi), \quad (2.59)$$

where $f^{l_1, l_2, l}$ is a prefactor and $\text{Cg}_{m_1, m_2, m}^{l_1, l_2, l}$ are the Clebsch-Gordan coefficients. In the present work, we define the coefficients G^{000} , G^{220} and G^{202} through the following rotational invariants for three dimensions as

$$\psi^{000} = 1, \quad \psi^{220} = 3/2(\hat{\mathbf{u}}_i \cdot \hat{\mathbf{u}}_j)^2 - 1/2, \quad \psi^{202} = 3/2(\hat{\mathbf{u}}_i \cdot \hat{\mathbf{r}}_{ij})^2 - 1/2,$$

and for two dimensions as

$$\psi^{000} = 1, \quad \psi^{220} = 2(\hat{\mathbf{u}}_i \cdot \hat{\mathbf{u}}_j)^2 - 1, \quad \psi^{202} = 2(\hat{\mathbf{u}}_i \cdot \hat{\mathbf{r}}_{ij})^2 - 1.$$

The radial distribution function - which involves no orientation dependence - is simply given through $G^{000}(r)$. The coefficient $G^{220}(r)$ is a measure of the mutual alignment of two molecules at a distance r . We further consider the function $G^{202}(r)$, which involves the average of $P_2(\hat{\mathbf{u}}_i \cdot \mathbf{r}_{ij})$ and thus measures the alignment relative to the connecting vector.

We next define a quantity similar to $G^{l_1 l_2 l}$, and denoted with $g^{l_1 l_2 l}$ but numerically feasible and satisfying $g \xrightarrow{r \rightarrow \infty} 1$ for vanishing bin size Δ . We define this function as

$$g^{l_1 l_2 l}(r) = \left\langle \frac{2V}{N(N-1)V_{\text{shell}}(r)} \sum_{i, j > i} \psi^{l_1 l_2 l}(\hat{\mathbf{r}}_{ij}, \hat{\mathbf{u}}_i, \hat{\mathbf{u}}_j) f(r, |\mathbf{r}_{ij}|) \right\rangle, \quad (2.60)$$

where $f(x, y)$ equals unity for $y \in (x, x + \Delta]$, otherwise $f = 0$. The function

$$V_{\text{shell}}(r) = \begin{cases} 4/3\pi((r + \Delta)^3 - r^3) & , D = 3 \\ \pi((r + \Delta)^2 - r^2) & , D = 2 \end{cases}$$

symbolizes the volume shell for a specific bin size Δ .

Another interesting pair distribution function in 3D is one that describes the dependence along (g_{\parallel}) and perpendicular (g_{\perp}) to a given vector $\hat{\mathbf{n}}$. These functions are calculated based on expressions suggested in Ref. 5. However, here we consider normalized versions (where the correlation functions yield unity if no correlation is present). Specifically, we have

$$g_{\parallel}(h) = \left\langle \frac{2V}{V_{\parallel} N(N-1)} \sum_j \sum_{k > j} f(h, \hat{\mathbf{n}} \cdot \mathbf{R}_{jk}) \right\rangle \quad (2.61a)$$

$$g_{\perp}(w) = \left\langle \frac{2V}{V_{\perp}(w) N(N-1)} \sum_j \sum_{k > j} f(w, |\hat{\mathbf{n}} \times \mathbf{R}_{jk}|) \right\rangle. \quad (2.61b)$$

The vectors \mathbf{L}_1 , \mathbf{L}_2 and \mathbf{L}_3 denote the simulation box vectors. In this work $\hat{\mathbf{n}}$ is

considered to lie perpendicular to the box vectors \mathbf{L}_1 and \mathbf{L}_2 . Furthermore, the volumes appearing in Eqs. (2.61a) and (2.61b) are defined as $V_{\parallel} = \Delta |\mathbf{L}_1 \times \mathbf{L}_2|$ and $V_{\perp}(w) = \pi \Delta (2w + \Delta) V |\mathbf{L}_1 \times \mathbf{L}_2|^{-1}$, respectively.

2.7.2 2D order parameters

In order to quantify both the positional and orientational order of the observed structures in Chapter 7, we introduce two different sets of order parameters. We first consider the positional order, which can be quantified using two-dimensional bond-orientational order parameters (BOOPs) modified by weight factors derived from the side lengths of the Voronoi polygon [77]

$$\Psi_n = \left\langle \sum_{i=1}^N \frac{1}{\sum_{j \in \mathcal{N}_i} l_{ij}} \left| \sum_{j \in \mathcal{N}_i} l_{ij} \exp(in\phi_{ij}) \right| \right\rangle, \quad (2.62)$$

where \mathcal{N}_i is the number of nearest neighbors of particle i and $l_{i,j}$ is the side length of the Voronoi polygon associated with neighbor j . The number n determines the n -fold symmetry that we want to investigate. Specifically, we have $\Psi_n = 0$ for random neighbor configurations and unity for perfect n -fold symmetry. In the entire investigation, we only present plots corresponding to $n = 4, 6$, i.e. four- or six-fold bond order. The Voronoi decomposition provides the neighbors for each particle. The Voronoi cell around a particle t is defined through

$$V_{\text{cell}}(t, P) = \bigcap_{q \in P \setminus \{t\}} D(t, q), \quad D(t, q) = \{x \in V_{\text{cell}} : \text{dist}(t, x) < \text{dist}(q, x)\}. \quad (2.63)$$

The set of all particles is hereby denoted with P and the region closer to particle t than to particle q is denoted with $D(t, q)$. The metric “*dist*” refers to the standard metric with respect to the periodic boundary conditions. Figure 2.6 graphically represents the region $D(t, q)$ for an exemplary set of particles. The Voronoi diagram defined through

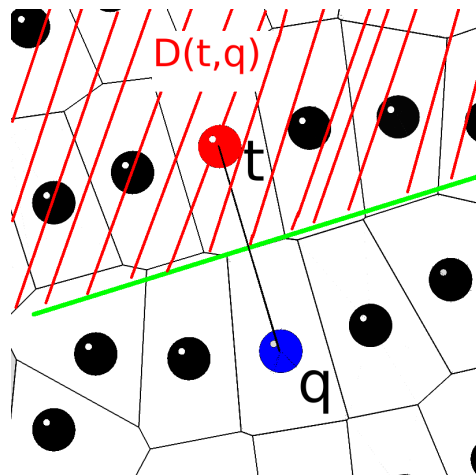


FIGURE 2.6: Voronoi decomposition of a sample configuration. The region $D(t, q)$ includes all points closer to particle t than to particle q .

$$V(P) = \mathbb{R}^2 \setminus \bigcup_{t \in P} V_{\text{cell}}(t, P) \quad (2.64)$$

comprises exactly of all points that form the boundary between the Voronoi cells. For given particle positions, it is thus possible to create this diagram as shown in Fig. 2.7. The implementation of the corresponding algorithm is based upon the program

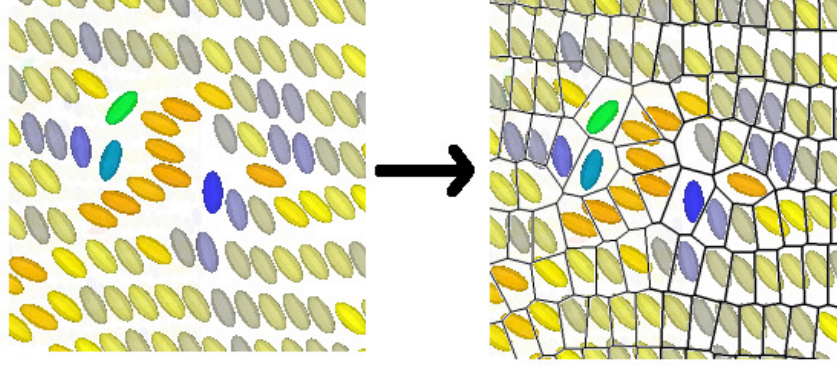


FIGURE 2.7: Voronoi decomposition of a simulation snapshot.

F.23 from Allen and Tildesley [3] and provided by Prof. Mazars (Université Paris Sud).

In the following, we introduce order parameters involving the particles orientation. To describe nematic order in 2D, we introduce the corresponding tensorial order parameter $\underline{\mathbf{Q}}^{2D}$ by

$$\underline{\mathbf{Q}}^{2D} = 2 \left\langle \frac{1}{N} \sum_i \hat{\mathbf{u}}_i \otimes \hat{\mathbf{u}}_i \right\rangle - 1. \quad (2.65)$$

The largest positive eigenvalue S denotes the orientation along or perpendicular to the nematic director, which is defined through the corresponding eigenvector. S itself can have values between 0 (no preferred orientation) and 1 (all particles are oriented parallel to the director).

A different way of measuring the orientational order involving the Voronoi side length l_{ij} is via the parameter β , defined as

$$\beta = \left\langle \frac{1}{N} \sum_{i=1}^N \frac{1}{\sum_{j \in \mathcal{N}_i} l_{ij}} \sum_{j \in \mathcal{N}_i} l_{ij} |(\hat{\mathbf{u}}_i \cdot \hat{\mathbf{u}}_j)| \right\rangle. \quad (2.66)$$

The absolute of the projection $\hat{\mathbf{u}}_i \cdot \hat{\mathbf{u}}_j$ leads to values of 1, for parallel alignment and 0 for orthogonal alignment. The contribution of each neighbor is weighted with the polygon side length l_{ij} to avoid strong neighbor fluctuations for similar configurations.

Furthermore, we introduce a parameter α involving orientational and positional order according to

$$\alpha = \left\langle \frac{1}{2N} \sum_{i=1}^N \frac{1}{\sum_{j \in \mathcal{N}_i} l_{ij}} \sum_{j \in \mathcal{N}_i} l_{ij} |(\hat{\mathbf{u}}_i \cdot \hat{\mathbf{r}}_{ij})^2 + (\hat{\mathbf{u}}_j \cdot \hat{\mathbf{r}}_{ij})^2| \right\rangle. \quad (2.67)$$

2.7.3 3D order parameters

In order to describe the alignment in three dimensions, we introduce a tensorial order parameter $\underline{\mathbf{Q}}^{3D}$ in analogy to Eq. (2.65) for three dimensions, namely

$$\underline{\mathbf{Q}}^{3D} = 1.5 \left\langle \frac{1}{N} \sum_i \hat{\mathbf{u}}_i \otimes \hat{\mathbf{u}}_i \right\rangle - 0.5. \quad (2.68)$$

The eigenvector corresponding to the largest eigenvalue (in positive direction) can be associated with the director $\hat{\mathbf{n}}$ of the system. The largest positive eigenvalue is also given through [50]

$$\bar{P}_2 = \frac{1}{N} \left\langle \sum_i P_2(\hat{\mathbf{u}}_i \cdot \hat{\mathbf{n}}) \right\rangle. \quad (2.69)$$

It yields zero for isotropic ordering and unity for nematic ordering. Furthermore, we consider a hexagonal bond order parameter (ψ_6) in analogy to Eq. (2.62) for 3D systems suitable for columnar configurations (see Chapter 6). The latter is defined as

$$\psi_6 = \frac{1}{N} \left\langle \sum_j \sum_{k \in \mathcal{N}_j} e^{i6\phi_{jk}} \right\rangle, \quad (2.70)$$

where ϕ_{jk} is the bond orientation angle and \mathcal{N}_j the number of neighbors of molecule j in its current layer perpendicular to the director.

Chapter 3

Simulation methods

3.1 Preface

Classical molecular dynamics (MD) is a method to calculate the motion of particles in a many-particle system based upon the Newtonian equations of motion. The translational movement of the particle with mass m_i , positions \mathbf{r}_i depends on the force \mathbf{F}_i pulling on particle i according to

$$m_i \dot{\mathbf{r}}_i = \mathbf{F}_i, \quad (3.1)$$

while for the rotational movement - where we have the orientation vector of particle i denoted with $\hat{\mathbf{u}}_i$, the angular velocity $\boldsymbol{\omega}_i$, torque \mathbf{M}_i and inertia tensor \mathbf{I}_i of particle i - the following holds

$$\ddot{\hat{\mathbf{u}}}_i = \dot{\boldsymbol{\omega}}_i \times \hat{\mathbf{u}}_i + \boldsymbol{\omega}_i \times \dot{\hat{\mathbf{u}}}_i \quad (3.2)$$

$$\mathbf{I}_i \dot{\boldsymbol{\omega}}_i = \mathbf{M}_i. \quad (3.3)$$

The dots in the previous equations represent the time derivative, i.e. $\dot{(\)} = d/dt$. Explicit expressions for the force and torque for the models considered in our work can be found in Appendix A.2. In the present work, a coupling of our many-particle system to a heat bath and pressure bath is performed. For this purpose, the Newtonian equations of motion [Eqs. (3.1)–(3.3)] have to be modified. There are various thermostats [29, 54, 81, 103, 107, 108, 118, 141, 142, 164] and barostats [27, 58, 86, 119, 126, 149, 156] in the literature. We hereby start with the Langevin dynamics (Sec. 3.2) used for tempering the atomistically-resolved two-molecule system (described in Chapter 4; results in Chapter 5). Later, we describe the Berendsen dynamics (Sec. 3.3) for temperature and pressure coupling, which we used for all our coarse-grained simulations (see Chapter 6 and 7). We also briefly present an elaborate method invented by Bussi *et al.* [29] (Sec. 3.4) for temperature coupling and thereby conserving the Maxwell-Boltzmann distribution (Sec. 2.4). The latter method was used to temper the atomistically-detailed two-molecule system for our coarse-graining method (see Sec. 4.2.1). The remaining sections in this chapter mainly deal with technical aspects. In this respect, we present our method to treat the periodic boundary conditions (Sec. 3.5), describe how we set up random configurations (Sec. 3.6), outline the numerical treatment of interactions (Sec. 3.7) and finally present techniques to speed up

our simulations (Sec. 3.8).

3.2 Langevin dynamics (LD)

In this kind of dynamics, there is a temperature control implicitly involved through a stochastic term. This dynamics extends molecular dynamics since it involves diffusive motion as caused by the solvent. The positions of the particles evolve in time according to

$$m_i \ddot{\mathbf{r}}_i(t) = -\nabla_i E_{\text{pot}}(\{\mathbf{r}\}, t) - \gamma m_i \dot{\mathbf{r}}_i(t) + \sqrt{2\gamma k_B T} m_i \mathbf{X}(t). \quad (3.4)$$

In Eq. (3.4), $\mathbf{X}(t)$ is a vector whose components $X_\alpha(t)$ are Gaussian random numbers with $\langle X_\alpha(t) \rangle = 0$, $\langle X_\alpha(t) X_\beta(t') \rangle = \delta_{\alpha\beta} \delta(t - t')$. The friction constant is denoted with γ , and the two non-conservative forces in the last two terms are coupled via the fluctuation-dissipation theorem. In the actual atomic simulations [1], the equations of motion [see Eq. (3.4)] are supplemented by constraints or bias potentials using umbrella sampling (US) as well as steered dynamics (SD) as described in Sec. 4.4. The resulting set of equations is solved with the GROMACS [197] simulation package, using version 4.5.4 for the SD method and version 4.5.5¹ for the US method.

3.3 Berendsen weak-coupling scheme

In order to investigate structural changes of our coarse-grained system at finite pressure and temperature, we perform MD simulations with specific modifications. In our implementation, we use a Berendsen weak-coupling scheme [17], which supplements the classical Newtonian MD scheme with a heat bath and pressure bath. The temperature coupling mechanism is essentially given through a LD scheme, albeit only with global coupling to the bath. Although the resulting dynamics does not correctly reproduce the energy or volume fluctuations in the isobaric-isothermal ensemble, it seems very useful for equilibrating a system at constant temperature and pressure [3]. Since we investigate the system in the equilibrium and do not calculate dynamic properties or fluctuations, this kind of coupling is an appropriate choice.

We next introduce the translational equations of motion proposed by Berendsen *et al.* [17] and later describe the dynamics for the rotational movement. We additionally provide the numerical algorithm and briefly present speed distributions from later calculations using this algorithm.

¹It was used due to a fatal bug in the previous build

3.3.1 Translation

The translational equations of motion for a particle with index i are given by

$$\dot{\mathbf{r}}_i = \mathbf{v}_i + \frac{K}{\tau_P} (\underline{\mathcal{P}} - \underline{\mathbf{P}}) \cdot \mathbf{r}_i \quad (3.5a)$$

$$m_i \dot{\mathbf{v}}_i = \mathbf{F}_i + m_i \frac{1}{2\tau_{\text{trans}}} \left(\frac{T}{\mathcal{T}_{\text{trans}}} - 1 \right) \mathbf{v}_i \quad (3.5b)$$

$$\dot{\mathbf{L}}_i = \left[\frac{K}{\tau_P} (\underline{\mathcal{P}} - \underline{\mathbf{P}}) \right] \cdot \mathbf{L}_i. \quad (3.5c)$$

In the above equations, the dotted symbols represent time-derivatives. Further, \mathbf{r}_i and \mathbf{v}_i denote the position and the velocity of particle with index i , respectively, while \mathbf{F}_i is the force on particle i with mass m_i . The microscopic temperature

$$\mathcal{T}_{\text{trans}} = \sum_i m v_i^2 / (D(N-1)) / k_B \quad (3.6)$$

is forced to relax towards the target temperature T . The symbols D and K_B represent the dimensionality of the system and the Boltzmann constant, respectively, while the denominator $D(N-1)$ stands for $D \cdot N$ translational degrees of freedom minus D momentum constraints in each spatial direction.

Furthermore, the vectors \mathbf{L}_i that define the simulation box have to fulfill Eq. (3.5c). The time constants for temperature and pressure are denoted with τ_{trans} and τ_P , respectively. They characterize the coupling of temperature $\mathcal{T}_{\text{trans}}$ and pressure tensor $\underline{\mathcal{P}}$ with the bath according to

$$\dot{\mathcal{T}}_{\text{trans}} = \frac{T - \mathcal{T}_{\text{trans}}}{\tau_{\text{trans}}} \quad (3.7a)$$

$$\dot{\underline{\mathcal{P}}} = \frac{\underline{\mathbf{P}} - \underline{\mathcal{P}}}{\tau_P}. \quad (3.7b)$$

To couple the pressure anisotropically to the system - whereby the box vectors \mathbf{L}_i can be changed independently - we have to calculate the difference of the pressure tensor, $\underline{\mathcal{P}}$, defined via [32]

$$\underline{\mathcal{P}} = \frac{1}{DV} \left[\sum_i m_i \mathbf{v}_i \otimes \mathbf{v}_i + \sum_{i < j} \mathbf{r}_{ij} \otimes \mathbf{F}_{ij} \right], \quad (3.8)$$

and the reference pressure tensor, $\underline{\mathbf{P}}$, defined as

$$\underline{\mathbf{P}} = \frac{P}{D} \underline{\mathbf{1}}, \quad (3.9)$$

with $\text{trace}(\underline{\mathbf{P}}) = P$ being the scalar pressure. The simulation box volume is denoted with $V(t) = \|\det[\mathbf{L}_1(t) \dots \mathbf{L}_D(t)]\|$ and $\underline{\mathbf{1}}$ is the identity matrix. The force \mathbf{F}_{ij} in Eq. (3.8) is the force on particle i exerted by particle j .

3.3.2 Rotation

We next include rotational dynamics into our system for the exemplary case of three spatial dimensions ($D = 3$). The two-dimensional case is recovered when considering all elements and their orientations to the x-y-plane. For the rotational movement of the particles, their translational equations of motion are supplemented with the following differential equations for the angular velocities, $\boldsymbol{\omega}_i$:

$$\ddot{\hat{\mathbf{u}}}_i = \dot{\boldsymbol{\omega}}_i \times \hat{\mathbf{u}}_i + \boldsymbol{\omega}_i \times \dot{\hat{\mathbf{u}}}_i \quad (3.10)$$

$$\underline{\mathbf{I}}_i \dot{\boldsymbol{\omega}}_i = \mathbf{M}_i + \frac{\underline{\mathbf{I}}_i}{2\mathcal{T}_{\text{rot}}} \left(\frac{T}{\mathcal{T}_{\text{rot}}} - 1 \right) \boldsymbol{\omega}_i. \quad (3.11)$$

As mentioned in the beginning of this chapter, \mathbf{M}_i and $\underline{\mathbf{I}}_i$ denote in the above equations the torque on particle i and the corresponding inertia tensor of particle i , respectively. The microscopic temperature for the rotation is defined as

$$\mathcal{T}_{\text{rot}} = \sum_i \boldsymbol{\omega}_i (\underline{\mathbf{I}}_i \boldsymbol{\omega}_i) / k_B / ((D - 1)N). \quad (3.12)$$

To solve the translational equations of motion, Eqs. (3.5a)–(3.5c), we use a modified leap-frog integrator, as proposed in Ref. 17. Regarding the rotational part in Eqs. (3.10)–(3.11), an analogous procedure is performed [59].

The evaluation of the torque on particle i using the pair potential U_{ij} is achieved according to

$$\mathbf{M}_i(t) = - \left[\mathbf{e}_{\theta_i} \frac{\partial}{\partial \theta_i} + \frac{1}{\sin(\theta_i)} \mathbf{e}_{\phi_i} \frac{\partial}{\partial \phi_i} \right] \sum_j U_{ij} = -\hat{\mathbf{u}}_i \times \sum_j \nabla_{\hat{\mathbf{u}}_i} U_{ij}, \quad (3.13)$$

where the unit vector of orientation of particle i is represented in spherical coordinates, i.e.

$$\hat{\mathbf{u}}_i(\theta_i, \phi_i) = \begin{pmatrix} \cos(\phi_i) \sin(\theta_i) \\ \sin(\phi_i) \sin(\theta_i) \\ \cos(\theta_i) \end{pmatrix}. \quad (3.14)$$

The spherical unit vectors appearing in Eq. (3.13) are defined as

$$\mathbf{e}_{\theta_i} = \begin{pmatrix} \cos(\phi_i) \cos(\theta_i) \\ \sin(\phi_i) \cos(\theta_i) \\ -\sin(\theta_i) \end{pmatrix}, \quad \mathbf{e}_{\phi_i} = \begin{pmatrix} -\sin(\phi_i) \sin(\theta_i) \\ \cos(\phi_i) \sin(\theta_i) \\ 0 \end{pmatrix}. \quad (3.15)$$

The angular acceleration $\boldsymbol{\alpha}_i$ is determined from the torque $\underline{\mathbf{M}}_i$ using the inertia tensor $\underline{\mathbf{I}}_i$ according to

$$\boldsymbol{\alpha}_i(t) = \underline{\mathbf{I}}_i^{-1} \underline{\mathbf{M}}_i(t). \quad (3.16)$$

The inertia tensor can be diagonalized in the following form

$$\underline{\mathbf{B}}^{-1}\underline{\mathbf{I}}_i\underline{\mathbf{B}} = \begin{pmatrix} I_i & 0 & 0 \\ 0 & I_i & 0 \\ 0 & 0 & I_{\hat{\mathbf{u}}_i} \end{pmatrix}, \quad (3.17)$$

where the z-z-component represents the moment of inertia around the symmetry axis $\hat{\mathbf{u}}_i$. However, since rotations around $\hat{\mathbf{u}}_i$ do not influence any interactions, we do not take this degree of freedom into account. For uniaxial particles, the following statement holds

$$\mathbf{M}_i(t) \perp \hat{\mathbf{u}}_i. \quad (3.18)$$

This means that the inertia tensor can be simply replaced by the scalar moment of inertia I_i for rotations orthogonal to $\hat{\mathbf{u}}_i$.

3.3.3 Solving the Berendsen equations of motion

The numerical implementation for one integration step of the Berendsen equations of motion are presented in the following. We start with the positions $\mathbf{r}^N(t)$, orientations $\hat{\mathbf{u}}^N(t)$ and linear and angular velocities $\mathbf{v}^N(t - \Delta t/2)$, $\boldsymbol{\omega}^N(t - \Delta t/2)$, and box vectors $\mathbf{L}_i(t)$. The following integrator reduces to the well-known leap frog algorithm used for classical MD simulations, if pressure and temperature control is neglected.

- The accelerations for each particle are determined with the actual force on each particle, i.e.

$$\mathbf{a}_i(t) = \frac{\mathbf{F}_i(t)}{m}, \quad \mathbf{F}_i(t) = \sum_j \mathbf{F}_{ij} = \sum_j \nabla U_{ij}.$$

In analogy, the angular accelerations are related to the actual torque, yielding

$$\boldsymbol{\alpha}_i(t) = \underline{\mathbf{I}}^{-1}\mathbf{M}_i(t), \quad \mathbf{M}_i(t) = -\hat{\mathbf{u}}_i \times \sum_j \nabla_{\hat{\mathbf{u}}_i} U_{ij}.$$

- The geometry matrix $\underline{\boldsymbol{\mu}}$ is given through

$$\underline{\boldsymbol{\mu}} = \underline{\mathbf{1}} + \frac{K\Delta t}{\tau_P} (\underline{\mathcal{P}} - \underline{\mathbf{P}}),$$

with the compressibility K and the pressure tensors

$$\underline{\mathcal{P}} = \frac{1}{2V} \left[\sum_i m \mathbf{v}_i(t - \Delta t/2) \otimes \mathbf{v}_i(t - \Delta t/2) + \sum_{i < j} \mathbf{r}_{ij}(t) \otimes \mathbf{F}_{ij}(t) \right], \quad \underline{\mathbf{P}} = \frac{P}{D} \underline{\mathbf{1}}.$$

- The microscopic temperatures for translation and rotation are given through

$$\mathcal{T}_{\text{trans}}(t - \Delta t/2) = \sum_i m v_i(t - \Delta t/2)^2 / (D(N - 1)) / k_B$$

$$\mathcal{T}_{\text{rot}}(t - \Delta t/2) = \sum_i I_i \omega_i(t - \Delta t/2)^2 / k_B / N.$$

These quantities are used to calculate the following rescaling factors

$$\lambda_{\text{trans}} = \sqrt{1 + \frac{\Delta t}{\tau_{\text{T}}^{\text{trans}}} \left(\frac{T}{\mathcal{T}_{\text{trans}}(t - \Delta t/2)} - 1 \right)}$$

$$\lambda_{\text{rot}} = \sqrt{1 + \frac{\Delta t}{\tau_{\text{T}}^{\text{rot}}} \left(\frac{T}{\mathcal{T}_{\text{rot}}(t - \Delta t/2)} - 1 \right)}.$$

- The new velocities for translation and rotation at $t + \Delta t/2$ can be determined through

$$\mathbf{v}_i(t + \Delta t/2) = \lambda_{\text{trans}} \cdot (\mathbf{v}_i(t - \Delta t/2) + \mathbf{a}_i(t)\Delta t)$$

$$\boldsymbol{\omega}_i(t + \Delta t/2) = \lambda_{\text{rot}} \cdot (\boldsymbol{\omega}_i(t - \Delta t/2) + \boldsymbol{\alpha}_i(t)\Delta t).$$

- The new positions and orientations at $t + \Delta t$ can now be determined. For the positions, the following expression is used

$$\mathbf{r}_i(t + \Delta t) = \underline{\boldsymbol{\mu}} \cdot (\mathbf{r}_i(t) + \mathbf{v}_i(t + \Delta t/2)\Delta t).$$

The new orientation vector $\hat{\mathbf{u}}_i(t + \Delta t)$ can be written as a rotation of the old orientation vector $\hat{\mathbf{u}}_i(t)$ around the axis $\hat{\mathbf{n}}$ with angle ϕ [both being functions of $\boldsymbol{\omega}(t + \Delta t/2)$]. The corresponding rotation matrix is denoted with $R_{\hat{\mathbf{n}},\phi}$. Specifically, we yield

$$\hat{\mathbf{u}}_i(t + \Delta t) = R_{\hat{\mathbf{n}},\phi} \hat{\mathbf{u}}_i(t). \quad (3.19)$$

The corresponding rotation axis is

$$\hat{\mathbf{n}} = \frac{\hat{\mathbf{u}}_i(t) \times \hat{\mathbf{u}}_i(t + \Delta t)}{\|\hat{\mathbf{u}}_i(t) \times \hat{\mathbf{u}}_i(t + \Delta t)\|} = \frac{\boldsymbol{\omega}(t + \Delta t/2)}{\|\boldsymbol{\omega}(t + \Delta t/2)\|}.$$

The right-hand angle to get from $\hat{\mathbf{u}}_i(t)$ to $\hat{\mathbf{u}}_i(t + \Delta t)$ around the axis is

$$\phi = \|\boldsymbol{\omega}(t + \Delta t/2)\| \cdot \Delta t.$$

To solve Eq. (3.19), the Rodriguez formula² is used. Specifically, we have

$$\begin{aligned} \hat{\mathbf{u}}_i(t + \Delta t) &= R_{\hat{\mathbf{n}},\phi} \hat{\mathbf{u}}_i(t) \\ &= \underbrace{\hat{\mathbf{n}} (\hat{\mathbf{n}} \cdot \hat{\mathbf{u}}_i)}_0 + \underbrace{\cos(\phi)}_{\approx \sqrt{1-\phi^2}} \underbrace{((\hat{\mathbf{n}} \times \hat{\mathbf{u}}_i) \times \hat{\mathbf{n}})}_{\hat{\mathbf{u}}_i} + \underbrace{\sin(\phi)}_{\approx \phi} (\hat{\mathbf{n}} \times \hat{\mathbf{u}}_i). \end{aligned}$$

This expression can be approximated when using $\sin(\phi) \approx \phi$, $\cos(\phi) \approx \sqrt{1 - \phi^2}$ to the following formula

$$\hat{\mathbf{u}}_i(t + \Delta t) = \sqrt{1 - \phi^2} \hat{\mathbf{u}}_i + (\phi \hat{\mathbf{n}} \times \hat{\mathbf{u}}_i).$$

² Rodriguez formula: rotation of \mathbf{v} around $\hat{\mathbf{n}}$ with right-hand angle ϕ given through $R_{\hat{\mathbf{n}},\phi} \mathbf{v} = \hat{\mathbf{n}} (\hat{\mathbf{n}} \cdot \mathbf{v}) + \cos(\phi) ((\hat{\mathbf{n}} \times \mathbf{v}) \times \hat{\mathbf{n}}) + \sin(\phi) (\hat{\mathbf{n}} \times \mathbf{v})$.

However, further normalization is required, i.e. $\hat{\mathbf{u}}_i(t + \Delta t) \rightarrow \frac{\hat{\mathbf{u}}_i(t + \Delta t)}{\|\hat{\mathbf{u}}_i(t + \Delta t)\|}$.

- Finally, the new box vectors are determined according to

$$\mathbf{L}_i(t + \Delta t) = \underline{\boldsymbol{\mu}} \mathbf{L}_i(t).$$

The particle positions $\mathbf{r}_i(t)$ are subsequently adjusted to the new simulation box geometry as described later in Sec. 3.5.1.

3.3.4 Speed probability distribution

The positional and angular speed distribution for uniaxial 3D and 2D particles using the Berendsen weak-coupling scheme is investigated in Fig. 3.1. For comparison, we added the reference curves for the positional (Eq. (2.37) and (2.38)) and angular speed distribution (Eq. (2.40) and (2.41)) from Sec. 2.4. We denote a very strong coincidence of our measured speed distributions with the reference values. Nonetheless, in the next section we present a method for the temperature coupling with accurate speed distribution.

3.4 Canonical velocity rescaling scheme

The canonical velocity rescaling thermostat is essentially a Berendsen thermostat (see above) with a minor modification [2]. It was used for atomistically-resolved simulations of the columnar hexagonal phase (see Sec. 6.2.2) by Karol Palczynski [1]. This temperature coupling method was invented by Bussi *et al.* [29]. Rather than Eq. (3.7a), this thermostat considers with

$$dE_{\text{kin}} = (\bar{E}_{\text{kin}} - E_{\text{kin}}) \frac{dt}{\tau_T} + 2 \sqrt{\frac{E_{\text{kin}} \bar{E}_{\text{kin}}}{N_f}} \frac{dW}{\sqrt{\tau_T}} \quad (3.20)$$

a correct kinetic energy distribution and according to Eqs. (2.37), (2.38) or Eqs. (2.40), (2.41) a correct speed distribution. Hereby, N_f is the number of degrees of freedom and dW is a Wiener process. The average kinetic energy is related to the temperature according to $\bar{E}_{\text{kin}} = N_f kT/2$. This thermostat produces a correct speed distribution of the canonical ensemble and still has the advantage of the Berendsen thermostat, namely first-order decay of temperature deviations and no oscillations.

The simplest realization is to rescale the velocities in each time step with a factor

$$\lambda_{\text{trans}} = \sqrt{\frac{E_{\text{kin}}^{\text{target}}}{E_{\text{kin}}}},$$

where the targeted kinetic energy $E_{\text{kin}}^{\text{target}}$ obeys the following distribution

$$\rho(E_{\text{kin}}^{\text{target}}) dE_{\text{kin}}^{\text{target}} \propto (E_{\text{kin}}^{\text{target}})^{N_f/2-1} e^{-\frac{E_{\text{kin}}^{\text{target}}}{kT}} dE_{\text{kin}}^{\text{target}}. \quad (3.21)$$

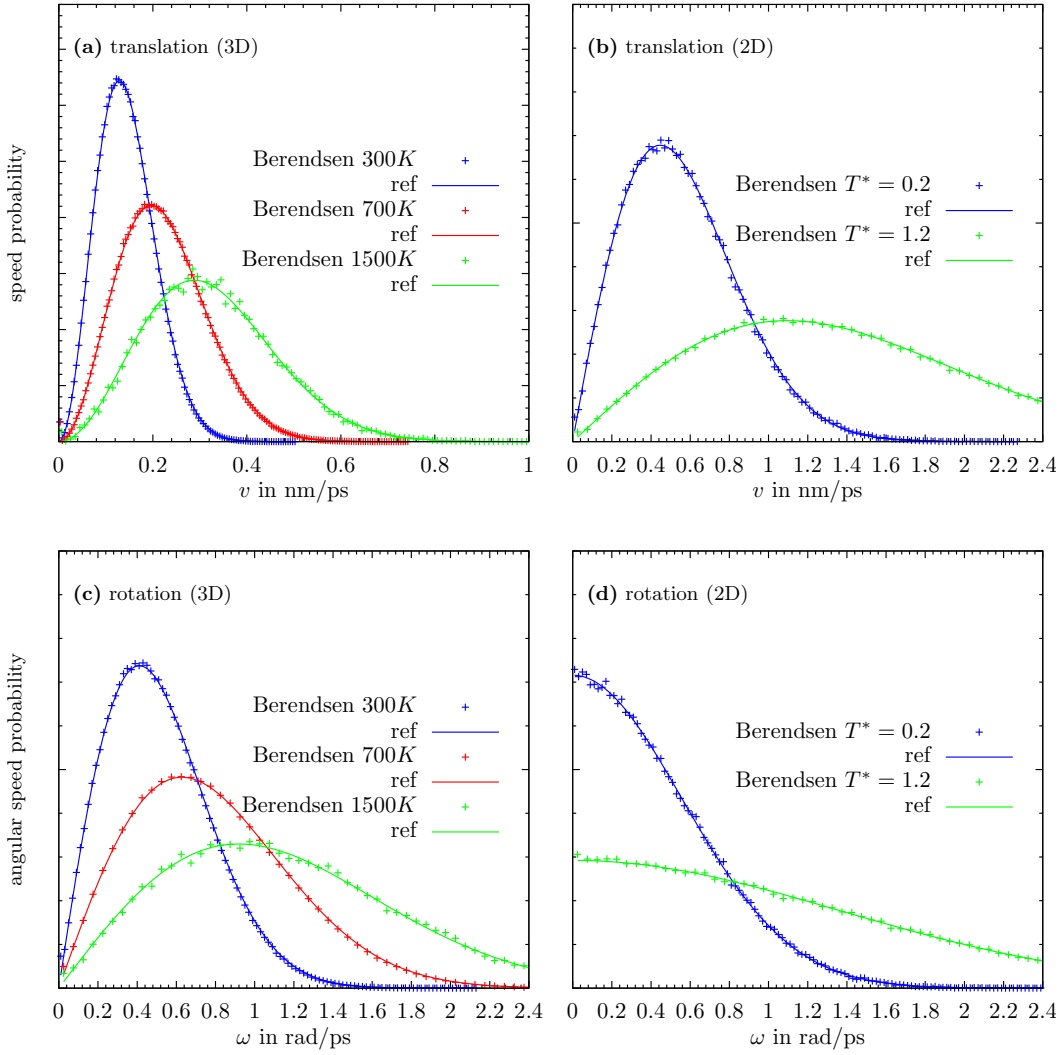


FIGURE 3.1: Speed distribution for (a) coronene (modeled through the implicit electrostatics model, see Sec. 5.4.4) at various temperatures (b) 2D particles, as described in Sec. 7.2, with an aspect ratio of $\kappa = 2.1$ for two different temperatures. Corresponding angular speed distributions are shown in (c) and (d), respectively. The solid lines describe the reference curves from Sec. 2.4.

However, when the rescaling procedure is distributed among several steps, the following expression for the rescaling factor holds

$$\lambda_{\text{trans}}^2 = e^{-\Delta t/\tau} + \frac{\overline{E}_{\text{kin}}}{N_f E_{\text{kin}}} (1 - e^{-\Delta t/\tau}) \left(X_1^2 + \sum_{i=2}^{N_f} X_i^2 \right) + 2 e^{-\Delta t/2\tau} \sqrt{\frac{\overline{E}_{\text{kin}}}{N_f E_{\text{kin}}} (1 - e^{-\Delta t/\tau})} X_1. \quad (3.22)$$

Hereby, X_i is defined as previously mentioned in Sec. 3.2.

3.5 Periodic boundary conditions

In the present section, we explain how we treat the boundary conditions in our many-particle systems with respect to particle positions and inter-particle connecting vectors.

3.5.1 Adjust positions

Each position \mathbf{r}_i has to be adjusted after its evaluation due to the periodic boundaries. First, the matrix containing all three box-vectors is introduced through

$$\underline{\mathbf{G}} = \begin{pmatrix} | & | & | \\ \mathbf{L}_1 & \dots & \mathbf{L}_D \\ | & | & | \end{pmatrix}. \quad (3.23)$$

The vector \mathbf{r}_i can be written as a linear combination of the box-vectors with the coefficients α_i according to

$$\mathbf{r}_i = \underline{\mathbf{G}} \cdot \begin{pmatrix} \alpha_1 \\ \vdots \\ \alpha_D \end{pmatrix}. \quad (3.24)$$

In its explicit form, the coefficients are

$$\begin{pmatrix} \alpha_1 \\ \vdots \\ \alpha_D \end{pmatrix} = \underline{\mathbf{G}}^{-1} \cdot \mathbf{r}_i. \quad (3.25)$$

Due to the centering of the simulation box around the zero vector, the coefficients have values between -0.5 and 0.5 if the particle is in the box. The boundary conditions are subsequently applied to these coefficients, according to

$$\alpha_i^{\text{new}} = \begin{cases} \alpha_i + 1 & , \alpha_i < -0.5 \\ \alpha_i - 1 & , \alpha_i > 0.5 \\ \alpha_i & , \text{else} \end{cases} \quad (3.26)$$

Finally, the new and adjusted positions are evaluated using Eq. (3.24) with the new coefficients, yielding

$$\mathbf{r}_i^{\text{new}} = \underline{\mathbf{G}} \cdot \begin{pmatrix} \alpha_1^{\text{new}} \\ \vdots \\ \alpha_D^{\text{new}} \end{pmatrix}. \quad (3.27)$$

3.5.2 Adjust relative positions

The adjustment of the distance vector between particles A and B is performed in the same way. Hereby, particle A with position \mathbf{r}_A is seen as the center of the simulation box. The relative vector $\mathbf{r}_{AB} = \mathbf{r}_B - \mathbf{r}_A$ is then adjusted using Eqs. (3.24)–(3.27). This kind of treating relative positions is also referred to as minimum image convention [3].

3.6 Random configurations

In cases whether random configurations are considered in this work, then the following scheme was used. Each particle is set one by one at random in space and orientation. If an overlap occurs, then the procedure repeats. Particles overlap if their inter-particle distance is 0.9 times the corresponding contact distance. The contact distance is equivalent to the inter-particle distance where the interaction potential has the value zero. In the following sections, it is denoted with σ .

3.7 Treatment of interactions

In general, the treatment of interactions has to be taken with care, since the system size is finite and the pair interactions are physically not dampened to exactly zero for finite inter-particle distances. In the present work, we do not include any long-range interactions. Strictly speaking, with long-range interactions we understand interactions where the forces between two particles decay less than R^{-D} , with D being the dimensionality and R the inter-particle distance. This means that in the proper sense we have no long-range interactions. The slowest decaying force in this work is the quadrupole-quadrupole force (see Appendix A.2.2) with

$$F_{ij} \propto R^{-6} = \begin{cases} R^{-2D}, & D = 3 \\ R^{-3D}, & D = 2 \end{cases}$$

However, the quadrupole-quadrupole torque has the same exponent minus one in the distance-dependent decay, i.e. its range is larger but still short-ranged by previous definition. We next introduce the way in which we treat our short-range interactions.

Our interactions are thus all short-ranged, although to verify our cutoff procedure we have to check the cutoff influence on the total energy. We later investigate long-range interactions starting exemplary with the Coulomb interactions and apply a similar method for quadrupole-quadrupole interactions. It is important to verify the short-range treatment, since a cutoff for short-range interactions imposed by an overly small simulation box would also lead to wrong potential energies.

3.7.1 Short-range treatment

The pair forces and torques are hereby cut at the cutoff inter-particle distance R_{cutoff} and shifted towards 0 at R_{cutoff} . This means that there are no interactions between two particles if they are larger than R_{cutoff} apart. However, in this work, we also checked the applicability of this treatment through comparing energies developed with the upcoming long-range treatment (see Sec. 5.4).

3.7.2 Long-range treatment

The treatment of long-range interactions is different from short-ranged interactions, where just a cutoff is sufficient. For charge and dipolar particles it is common to treat underlying interactions with the Ewald method. The charge-charge interaction (or

Coulomb) potential decays with R^{-1} and the dipole-dipole term with R^{-3} . Since the quadrupole-quadrupole potential decays with R^{-5} , it is useful to proof that a force-shifted ansatz (Sec. 3.7.1) is useful or whether it is more appropriate to involve all particles and its periodic images in the interaction potential. In the following, we present the Ewald method for charges and extend it towards quadrupoles using the method described by Smith *et al.* [178].

3.7.2.1 Coulomb interactions

A charge inside a 3D simulation box with periodic boundary conditions does not exhibit a true coulomb potential of $1/R$ due to its periodic images.

A charge at $\mathbf{r}_i + \mathbf{x}$ leads to the following electrostatic potential at \mathbf{r}

$$\phi_{i,\mathbf{x}}(\mathbf{r}) = \frac{1}{4\pi\epsilon_0} \frac{q_i}{|\mathbf{r}_i + \mathbf{x} - \mathbf{r}|}. \quad (3.28)$$

The electrostatic potential at \mathbf{r} due to all particles in the simulation box and its periodic images is thus given through

$$\Phi(\mathbf{r}) = \sum_{\mathbf{x} \in \mathbf{L}^n} \sum_i^N \phi_{i,\mathbf{x}}(\mathbf{r}), \quad (3.29)$$

where the set $\mathbf{L}^n = \{n_1 \cdot \mathbf{L}_1 + n_2 \cdot \mathbf{L}_2 + n_3 \cdot \mathbf{L}_3 | n_i \in \mathbb{Z}\}$ describes the distance to the periodic images of the simulation box. This lattice sum has a poor convergence for small box sizes since each potential $\phi_{i,\mathbf{x}}(\mathbf{r})$ is long-ranged. The idea is to split $\phi_{i,\mathbf{x}}(\mathbf{r})$ - which is long-ranged and singular - into a part where the latter summation rapidly converges (i.e., short-ranged, singular) and a second part that quickly converges in Fourier space (long-ranged, non-singular).

$$\phi_{i,\mathbf{x}}(\mathbf{r}) = \phi_{i,\mathbf{x}}^S(\mathbf{r}) + \phi_{i,\mathbf{x}}^L(\mathbf{r}) \quad (3.30)$$

$\phi_{i,\mathbf{x}}(\mathbf{r})$ is becoming short-ranged and singular with a factor $\alpha_{i,\mathbf{x}}(\mathbf{r})$, while the long-range non-singular part remains, i.e.

$$\phi_{i,\mathbf{x}}(\mathbf{r}) = \phi_{i,\mathbf{x}}(\mathbf{r}) \cdot \alpha_{i,\mathbf{x}}(\mathbf{r}) + \phi_{i,\mathbf{x}}(\mathbf{r}) \cdot (1 - \alpha_{i,\mathbf{x}}(\mathbf{r})). \quad (3.31)$$

The choice of $\alpha_{i,\mathbf{x}}(\mathbf{r}) = \text{erfc}(\epsilon |\mathbf{r}_i + \mathbf{x} - \mathbf{r}|) = 1 - \text{erf}(\epsilon |\mathbf{r}_i + \mathbf{x} - \mathbf{r}|)$ fulfills these requirements.³ We thus consider

$$\phi_{i,\mathbf{x}}^S(\mathbf{r}) = \frac{q_i}{4\pi\epsilon_0} \frac{\text{erfc}(\epsilon |\mathbf{r}_i + \mathbf{x} - \mathbf{r}|)}{|\mathbf{r}_i + \mathbf{x} - \mathbf{r}|} \quad (3.32)$$

$$\phi_{i,\mathbf{x}}^L(\mathbf{r}) = \frac{q_i}{4\pi\epsilon_0} \frac{\text{erf}(\epsilon |\mathbf{r}_i + \mathbf{x} - \mathbf{r}|)}{|\mathbf{r}_i + \mathbf{x} - \mathbf{r}|}. \quad (3.33)$$

Hereby, ϵ acts as a free parameter. This parameter determines whether an inter-particle distance is short or long (for a correct choice see next Sec. 3.7.2.2 for more details). The interpretation of Eq. (3.30) in terms of particle density, is given through

³The error function is defined as $\text{erf}(z) = \frac{2}{\sqrt{\pi}} \int_0^z e^{-t^2} dt$.

the poisson equation

$$-\frac{\rho_{i,\mathbf{x}}(\mathbf{r})}{\epsilon_0} = \nabla^2 \phi_{i,\mathbf{x}}(\mathbf{r}). \quad (3.34)$$

More specifically, the charge density is decomposed into the dirac delta minus a Gaussian distribution for the short-range part and the same Gaussian distribution for the long-range part, i.e.

$$\rho_{i,\mathbf{x}}(\mathbf{r}) = \left[q_i \delta(\mathbf{r}_i + \mathbf{x} - \mathbf{r}) - q_i \left(\frac{\epsilon}{\sqrt{\pi}} \right)^3 \exp(-\epsilon^2(\mathbf{r}_i + \mathbf{x} - \mathbf{r})^2) \right] + \left[q_i \left(\frac{\epsilon}{\sqrt{\pi}} \right)^3 \exp(-\epsilon^2(\mathbf{r}_i + \mathbf{x} - \mathbf{r})^2) \right]. \quad (3.35)$$

Eq. (3.29) is now rewritten into a short- and a long-range part according to

$$\Phi = \Phi^S + \Phi^L \quad (3.36)$$

$$\Phi^S(\mathbf{r}) = \sum_{\mathbf{x} \in \mathbf{L}^n} \sum_i \phi_{i,\mathbf{x}}^S(\mathbf{r}) = \frac{1}{4\pi\epsilon_0} \sum_{\mathbf{x} \in \mathbf{L}^n} \sum_i q_i \frac{\operatorname{erfc}(\epsilon|\mathbf{r}_i + \mathbf{x} - \mathbf{r}|)}{|\mathbf{r}_i + \mathbf{x} - \mathbf{r}|} \quad (3.37)$$

$$\Phi^L(\mathbf{r}) = \sum_{\mathbf{x} \in \mathbf{L}^n} \sum_i \phi_{i,\mathbf{x}}^L(\mathbf{r}) = \frac{1}{4\pi\epsilon_0} \sum_{\mathbf{x} \in \mathbf{L}^n} \sum_i q_i \frac{\operatorname{erf}(\epsilon|\mathbf{r}_i + \mathbf{x} - \mathbf{r}|)}{|\mathbf{r}_i + \mathbf{x} - \mathbf{r}|}. \quad (3.38)$$

As expected the long-range part $\Phi^L(\mathbf{r})$ is conditionally converging. Nonetheless its Fourier transform

$$\hat{\Phi}^L(\mathbf{k}) = \int_V \Phi^L(\mathbf{r}') e^{-i\mathbf{k}\mathbf{r}'} d\mathbf{r}' = \frac{1}{\epsilon_0} \sum_i q_i e^{-i\mathbf{k}\mathbf{r}_i} \frac{e^{-k^2/4\epsilon^2}}{k^2} \quad (3.39)$$

is rapidly converging. By transforming back into the real space

$$\Phi^L(\mathbf{r}) = \frac{1}{V} \sum_{\mathbf{k}} \hat{\Phi}^L(\mathbf{k}) e^{i\mathbf{k}\mathbf{r}} = \frac{1}{V\epsilon_0} \sum_{\mathbf{k} \neq 0} \sum_i \frac{q_i}{k^2} e^{i\mathbf{k}\cdot(\mathbf{r}-\mathbf{r}_i)} e^{-k^2/4\epsilon^2} \quad (3.40)$$

we sum over all reciprocal vectors $\mathbf{k} \in \{n_1 \cdot \mathbf{k}_1 + n_2 \cdot \mathbf{k}_2 + n_3 \cdot \mathbf{k}_3 | n_i \in \mathbb{Z}\}$ with reciprocal lattice vectors $[\mathbf{k}_1, \mathbf{k}_2, \mathbf{k}_3]^T = 2\pi[\mathbf{L}_1, \mathbf{L}_2, \mathbf{L}_3]^{-1}$. In Eq. (3.40) the zero vector $\mathbf{k} = 0$ is omitted since charge neutrality ($\sum_i q_i = 0$) holds. In order to calculate the electrostatic energy of the system given through

$$E_{\text{pot}} = \frac{1}{2} \sum_i^N q_i \Phi_{[i]} = \frac{1}{2} \sum_i^N q_i \left[\Phi_{[i]}^S + \Phi_{[i]}^L \right], \quad (3.41)$$

the electrostatic potential due to all particles except particle i , denoted with $\Phi_{[i]}$, is required. Nonetheless, the contribution due to its periodic images should still be

included. The corresponding short- and long-range part are defined by

$$\Phi_{[i]}^S(\mathbf{r}) = \sum_{\mathbf{L}^n} \sum_j' \phi_{j,\mathbf{L}^n}^S(\mathbf{r}) = \frac{1}{4\pi\epsilon_0} \sum_{\mathbf{L}^n} \sum_j' q_j \frac{\operatorname{erfc}(\epsilon|\mathbf{r}_j + \mathbf{L}^n - \mathbf{r}|)}{|\mathbf{r}_j + \mathbf{L}^n - \mathbf{r}|} \quad (3.42)$$

$$\Phi_{[i]}^L(\mathbf{r}) = \Phi^L(\mathbf{r}) - \phi_{i,\mathbf{0}}^L(\mathbf{r}) = \frac{1}{V\epsilon_0} \sum_{\mathbf{k}\neq\mathbf{0}} \sum_j \frac{q_j}{k^2} e^{i\mathbf{k}\cdot(\mathbf{r}-\mathbf{r}_j)} e^{-k^2/4\epsilon^2} - \phi_{i,\mathbf{0}}^L(\mathbf{r}). \quad (3.43)$$

The symbol \sum_j' denotes a summation over all $j \in \{1, \dots, N\} \neq i$ for $\mathbf{L}^n = \mathbf{0}$ and a summation over all $j \in \{1, \dots, N\}$ for $\mathbf{L}^n \neq \mathbf{0}$.

Calculating E_{pot} requires the evaluation of $\Phi_{[i]}^{S/L}(\mathbf{r})$ at $\mathbf{r} = \mathbf{r}_i$. This means that $\phi_{i,\mathbf{0}}^L(\mathbf{r})$ for $\mathbf{r} \rightarrow \mathbf{r}_i$ has to be calculated, yielding

$$\phi_{i,\mathbf{0}}^L(\mathbf{r}) = \frac{q_i}{4\pi\epsilon_0} \frac{\operatorname{erf}(\epsilon|\mathbf{r}_i - \mathbf{r}|)}{|\mathbf{r}_i - \mathbf{r}|} \xrightarrow{\mathbf{r} \rightarrow \mathbf{r}_i} \frac{1}{4\pi\epsilon_0} \frac{2\epsilon}{\sqrt{\pi}} q_i \equiv -\phi_i^{\text{self}}. \quad (3.44)$$

The latter limit is also called electrostatic self-interaction potential ϕ_i^{self} . The entire potential energy according to Eq (3.41) can now be explicitly defined, leading to

$$E_{\text{pot}} = \frac{1}{8\pi\epsilon_0} \sum_{\mathbf{L}^n} \sum_i \sum_j' q_i q_j \frac{\operatorname{erfc}(\epsilon|\mathbf{r}_j + \mathbf{L}^n - \mathbf{r}|)}{|\mathbf{r}_j + \mathbf{L}^n - \mathbf{r}|} + \frac{1}{2V\epsilon_0} \sum_{\mathbf{k}\neq\mathbf{0}} \sum_i \sum_j \frac{q_i q_j}{k^2} e^{i\mathbf{k}\cdot(\mathbf{r}-\mathbf{r}_j)} e^{-k^2/4\epsilon^2} - \frac{1}{4\pi\epsilon_0} \frac{\epsilon}{\sqrt{\pi}} \sum_i q_i^2. \quad (3.45)$$

3.7.2.2 Quadrupole-quadrupole interactions

The quadrupole-quadrupole interaction in 3D is treated in a similar fashion. Rather than the particle charge q_i , the following operator incorporating the quadrupole tensor $\underline{\mathbf{Q}}_i = 1/2 \sum_i q_i \mathbf{r}_i \otimes \mathbf{r}_i$ is used [178]

$$\hat{M}_i = \underline{\mathbf{Q}}_i : (\nabla \otimes \nabla) = \sum_{a,b} [\underline{\mathbf{Q}}_i]_{ab} \partial_a \partial_b. \quad (3.46)$$

Eqs. (3.32) and (3.33) transform to

$$\phi_{i,\mathbf{x}}^S(\mathbf{r}) = \frac{1}{4\pi\epsilon_0} \hat{M}_i \left[\frac{\operatorname{erfc}(\epsilon|\mathbf{r}_i + \mathbf{x} - \mathbf{r}|)}{|\mathbf{r}_i + \mathbf{x} - \mathbf{r}|} \right] \quad (3.47a)$$

$$\phi_{i,\mathbf{x}}^L(\mathbf{r}) = \frac{1}{4\pi\epsilon_0} \hat{M}_i \left[\frac{\operatorname{erf}(\epsilon|\mathbf{r}_i + \mathbf{x} - \mathbf{r}|)}{|\mathbf{r}_i + \mathbf{x} - \mathbf{r}|} \right]. \quad (3.47b)$$

The electrostatic potential at \mathbf{r} subsequently reads

$$\Phi(\mathbf{r}) = \Phi^S(\mathbf{r}) + \Phi^L(\mathbf{r}) \quad (3.48a)$$

$$\Phi^S(\mathbf{r}) = \sum_{\mathbf{L}^n} \sum_i \phi_{i,\mathbf{L}^n}^S(\mathbf{r}) = \frac{1}{4\pi\epsilon_0} \sum_{\mathbf{L}^n} \sum_i \hat{M}_i \left[\frac{\operatorname{erfc}(\epsilon|\mathbf{r}_i + \mathbf{L}^n - \mathbf{r}|)}{|\mathbf{r}_i + \mathbf{L}^n - \mathbf{r}|} \right] \quad (3.48b)$$

$$\Phi^L(\mathbf{r}) = \frac{1}{V\epsilon_0} \sum_{\mathbf{k}\neq\mathbf{0}} \sum_i \frac{1}{k^2} \hat{M}_i \left[e^{i\mathbf{k}\cdot(\mathbf{r}-\mathbf{r}_i)} e^{-k^2/4\epsilon^2} \right]. \quad (3.48c)$$

By excluding particle i in the upper definitions of the electrostatic potential, it is possible to calculate the entire electrostatic energy through

$$E_{\text{pot}} = \frac{1}{2} \sum_i^N \hat{M}_i \Phi_{[i]} = \frac{1}{2} \sum_i^N \hat{M}_i \left[\Phi_{[i]}^{\text{S}} + \Phi_{[i]}^{\text{L}} \right]. \quad (3.49)$$

The explicit expression is given through the following expression

$$E_{\text{pot}} = \frac{1}{2V\epsilon_0} \sum_{\mathbf{k} \neq \mathbf{0}}^{\infty} A(k) \left| \sum_j^N f_j(\mathbf{k}) e^{-i\mathbf{k}\mathbf{r}_j} \right|^2 + \frac{1}{4\pi\epsilon_0} \sum_l^4 \sum_i^N \sum_{j>i}^{\infty} G_{ij}^l(\mathbf{r}_{ji}) B_l(r_{ji}) + \frac{1}{2} \sum_i^N \phi_i^{\text{self}}. \quad (3.50)$$

The first term describes a summation over all nontrivial k-space vectors, while the second term describes the summation over distances in the real space. The last term represents the self interaction, i.e. the interaction of the particle with its periodic images. The missing expressions are given through the following set of equations (for a detailed explanation, see Ref. 178)

$$A(k) = \frac{1}{k^2} e^{-k^2/4\epsilon^2} \quad (3.51a)$$

$$f_j(k) = -\underline{\mathbf{Q}}_j : (\mathbf{k} \otimes \mathbf{k}) \quad (3.51b)$$

$$G_{ji}^1(\mathbf{r}_{ji}) = 0 \quad (3.51c)$$

$$G_{ji}^2(\mathbf{r}_{ji}) = 4\underline{\mathbf{Q}}_j \times \underline{\mathbf{Q}}_i \quad (3.51d)$$

$$G_{ji}^3(\mathbf{r}_{ji}) = -2(\underline{\mathbf{Q}}_j : \underline{\mathbf{1}}) R_{ji} \times \underline{\mathbf{Q}}_i - 4\Theta_{ji} \times \underline{\mathbf{Q}}_i - 4\Theta_{ji}^\dagger \times \underline{\mathbf{Q}}_i \quad (3.51e)$$

$$G_{ji}^4(\mathbf{r}_{ji}) = 2(\underline{\mathbf{Q}}_j : (\mathbf{r} \otimes \mathbf{r})) (\mathbf{r} \otimes \mathbf{r}) \times \underline{\mathbf{Q}}_i \quad (3.51f)$$

$$\Theta_{ji} = r_{ji}^\alpha \sum_\gamma Q_j^{\beta\gamma} r_{ji}^\gamma \quad (3.51g)$$

$$B_l(u) = \frac{1}{u^2} \left[(2l-1)B_{l-1}(u) + \frac{(2\epsilon^2)^l}{\epsilon\sqrt{\pi}} e^{-\epsilon^2 u^2} \right], \quad B_0(u) = \frac{1}{u} \text{erfc}(\epsilon u) \quad (3.51h)$$

$$\phi_i^{\text{self}} = -\frac{2\xi}{4\epsilon_0\sqrt{\pi^3}} \left\{ 2\xi^2 \left[\frac{2\xi^2}{5} (2\underline{\mathbf{Q}}_i : \underline{\mathbf{Q}}_i + (\underline{\mathbf{Q}}_i : \underline{\mathbf{1}})^2) \right] \right\}. \quad (3.51i)$$

A remaining issue is the correct choice of ϵ . As pointed out before, this parameter determines whether an inter-particle distance is short or long. If ϵ is chosen small, many real space vectors have to be taken into account. By contrast, when using a large value, many k-space vectors \mathbf{k} must be chosen for the summation [122].

In the present work, we considered the same number of real and k-space vectors and hereby choose $n_i = n$. We build a crystal as presented in Fig. 6.7 in Chapter 6. The influence of the truncation n on the potential energy of a system with one quadrupole is shown in Fig. 3.2. Specifically, $n = 4$ and $n = 8$ are considered. We can clearly see a

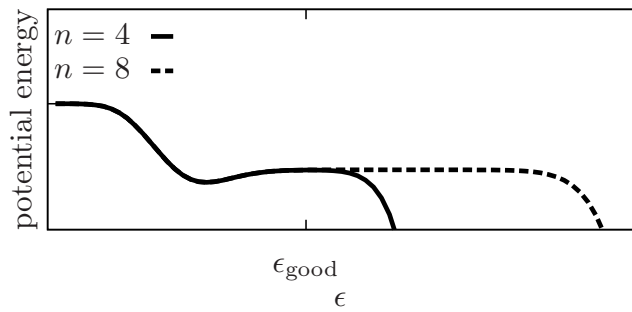


FIGURE 3.2: Potential energy of one quadrupole in a simulation box as a function of range parameter ϵ . Simulation box repeated at $n_1 \cdot \mathbf{L}_1 + n_2 \cdot \mathbf{L}_2 + n_3 \cdot \mathbf{L}_3$. $n_i \in \{-n, \dots, n\}$; Results shown for $n = 4$ and $n = 8$.

dependence of the potential energy on the ϵ . However, when the number of real and k-space vectors is increased, the plateau in ϵ - in which the convergence of real and k-space vectors is sufficient - becomes larger. For $\epsilon = \epsilon_{\text{good}}$, the maximum number of real and k-space vectors is not so sensitive towards the value of the potential energy. An optimal set of ϵ , real- and k-space lattice vectors can be determined according to a technique presented in Ref. 178.

3.8 Speed-up techniques

Besides the aforementioned cutoff in the interaction, we further introduce the cell index method, which allows an efficient treatment of neighbor lists, first for two-dimensional quadratic simulation boxes and subsequently for simulation boxes in any dimension for arbitrary box vectors. Moreover, we briefly explain the multiple time step method used.

3.8.1 Neighbor lists

In order to reduce the number of (i,j)-pairs to check during the particle-particle interactions, a technique that allows considering a reduced set of pairs for each particle is used. The simplest solution is a particle list for each particle naming particles in proximity (Verlet list [3]). This list is subsequently updated every few time steps. However, one still has to calculate N^2 distances every few time steps. A more elaborate approach is to partition the simulation box in smaller boxes in a way that each particle can only interact with particles in the current sub-box and with particles in the next neighboring boxes. This so-called “cell index” method is presented in the following for a simple 2D quadratic system and later extended towards systems revealing parallelogram or triclinic box geometry. We first present the demonstrative case of a 2D box geometry and later present an extension of the neighbor list method for parallelogram or triclinic simulation boxes.

3.8.1.1 2D-quadratic simulation box

The cell index method [3] for rectangular simulation box geometries with side length of L is presented in the following (see also Fig. 3.3). The partition M is an integer number and chosen to satisfy $r_c \leq l = \max_{M \in \mathbb{N}, M \geq 3} \frac{L}{M}$. In the following, three functions are

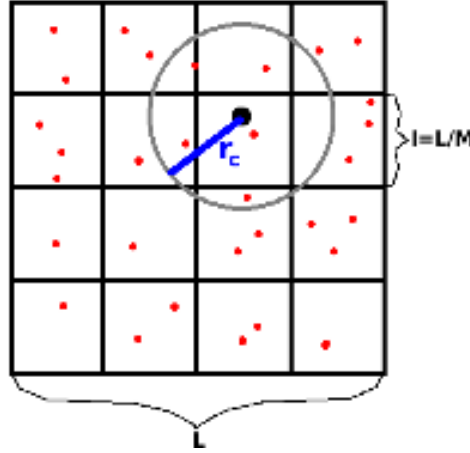


FIGURE 3.3: Illustration of the cell index method in a two-dimensional system. One particle is singled out and shown with its cutoff radius.

introduced:

$$\text{cell} : \{1, \dots, N\} \rightarrow \mathcal{M} \times \mathcal{M}, \mathcal{M} = \{1, \dots, M\} \quad (3.52a)$$

$$\text{particle_list} : \mathcal{M} \times \mathcal{M} \rightarrow P(\{1, \dots, N\}) \quad (3.52b)$$

$$\text{cell_list} : \mathcal{M} \times \mathcal{M} \rightarrow (\mathcal{M} \times \mathcal{M})^{3^D} \quad (3.52c)$$

The cell function maps the specific particle number onto the corresponding cell in the simulation box. Each cell in a simulation box incorporates a list of particles. This list can be received via the particle_list function. As seen in the following, not only the particles in the current list are relevant but also the particles in the next neighboring cells (in total 3^D cells). The cell_list function calculates a list of cell numbers comprising the current cell and all next neighbor cells (in 2D: 9 neighbor cells). Using these functions, the algorithm to obtain the neighbor list of a given particle i is introduced.

Algorithm to create neighbor list

```

for  $k$  in cell_list(cell( $i$ )); do{
  for  $j$  in particle_list( $i$ ); do{
    consider particle  $j$  as neighbor if  $\text{dist}(\mathbf{x}_j - \mathbf{x}_i) \leq r_c$ .
  }
}

```

3.8.1.2 Parallelogram / Triclinic simulation box

The previously-introduced algorithm is now generalized to systems with arbitrary linear independent box vectors $\mathbf{L}_1 \dots \mathbf{L}_D$. Exemplary are parallelogram ($D = 2$) or triclinic ($D = 3$) simulation boxes (see Fig. 3.4).

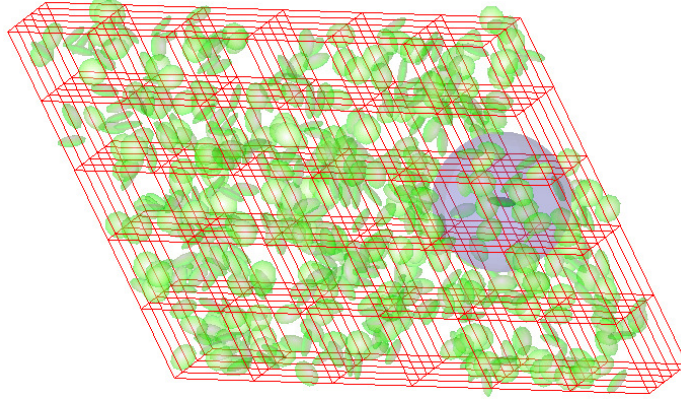


FIGURE 3.4: Illustration of the cell index method in a system with triclinic box shape. One particle is singled out and shown with its cutoff radius.

Eqs. (3.52a)–(3.52c) are adapted to the present case, according to

$$\text{cell} : \{1, \dots, N\} \rightarrow \mathcal{M} \times \dots \times \mathcal{M}_D, \mathcal{M}_i = \{1, \dots, M_i\} \quad (3.53a)$$

$$\text{particle_list} : \mathcal{M} \times \dots \times \mathcal{M}_D \rightarrow P(\{1, \dots, N\}) \quad (3.53b)$$

$$\text{cell_list} : \mathcal{M} \times \dots \times \mathcal{M}_D \rightarrow (\mathcal{M}_1 \times \dots \times \mathcal{M}_D)^{3^D} \quad (3.53c)$$

However, in a tilted box geometry, calculating the partition is more complex than in previous case. Rather than one partition M , there are now D partitions M_1, \dots, M_D . To correctly partition the box, the projection of a sphere with radius R_{cutoff} onto each simulation box-vector ($\mathbf{L}_1, \dots, \mathbf{L}_D$) has to be determined. The entire box geometry is characterized through the following matrix

$$\underline{\mathbf{G}} = \begin{pmatrix} | & | & | \\ \mathbf{L}_1 & \dots & \mathbf{L}_D \\ | & | & | \end{pmatrix}. \quad (3.54)$$

The corresponding box vectors in reciprocal space are given through the columns of $(\underline{\mathbf{G}}^T)^{-1}$. The norm of each column vector is $1/(\text{plane} - \text{to} - \text{plane distance})$. Now each column vector is rescaled in a way that the new norm is $1/R_{\text{cutoff}}$. Specifically, we have

$$\mathbf{n}_i = 1/R_{\text{cutoff}} \cdot \frac{(\underline{\mathbf{G}}^T)^{-1} \mathbf{e}_i}{\|(\underline{\mathbf{G}}^T)^{-1} \mathbf{e}_i\|}. \quad (3.55)$$

By transforming the matrix with the modified column vectors back to real space, one yields the matrix

$$\underline{\tilde{\mathbf{G}}} = \left[\left(\begin{array}{ccc} | & | & | \\ \mathbf{n}_1 & \dots & \mathbf{n}_D \\ | & | & | \end{array} \right)^T \right]^{-1}, \quad (3.56)$$

where the column vectors describe a triclinic box with the same orientations and the same angles between the edges like the simulation box, albeit with opposing planes having a distance of R_{cutoff} . The i -th partition is finally given through the floor value of the norm of the i -th column of $\underline{\tilde{\mathbf{G}}}$, according to

$$M_i = \max \left\{ \text{Floor} \left[\left\| \underline{\tilde{\mathbf{G}}} \cdot \begin{pmatrix} \delta_{1,i} \\ \vdots \\ \delta_{D,i} \end{pmatrix} \right\| \right], 3 \right\}. \quad (3.57)$$

Thereby a minimum value of 3 is introduced to be consistent with the definition of the functions (3.53a)–(3.53c).

3.8.2 Time step variation

The idea behind time step variation methods (see [3]) that the frequency of the force and torque evaluation depends on the inter-particle distance. We hereby used the so-called primary radius R_{prim} , which is chosen smaller than the cutoff radius R_{cutoff} . For distances smaller than R_{prim} , we used the normal time step of Δt . When the distance is larger yet still smaller than R_{cutoff} , we used a time step for our force and torque evaluation of $5\Delta t$.

Chapter 4

From microscopic to coarse-grained systems

4.1 Preface

In this chapter, we present the underlying principles of the transition from the atomistic towards the molecular or coarse-grained (CG) level of detail. Throughout the entire work, we focus in the molecular level of detail on effective inter-molecular pair interactions. As a benchmark system, we consider a pair of coronene molecules (see Fig. 4.1) that are discotic and possess a high axial symmetry. To describe the effective pair potential between both coronene molecules, we use only a few CG coordinates.

In contrast to other work in the literature, where each CG configuration is characterized via the distance between the center of masses [18, 98, 111, 158, 212], we hereby consider the CG molecules to have an axial orientation. A molecular orientation vector (uniaxial) or tensor (biaxial particle) is a frequently-used example to account for orientational internal degrees of freedom. Such an approach also allows modeling anisotropic shape. Corresponding examples are the Gaussian-overlap [19] or the Gay-Berne potential [63], as well as their derivatives [55, 78, 92]. The fundamental principle of the effective potential dates back to Kirkwood, who defined the potential of mean force [98]. He originally introduced it to describe effective pair interactions of particles among a bath of particles of the same species. The particles themselves interact only according to their distance. His goal was to include higher particle interactions into an effective pair potential. By contrast, we want to build a pair potential that effectively includes the atomistic detail of each molecule as described in a review by Likos [111].

This chapter is organized as follows. We start with the microscopic description of our system of two coronene molecules in Sec. 4.2. Subsequently, we present a way to characterize CG systems in terms of CG coordinates in Sec. 4.3. For this purpose, we provide several sets of CG coordinates. In order to determine the effective pair potential, we calculate the histogram function of CG coordinates using Langevin dynamics at atomistic detail (see Sec. 3.2) [1]. The histogram functions are defined in Sec. 4.4, where we additionally present sampling techniques like umbrella sampling (US) or steered dynamics (SD), which lead to more sampling data in rarely-sampled phase space areas. We hereby want to point out that we extended the SD method to create a histogram as a function of all CG coordinates, i.e. beyond the pull coordinate

(center of mass distance). We finally provide a definition of the effective potential in Sec. 4.5. This chapter builds on our published article with reference No. 78.

4.2 Microscopic description

We start with the atomistic model for a pair of coronene molecules and explain the fundamental method of describing the electrostatics on the atomistic level of detail. Specifically, the electronic density functional theory, which is used to calculate the ground state charge density, is introduced. Furthermore, we present a technique to represent the charge density with atomic point charges (corresponding results for coronene are taken from Ref. 143, as described in further detail in Sec. 5.4). However, we first neglect the involved electrostatics in the atomistically-resolved model for the current CG procedure but effectively include it later in our work (see Sec. 5.4).

4.2.1 Atomistically-resolved model

The system of interest comprises two atomistically-detailed coronene molecules (with chemical formula $C_{24}H_{12}$) in a large cubic box with volume $V = l^3$, temperature T and periodic boundary conditions (l is the box length). Each coronene molecule contains $N = 36$ atoms indexed by $1, \dots, N$ and $N + 1, \dots, 2N$, respectively. Every atom i in our model system is represented by a point mass m_i at the position \mathbf{r}_i . Figure 4.1 shows an exemplary snapshot of this system. The interactions between all atoms are described

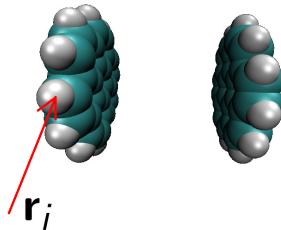


FIGURE 4.1: Sketch of a coronene dimer system. The blue atoms represent carbon while the white ones are hydrogen.

by Lennard-Jones (LJ) potentials for non-bonded interactions and harmonic potentials for the intra-molecular bond, angular and dihedral interactions. For the present study all Coulomb interactions are set to zero. The potential energy as a function of all $2N$ atomic coordinates can subsequently be written as

$$\begin{aligned}
 U(\{\mathbf{r}_i\}_{i=1,\dots,2N}) &= \sum_{i,j} \left[\left(\frac{(C_6)_{ij}}{r_{ij}} \right)^6 - \left(\frac{(C_{12})_{ij}}{r_{ij}} \right)^{12} \right] \\
 &+ \frac{1}{2} \sum_{i,j} K_{ij}^b (r_{ij} - r_{\text{eq}})^2 \\
 &+ \frac{1}{2} \sum_{i,j,k} K_{ijk}^\theta (\theta_{ijk} - \theta_{\text{eq}})^2 \\
 &+ \frac{1}{2} \sum_{i,j,k,l} K_{ijkl}^\phi [1 + \cos(n\phi_{ijkl} - \varepsilon)],
 \end{aligned} \tag{4.1}$$

where $(C_6)_{ij}$ and $(C_{12})_{ij}$ are the LJ parameters between atoms i and j . Atomic distances are denoted with $r_{ij} = |\mathbf{r}_i - \mathbf{r}_j|$. Furthermore, K_{ij}^b and K_{ijk}^θ are force constants for the intra-molecular bond- and angular- interactions, and r_{eq} and θ_{eq} are the corresponding equilibrium bond lengths and bond angles, respectively. The quantity K_{ijkl}^ϕ is a dihedral parameter and ϕ_{ijkl} is the corresponding dihedral angle, while ε serves as a phase angle, which is either 0° or 180° . The factor n appearing in the last term stands for the proper-dihedral multiplicity [208]. The cutoff-lengths for the atomic LJ interactions are set to 2 nm. All specific parameter values are taken from the generalized AMBER force field, designed for organic molecules [208]. This force-field was already successfully used in growth studies of another conjugated organic molecule, namely para-sexiphenyl [147]. It was shown that the force field yields the correct phase behavior (for a more detailed discussion of the validation of the AMBER force-field for aromatics, see Olivier *et al.* [145]).

4.2.2 Electronic density functional theory

The ground state electron density can be calculated using density functional theory (DFT) [80]. An important approximation is that the ions can be seen as fixed, while the electrons can “move” freely (Born-Oppenheimer approximation [25]). The latter fact is based upon the different time scales for atoms (\approx fs) and electrons (\approx as). In this theory, the ions interact with the electrons with mass m through an external potential $V(\mathbf{r}_i)$, with \mathbf{r}_i being the position of the i -th electron. The electrons itself interact with the Coulomb potential $U(\mathbf{r}_i, \mathbf{r}_j)$. The corresponding Schrödinger equation with the \tilde{N} -electron (antisymmetric) wave function $\Psi(\mathbf{r}_1, \dots, \mathbf{r}_{\tilde{N}})$ is defined through

$$\hat{H}\Psi(\mathbf{r}_1, \dots, \mathbf{r}_{\tilde{N}}) = \left[\sum_{i=1}^{\tilde{N}} \left(-\frac{\hbar^2}{2m} \nabla_i^2 \right) + \sum_{i=1}^{\tilde{N}} V(\mathbf{r}_i) + \sum_{i<j}^{\tilde{N}} U(\mathbf{r}_i, \mathbf{r}_j) \right] \Psi(\mathbf{r}_1, \dots, \mathbf{r}_{\tilde{N}}) \quad (4.2)$$

$$= E\Psi(\mathbf{r}_1, \dots, \mathbf{r}_{\tilde{N}}). \quad (4.3)$$

The electron density $n(\mathbf{r})$ can be determined using the electron wave function Ψ according to

$$n(\mathbf{r}) = \langle \Psi | \sum_i \delta(\mathbf{r} - \mathbf{r}_i) | \Psi \rangle \quad (4.4)$$

$$= \tilde{N} \int_{\mathbb{R}^3} d\mathbf{r}_2 \cdots \int_{\mathbb{R}^3} d\mathbf{r}_{\tilde{N}} \Psi^*(\mathbf{r}, \mathbf{r}_2, \dots, \mathbf{r}_{\tilde{N}}) \Psi(\mathbf{r}, \mathbf{r}_2, \dots, \mathbf{r}_{\tilde{N}}). \quad (4.5)$$

Hereby, $\tilde{N} - 1$ particles are integrated out. The Hohenberg-Kohn theorem states that the density that minimizes the energy functional is bijective to the ground state wave function Ψ_{GS} . We thus minimize the energy with respect to the density $n(\mathbf{r})$ given through

$$E\{n(\mathbf{r})\} = T\{n(\mathbf{r})\} + U\{n(\mathbf{r})\} + V\{n(\mathbf{r})\}, \quad (4.6)$$

with the corresponding energy contributions

$$T\{n(\mathbf{r})\} = \langle \Psi | \sum_i \frac{\mathbf{p}_i^2}{2m} | \Psi \rangle \quad (4.7a)$$

$$U\{n(\mathbf{r})\} = \frac{e^2}{2} \int_{\mathbb{R}^3} d\mathbf{r} \int_{\mathbb{R}^3} d\mathbf{r}' \frac{n(\mathbf{r})n(\mathbf{r}')}{|\mathbf{r} - \mathbf{r}'|} + E_{\text{XC}}\{n(\mathbf{r})\} \quad (4.7b)$$

$$V\{n(\mathbf{r})\} = \int_{\mathbb{R}^3} d\mathbf{r} V(\mathbf{r}) n(\mathbf{r}), \quad (4.7c)$$

describing the kinetic, electron-electron and electron-core contributions. The energy functional is minimized using the Lagrangian method of undetermined multipliers [102], where we force the volume integral of the density to be equal to the electron particle number \tilde{N} . In particular, the following minimization procedure

$$\delta \left[E\{n(\mathbf{r})\} - \mu \left(\int_{\mathbb{R}^3} n(\mathbf{r}) d\mathbf{r} - \tilde{N} \right) \right] = 0 \quad (4.8)$$

leads to the ground state density. However, the explicit functional dependence of the kinetic energy functional $T\{n(\mathbf{r})\}$ and the so-called exchange-correlation energy functional $E_{\text{XC}}\{n(\mathbf{r})\}$ is unknown. Therefore, orbitals Ψ_i defined through

$$n(\mathbf{r}) = \sum_i^{\tilde{N}} |\Psi_i(\mathbf{r})|^2 \quad (4.9)$$

are used. The kinetic energy functional in terms of the orbital wave functions can be expressed through

$$T\{n(\mathbf{r})\} = \sum_i -\frac{\hbar^2}{2m} \int_{\mathbb{R}^3} d\mathbf{r} \Psi_i^*(\mathbf{r}) \nabla^2 \Psi_i(\mathbf{r}). \quad (4.10)$$

The energy minimization procedure defined in Eq. (4.8) is now written as

$$\delta_{\Psi_i^*} \left[E\{n(\mathbf{r})\} - \sum_j \epsilon_j \left(\int_{\mathbb{R}^3} d\mathbf{r} |\Psi_j|^2 - 1 \right) \right] = 0. \quad (4.11)$$

We arrive at the single-particle Schrödinger equation, the so-called Kohn-Sham equation

$$\left[-\frac{\hbar^2}{2m} \nabla^2 + V_{\text{eff}}(\mathbf{r}) \right] \Psi_i(\mathbf{r}) = \epsilon_i \Psi_i(\mathbf{r}), \quad (4.12)$$

with the effective external potential

$$V_{\text{eff}}(\mathbf{r}) = V(\mathbf{r}) + \int_{\mathbb{R}^3} \frac{e^2 n(\mathbf{r}')}{|\mathbf{r} - \mathbf{r}'|} d\mathbf{r}' + \frac{\delta E_{\text{XC}}\{n(\mathbf{r})\}}{\delta n(\mathbf{r})}, \quad (4.13)$$

and the eigenenergy ϵ_i . The second term is called the Hartree term and describes the electron-electron (Coulomb) repulsion. The last term characterizes the exchange

correlation that incorporates all many-particle interactions. If the latter is known exactly then the DFT provides exact results. There are various approaches, such as local density approximation, PBE-functionals [150], generalized gradient approximation [13, 106] or hybrid functionals [97].

The standard way to calculate the density is to first use a guess and calculate single body effective potential [Eq. (4.13)] and later calculate the eigenfunctions through solving the eigenvalue problem in Eq. (4.12). This procedure is repeated until convergence is reached. The final density is the ground state density $n_0(\mathbf{r}) = \langle \Psi_{\text{GS}} | \sum_i \delta(\mathbf{r} - \mathbf{r}_i) | \Psi_{\text{GS}} \rangle$.

4.2.3 Electrostatic potential fit

Having determined an effective potential energy by using the electronic DFT from the previous paragraph, it is now possible to define an electrostatic potential through

$$\Phi(\mathbf{r}) = \frac{1}{e} V_{\text{eff}}(\mathbf{r}). \quad (4.14)$$

In order to reproduce Φ with point charges at, e.g. our N atomic positions (representative for one isolated coronene molecule), we first express Φ at s different positions, which we denote with \mathbf{x}_i . We now introduce the vector $\Phi \in \mathbb{R}^s$, which represents the values of $\Phi(\mathbf{x}_i)$, $i \in \{1, \dots, s\}$. In analogy, the charge values of the atomic positions \mathbf{r}_i , $i \in \{1, \dots, N\}$ are represented through vector \mathbf{q} . Furthermore, a matrix containing all distances between the \mathbf{r}_i and \mathbf{x}_j is defined through

$$\mathbf{A}_{ij} = \frac{1}{|\mathbf{r}_i - \mathbf{x}_j|}.$$

The following minimization procedure (least square method)

$$\|\mathbf{A} \mathbf{q} - \Phi\|_2 \stackrel{!}{=} \min \quad (4.15)$$

under the constraint that $\sum_i \mathbf{q}_i = C$ holds, leads to results for the point charges. Hereby, C denotes the molecular net charge (zero in our work, since we consider uncharged particles). This whole procedure is called electrostatic potential fit. For further reading, we refer to Ref. 61.

4.3 Coarse-grained (CG) description

An important step in any coarse-graining procedure is to define variables that represent the CG system. A systematic way of choosing CG coordinates is given by the Martini force-field [115, 206], where atoms are grouped into chemical building blocks. However, in this work, we describe each coronene molecule i by the center of mass position \mathbf{R}_i and an orientation vector $\hat{\mathbf{u}}_i$, pointing along the axis related to the largest eigenvalue of the inertia tensor of the atomistically-detailed molecule. As pointed out later, we can reduce the number of CG variables when considering a dimer with additional symmetries. In the upcoming subsections, we outline our strategy to choose CG

coordinates specifically designed for our coronene dimer system and further explain the transition from the atomistic to the CG level of detail using mapping functions.

4.3.1 Coronene dimer

For a coronene dimer system, we first consider the already-introduced vectorial CG coordinates \mathbf{R}_A , \mathbf{R}_B , $\hat{\mathbf{u}}_A$ and $\hat{\mathbf{u}}_B$ (in the beginning of Sec. 4.3). This choice of CG variables seems most natural due to several reasons: first, the inertia tensor is symmetric implying that the resulting CG variables do not change under simultaneous change of the atomic masses; second, the chosen set of variables is compatible with those variables used in the Gay-Berne model, which we will later use to parametrize our CG potential (see Sec. 5.3); and third, the center of mass description provides a particularly comfortable route to calculate the virial pressure. The number of variables

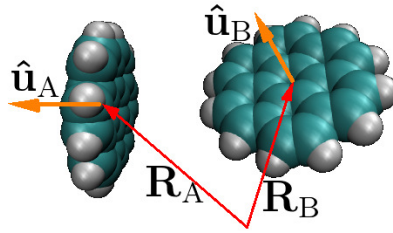


FIGURE 4.2: Sketch of a discotic dimer system with its corresponding vectorial CG coordinates \mathbf{R}_A , \mathbf{R}_B , $\hat{\mathbf{u}}_A$ and $\hat{\mathbf{u}}_B$.

describing the coronene “dimer” can be further reduced by transforming to the body-fixed frame of the particles. A common choice involves using the effective coordinates appearing in Ref. 19, namely

$$R = |\mathbf{R}_B - \mathbf{R}_A| \quad (4.16a)$$

$$\mathbf{a} = \hat{\mathbf{u}}_A \cdot \hat{\mathbf{R}} \quad \text{with } \hat{\mathbf{R}} = \frac{\mathbf{R}_B - \mathbf{R}_A}{|\mathbf{R}_B - \mathbf{R}_A|} \quad (4.16b)$$

$$\mathbf{b} = \hat{\mathbf{u}}_B \cdot \hat{\mathbf{R}} \quad (4.16c)$$

$$\mathbf{c} = \hat{\mathbf{u}}_A \cdot \hat{\mathbf{u}}_B. \quad (4.16d)$$

The coordinate R stands for the inter-molecular distance, while \mathbf{a} , \mathbf{b} and \mathbf{c} represent angular configurations of the dimer. We require the effective interaction of the two molecules to have head-to-tail as well as chiral symmetry (i.e., it should be invariant against mirroring the dimer system). This finally leads to a set of the following CG variables with a smaller parameter range

$$R = |\mathbf{R}_B - \mathbf{R}_A| \quad (4.17a)$$

$$a = |\hat{\mathbf{u}}_A \cdot \hat{\mathbf{R}}| \quad (4.17b)$$

$$b = |\hat{\mathbf{u}}_B \cdot \hat{\mathbf{R}}| \quad (4.17c)$$

$$c = \text{sgn}(\hat{\mathbf{u}}_A \cdot \hat{\mathbf{R}}) \text{sgn}(\hat{\mathbf{u}}_B \cdot \hat{\mathbf{R}}) \hat{\mathbf{u}}_A \cdot \hat{\mathbf{u}}_B. \quad (4.17d)$$

We hereby do not consider that particles are indistinguishable to have a set of variables compatible with the variables used in the Gay-Berne potential [63]. In Eq. (4.17d), the “sgn” is the sign function, defined as

$$\text{sgn}(x) = 1 \text{ for } x > 0; \text{sgn}(x) = -1 \text{ for } x < 0; \text{ and } \text{sgn}(0) = 0.$$

For further investigation, we also introduce the corresponding functions that map the atomic description directly on the CG description. They are denoted with \tilde{R} , \tilde{a} , \tilde{b} and \tilde{c} . A definition is provided in the forthcoming paragraph.

4.3.2 Mapping functions

In the following, we define the functions that map the detailed atomistic dimer system onto a CG level of resolution. The mapping functions that describe molecules' position are described through

$$\tilde{\mathbf{R}}_A(\{\mathbf{r}_i\}_{i \in \{1, \dots, 2N\}}) = \frac{1}{N} \sum_{i=1}^N \mathbf{r}_i, \quad \tilde{\mathbf{R}}_B(\{\mathbf{r}_i\}_{i \in \{1, \dots, 2N\}}) = \frac{1}{N} \sum_{i=N+1}^{2N} \mathbf{r}_i. \quad (4.18)$$

To obtain the molecules' orientations $\hat{\mathbf{u}}_A$ and $\hat{\mathbf{u}}_B$, the following inertia tensors are introduced

$$\underline{\mathbf{I}}_A(\{\mathbf{r}_i\}_{i \in \{1, \dots, 2N\}}) = \sum_{i=1}^N m_i (\mathbf{r}_i^2 \cdot \underline{\mathbf{1}} - \mathbf{r}_i \otimes \mathbf{r}_i), \quad \underline{\mathbf{I}}_B(\{\mathbf{r}_i\}_{i \in \{1, \dots, 2N\}}) = \sum_{i=N+1}^{2N} m_i (\mathbf{r}_i^2 \cdot \underline{\mathbf{1}} - \mathbf{r}_i \otimes \mathbf{r}_i). \quad (4.19)$$

The vectors $\hat{\mathbf{u}}_A$ and $\hat{\mathbf{u}}_B$ are chosen parallel to the eigenvector corresponding to the largest eigenvalue of $\underline{\mathbf{I}}_A$ and $\underline{\mathbf{I}}_B$. The corresponding mapping functions are denoted with $\tilde{\mathbf{u}}_A$ and $\tilde{\mathbf{u}}_B$. It should be noted that the sign for the direction may not be crucial – it is free to choose (the choice should be unique to make $\tilde{\mathbf{u}}_{A/B}$ well-defined). Changing the sign if the direction in $\hat{\mathbf{u}}_A$ or $\hat{\mathbf{u}}_B$ influences the Eqs. (4.16a)–(4.16d), but not our elaborate choice of CG variables defined in Eqs. (4.17a)–(4.17d). For coronene, the largest eigenvalue is along the symmetry axis, as shown in Fig. 4.3 and indicated by I_{zz} . The corresponding value $I_{zz} = 29.5 \text{ u nm}^2$ is around twice as large as the other eigenvalues. This inertia tensor thus clearly defines an orientation. Having determined $\tilde{\mathbf{R}}_A$, $\tilde{\mathbf{R}}_B$, $\tilde{\mathbf{u}}_A$ and $\tilde{\mathbf{u}}_B$, it is straight-forward to define \tilde{R} , \tilde{a} , \tilde{b} and \tilde{c} with the definitions in Sec. 4.3.1.

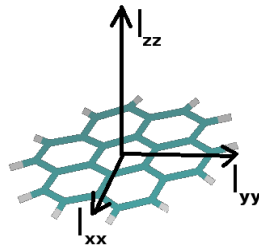


FIGURE 4.3: Scheme of the main inertia axes of a single coronene molecule. The largest moment of inertia, \mathbf{I}_{zz} , is aligned perpendicular to the molecular plain.

4.4 Histogram function

We next introduce histogram functions of CG coordinates, which - as we point out in Sec. 4.5 - lead to a definition of an effective pair potential. After the definition, we present techniques to improve the configurational sampling for rarely-sampled configurations. Specifically, this involves umbrella sampling, thermodynamic integration and steered dynamics.

4.4.1 Definition

The histogram function of an arbitrary set of CG variables $q_1, \dots, q_M \equiv q^M$ is defined through

$$P(q^M) = \langle \delta(q_1 - \tilde{q}_1) \dots \delta(q_M - \tilde{q}_M) \rangle,$$

where the brackets $\langle \dots \rangle$ denote an ensemble average and the \tilde{q}_i (with $i = 1, \dots, M$) represent mapping functions as defined in Sec. 4.3.2. For our coronene dimer system, the histogram function is thus defined through

$$P(R) = \langle \delta(R - \tilde{R}) \rangle \quad (4.20)$$

for the pure distance or R -dependent case and by

$$P(R, a, b, c) = \langle \delta(R - \tilde{R}) \delta(a - \tilde{a}) \delta(b - \tilde{b}) \delta(c - \tilde{c}) \rangle \quad (4.21)$$

for the distance and angle-dependent case. As we later see, Eq. (4.21) leads to the effective pair potential with the following relation to the histogram function

$$U_{\text{eff}}(R, a, b, c) = -kT \ln [\alpha P(R, a, b, c)] + \text{entropic contributions}(R, a, b, c), \quad (4.22)$$

with α imposing a unit of length. To perform the configurational sampling, i.e. to actually calculate the function $P(R)$ or $P(R, a, b, c)$, we perform all-atom Langevin dynamics simulations as described in Sec. 3.2. The noise term in the corresponding equations of motion [see Eq. (3.4)] generates internal translational and rotational motion, i.e., translational motion of individual atoms and rotations of the entire molecule around the molecules' center of mass. Accordingly, the full orientational configuration space is sampled at each distance R . However, standard sampling is hampered by the fact that the two molecules strongly attract each other. In the next paragraphs, we describe three methods used to overcome this drawback by restraining or constraining the molecules to a certain center of mass distance R , while the orientational motion remains undisturbed. The methods are umbrella sampling (US), thermodynamic integration and steered dynamics (SD). It is worth mentioning that, the parallel tempering method - which improves the sampling in rare phase space regions [33] - can be used as an alternative way to improve the sampling for rare (pair) configurations.

4.4.2 Umbrella sampling

In the framework of umbrella sampling [188, 189], the Hamiltonian of the system is supplemented by a bias potential to support the sampling in rare sampled regions of the configuration space. Together with the weighted histogram analysis method (WHAM) [104, 163, 180], umbrella sampling was already used to construct purely distance-dependent effective molecular pair potentials, e.g. for methane in aqueous solution [212]. In this work, we use bias potentials that correspond to harmonic springs (see Fig. 4.4), yielding

$$V_k(\{\mathbf{r}\}) = \frac{c_k^{\text{spring}}}{2} (\tilde{R}(\{\mathbf{r}\}) - R_k^{\text{eq}})^2. \quad (4.23)$$

Each of the N_w springs acts on the molecular centers of mass and is used for one specific simulation, called umbrella window run. The equilibrium length for each spring, R_k^{eq} , and the spring constants, c_k^{spring} , are chosen to guarantee a strong overlap of the R -dependent biased histogram functions $P_k^{\text{bias}}(R) = \langle \delta(R - \tilde{R}) \rangle_k$ for neighboring umbrella windows ($k, k+1$).

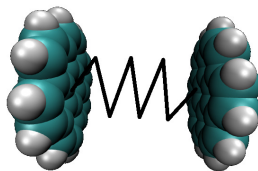


FIGURE 4.4: Coronene dimer with a spring connecting the center of masses of both coronene molecules. The spring acts as an inter-molecular bias.

The brackets $\langle \dots \rangle_k$ denote an ensemble or time average in the umbrella window k . Out of $P_k^{\text{bias}}(R)$, we can obtain the purely distance-dependent, unbiased histograms $P(R)$ by using the one-dimensional WHAM equations. We further extend these equations to the multidimensional case [104] involving additional reaction coordinates a, b, c . In our case, the bias potential V_k is a function of R alone [see Eq. (4.23)]. By contrast, we are interested in the four-dimensional histogram $P(R, a, b, c)$.

The WHAM equations [104] serve to calculate the unbiased histogram P from biased histograms P_k^{bias} . They comprise the following self-consistent set of equations (here shown for the reaction coordinate R alone)

$$P(R) = \sum_{k=1}^{N_w} \gamma_k(R) P_k^{\text{bias}}(R) \quad (4.24a)$$

$$\gamma_k(R) = \frac{n_k}{\sum_{i=1}^{N_w} n_i e^{-\frac{1}{kT}(V_i(R)-F_i)}} \quad (4.24b)$$

$$F_k = -kT \ln \left[\int_0^\infty dR e^{-\frac{1}{kT} V_k(R)} P(R) \right]. \quad (4.24c)$$

In Eq. (4.24b), n_k represents the number of sampling points in umbrella window k . Furthermore, the weights $\gamma_k(R)$ represent the coefficients in the decomposition of the unbiased histogram into the biased ones [see Eq. (4.24a)]. Finally, F_k are the free

energy constants, which are initialized by the non-iterative free energy perturbation method [76, 163], where the difference between the free energy constants is given through

$$\Delta F_{k,k-1} = F_k - F_{k-1} = -kT \ln \left[\int_0^\infty dR e^{-\left(\frac{1}{kT} V_k(R) - \frac{1}{kT} V_{k-1}(R)\right)} P_{k-1}^{\text{bias}}(R) \right]. \quad (4.25)$$

The fact that the bias potentials V_k do not depend on the angular configurations described through a , b and c leads to a simple generalization for our angle-resolved case. Specifically, we employ Eqs. (4.24b) and (4.24c) together with the following decomposition of the full unbiased histogram function

$$P(R, a, b, c) = \sum_{k=1}^{N_w} \gamma_k(R) \cdot P_k^{\text{bias}}(R, a, b, c), \quad (4.26)$$

where γ_k represents R -dependent coefficients defined in Eq. (4.24a). A similar strategy has been used in Ref. 64, where the goal was to obtain the effective pair potential of a methanol pair dissolved in water with two reaction coordinates.

4.4.3 Thermodynamic integration

The thermodynamic integration [98] allows us to calculate the difference in free energies between two systems. Differences in the free energy can be used to calculate the histogram function. Specifically, the Hamiltonian of system A can be continuously changed towards the Hamiltonian of system B using the coupling parameter $\lambda \in [0, 1]$. The Hamiltonian or energy function E of the system is thus

$$E(\lambda) = E_A + \lambda \cdot (E_B - E_A). \quad (4.27)$$

For the free energy difference holds

$$\Delta F = F(\lambda) - F(0) = \int_0^\lambda d\lambda' \frac{\partial F}{\partial \lambda'}(\lambda') = \int_0^\lambda d\lambda' \left\langle \frac{\partial E_{\text{pot}}(\lambda')}{\partial \lambda'} \right\rangle. \quad (4.28)$$

Let us consider the following coupling parameter

$$\lambda(R') = \frac{R' - R_0}{R - R_0},$$

where the variable R' with $R_0 \leq R' \leq R$ is mapped onto the interval $[0, 1]$. By using Eqs. (2.5) and (2.7) we can reformulate the derivative of the free energy into a derivative of the potential energy, according to

$$\frac{\partial F}{\partial R'}(R') = \frac{1}{kT} \frac{\partial \ln Z}{\partial R'}(R') \quad (4.29a)$$

$$= \frac{1}{kT} \frac{1}{Z} \frac{\partial}{\partial R'} \left[\frac{1}{C} \int_{\Pi^{2DN}} d\mathbf{p}^{2N} \int_{V^{2N}} d\mathbf{r}^{2N} \exp\left(-\frac{1}{kT} E(\lambda(R'))\right) \right] \quad (4.29b)$$

$$= \frac{1}{kT} \frac{1}{Z} \frac{\partial}{\partial R'} \left[\frac{1}{C'} \int_{V^{2N}} d\mathbf{r}^{2N} \exp\left(-\frac{1}{kT} E_{\text{pot}}(R')\right) \right] \quad (4.29c)$$

$$= \frac{1}{kT} \frac{1}{Z} \left(\frac{1}{C'} \int_{V^{2N}} d\mathbf{r}^{2N} \exp\left(-\frac{1}{kT} E_{\text{pot}}(R')\right) \right) \cdot \frac{\partial}{\partial R'} \left(-\frac{1}{kT} E_{\text{pot}}(R') \right) \quad (4.29d)$$

$$= \left\langle \frac{\partial E_{\text{pot}}(R')}{\partial R'} \right\rangle_{R'}. \quad (4.29e)$$

The derivative $\frac{\partial E_{\text{pot}}(R')}{\partial R'}$ marks the constraint force and for the constant C' we have

$$\frac{1}{C'} = \frac{1}{C} \int_{\Pi^{2DN}} d\mathbf{p}^{2N} \exp\left(-\frac{1}{kT} E_{\text{kin}}(\mathbf{p}^{2N})\right) = \frac{1}{\alpha^{6N}}.$$

Furthermore, the brackets $\langle \dots \rangle_{R'}$ denote the ensemble average for the the constraint $R = R'$ (a time average under this constraint is also possible). Alternatively to the ensemble average or time average with respect to a certain constraint, we can use averages over so-called pull trajectories. Specifically, the second law of thermodynamics states that the work W applied to the system cannot be smaller than the difference between the free energies [148], i.e.

$$\Delta F \leq \langle W \rangle, \quad (4.30)$$

with an explicit expression given through the Jarzynski relation

$$e^{-\frac{1}{kT} \Delta F} = \left\langle e^{-\frac{1}{kT} W} \right\rangle. \quad (4.31)$$

The inequality (4.30) reduces to an equality, if the work applied the system is made via a quasi-static process. In this case, we have

$$\Delta F = \langle W \rangle = \left\langle \int_{t_0}^t dt' \frac{\partial R'}{\partial t'} \frac{\partial E(R')}{\partial R'} \right\rangle = c_{\text{pull}} \left\langle \int_{t_0}^t dt' \frac{\partial E(R')}{\partial R'} \right\rangle, \quad (4.32)$$

with c_{pull} being the pull rate. The brackets $\langle \dots \rangle$ denote the average over simulation runs. The distribution $P(R)$ can be calculated via the free energy difference $\Delta \mathcal{F}(R) = \mathcal{F}(R) - \mathcal{F}(R_0)$. Specifically, we have

$$P(R) = \frac{1}{\alpha} \frac{Z(R)}{Z} = \frac{e^{-\frac{1}{kT} \mathcal{F}(R)}}{\alpha Z} = \frac{e^{-\frac{1}{kT} \Delta \mathcal{F}(R) + \mathcal{F}(R_0)}}{\alpha Z} \propto e^{-\frac{1}{kT} \Delta \mathcal{F}(R)}, \quad (4.33)$$

with $Z(R) = \alpha Z \langle \delta(R - \tilde{R}) \rangle$, $\frac{1}{\alpha} \int_0^\infty dR Z(R) = Z$ and $\mathcal{F}(R) = -kT \ln Z(R)$.

4.4.4 Non-equilibrium sampling – steered dynamics

In a steered dynamics (SD) simulation [83, 134], a reaction coordinate is changed in time by applying external constraining forces. In the present work, we pull one coronene molecule away from the other along the connecting vector \mathbf{R} . Specifically, the molecular distance is steered according to the following law

$$R(t) = R_0 + c_{\text{pull}} \cdot t, \quad (4.34)$$

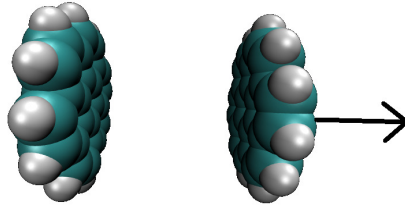


FIGURE 4.5: Sketch of a coronene dimer where one molecule is slowly pulled away from the other in a SD simulation.

where c_{pull} is the pull rate. The latter is so small that the entire simulation can be seen as a quasi-static process. Therefore, given a small time interval, the system evolves according to the so-called constrained-reaction-coordinate-dynamics ensemble [31]. Meanwhile, all rotational degrees of freedom remain unconstrained. The scheme in Eq. (4.34) implies an equal weighting of all values of R . Therefore the corresponding R -dependent histogram function $P(R)$ forms a flat distribution. Accordingly, $P(R)$ does not provide any information about the distance-dependent effective potential. Hence $P(R, a, b, c)$ is not measurable in this way. In order to overcome this drawback, we introduce a factorization of the unconstrained histogram function, as follows

$$P(R, a, b, c) = P(R) \cdot \left(\frac{P(R, a, b, c)}{P(R)} \right). \quad (4.35)$$

The pure distance-dependent part $P(R)$ can be determined using the thermodynamic integration method, as pointed out in Sec. 4.4.3. To calculate the remaining function $P(R, a, b, c)$, we use Eq. (4.21), yielding

$$\begin{aligned} \frac{P(R, a, b, c)}{P(R)} &= \frac{\mathcal{Z}(R, a, b, c)}{\mathcal{Z}(R)} = \\ &= \frac{\frac{1}{\alpha^{\delta N-1}} \int_V d\mathbf{r}_1 \cdots \int_V d\mathbf{r}_{2N} e^{-\frac{1}{kT} U(\mathbf{r}_1, \dots, \mathbf{r}_{2N})} \delta(R - \tilde{R}) \delta(a - \tilde{a}) \delta(b - \tilde{b}) \delta(c - \tilde{c})}{\frac{1}{\alpha^{\delta N-1}} \int_V d\mathbf{r}_1 \cdots \int_V d\mathbf{r}_{2N} e^{-\frac{1}{kT} U(\mathbf{r}_1, \dots, \mathbf{r}_{2N})} \delta(R - \tilde{R})}. \end{aligned} \quad (4.36)$$

The right-hand side can be considered as an ensemble average over all atomic configurations that correspond to the specific center of mass distance R , i.e.

$$\begin{aligned} \frac{P(R, a, b, c)}{P(R)} &= \left\langle \delta(a - \tilde{a}) \delta(b - \tilde{b}) \delta(c - \tilde{c}) \right\rangle_{\text{ensemble}}^{\text{distance}=R} \\ &= P(R, a, b, c|R). \end{aligned} \quad (4.37)$$

We can conclude that $P(R, a, b, c|R)$ is the conditional histogram function of the angle-dependent reaction coordinates for a fixed distance R . For small time intervals Δt (sufficiently small to ensure that R is fixed, but sufficiently large to sample the entire angular configuration space), we can replace the ensemble average in Eq. (4.37) by a

time average, that is

$$P(R, a, b, c|R) \rightarrow \left\langle \delta(a - \tilde{a}) \delta(b - \tilde{b}) \delta(c - \tilde{c}) \right\rangle_{\Delta t}^{\text{distance}=R}. \quad (4.38)$$

It is worth mentioning that the smaller the pull rate c_{pull} , the larger the time interval Δt can be. Finally, by combining Eqs. (4.33), (4.35) and (4.38), we obtain the unconstrained histogram function $P(R, a, b, c)$.

4.5 Definition of the effective pair potential

In the current section, we define the effective pair potential between two molecules, which depends on the center of mass distance and the axial orientation of each molecule in this dimer system. We first start with Kirkwood's potential of mean force and gradually extend his ideas towards our distance- and angle-dependent effective potential (between coronene molecules) in Sec. 4.5.3. Finally, in Sec. 4.5.4 we define the configurational entropy that corrects the variation of the microscopic phase space volume element related to a specific set of CG coordinates.

4.5.1 Kirkwood's potential of mean force

In 1935, Kirkwood defined the potential of mean force (PMF) [98] between two particles in a many-particle system. Explicitly, it is defined through the mean inter-molecular force between two particles, where the influence of the other particles is effectively taken into account. The mean force on particle 1 due to particle 2 is defined through

$$\langle \mathbf{F}_{12} \rangle = \frac{\int_V d\mathbf{r}_3 \cdots \int_V d\mathbf{r}_N e^{-\frac{1}{kT} E_{\text{pot}}(\{\mathbf{r}_k\})} (\nabla_1 E_{\text{pot}}(\{\mathbf{r}_k\}))}{\int_V d\mathbf{r}_3 \cdots \int_V d\mathbf{r}_N e^{-\frac{1}{kT} E_{\text{pot}}(\{\mathbf{r}_k\})}} \equiv \nabla_1 w. \quad (4.39)$$

The PMF - as further denoted with w - is related to the pair distribution function g (see Sec. 2.7.1) according to

$$w = -kT \ln g. \quad (4.40)$$

An expression for the R -dependent PMF between any pair of particles in a system of N particles is thus given through (see also Sec. 2.7.1)

$$w(R) = -kT \ln[g(R)] = -kT \ln[G^{000}(R)\psi^{000}] \quad (4.41)$$

$$= -kT \ln \left[\left\langle \frac{V}{4\pi R^2} \frac{1}{N^2} \sum_{ij} \delta(|\mathbf{R}_{ij}| - R) \right\rangle \right]. \quad (4.42)$$

It follows that the PMF between two particles in a system of N particles is defined as

$$w(R_{12}) = -kT \ln \left[\frac{\left\langle \frac{1}{4\pi V R_{12}^2} \delta(R_{12} - |\mathbf{r}_2 - \mathbf{r}_1|) \right\rangle}{\left(\frac{1}{V}\right)^2} \right] \quad (4.43a)$$

$$= -kT \ln \left[\frac{V \cdot P(R_{12})}{R_{12}^2 \cdot 4\pi} \right]. \quad (4.43b)$$

This investigation leads us to define effective potentials for arbitrary sets of CG variables. For this purpose, we approach this topic from another perspective. In the following, we consider a canonical configuration integral of an n -particle system (all particles are distinguishable) by

$$Z = \frac{1}{\alpha^{3n}} \int_V d\mathbf{r}_1 \cdots \int_V d\mathbf{r}_n e^{-\frac{1}{kT} E_{\text{pot}}(\mathbf{r}_1, \dots, \mathbf{r}_n)}. \quad (4.44)$$

We now use the identity $1 = \int_0^\infty dR_{12} \delta(R_{12} - \tilde{R}_{12}(\mathbf{r}_1, \dots, \mathbf{r}_n))$, with the mapping function $\tilde{R}_{12}(\mathbf{r}_1, \dots, \mathbf{r}_n) = |\mathbf{r}_2 - \mathbf{r}_1|$, stating that each microscopic configuration corresponds exactly to one distance value R_{12} . Accordingly, we yield for the configuration integral

$$Z = \frac{1}{\alpha^{3n}} \int_V d\mathbf{r}_1 \cdots \int_V d\mathbf{r}_n \int_0^\infty dR \delta(R_{12} - \tilde{R}_{12}(\mathbf{r}_1, \dots, \mathbf{r}_n)) e^{-\frac{1}{kT} E_{\text{pot}}(\mathbf{r}_1, \dots, \mathbf{r}_n)} \quad (4.45a)$$

$$= \frac{1}{\alpha} \int_0^\infty dR \underbrace{\frac{1}{\alpha^{3n-1}} \int_V d\mathbf{r}_1 \cdots \int_V d\mathbf{r}_n \delta(R_{12} - \tilde{R}_{12}(\mathbf{r}_1, \dots, \mathbf{r}_n)) e^{-\frac{1}{kT} E_{\text{pot}}(\mathbf{r}_1, \dots, \mathbf{r}_n)}}_{\mathcal{Z}(R_{12})} \quad (4.45b)$$

We further note that in Eq. (4.45b) the appearance of $\int_V d\mathbf{r}_1 \cdots \int_V d\mathbf{r}_n \delta(R_{12} - \tilde{R}_{12}(\{\mathbf{r}\}))$ indicates the constrained integration over the subclass of microstates, which corresponds to the inter-particle distance R_{12} . The corresponding configuration integral of this subclass is defined as

$$\mathcal{Z}(R_{12}) = \frac{1}{\alpha^{3n-1}} \int_V d\mathbf{r}_1 \cdots \int_V d\mathbf{r}_n \delta(R_{12} - \tilde{R}_{12}(\mathbf{r}_1, \dots, \mathbf{r}_n)) e^{-\frac{1}{kT} E_{\text{pot}}(\mathbf{r}_1, \dots, \mathbf{r}_n)} \quad (4.46a)$$

$$= \alpha Z \langle \delta(R_{12} - \tilde{R}_{12}(\mathbf{r}_1, \dots, \mathbf{r}_n)) \rangle \quad (4.46b)$$

$$= \alpha Z P(R_{12}). \quad (4.46c)$$

The idea is now to define an effective potential leaving $\mathcal{Z}(R_{12})$ and thus $P(R_{12})$ “untouched”. This means that the frequency of occurrence for a configuration separated by R_{12} is invariant concerning both levels of detail. A remaining problem is that the number of microstates forming a configuration - with R_{12} being the distance between particle 1 and 2 - varies with R_{12} . We thus introduce a new effective configuration integral $\mathcal{Z}_{\text{eff}}(R_{12})$, which is normalized by the amount of configuration space volume, namely

$$\mathcal{Z}_{\text{eff}}(R_{12}) = \frac{\mathcal{Z}(R_{12})}{\mathcal{Z}_{\text{mic}}(R_{12})}, \quad (4.47)$$

where \mathcal{Z}_{mic} is a “microcanonical” integral, “counting” the number of microstates belonging to a fixed R_{12} and is defined as

$$\mathcal{Z}_{\text{mic}}(R_{12}) = \frac{1}{\alpha^{3n-1}} \int_V d\mathbf{r}_1 \cdots \int_V d\mathbf{r}_n \delta(R_{12} - \tilde{R}_{12}(\{\mathbf{r}\})) \quad (4.48a)$$

$$= \frac{1}{\alpha^{3n-1}} \int_V d\mathbf{r}_1 \int_V d\mathbf{r}_2 \delta(R_{12} - |\mathbf{r}_2 - \mathbf{r}_1|) \int_V d\mathbf{r}_3 \dots \int_V d\mathbf{r}_n \quad (4.48b)$$

$$= \frac{1}{\alpha^{3n-1}} 4\pi R_{12}^2 V^{n-1}. \quad (4.48c)$$

The canonical configuration integral can thus be written as

$$\mathcal{Z}(R_{12}) = \frac{1}{\alpha} \int_0^\infty dR_{12} \mathcal{Z}_{\text{mic}}(R_{12}) \cdot \mathcal{Z}_{\text{eff}}(R_{12}). \quad (4.49)$$

For each inter-molecular distance R_{12} the infinitesimal volume element in Eq.(4.49) is defined as $\mathcal{Z}_{\text{mic}}(R_{12}) dR_{12}$. The idea is to associate $\mathcal{Z}_{\text{eff}}(R_{12})$ with a Boltzmann factor comprising the effective potential. However, in order to define a PMF that decays to zero, we have to normalize $\mathcal{Z}_{\text{eff}}(R_{12})$ with a constant Λ that represents $\mathcal{Z}_{\text{eff}}(R_{12} \rightarrow \infty)$. Specifically, we yield

$$U_{\text{eff}}(R_{12}) = -kT \ln \left[\frac{\mathcal{Z}_{\text{eff}}(R_{12})}{\Lambda} \right]. \quad (4.50)$$

In order to determine this constant, we focus on the canonical configuration integral for $R_{12} \rightarrow \infty$, i.e.

$$\mathcal{Z}(R_{12} \rightarrow \infty) = \frac{1}{\alpha^{3n}} \int_V d\mathbf{r}_1 \int_V d\mathbf{r}_2 \delta(R_{12} - |\mathbf{r}_2 - \mathbf{r}_1|) \int_V d\mathbf{r}_3 \dots \int_V d\mathbf{r}_n e^{-\frac{1}{kT} E_{\text{pot}}(\mathbf{r}_1, \dots, \mathbf{r}_n)} \quad (4.51a)$$

$$= 4\pi R_{12}^2 V \alpha \cdot \frac{Z}{V^2} = 4\pi R_{12}^2 \alpha \cdot \frac{Z}{V}. \quad (4.51b)$$

The resulting effective configuration integral is independent of its variables at large distances, i.e.

$$\mathcal{Z}_{\text{eff}}(R_{12}) \xrightarrow{R_{12} \rightarrow \infty} \Lambda = \frac{\alpha^{3n} Z}{V^n} = \text{const.} \quad (4.52)$$

From Eqs. (4.50) and (4.52), it follows that $U_{\text{eff}}(R_{12}) \rightarrow 0$ for $R_{12} \rightarrow \infty$, as one would expect. Finally, we can conclude the following expressions using Eq. (4.46c)

$$\begin{aligned} U_{\text{eff}}(R_{12}) &= -kT \ln \left[\frac{\mathcal{Z}_{\text{eff}}(R_{12})}{\Lambda} \right] = -kT \ln \left[\frac{\alpha Z \langle \delta(R_{12} - |\mathbf{r}_2 - \mathbf{r}_1|) \rangle}{\Lambda \cdot \mathcal{Z}_{\text{mic}}} \right] \\ &= -kT \ln \left[\frac{V \langle \delta(R_{12} - |\mathbf{r}_2 - \mathbf{r}_1|) \rangle}{4\pi R_{12}^2} \right] \end{aligned} \quad (4.53)$$

$$= -kT \ln \left[\frac{V \cdot P(R_{12})}{R_{12}^2 \cdot 4\pi} \right]. \quad (4.54)$$

The last expression is thus equivalent to Eq. (4.43b), meaning that our effective potential is introduced in a way compatible with the PMF, i.e. $U_{\text{eff}} = w$.

4.5.2 Pure distance-dependent effective potential in a molecular dimer

In contrast to Kirkwood, we next focus on a system comprising only two molecular particles (see Sec. 4.2.1), although we consider internal degrees of freedom for each of the two molecules. An effective pair potential as a function of the inter-molecular center of mass distance is subsequently derived in analogy to the presented PMF.

The coronene dimer (see Fig. 4.1) - which comprises $2N$ atoms (with the atoms at the positions $\mathbf{r}_1, \dots, \mathbf{r}_N$ belonging to molecule A and the rest belonging to molecule B; $N = 36$) - thus leads to the following canonical configuration integral

$$Z = \frac{1}{\alpha^{6N}} \int_V d\mathbf{r}_1 \cdots \int_V d\mathbf{r}_{2N} e^{-\frac{1}{kT} E_{\text{pot}}(\mathbf{r}_1, \dots, \mathbf{r}_{2N})}. \quad (4.55)$$

The mapping function \tilde{R} [see Eq. (4.18)] maps the atomic positions on the distance between the center of masses of molecule A and B, denoted by \mathbf{R}_A and \mathbf{R}_B , respectively. The configuration integral can thus be written as

$$Z = \frac{1}{\alpha^{6N}} \int_V d\mathbf{r}_1 \cdots \int_V d\mathbf{r}_{2N} \int_0^\infty dR \delta(R - \tilde{R}(\mathbf{r}_1, \dots, \mathbf{r}_{2N})) e^{-\frac{1}{kT} E_{\text{pot}}(\mathbf{r}_1, \dots, \mathbf{r}_{2N})} \quad (4.56)$$

$$= \frac{1}{\alpha} \int_0^\infty dR \mathcal{Z}(R). \quad (4.57)$$

where the integrand appearing in the last equation is defined as

$$\mathcal{Z}(R) = \frac{1}{\alpha^{6N-1}} \int_V d\mathbf{r}_1 \cdots \int_V d\mathbf{r}_{2N} \delta(R - \tilde{R}(\mathbf{r}_1, \dots, \mathbf{r}_{2N})) e^{-\frac{1}{kT} E_{\text{pot}}(\mathbf{r}_1, \dots, \mathbf{r}_{2N})}. \quad (4.58)$$

In Eq. (4.57) the appearance of $\int_V d\mathbf{r}_1 \cdots \int_V d\mathbf{r}_{2N} \delta(R - \tilde{R}(\{\mathbf{r}\}))$ indicates the constrained integration over the subclass of microstates, which corresponds to the inter-molecular distance R . In analogy to Eq. (4.47), we introduce the effective configuration integral $\mathcal{Z}_{\text{eff}}(R)$, which is normalized by the amount of configuration space volume, namely

$$\mathcal{Z}_{\text{eff}}(R) = \frac{\mathcal{Z}(R)}{\mathcal{Z}_{\text{mic}}(R)}, \quad (4.59)$$

with

$$\mathcal{Z}_{\text{mic}}(R) = \frac{1}{\alpha^{6N-1}} \int_V d\mathbf{r}_1 \cdots \int_V d\mathbf{r}_{2N} \delta(R - \tilde{R}(\{\mathbf{r}\})) \quad (4.60)$$

$$= \frac{4\pi R^2 V^{2N-1}}{\alpha^{6N-1}}. \quad (4.61)$$

Eq. (4.58) has the following limit for infinite R , yielding

$$\mathcal{Z}(R) \xrightarrow{R \rightarrow \infty} 4\pi R^2 V \alpha \cdot \frac{Z}{V^2} = 4\pi R^2 \alpha \cdot \frac{Z}{V}. \quad (4.62)$$

The resulting effective configuration integral is independent of its variables at large distances, i.e.

$$\mathcal{Z}_{\text{eff}}(R) \xrightarrow{R \rightarrow \infty} \Lambda = \frac{\alpha^{6N} Z}{V^{2N}} = \text{const.} \quad (4.63)$$

For the R -dependent effective potential thus follows

$$U_{\text{eff}}(R) = -kT \ln \left[\frac{\mathcal{Z}_{\text{eff}}(R)}{\Lambda} \right]. \quad (4.64)$$

With Eq. (4.59) and $P(R) = \frac{\mathcal{Z}(R)}{\alpha Z}$, we obtain

$$U_{\text{eff}}(R) = -kT \ln \left[\frac{V \langle \delta(R - \tilde{R}(\{\mathbf{r}\})) \rangle}{4\pi R^2} \right] = -kT \ln \left[\frac{V P(R)}{4\pi R^2} \right]. \quad (4.65)$$

Numerically, we determine the quantity $P(R)$ through sampling methods as described in Section 4.4. Although, yielding the same expression like Eq. (4.54), we here consider another kind of system with internal degrees of freedom. We next extend this investigation towards additional angular dependence.

4.5.3 Distance and orientation dependent effective potential in a molecular dimer

In this section, we derive an effective pair potential that depends on the CG coordinates defined in Eq. (4.17). Each atomic configuration $\{\mathbf{r}\} = \{\mathbf{r}_i\}_{i=1, \dots, 2N}$ corresponds to a unique set of reaction coordinates, i.e.

$$1 = \int_0^\infty dR \delta(R - \tilde{R}(\{\mathbf{r}\})), \dots, 1 = \int_{\mathbb{R}} dc \delta(c - \tilde{c}(\{\mathbf{r}\})).$$

Therefore, the canonical configuration integral can be written as an integration over the reaction coordinates R , a , b and c , yielding

$$Z = \frac{1}{\alpha} \int_0^\infty dR \dots \int_{\mathbb{R}} dc \mathcal{Z}(R, a, b, c), \quad (4.66)$$

with integrand

$$\mathcal{Z}(R, a, b, c) = \frac{1}{\alpha^{6N-1}} \int_V d\mathbf{r}_1 \dots \int_V d\mathbf{r}_{2N} \delta(R - \tilde{R}(\{\mathbf{r}\})) \dots \delta(c - \tilde{c}(\{\mathbf{r}\})) e^{-\frac{1}{kT} U(\{\mathbf{r}\})}. \quad (4.67)$$

In analogy to Eq. (4.59), we now introduce the effective configuration integral for the coordinates R , a , b and c , yielding

$$\mathcal{Z}_{\text{eff}}(R, a, b, c) = \frac{\mathcal{Z}(R, a, b, c)}{\mathcal{Z}_{\text{mic}}(R, a, b, c)}, \quad (4.68)$$

with the microcanonical integral

$$\mathcal{Z}_{\text{mic}}(R, a, b, c) = \frac{1}{\alpha^{6N-1}} \int_V d\mathbf{r}_1 \dots \int_V d\mathbf{r}_{2N} \delta(R - \tilde{R}(\{\mathbf{r}\})) \dots \delta(c - \tilde{c}(\{\mathbf{r}\})). \quad (4.69)$$

A distance and orientation dependent effective potential is given through

$$U_{\text{eff}}(R, a, b, c) = -kT \ln \left[\frac{\mathcal{Z}_{\text{eff}}(R, a, b, c)}{\Lambda} \right], \quad (4.70)$$

with $\mathcal{Z}_{\text{eff}}(R, a, b, c) \xrightarrow{R \rightarrow \infty} \mathcal{Z}_{\text{eff}}(R) \xrightarrow{R \rightarrow \infty} \Lambda = \text{const}$ to satisfy that $U_{\text{eff}}(R, a, b, c) \rightarrow 0$ for $R \rightarrow \infty$. We determine the quantity $\mathcal{Z}(R, a, b, c)$ entering $\mathcal{Z}_{\text{eff}}(R, a, b, c)$ [see Eq. (4.68)] by solving Eq. (4.67) through numerical sampling methods as described in Section 4.4. For the effective potential thus holds

$$U_{\text{eff}}(R, a, b, c) = -kT \ln \left[\frac{\alpha Z \langle \delta(R - \tilde{R}(\{\mathbf{r}\})) \dots \delta(c - \tilde{c}(\{\mathbf{r}\})) \rangle}{\Lambda \mathcal{Z}_{\text{mic}}(R, a, b, c)} \right] \quad (4.71a)$$

$$= -kT \ln \left[\frac{V^{2N} P(R, a, b, c)}{\alpha^{6N-1} \mathcal{Z}_{\text{mic}}(R, a, b, c)} \right]. \quad (4.71b)$$

4.5.4 Configurational entropy

The microcanonical configuration integrals $\mathcal{Z}_{\text{mic}}(R)$ and $\mathcal{Z}_{\text{mic}}(R, a, b, c)$ from previous investigations can be related to a Boltzmann entropy. In the following, we provide explicit expressions for the configurational entropy.

4.5.4.1 Pure distance dependence

The pure distance-dependent effective potential as defined in Eq. (4.64) can be split into a free energy and a configurational entropy part, yielding

$$U_{\text{eff}}(R) = -kT \ln [\mathcal{Z}(R)] + T \cdot S_{\text{B}}(R), \quad (4.72)$$

with the entropy

$$S_{\text{B}}(R) = k \ln [\Lambda \mathcal{Z}_{\text{mic}}(R)]. \quad (4.73)$$

Taken altogether, we can thus interpret U_{eff} as a configuration-dependent free energy, corrected by the Boltzmann entropy related to the configuration space spanned by the CG variables. It can be related to the histogram function as follows

$$U_{\text{eff}}(R) = -kT \ln [P(R)\alpha Z] + T \cdot S_{\text{B}}(R). \quad (4.74)$$

If the distance R is the only variable on the CG level, the entropy reduces to

$$S_{\text{B}}(R) = k \ln \left(\frac{\alpha Z}{V} \cdot 4\pi R^2 \right) \quad (4.75)$$

$$= 2k \ln(R/\alpha) + k \ln \left(\frac{4\pi\alpha^2 Z}{V} \right) \quad (4.76)$$

as outlined in Ref. 138.

4.5.4.2 Distance and orientation dependence

Analogously to the previous paragraph, we can split the distance and angle-dependent effective potential as defined in Eq. (4.70) into a free energy and a configurational entropy part, yielding

$$U_{\text{eff}}(R, a, b, c) = -kT \ln[\alpha Z P(R, a, b, c)] + T \cdot S_{\text{B}}(R, a, b, c). \quad (4.77)$$

The denominator in Eq. (4.68), $\mathcal{Z}_{\text{mic}}(R, a, b, c)$, can be associated to a Boltzmann entropy

$$S_{\text{B}}(R, a, b, c) = k \ln[\Lambda \mathcal{Z}_{\text{mic}}(R, a, b, c)]. \quad (4.78)$$

We next calculate the quantity $\mathcal{Z}_{\text{mic}}(R, a, b, c)$ and thereby the related configurational entropy. For this purpose, we make use of the mapping functions introduced in Sec. 4.3. First, the microscopic configuration integral is defined as

$$\mathcal{Z}_{\text{mic}}(R, a, b, c) = \frac{1}{\alpha^{6N-1}} \int_V d\mathbf{r}_1 \dots \int_V d\mathbf{r}_{2N} \delta(R - \bar{R}(\{\mathbf{r}\})) \dots \delta(c - \bar{c}(\{\mathbf{r}\})). \quad (4.79)$$

In the following, the functions labeled with circles (i.e. $\mathring{\mathbf{R}}_{\text{A}}$, $\mathring{\mathbf{R}}_{\text{B}}$, $\mathring{\hat{\mathbf{u}}}_{\text{A}}$, $\mathring{\hat{\mathbf{u}}}_{\text{B}}$) map atomic coordinates on corresponding position and orientation vectors of each molecule, while functions with a bar (i.e. \bar{R} , \bar{a} , \bar{b} , \bar{c}) map those vectors onto the reaction coordinates R , a , b and c . By using identities such as $\int_V d\mathbf{R}_{\text{A}} \delta(\mathbf{R}_{\text{A}} - \mathring{\mathbf{R}}_{\text{A}}(\{\mathbf{r}\})) = 1$ and expressions like $\bar{R}(\{\mathbf{r}\}) = \bar{R}(\mathring{\mathbf{R}}_{\text{A}}(\{\mathbf{r}\}), \mathring{\mathbf{R}}_{\text{B}}(\{\mathbf{r}\}))$, Eq. (4.79) reads

$$\begin{aligned} \mathcal{Z}_{\text{mic}}(R, a, b, c) = & \\ & \frac{1}{\alpha^{6N-1}} \int_V d\mathbf{R}_{\text{A}} \int_V d\mathbf{R}_{\text{B}} \int_{S^2} d\hat{\mathbf{u}}_{\text{A}} \int_{S^2} d\hat{\mathbf{u}}_{\text{B}} \delta(R - \bar{R}(\mathbf{R}_{\text{A}}, \mathbf{R}_{\text{B}})) \dots \delta(c - \bar{c}(\mathbf{R}_{\text{A}}, \mathbf{R}_{\text{B}}, \hat{\mathbf{u}}_{\text{A}}, \hat{\mathbf{u}}_{\text{B}})) \\ & \int_V d\mathbf{r}_1 \dots \int_V d\mathbf{r}_{2N} \delta(\mathbf{R}_{\text{A}} - \mathring{\mathbf{R}}_{\text{A}}(\{\mathbf{r}\})) \delta(\mathbf{R}_{\text{B}} - \mathring{\mathbf{R}}_{\text{B}}(\{\mathbf{r}\})) \delta(\hat{\mathbf{u}}_{\text{A}} - \mathring{\hat{\mathbf{u}}}_{\text{A}}(\{\mathbf{r}\})) \delta(\hat{\mathbf{u}}_{\text{B}} - \mathring{\hat{\mathbf{u}}}_{\text{B}}(\{\mathbf{r}\})). \end{aligned} \quad (4.80)$$

The expression in the last line is denoted by $X(\mathbf{R}_{\text{A}}, \mathbf{R}_{\text{B}}, \hat{\mathbf{u}}_{\text{A}}, \hat{\mathbf{u}}_{\text{B}})$. We split this integral with respect to the two molecules, namely

$$\begin{aligned} X(\mathbf{R}_{\text{A}}, \mathbf{R}_{\text{B}}, \hat{\mathbf{u}}_{\text{A}}, \hat{\mathbf{u}}_{\text{B}}) = & \left(\int_V d\mathbf{r}_1 \dots \int_V d\mathbf{r}_N \delta(\mathbf{R}_{\text{A}} - \mathring{\mathbf{R}}_{\text{A}}(\{\mathbf{r}^{\text{A}}\})) \delta(\hat{\mathbf{u}}_{\text{A}} - \mathring{\hat{\mathbf{u}}}_{\text{A}}(\{\mathbf{r}^{\text{A}}\})) \right) \times \\ & \times \left(\int_V d\mathbf{r}_{N+1} \dots \int_V d\mathbf{r}_{2N} \delta(\mathbf{R}_{\text{B}} - \mathring{\mathbf{R}}_{\text{B}}(\{\mathbf{r}^{\text{B}}\})) \delta(\hat{\mathbf{u}}_{\text{B}} - \mathring{\hat{\mathbf{u}}}_{\text{B}}(\{\mathbf{r}^{\text{B}}\})) \right), \end{aligned} \quad (4.81)$$

where $\{\mathbf{r}^{\text{A}}\} = (\mathbf{r}_1, \dots, \mathbf{r}_N, \mathbf{0}, \dots, \mathbf{0})$ and $\{\mathbf{r}^{\text{B}}\} = (\mathbf{0}, \dots, \mathbf{0}, \mathbf{r}_{N+1}, \dots, \mathbf{r}_{2N})$. The first factor symbolizes a measure for the number of microscopic realizations for a molecule A at \mathbf{R}_{A} with orientation $\hat{\mathbf{u}}_{\text{A}}$. This measure is invariant concerning the position and orientation of molecule A. The second factor in Eq. (4.81) can be treated analogously for molecule B. As a result, $X(\mathbf{R}_{\text{A}}, \mathbf{R}_{\text{B}}, \hat{\mathbf{u}}_{\text{A}}, \hat{\mathbf{u}}_{\text{B}}) =: X$ is constant. Therefore Eq. (4.80)

can be simplified to

$$\mathcal{Z}_{\text{mic}} = \frac{1}{\alpha^{6N-1}} X \int_V d\mathbf{R}_A \int_V d\mathbf{R}_B \delta(R - \bar{R}(\mathbf{R}_A, \mathbf{R}_B)) \int_{S^2} d\hat{\mathbf{u}}_A \int_{S^2} d\hat{\mathbf{u}}_B \delta(a - \bar{a}(\mathbf{R}_A, \mathbf{R}_B, \hat{\mathbf{u}}_A)) \dots \delta(c - \bar{c}(\mathbf{R}_A, \mathbf{R}_B, \hat{\mathbf{u}}_A, \hat{\mathbf{u}}_B)). \quad (4.82)$$

By using translational and rotational invariance of the molecular dimer system, then it follows

$$\mathcal{Z}_{\text{mic}}(R, a, b, c) = \frac{1}{\alpha^{6N-1}} X V 4\pi R^2 \int_{S^2} d\hat{\mathbf{u}}_A \int_{S^2} d\hat{\mathbf{u}}_B \delta(a - \bar{a}(\mathbf{R}_A, \mathbf{R}_B, \hat{\mathbf{u}}_A)) \dots \delta(c - \bar{c}(\mathbf{R}_A, \mathbf{R}_B, \hat{\mathbf{u}}_A, \hat{\mathbf{u}}_B)). \quad (4.83)$$

Finally, the integration over different orientations $\hat{\mathbf{u}}_A$, $\hat{\mathbf{u}}_B$ can be written in polar coordinates with polar angles θ_1 and θ_2 and azimuthal angles ϕ_1 and ϕ_2 . Furthermore, by taking into account chirality invariance, i.e. $\phi_2 \rightarrow 2\phi_1 - \phi_2$, we can define the enclosed angle $\psi = |\phi_1 - \phi_2|$ instead of ϕ_1 and ϕ_2 . We find

$$\mathcal{Z}_{\text{mic}}(R, a, b, c) = \frac{1}{\alpha^{6N-1}} X V R^2 64\pi^2 \int_0^{\frac{\pi}{2}} d\theta_1 \sin(\theta_1) \delta(a - \cos(\theta_1)) \int_0^{\frac{\pi}{2}} d\theta_2 \sin(\theta_2) \delta(b - \cos(\theta_2)) \int_0^\pi d\psi \delta(c - (\sin(\theta_2) \cos(\psi) + \cos(\theta_1) \cos(\theta_2))). \quad (4.84)$$

From Eq. (4.84), the configurational entropy follows with the logarithm of the latter expression as defined in Eq. (4.78).

Chapter 5

Effective pair potential for coronene molecules

5.1 Preface

In this chapter we first analyze in Sec. 5.2 the effective pair potential for coronene for the angle-averaged, i.e. pure distance-dependent, case and the angle-resolved case as defined in Sec. 4.5. For this purpose we focus on the van der Waals part of the intermolecular pair interaction between the coronene molecules (underlying microscopic interactions described in Sec. 4.2.1). As already mentioned in the introduction, other coarse-grained potentials developed for coronene in the literature [7, 128, 143, 205] do not take into account the full angle- and temperature dependence. To extract the required information from underlying all-atom simulations we use atomistic trajectory data from Langevin dynamics (LD) with two sampling modifications, namely umbrella sampling (US) and steered dynamics (SD) [see Sec. 4.4.2–4.4.4].

Our analysis covers the effective potential for various molecular configurations as well as temperatures. These tabulated (numerical) effective potentials are then fitted to various anisotropic Lennard-Jones like models in Sec. 5.3, where each molecule is represented by one central interaction site. Of course, more complexity can be introduced by considering many (instead of one central) interaction sites [123, 209]. However, we instead aim at developing a model which has as few degrees of freedom as possible while still conserving the uniaxiality and head-to-tail symmetry of typical disc-shaped molecules. In Sec. 5.4, we include in a second step electrostatic contributions to our best model. The general purpose is to provide an approach that is appropriate to describe not only fluid phases, but also stable crystalline phases for these molecules. Even more, the crystal structure gives a relation to electronic properties, like band gaps [166]. Concerning the coarse-grained electrostatic contributions, we use two fundamentally different approaches. One is based on a point quadrupole representation and the other on extended ring-shaped charge distributions. The entire electrostatic contribution is assumed not to be dependent of temperature and is treated separately from the remaining interactions via a direct sum. We further check the performance of our developed models in bulk systems of many molecules via MD simulations in Chapter 6. These findings build on our published articles corresponding to reference Nos. 78 and 79.

5.2 Van der Waals interaction

In this section we apply the two sampling methods (US, SD) introduced in Chapter 4 for the atomistic simulations to calculate the effective pair potential of a coronene dimer system comprising of inter-molecular van der Waals interactions at various temperatures T . The atomistic model as given in Sec. 4.2.1 does not depend on electrostatic interactions for the current investigation (for a detailed discussion about the electrostatic contribution see Sec. 5.4). A fundamental quantity required to calculate effective potentials are the histogram functions of the coarse-grained variables as pointed out in Eq. (4.65) and (4.71b).

We next provide numerical details for the atomistic simulations that were performed by Karol Palczynski (Helmholtz-Zentrum Berlin). Later on, we investigate the angle-averaged effective potential $U_{\text{eff}}(R)$ [see Eq. (4.65)] and turn afterwards to the angle-resolved case, i.e. $U_{\text{eff}}(R, a, b, c)$, as defined in Eq. (4.71b) [coarse-grained coordinates given in Sec. 4.3.1].

5.2.1 Numerical details

In order to determine the histogram functions $P_k^{\text{bias}}(R)$ and $P_k^{\text{bias}}(R, a, b, c)$ from US simulations or $P(R, a, b, c|R)$ from SD simulations from the atomistic trajectory data, we use the following scheme. For both sampling methods the molecular distance R is sub-divided into 800 bins covering the interval $[0.23 \text{ nm}, 4.5 \text{ nm}]$. A graphical representation of the P_k^{bias} as a function of the bin number is represented in Fig. 5.1. To

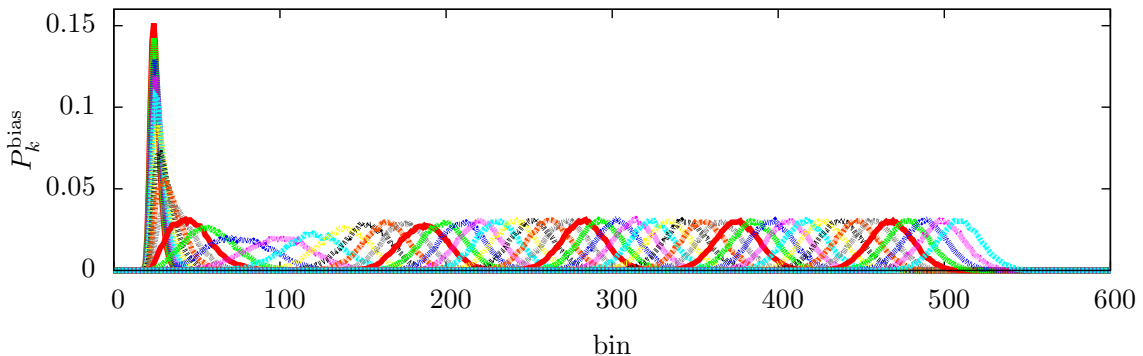


FIGURE 5.1: Biased histograms P_k^{bias} as a function of the binned inter-molecular center of mass distance of two coronene molecules is shown for 50 different umbrella sampling setups. The equilibrium lengths of the springs is chosen as $R_k^{\text{eq}} = (0.253 + k \cdot 0.055) \text{ nm}$. Hereby 800 bins cover the interval $[0.23 \text{ nm}, 4.5 \text{ nm}]$.

capture the angle dependence, we focus on eight configurations, namely the face-face (FF), parallel weakly displaced, parallel displaced (PD), T-, herringbone, V-, edge-edge and the cross configuration. Graphical representations as well as explicit definitions in terms of the CG coordinates a , b and c are given in Table 5.1 on page 72. In order to assign a set of coordinates (a, b, c) to one of these configurations, we use the tolerances given in this table. To obtain a smooth result for the effective interactions $U_{\text{eff}}(R, a, b, c)$ for the previously introduced configurations, we reduce the number of bins in the angle-resolved unbiased histogram function $P(R, a, b, c)$ that determines

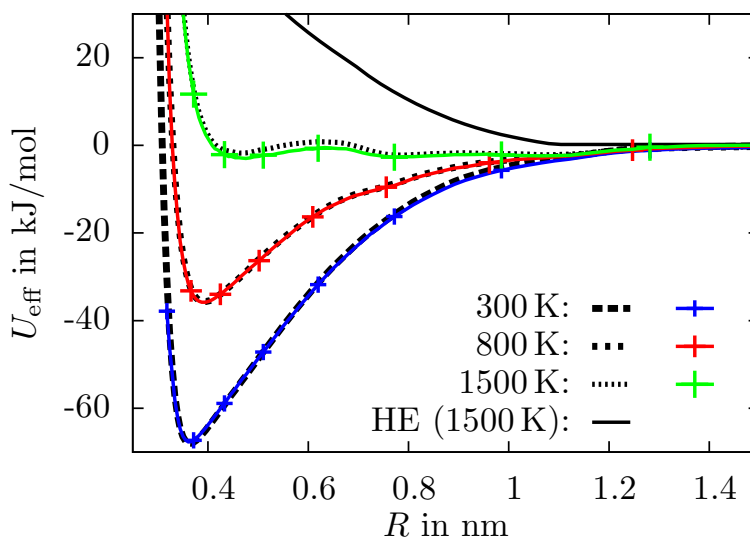


FIGURE 5.2: The angle-averaged effective potential at different temperatures using steered dynamics (SD, broken lines) and umbrella sampling (US, solid colored lines). For comparison the angle-averaged hard ellipsoidal (HE) potential for 1500 K is added.

$U_{\text{eff}}(R, a, b, c)$ [see Eq. (4.22)] to 100. This is realized by associating bin x to bin $y(x) = 30.167 \ln[x/30.167 + 1]$, yielding $y(0) = 0$, $y(800) \approx 100$ and $y'(0) = 1$. As a consequence the first bins are small, while bins for larger distances are bigger to account for the weaker sampling in these regions. In the US simulations we use 50 umbrella windows ($k = 0, \dots, 49$) each lasting for 5.5 ns . The initial configuration is always set to the face-face configuration. Each spring is characterized by a spring constant of $c_k^{\text{spring}} = 500 \text{ kJ/mol/nm}$ and an equilibrium length of $R_k^{\text{eq}} = (0.253 + k \cdot 0.055) \text{ nm}$. The WHAM-equations for the distance R (see Sec. 4.4.2) are repeatedly solved until the change in the free energy constants F_k is below 10^{-5} kJ/mol . Resulting weights $\gamma(R)$ serve as new weights in the multidimensional decomposition [see Eq. (4.26)].

The start distance in the SD simulations is set to 0.253 nm in a face-face configuration. Then, the second molecule is pulled away from the first with a rate of $c_{\text{pull}} = 10^{-5} \text{ nm/ps}$.

5.2.2 Angle-averaged effective potentials

We calculated the effective potential $U_{\text{eff}}(R)$ at three temperatures, namely 300 K, 800 K and 1500 K [definition in Eq. (4.65)]. Numerical results obtained via the US and the SD method are presented in Fig. 5.2. The data reveal a strong temperature dependence of $U_{\text{eff}}(R)$. At the lowest temperature considered (300 K) we observe a pronounced attractive potential well with large negative values, corresponding to a coupling strength of about $27 k_B T$. Conversely, the potential at 1500 K is weakly positive nearly everywhere, reflecting a (weak) effective repulsion. The pronounced temperature dependence of $U_{\text{eff}}(R)$ seems not too surprising in view of the amount of variables which have been integrated out. In particular, averaging out the rotations at fixed R implies that energetically most attractive configurations are mixed with less attractive ones; this mixing effect clearly becomes the more important the higher the

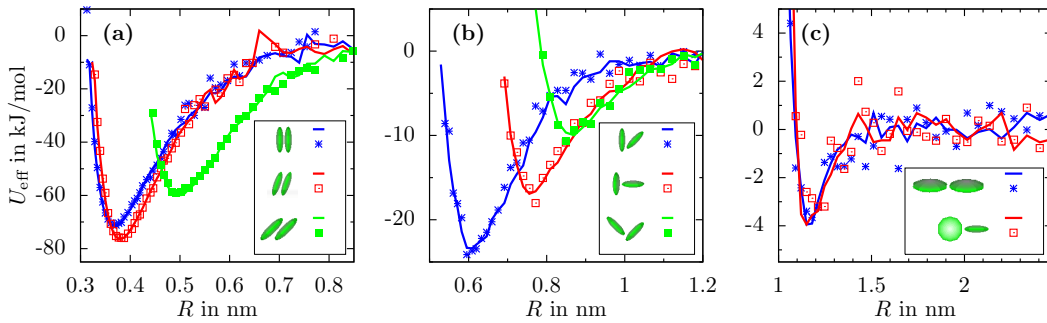


FIGURE 5.3: Angle-resolved effective potentials at $T = 800\text{K}$ obtained from umbrella sampling (solid lines) and steered dynamics (points). (a) FF, parallel weakly displaced and PD-configuration; (b) T-, V-, and herringbone configuration; (c) edge-edge and cross configuration (configurations defined in Tab. 5.1).

temperature. In fact, in the limit of *infinite* temperature one would expect attractive atom-atom interactions to become entirely irrelevant, yielding a purely entropic effective interaction determined by only the steric repulsion between the particles. This "entropic limit" of $U_{\text{eff}}(R)$ should be close to the angle-averaged potential of two hard ellipsoidal (HE) discs (see Sec. 5.3.1). Numerical results for the latter are included in Fig. 5.2 (the data have been obtained in analogy to that between coronene molecules). Inspecting then the temperature dependence of $U_{\text{eff}}(R)$ we see that, at 1500 K, we are not yet in the entropic limit but are clearly approaching it.

A further interesting feature revealed by Fig. 5.2 is that, quite independent of the temperature, the range of $U_{\text{eff}}(R)$ is always about 1.2 nm. Finally, we see that the two sampling methods yield numerically consistent results except for minor differences in the range $R \approx 0.4\text{--}0.8\text{ nm}$ at $T = 1500\text{ K}$.

5.2.3 Angle-resolved effective potentials

We now turn to one of the central issues of this work, that is, the angle dependence of the effective potentials. We first focus on the case $T = 800\text{ K}$. Corresponding results for the angle-resolved potentials are shown in Fig. 5.3, where we concentrate on the configurations introduced in Sec. 5.2.1 [see also Tab. 5.1]. It is seen that all configurations are characterized by an attractive well at short distances. However, the position of the potential minimum and its depth strongly depend on the specific orientation. The most attractive configurations are those with a large contact area of the particles, that is, the FF- and PD-configurations [see Fig. 5.3(a)]. Among these, the most attractive one is not the perfect FF-configuration (as one might have expected), but the weakly PD-configuration. The corresponding potential depth is larger by a factor of about twenty as compared to that of the edge-edge and cross configuration. Comparing now the two sampling methods, we find the US and SD methods to be generally consistent, with the accuracy of each method depending somewhat on the inter-molecular distance considered. At short distances, the potential curves are better described by the SD technique, while the US method is superior (in terms of roughness) at larger distances. Moreover, the US technique provides a particularly efficient sampling of

the orientation configuration at fixed distance R . To improve the performance of this latter technique at small distances one could use larger spring constants or adaptive US techniques [127]. We also note the two methods, US and SD, have already been compared in Ref. 8 for the case of one CG coordinate. In that study, it was found that SD requires an order of magnitude longer simulation runs to obtain the same accuracy as the US method. This is consistent with our observations and can be seen for configurations with a large contact distance [see Fig. 5.3(c)].

We next consider the influence of temperature on the angle-dependent potentials. Figure 5.4(a) shows as an example SD results for the FF-configuration at three temperatures. It is seen that there is, indeed, a temperature dependence, but this dependence is less pronounced than in the case of the angle-averaged potential $U_{\text{eff}}(R)$ (see Fig. 5.2). This is plausible in view of the less severe coarse-graining: instead of integrating out *all* "dimer" configurations (including rotations) at fixed R , the configurational average yielding the potential in Fig. 5.4(a) only involves FF configurations with different degrees of "bending", that is, thermal fluctuations of the atoms at fixed mean orientation. In other words, the temperature dependence is strongly correlated with the fact that, on the atomistic level, the molecules are not rigid. This is also demonstrated by the difference between our finite-temperature results and those related to *ground state* configurations [included in Fig. 5.4(a)], where the atomistically resolved molecules are rigid. Less temperature dependence is found for configurations with larger contact distance, such as the T-configuration [see Fig. 5.4(b)]. We understand this as a consequence of the fact that the energy related to T-configurations is less affected by bending fluctuations. Still one clearly observes, similar to the FF case, the tendency that a decrease of the temperature yields a decrease of the well-depth, that is, an increase of attraction.

TABLE 5.1: This table summarizes the tolerances used to define specific dimer configurations, which are particularly relevant. Note that each configuration remains its character by swapping the particles, which can be done by swapping a and b . The herringbone configuration is taken from Ref. 47.

	face-face (FF) 			parallel weakly displaced 			parallel displaced (PD) 			T 		
	a	b	c	a	b	c	a	b	c	a	b	c
value	1	1	1	0.94	0.94	1	$1/\sqrt{2}$	$1/\sqrt{2}$	1	0	1	0
min	0.96	0.96	-1	0.92	0.92	0.96	0.68	0.68	0.96	0	0.88	-0.12
max	1	1	1	0.96	0.96	1	0.72	0.72	1	0.12	1	0.12
	herringbone 			V 			edge-edge 			cross 		
	a	b	c	a	b	c	a	b	c	a	b	c
value	0.8767	0.481	0	1	$1/\sqrt{2}$	$1/\sqrt{2}$	0	0	1	0	0	0
min	0.8	0.44	-0.12	0.88	0.64	0.64	0	0	0.8	0	0	-0.2
max	0.92	0.56	0.12	1	0.76	0.76	0.2	0.2	1	0.2	0.2	0.2

5.3 Fitting the effective potential

So far we have determined the effective pair potential numerically from the atomic trajectories. We are now in the position to parametrize our coarse-grained potentials.

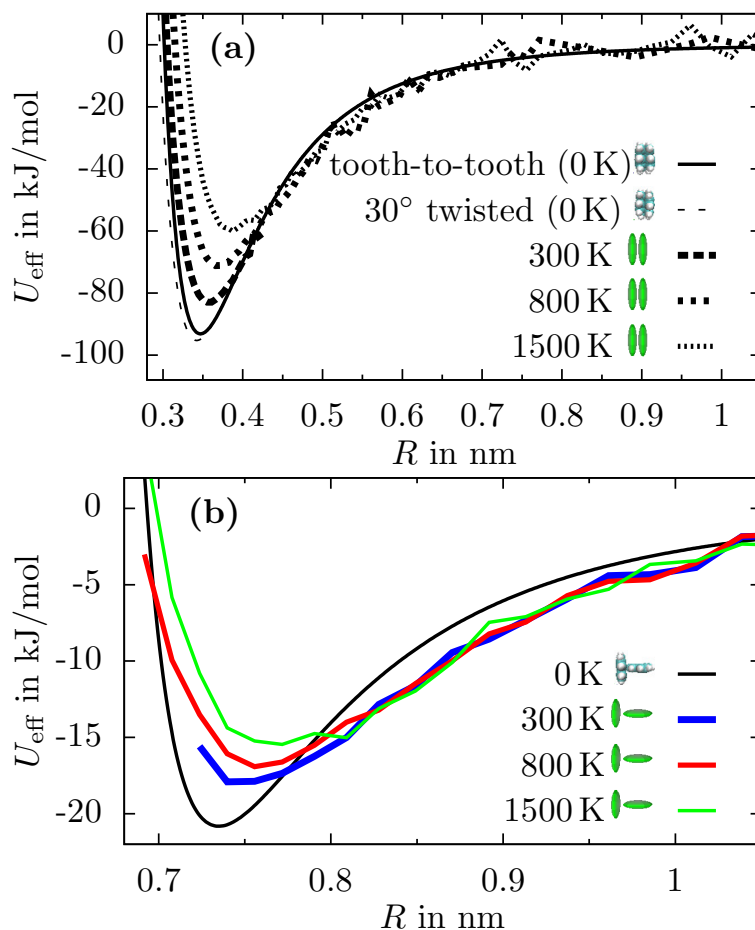


FIGURE 5.4: (a) Steered dynamics (SD) results for the FF-configuration at different temperatures. Included are two curves corresponding to FF results for atomistically-resolved coronene molecules in its ground state ($T = 0$). (b) Umbrella sampling (US) results for the T-configuration at different temperatures. For comparison, a T-configuration for atomistic coronene molecules in their ground state ($T = 0$) is included as well.

In a further step we fit the coarse-grained potentials onto variants of Gay-Berne(GB)-potentials [63]. These potentials involve, in principle, all aspects observed in our numerical data, that is, anisotropy, softness, and attraction at short length scales. The advantage of such a parametrization is that all potential values can be accessed without any smoothing or extrapolation. Moreover, the calculation of forces and torques is strongly simplified.

We next provide several potentials that possess a “hard” ellipsoidal core. Starting first with a hard ellipsoid potential (for which we calculated an effective pair potential at $T = 1500$ K in Fig. 5.2), we further present the Kabadi potential [92] (a frequently used extension of the Gay-Berne potential), which also has short-ranged attraction and simultaneously provide two parametrizations, K1 and K2. Later on, we introduce our own modification of the GB potential, for which we introduce a parameter choice M, which turned out to be superior in representing various dimer configurations as compared to other parameter choices. For completeness, we also consider a pure

distance-dependent potential and denote it further “spherical model” (S). The quality of the resulting models is evaluated by comparing the resulting many-particle behavior at different thermodynamic state points with that of the underlying atomistic system in Chapter 6.

5.3.1 Hard ellipsoid (HE) potential

The hard ellipsoid pair potential simply incorporates the shape of an ellipsoid and is defined through

$$U_{\text{HE}}(R, a, b, c) = \begin{cases} \infty & , R < \sigma(a, b, c) \\ 0 & , \text{else} \end{cases} \quad (5.1)$$

with the ellipsoidal contact distance (i.e., $U(\sigma) = 0$) [42]

$$\sigma(a, b, c) = \sigma_0 \left[1 - \frac{\chi}{2} (A^+ + A^-) + (1 - \chi) \chi_t (A^+ A^-)^\gamma \right]^{-\frac{1}{2}}. \quad (5.2)$$

For the coefficients in Eq. (5.2), we have $A^\pm = (a \pm b)^2 / (1 \pm \chi c)$, and the anisotropy parameters $\chi = (\kappa^2 - 1) / (\kappa^2 + 1)$ and $\chi_t = [(\kappa - 1) / (\kappa + 1)]^2$, where $\kappa = \sigma_{\text{FF}} / \sigma_0$ is the quotient of the face-face and edge-edge contact distance. Neither ellipsoid attracts the other. Regarding the effective distance-dependent potential of two ellipsoids, there is a temperature dependent soft-repulsive potential defined through

$$U_{\text{eff}}(R) = -\frac{1}{\beta} \ln \left(\int_{S^2} d\hat{\mathbf{u}}_1 \int_{S^2} d\hat{\mathbf{u}}_2 e^{-\beta U_{\text{HE}}} \right) + \text{const} \quad (5.3a)$$

$$= -\frac{1}{\beta} \ln \left(\int_0^\pi d\theta_1 \int_0^\pi d\theta_2 \int_0^\pi d\psi \sin(\theta_1) \sin(\theta_2) f(R, \theta_1, \theta_2, \psi) \right) + \text{const}, \quad (5.3b)$$

with

$$f(R, \theta_1, \theta_2, \psi) = \begin{cases} 1 & , R > \sigma(R, \dots) \\ 0 & , \text{else} \end{cases}.$$

The constants in Eqs. (5.3a) and (5.3b) are chosen to satisfy $U_{\text{eff}}(R \rightarrow \infty) = 0$. We calculated this potential at 1500 K, assuming hard coronene ellipsoids in Fig. 5.2.

5.3.2 Kabadi potential

We next consider an extension of the original GB model [63] which was introduced by Kabadi [92]. The extension involves a coefficient d_w which acts as a factor on the well width of the original GB potential. This potential reads in analogy to the familiar Lennard-Jones potential

$$U(R, a, b, c) = 4 \epsilon(a, b, c) \cdot \left[\left(\frac{1}{R^*} \right)^{12} - \left(\frac{1}{R^*} \right)^6 \right], \quad (5.4)$$

where $R^* = (R - \sigma(a, b, c) + d_w \sigma_0) / (d_w \sigma_0)$ represents the reduced distance, $\sigma(a, b, c)$ the contact distance and $\epsilon(a, b, c)$ the well depth. The definition of the contact distance,

$$\sigma(a, b, c) = \sigma_0 \left[1 - \frac{\chi}{2} (A^+ + A^-) \right]^{-\frac{1}{2}} \quad (5.5)$$

has a drawback compared to Eq. (5.2), since for orthogonal facing particles, i.e. $c = 0$, the potential becomes independent of a and b . Regarding the well depths ϵ , we use the following formula

$$\epsilon(a, b, c) = \epsilon_0 \cdot \left[1 - \chi^2 c^2 \right]^{-\frac{1}{2}\nu} \cdot [\epsilon_M(a, b, c)]^\mu, \quad (5.6)$$

where the factor ϵ_M is defined as

$$\epsilon_M(a, b, c) = 1 - \frac{\chi'}{2} (A'^+ + A'^-). \quad (5.7)$$

The coefficients $A'^{\pm} = (a \pm b)^2 / (1 \pm \chi' c)$ in Eq. (5.7) resemble the quantities A^{\pm} (defined in the HE potential), but incorporate the anisotropy parameter χ' . The ϵ_0 marks the interaction strength for the cross configuration. The Kabadi potential has two parameters to characterize the interaction strength, namely ϵ_0 and κ' . Furthermore, two additional parameters characterize the pure distance dependent part $\left[\left(\frac{1}{R^*} \right)^{12} - \left(\frac{1}{R^*} \right)^6 \right]$ which are d_w and κ .

We next introduce two parametrizations, called K1 and K2, of the Kabadi potential. The following properties are equal among both parametrizations. The well width d_w is calculated using the face-face contact distance σ_{FF} and the distance corresponding to the minimum of the face-face potential, $R_{\text{FF}}^{\text{min}}$, yielding

$$d_w = \frac{R_{\text{FF}}^{\text{min}} - \sigma_{\text{FF}}}{\sigma_0 (2^{1/6} - 1)}. \quad (5.8)$$

The edge-edge contact distance σ_0 is determined directly from the edge-edge potential curve. The exponents in Eq. (5.6), μ and ν are set to 1. The remaining fitting parameters κ' and ϵ_0 are adjusted in two different ways: Model K1 aims at a correct reproduction of the potential depths of the weakly PD-configuration and the V-configuration. The latter is important for collisions in the isotropic phase. Model K2 aims also at a correct weakly PD well depth but in contrast to K1 also at a correct edge-edge well depth, which is a crucial configuration in the crystalline regime. The fit parameters for further models at different temperatures are summarized in Tab. A.1 and A.2 in Appendix A.3.

5.3.3 Modified Gay-Berne (mGB) potential

The Kabadi potential is now extended to possess more parameters. First, we replace the contact distance defined in Eq. (5.5) by the more elaborate contact distance from Eq. (5.2), which does not have the previously mentioned drawback. Regarding the

well depths ϵ , we still use the formula defined in Eq. (5.6), but define the factor ϵ_M as

$$\epsilon_M(a, b, c) = 1 - \frac{\chi'}{2} (A'^+ + A'^-) + \theta \cdot (A'^+ A'^-)^{\gamma'} + \xi \cdot K(a, b, c). \quad (5.9)$$

The function

$$K(a, b, c) = [1 - 5a - 5b - 15a^2b^2 + 2(c - 5ab)^2] \quad (5.10)$$

has the symmetry of a linear quadrupole-quadrupole interaction [11, 26, 68, 181]. In Eq. (5.9) the term $\theta \cdot (A'^+ A'^-)^{\gamma'}$ is introduced to modify the strength of T-like configurations, while the last term is introduced to increase the attraction strength for the PD-configurations. However, it should be noted that the strength multiplier ϵ_0 no longer corresponds to the potential depth of the cross configuration. The potential is further denoted with U_{mGB} .

In the following, we discuss a parametrization ‘‘M’’ for this potential to represent the van der Waals interaction given through $U_{\text{eff}}(R, a, b, c)$ and denote it with $U_{\text{mGB}}^{\text{vdW}}(R, a, b, c)$. Within this parametrization, we fix the following parameters for all temperatures: $\mu = 1$, $\nu = 1$, $\gamma = 4$ and $\gamma' = 4$. The anisotropy parameter χ is calculated by measuring the FF contact distance σ_{FF} , which is always sampled in our setup of SD simulations, and the edge-edge contact distance σ_0 . The well width d_w and the aspect ratio κ are calculated in the same way like the Kabadi models. To summarize, the two parameters which determine the shape, are extracted from the FF- and edge-edge configuration. Further configurations come into play when we determine the remaining parameters ϵ_0 , χ' , θ and ξ by fitting the simulation results for $U_{\text{eff}}(R, a, b, c)$ according to Eq. (5.6). Specifically, our parameter fit builds on the four attractive wells stemming from the parallel weakly displaced, PD-, T- and edge-edge configuration. The main reason to pick those configurations is that, according to our many-particle simulations presented in Sec. 6.2, these are the four most frequent configurations at high densities.

The corresponding parameters at different temperatures are contained in Table A.3 in Appendix A.3.

5.3.4 Spherical model (S)

For completeness, we also introduce a model (S) involving a pure distance-dependent potential. To this end we use the angle-averaged potential taken from the SD simulations presented in Fig. 5.2.

5.3.5 Parametrized curves

We present in Figs. 5.5(a)-(i) potential curves for various pair constellations using our previously defined models at a temperature of 800K. Furthermore, the angle-averaged curves for all our models are presented in Fig. 5.5(j) at the temperatures 300K, 800K, and 1500K [they are determined in analogy to Eq. (5.3a)].

As expected the Kabadi models, K1 (with correct potential strength for parallel weakly displaced and V-configuration) and K2 (with correct strength for parallel weakly displaced and edge-edge configuration), are inconsistent in that they do not

reproduce the coarse-grained angle-resolved potential, since they are constructed by considering only two orientational configurations to fit the potential strength.

In contrast, model M, which is a parametrization of our mGB potential, gives good results (as compared to the original coarse-grained potential) for other configurations, such as V-configuration. This is due to the fact that this model involves the correct strength for four different configurations, i.e. parallel weakly displaced, PD-, T- and edge-edge configuration. Only the FF-configuration is slightly overestimated. In addition, model M is *intrinsically consistent* in the sense that, when performing an angle average over the fit results, one arrives at a potential which is very close to the angle-averaged numerical coarse-grained potential discussed in Sec. 5.2.2 (see also Sec. 5.3.4).

The performance of our models is further evaluated by comparing the resulting many-particle behavior at different thermodynamic state points with that of the underlying atomic system in Chapter 6. However, we next introduce electrostatic effects first.

5.4 Coarse-grained electrostatics

In this section we present different approaches to model the full pair interaction, i.e. with electrostatics, between coronene molecules. Again, coronene serves as an exemplary discotic molecule with head-to-tail symmetry desired for our electrostatic investigation. For this purpose, we start from our previously introduced model M (see Sec. 5.3.3), which models the temperature-dependent inter-molecular van der Waals interactions of coronene.

For true coronene (or other conjugated molecules) one obvious drawback of our van der Waals study is that electrostatics are required to stabilize the herringbone structure we later observe in the condensed phase (Sec. 6.2.2). We note again that a full treatment of this problem would involve taking into account not only static charges (which could be estimated by the ground state energy values given in Ref. 213), but also polarizability effects. On a coarse-grained level, one intuitive starting point to include electrostatics without polarizability is to include a quadrupole moment. The quadrupole corresponds to the lowest-order multipole moment of coronene. There already exist some simulation studies involving discotics with quadrupole moments [11, 146], including applications to benzene [65] (represented by a Gay-Berne disc with a linear quadrupole moment) and micron-sized colloidal (e.g., clay) particles [45, 192]. Inspired by these studies we later propose an extension of the present approach, where model M is supplemented by the interaction of two linear quadrupoles placed along the symmetry axes of the particles.

In principle, the kind of coarse-graining method presented in Chapter 4 could be applied to molecules with electrostatic contributions, where ab-initio simulations (which combine MD and DFT) are used. Though ab-initio simulations are very time consuming from a computational perspective, a common compromise consists in using static partial charges distributed among the atoms of the underlying microscopic model in the coarse-graining procedure [7]. By implication, as shown in previous studies involving quantum-chemical calculations [57], it is generally not sufficient to use the static atomic partial charges characterizing an isolated coronene dimer (except for

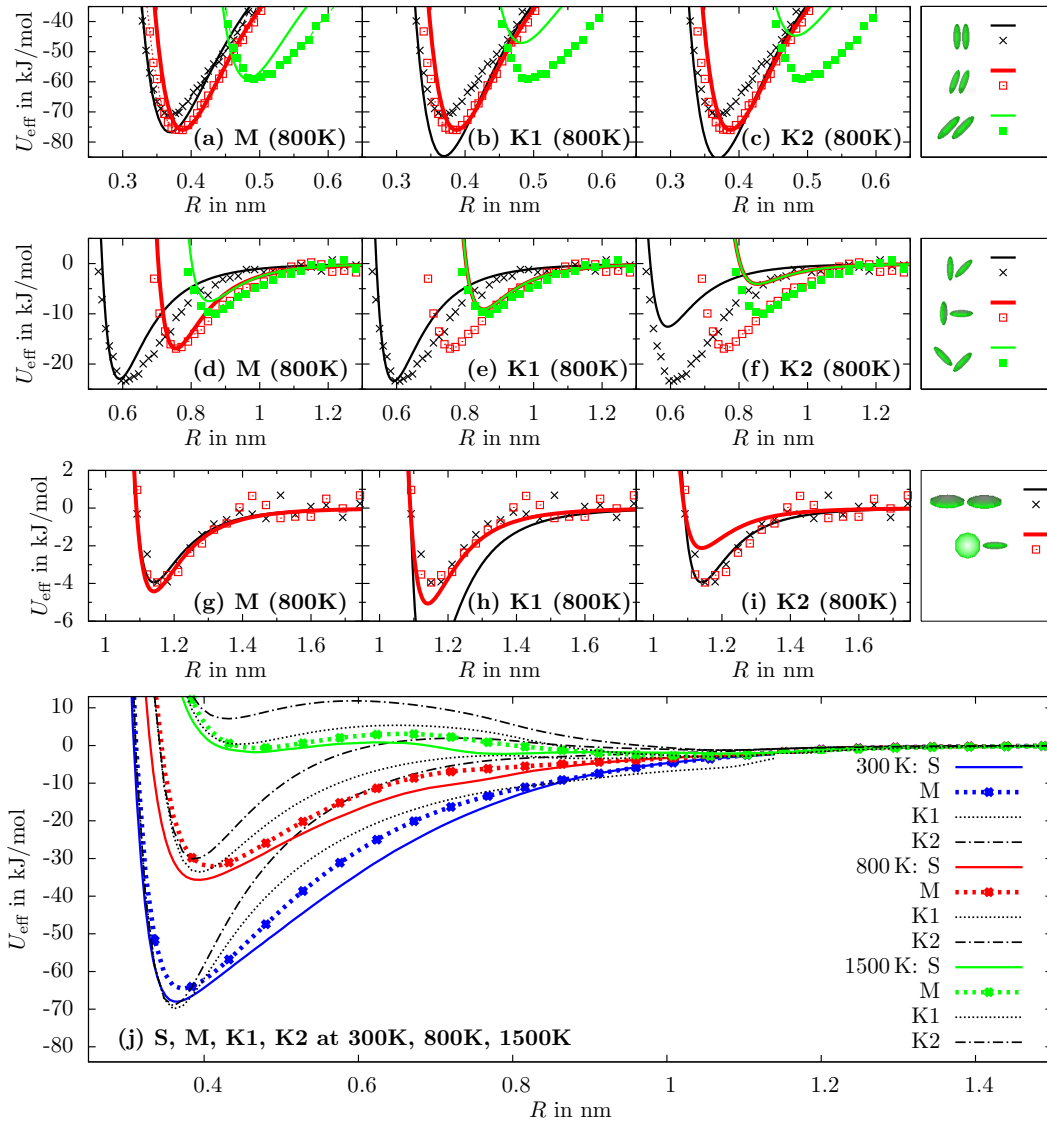


FIGURE 5.5: (a) - (i) Effective potentials for selected configurations and corresponding fits at 800 K. In each subfigure the dots represent the corresponding reference curves. Reference curves in the top row [(a), (b), (c)] stem from steered dynamics, while the remaining reference curves stem from US calculations. The left column shows the performance of our proposed model (M). The two right columns represent the fits according to the Kabadi models K1 and K2. Fig. (j) displays angle-averaged effective potentials for all considered models at 300 K, 800 K and 1500 K. Model S (angle-averaged curve from steered dynamics) provides reference curves.

selected configurations such as a PD one [213]). We deliberately do not use any kind of point charge electrostatic implementations in the models since point charge patterns overestimate the charge localization, are long-ranged and do not fulfill our symmetry requirements. However, for static partial charges an angle and temperature dependent coarse-grained pair potential for perylene, a flat but non-discotic molecule, was already developed by Babadi *et al.* [7] using the SD method for specific configurations desired to fit an ellipsoidal soft-potential [55]. They also present a non-temperature dependent

and biaxial model for coronene which implicitly involves static partial charges.

In particular, the base model for our investigations is an additive combination of the model M and a coarse-grained electrostatic potential. The entire temperature dependence stems from the van der Waals part alone. The model thus implies the impact of slight changes in the charge distribution on the inter-atomic forces is small in comparison to the van der Waals forces which dominate at short length scales. If temperature effects on the charge distribution are not important, we can focus on ground state charge distributions with the desired symmetry.

We are now looking for a simple electrostatic contribution. The treatment of electrostatics can be realized through an electric multipole attached to the interaction site in a centered [65, 128, 172] or off-centered [66, 211] arrangement. Moreover, by optimizing the arrangement of different electric multipoles per interaction site [175, 179] one comes to more and more realistic models [4, 67].

An elegant approach for the electrostatics in coronene is presented by Obolensky *et al.* [143]. They propose a uniaxial model for coronene consisting of concentric charged rings. Unfortunately, this model is not temperature dependent, it is based on static partial charges (see Sec. 4.2.2 and Sec. 4.2.3) and the evaluation of the interaction potential is quite involved due to numerical integrations for each pair interaction, inconvenient for many-particle simulations. Nonetheless, we consider this electrostatic contribution, which already has the desired symmetries, namely uniaxiality and head-to-tail symmetry.

We next introduce two different approaches to include the electrostatics in a new model. The first approach (see Sec. 5.4.3) uses the van der Waals model M and considers electrostatic interactions via a linear point quadrupole at the molecular center along the symmetry axis as discussed before. This kind of approach was already applied for coronene [128] where an unusually strong repulsion for planar configurations was observed. We address this issue in more detail later in our work. Nonetheless, this approach was successfully applied to benzene molecules [65] in the liquid phase with an additional dampening field for closed distances. Moreover, by considering only fluid phases, a very simple approach is given by Mognetti *et al.* [130] who use angle-averaged quadrupole-quadrupole interactions to describe quadrupolar molecules (e.g. carbon dioxide or benzene). In the second approach (see Sec. 5.4.4), we include the pure ring electrostatics, suggested by Obolensky *et al.* [143], implicitly in our van der Waals model.

Both of the present approaches allow a better representation of the $\pi - \pi$ stacking [82, 195] which is also observed in similar aromatic molecules, e.g. benzene dimers [195, 196] and hexabenzocoronene crystals [159].

5.4.1 Including electrostatics via a direct sum

To include electrostatics, we assume additivity of the van der Waals and electrostatic contributions to the coronene-coronene interactions. In particular, the full pair potential is given through

$$U(\mathbf{R}_A, \mathbf{R}_B, \hat{\mathbf{u}}_A, \hat{\mathbf{u}}_B) = U_{\text{vdW}}(\mathbf{R}_A, \mathbf{R}_B, \hat{\mathbf{u}}_A, \hat{\mathbf{u}}_B) + U_{\text{elec.}}(\mathbf{R}_A, \mathbf{R}_B, \hat{\mathbf{u}}_A, \hat{\mathbf{u}}_B), \quad (5.11)$$

where U_{vdW} and $U_{\text{elec.}}$ are the van der Waals and electrostatic parts, respectively.

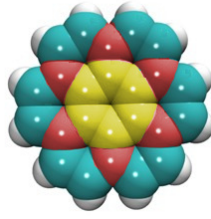


FIGURE 5.6: Sketch of a coronene molecule. The outer twelve small spheres represent hydrogen atoms while the remaining spheres represent carbon atoms. Identical color means equal distance from the center and equal charge contribution.

As seen from Fig. 5.6, there are four different distances from the molecular center of coronene where the atoms are placed in a sixfold symmetry. All atoms with the same distance are considered to carry the same partial charge.

5.4.2 Multipole expansion

We next focus on the spherical multipole expansion of the electrostatic potential, that is [68]

$$\Phi(r, \phi, \theta) = \frac{1}{4\pi\epsilon_{\text{pm}}} \sum_{\ell=0}^{\infty} \sum_{m=-\ell}^{\ell} \frac{\left(\frac{4\pi}{2\ell+1}\right) Q_{\ell,m}}{r^{\ell+1}} Y_{\ell m}^*(\theta, \phi), \quad (5.12)$$

where the spherical harmonics defined through

$$Y_{\ell m}(\theta, \phi) = (-1)^m \sqrt{\frac{(2\ell+1)(\ell-m)!}{4\pi(\ell+m)!}} P_{\ell}^m(\cos\theta) e^{im\phi}$$

depend on the polar angle θ and the azimuthal angle ϕ . The P_{ℓ}^m represent the associated Legendre polynomials. The dielectric constant is denoted by ϵ_{pm} , and the multipole moments are defined through

$$Q_{\ell,m} = \sum_i q_i \|\mathbf{r}_i\|^{\ell} Y_{\ell m}(\theta_i, \phi_i). \quad (5.13)$$

Several symmetries in the charge distribution effectively lead to a reduction of the number of $Q_{\ell,m}$. In particular, the net charge and the dipole moment of the proposed charge distribution are zero, i.e. $Q_{0,0} = 0$ and $Q_{1,m} = 0$. The head-tail-symmetry ($\theta_i = \pi/2 \rightarrow \pi - \theta_i$) reduces l -values to even numbers. Summing up, our multipole decomposition of the electrostatic potential consists of a quadrupole moment ($l = 2$) and higher multipoles with $l \in (4, 6, 8, \dots)$.

For molecules with continuous axial symmetry, we only have to consider multipole moments with $m = 0$. However, the underlying atomistic model of coronene (see Fig. 5.6) does not have full (continuous) axial symmetry. Nonetheless, the sixfold symmetry suggests that the linear quadrupole moment ($Q_{2,0}$) is the only non-zero quadrupole moment. That means the next non-vanishing multipole contribution after

the linear quadrupole is the linear hexadecapole ($Q_{4,0}$). We next consider the quotient of the coefficients in the multipole expansion corresponding to $Q_{2,0}$ and $Q_{4,0}$ [see Eq. (5.12)] to evaluate the possibility of neglecting higher multipole terms ($\ell = 4$ and beyond). Specifically, we consider

$$\mathcal{Q} = \frac{Q_{\ell,m}/(2\ell+1)/r^{\ell+1}}{Q_{\bar{\ell},\bar{m}}/(2\bar{\ell}+1)/r^{\bar{\ell}+1}} \Big|_{\ell=2,m=0,\bar{\ell}=4,\bar{m}=0}. \quad (5.14)$$

At large distances, such as $r \geq 2.4$ nm, the absolute value of \mathcal{Q} is over 30, i.e. the linear quadrupole approach is reasonable. However, for distances smaller than $r = 0.44$ nm (a typical distance in the crystalline phase) the quotient \mathcal{Q} produces values below unity. Thus, the quadrupole approximation is not valid at small distances. To somewhat compensate this effect we consider also a small quadrupole interaction strength to avoid an overestimation of the bonding.

5.4.3 Point quadrupole approach

In this approach the electrostatics are represented by a quadrupole tensor. This approach is aimed at maintaining the electrostatics in the far field. The quadrupole tensor is given by [68] (a different definition is used in Sec. 3.7.2.2)

$$\underline{\mathbf{Q}} = \frac{1}{2} \sum_i q_i [3\mathbf{r}_i \otimes \mathbf{r}_i - (\mathbf{r}_i)^2 \mathbf{1}], \quad (5.15)$$

where q_i is the charge of atom i placed at \mathbf{r}_i from the geometric center. In the eigenbasis $\underline{\mathbf{P}}$, the quadrupole tensor of a uniaxial charge distribution has the following symmetry

$$\underline{\mathbf{PQP}}^{-1} = Q \begin{bmatrix} -1/2 & 0 & 0 \\ 0 & -1/2 & 0 \\ 0 & 0 & 1 \end{bmatrix}. \quad (5.16)$$

Thus, the quadrupole tensor can be written in terms of a linear quadrupole pointing along the molecular symmetry axis. The prefactor in Eq. (5.16), $Q = \sqrt{4\pi/5} Q_{2,0}$, marks the quadrupole strength of the linear quadrupole [68].

At this point, we can define the ‘‘point quadrupole model’’ (pq model) through the following additive formula

$$U_{\text{pq}}(\mathbf{R}, \hat{\mathbf{u}}_A, \hat{\mathbf{u}}_B) = U_{\text{mGB}}^{\text{vdW}}(\mathbf{R}, \hat{\mathbf{u}}_A, \hat{\mathbf{u}}_B) + \frac{1}{4\pi\epsilon_{\text{pm}}} \frac{3Q^2}{4R^5} \cdot K(\hat{\mathbf{R}}, \hat{\mathbf{u}}_A, \hat{\mathbf{u}}_B), \quad (5.17)$$

where the second term on the right side describes the energy of one linear quadrupole in the field of another linear quadrupole of equal strength Q , and the function K is defined in Eq. (5.10).

For simplicity, we henceforth use the dimensionless quadrupole moment

$$Q^* = \left\| \frac{Q}{\sqrt{4\pi\epsilon_{\text{pm}}} \text{kJ/mol nm}^5} \right\|. \quad (5.18)$$

The absolute value is used because the sign does not influence the pair potential defined in Eq. (5.17). The values of Q^* obtained through different approaches for the density functional theory (DFT) [see also Sec. 4.2.2], performed in Ref. 143, range from 0.617 to 0.83 (see Tab. 5.2). A well-known problem with a point multipole

DFT-approach	C1	C2	C3	H	Q^*
B3LYP/6-312G(d)	-0.002	0.129	-0.207	0.148	0.787123
B3LYP/D95	0.002	0.13	-0.237	0.168	0.830024
B3LYP/cc-pVDZ	-0.004	0.095	-0.171	0.129	0.719569
PBE/6-312G(d)	-0.003	0.121	-0.223	0.148	0.61675
PBE/D95	-0.003	0.133	-0.236	0.16	0.71978
PBE/cc-pVDZ	-0.0002	0.086	-0.18	0.13	0.629325
PBE/cc-pVTZ	0.002	0.114	-0.205	0.149	0.780019
simple approach	0	0	-0.15	0.15	0.963395

TABLE 5.2: Charge distribution from Ref. 143 in a coronene molecule according to different approaches for the density functional theory (DFT). The “simple approach” refers to the approximated two-ring model, as pointed out in Ref. 143. Carbon atoms on the inner ring are denoted with C1, those on the second and third with C2 and C3 while the outer ring is formed by hydrogen atoms (H) (see Fig. 5.6). Corresponding center-to-atom distances are 1.438, 2.876, 3.595, and 4.691Å respectively. The reduced quadrupole strength is denoted with Q^* .

representation [65, 186, 187] of the electrostatic interaction of extended molecules is its failure for close distances, due to the spatially extended charge distribution and induced dipoles. In particular, attractive configurations become infinitely strong for vanishing quadrupole-quadrupole distances. Indeed, we will later see in Sec. 5.4.5 and 5.4.6 that the latter effect leads to an overestimation of the binding energy for PD-configurations.

We here consider quadrupole strengths that are in the range of the previously termed reference values. Specifically, we use: $Q^* = 0, 0.5, 1, 1.5$. It is thus possible to gradually study the influence of the point quadrupole on the cohesion energy.

5.4.4 Charged-ring approach

The idea of this approach is to better take into account interactions at small distances. Equal atomic partial charges in the atomistic model of Obolensky et al. [143], have the same distance to the geometrical center (see Fig. 5.6) and are equally distributed along a ring. This makes it plausible to describe each ring as uniformly charged, thus fulfilling the symmetry requirements of our coarse-grained potential (uniaxiality and head-to-tail symmetry). We also note that considering a smeared charge distribution due to the rings is not necessarily less accurate compared to an atomistic point charge distribution. Indeed, it seems plausible that mapping the quantum mechanical charge density onto atomic point charges could lead to charges being localized more than is realistic.

For simplicity, we here consider (as proposed in Ref. 143) only the two outer rings for the electrostatics. Hereby the hydrogen ring is charged with $q_1 = 12 \cdot 0.15e$ and the

next inner ring is oppositely charged, i.e. $\mathbf{q}_2 = -\mathbf{q}_1$. The sum of all ring-ring interactions is thus given by

$$U_{\text{ring-ring}}(\mathbf{R}, \hat{\mathbf{u}}_A, \hat{\mathbf{u}}_B) = \sum_i^{\text{rings of A}} \sum_j^{\text{rings of B}} U_{\text{ring } i\text{-ring } j}(\mathbf{R}, \hat{\mathbf{u}}_A, \hat{\mathbf{u}}_B). \quad (5.19)$$

Hereby a single ring-ring interaction is given by a line integral [143],

$$U_{\text{ring } i\text{-ring } j}(\mathbf{R}, \hat{\mathbf{u}}_A, \hat{\mathbf{u}}_B) = \frac{\mathbf{q}_j}{2\pi R_j} \oint_{\text{ring } j} d\mathbf{r} \Phi(R_i, \sin(\theta), r), \quad (5.20)$$

where the vector $\mathbf{r} = R\hat{\mathbf{R}} + \underline{\mathcal{R}}(\hat{\mathbf{u}}_B) \begin{bmatrix} R_j \cos \phi \\ R_j \sin \phi \\ 0 \end{bmatrix}$ points from the center of ring i to a point on ring j . The symbol $\underline{\mathcal{R}}$ indicates a rotation matrix that rotates the x-y-plane orthogonal to $\hat{\mathbf{u}}_B$, while R_j and ϕ denote the polar coordinates of ring j . The electrostatic potential exerted by ring i with radius R_i on a position, described by the relative spherical coordinates θ and r , is defined through

$$\Phi(R_i, \sin(\theta), r) = \frac{1}{4\pi\epsilon_{\text{pm}}} \frac{\mathbf{q}_i}{2\pi} \cdot \left(\frac{2\mathcal{K} \left[\frac{4rR_i \sin(\theta)}{r^2 + 2R_i \sin(\theta)r + R_i^2} \right]}{\sqrt{r^2 + 2rR_i \sin(\theta) + R_i^2}} + \frac{2\mathcal{K} \left[-\frac{4rR_i \sin(\theta)}{r^2 - 2R_i \sin(\theta)r + R_i^2} \right]}{\sqrt{r^2 - 2rR_i \sin(\theta) + R_i^2}} \right), \quad (5.21)$$

where $\sin(\theta) = \|\mathbf{r}/r \times \hat{\mathbf{u}}_A\|$ and \mathcal{K} stands for the elliptic integral K.

Direct combination of the van der Waals model M, described in Sec. 5.3.3, and the ring-ring potential [Eq. (5.19)] yields

$$U_{\text{direct}}(\mathbf{R}, \hat{\mathbf{u}}_A, \hat{\mathbf{u}}_B) = U_{\text{mGB}}^{\text{vdW}}(\mathbf{R}, \hat{\mathbf{u}}_A, \hat{\mathbf{u}}_B) + U_{\text{ring-ring}}(\mathbf{R}, \hat{\mathbf{u}}_A, \hat{\mathbf{u}}_B). \quad (5.22)$$

Henceforth, we term the latter potential as “direct” potential. We note that U_{direct} is temperature-dependent as a consequence of the temperature-dependent parametrizations used for the van der Waals model M. From a computational perspective, however, this kind of potential is not very suitable, particularly for many-particle simulations. This is due to the fact that one has to calculate ring integrals numerically for each pair of particles. Therefore, we here propose a way to effectively include the ring-ring interactions from above by simply reparametrizing the GB model used for the van der Waals interaction (see Sec. 5.3.3) with new parameters chosen to match the “direct” potential [see Eq. (5.22)] for different angular arrangements. This computationally more simple approach is aimed at correctly describing the direct potential in the near field. We name it the “implicit electrostatics model”. Specifically, we have

$$U_{\text{implicit}}(\mathbf{R}, \hat{\mathbf{u}}_A, \hat{\mathbf{u}}_B) = U_{\text{mGB}}(\mathbf{R}, \hat{\mathbf{u}}_A, \hat{\mathbf{u}}_B) \Bigg|_{\substack{\text{implic. electr.} \\ \text{parametrization}}}. \quad (5.23)$$

The consequences for the long-range behavior are discussed later in this section. In our implicit electrostatics parametrization, we fix the following parameters to the corresponding van der Waals values for all temperatures: $\mu = 1$, $\nu = 1$, $\gamma = 4$ and $\gamma' = 4$. The

remaining parameters are extracted from the direct potential [Eq. (5.22)] using the same angular configurations as those used in Sec. 5.3.3 describing the van der Waals interaction (model M). An overview of different pair configurations, including those needed to fit the implicit electrostatics potential [Eq. (5.23)] with the direct potential [Eq. (5.22)], is presented in Tab. 5.1. The anisotropy parameter χ is calculated by measuring the FF contact distance σ_{FF} and the edge-edge contact distance σ_0 . The well width d_w is calculated in analogy to Eq. (5.8).

The remaining parameters ϵ_0 , χ' , θ and ξ are determined by fitting the results for $U_{\text{direct}}(\mathbf{R}, \hat{\mathbf{u}}_A, \hat{\mathbf{u}}_B)$ according to Eq. (5.6) (as pointed out in Sec. 5.3.3). Finally, the specific parameters for all considered temperatures are given in Appendix A.3 (“implicit electrostatics parametrization”).

An important aspect in this investigation is the long-range behavior of the pure ring-ring interactions. The implicit electrostatics model [see Eq. (5.23)], which seems most promising so far, decays with the center-of-mass distance R as R^{-6} . This means that (contrary to the point quadrupole model) the implicit electrostatics model cannot reproduce the long-range behavior expected by the electrostatic interactions, which is R^{-5} (because the quadrupole is the smallest non-vanishing multipole; see Sec. 5.4.2). We note that the ring-ring potential [see Eq. (5.19)], which is the underlying electrostatics for the implicit electrostatics model, reveals a correct R^{-5} decay. How does this ring-ring potential decay at short and intermediate distances, which are particularly relevant in the present context? To this end we consider the function

$$S(R) = \frac{\partial \log(U_{\text{ring-ring}}(\mathbf{R}, \hat{\mathbf{u}}_A, \hat{\mathbf{u}}_B))}{\partial \log(R)}. \quad (5.24)$$

This function is depicted in Fig. 5.7 for various configurations (see Table 5.1). It turns

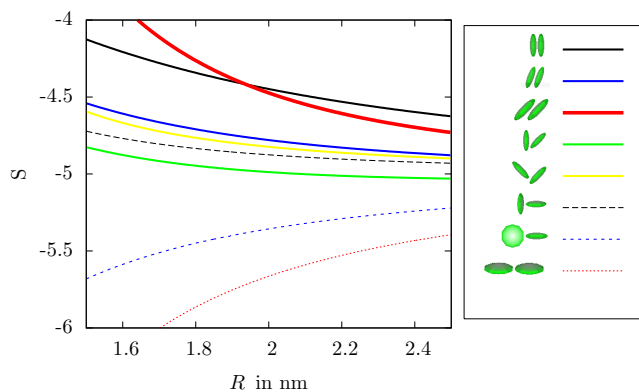


FIGURE 5.7: Power-law exponent of the ring-ring potential for several molecular configurations as function of R .

out that $S(R)$ does not approach the far-field limit of -5 in the range of interest, that is, $R < 2.4$ nm. Therefore, it is sufficient to model the electrostatics in our range of interest implicitly with a van der Waals model revealing a slightly different long-range behavior. A similar strategy has been used to treat the electrostatics and the van der Waals interactions in DNA [131].

5.4.5 Ground state curves

In order to compare our results with ground state (GS) results in the literature, we consider an additional model, which combines the van der Waals potential pertaining to the atomistic level $U_{\text{vdW}}^{\text{GS}}$ (using generalized AMBER force field [208] without partial charges) at $T = 0$ K and our ring-ring potential from Eq. (5.19). Specifically, we use the direct sum

$$U_{\text{direct}}^{\text{GS}} = U_{\text{vdW}}^{\text{GS}} + U_{\text{ring-ring}}. \quad (5.25)$$

In analogy to Eq. (5.22), this potential is termed the “ground state direct model”. In Fig. 5.8 we present the ground state potential curves $U_{\text{vdW}}^{\text{GS}}$ (without electrostatics) and $U_{\text{direct}}^{\text{GS}}$ [with ring-ring electrostatics from Eq. (5.19)] using various configurations suitable for comparison with literature results [157, 213]. In addition, we add the potential curves showing the ground state analog of the point quadrupole model, that is

$$U_{\text{pq}}^{\text{GS}} = U_{\text{vdW}}^{\text{GS}}(\mathbf{R}, \hat{\mathbf{u}}_A, \hat{\mathbf{u}}_B) + \frac{1}{4\pi\epsilon_{\text{pm}}} \frac{3Q^2}{4R^5} \cdot K(\hat{\mathbf{R}}, \hat{\mathbf{u}}_A, \hat{\mathbf{u}}_B). \quad (5.26)$$

We recognize that $U_{\text{direct}}^{\text{GS}}$ is characterized by similar values of the binding energy for the FF-configuration in Fig. 5.8(a) (−58.31 kJ/mol with tooth-to-tooth setup) and the PD-configuration in Fig. 5.8(b) (−61.37 kJ/mol), consistent to what was observed in the work of Rapacioli *et al.* [157]. More specifically, they have performed ground state calculations of coronene and found similar values for the binding energy in the FF-configuration (−94.9 kJ/mol for tooth-to-tooth alignment and −92.35 kJ/mol for a 30° twisted setup) and the PD-configuration (−93.66 kJ/mol). However, our calculated magnitudes of $U_{\text{direct}}^{\text{GS}}$ are only about two thirds of that obtained in Ref. 157. Similar numerical values are also found by Zhao *et al.* [213] except for the perfectly stacked FF-configuration (“tooth-to-tooth” setup), which is only half the magnitude of the twisted stacking configuration in their calculations. These differences stem from different charge distributions used by us and in Ref. 157, and from the fact that our atomistic parameters are taken from the generalized AMBER force field [208] while in Ref. 157 van de Waal parameters have been used.

Concerning the ground state point quadrupole model, we notice a strong repulsion for the FF-configuration as depicted in Fig. 5.9 (a), even at the smallest considered non-vanishing quadrupole strength of $Q^* = 0.5$. This behavior was already observed in Ref. 128. In order to reach the potential depth of the direct model in this configuration, the quadrupole strength should be very close to zero, which implies a weak far-field behavior. Moreover, even the smallest quadrupole strength further increases the potential depth of the PD-configuration [see Fig. 5.8 (b)] away from its reference value. Considering at $Q^* = 0.5$ only a fraction of the quadrupole strength (reference values [143] between $Q^* = 0.617$ to 0.83 for various charge distributions; $Q^* = 0.963$ for the proposed two-ring model), leads to a potential depth twice as large for the PD-configuration compared to the FF-configuration of the direct model. This is not consistent with other ground state results [157, 213]. Even though, we want to investigate in Sec. 6.3.2, whether this crude model is able to predict the correct melting

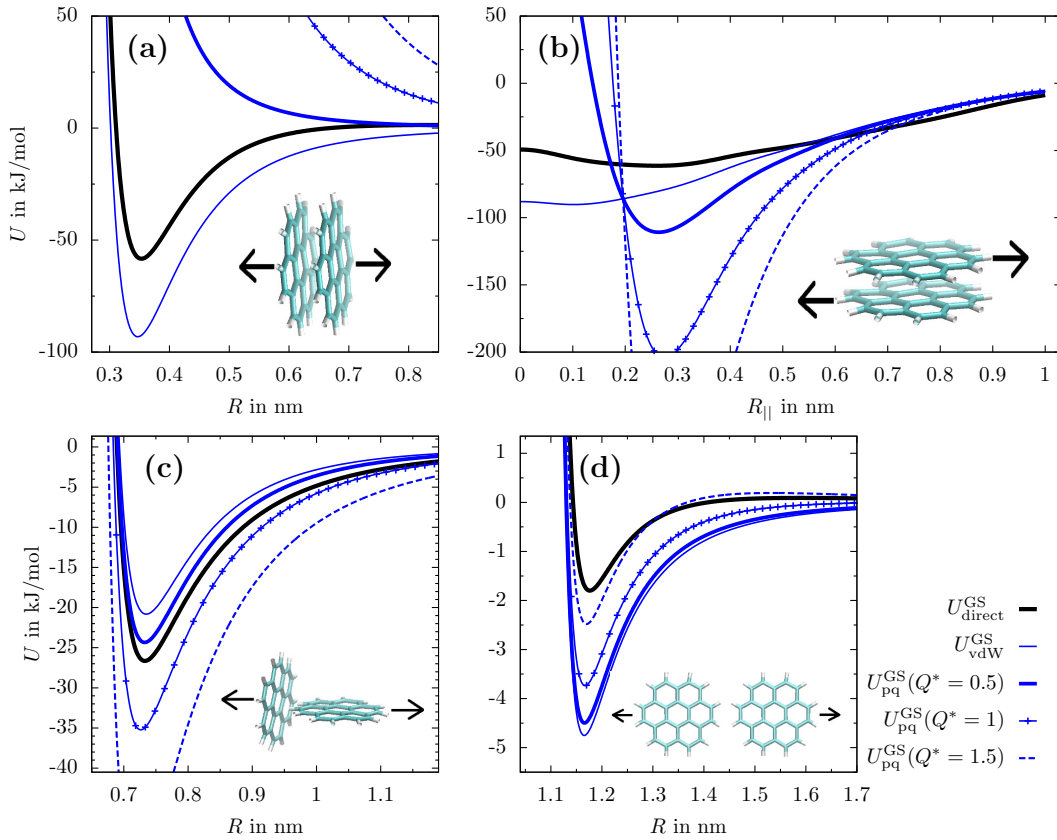


FIGURE 5.8: Potential curves of the ground state models $U_{\text{direct}}^{\text{GS}}$ and $U_{\text{vdW}}^{\text{GS}}$, the direct model U_{direct} , the implicit electrostatics model $U_{\text{implic.}}$ and the point quadrupole model $U_{\text{pq}}^{\text{GS}}$ (reduced strengths: 0, 0.5, 1) at $T = 300$ K. (a) FF-configuration (with tooth-to-tooth setup); (b) PD-configurations for a layer distance of 0.332 nm; (c) T-configuration; (d) edge-edge configuration.

behavior of the coronene crystal.

For the sake of completeness, we also present curves for the T- and edge-edge configuration in Fig. 5.8(c) and 5.8(d), which are both in part responsible for the binding between columnar arrangements in a crystal. The general impact of the electrostatics is reflected by the difference between $U_{\text{direct}}^{\text{GS}}$ and $U_{\text{vdW}}^{\text{GS}}$ and is quite pronounced in all configurations. As mentioned in Sec. 5.4.3 the point quadrupole curves strongly affect the binding energies for all configurations.

5.4.6 Temperature dependent curves

The potential curves resulting from Eq. (5.17) (point quadrupole model), Eq. (5.22) (direct model) and Eq. (5.23) (implicit electrostatics model) are now investigated for different molecular configurations at a temperature of $T = 300$ K and for the FF-configuration at a broad range of temperatures.

In Fig. 5.9(a-c), these potential curves are presented for three molecular pair configurations, namely the FF-, PD- and edge-edge configuration. Our present analysis shows that the direct model is characterized by a similar binding energy for the FF-configuration (-50.02 kJ/mol) in comparison with the PD-configuration (-52.778 kJ/mol).

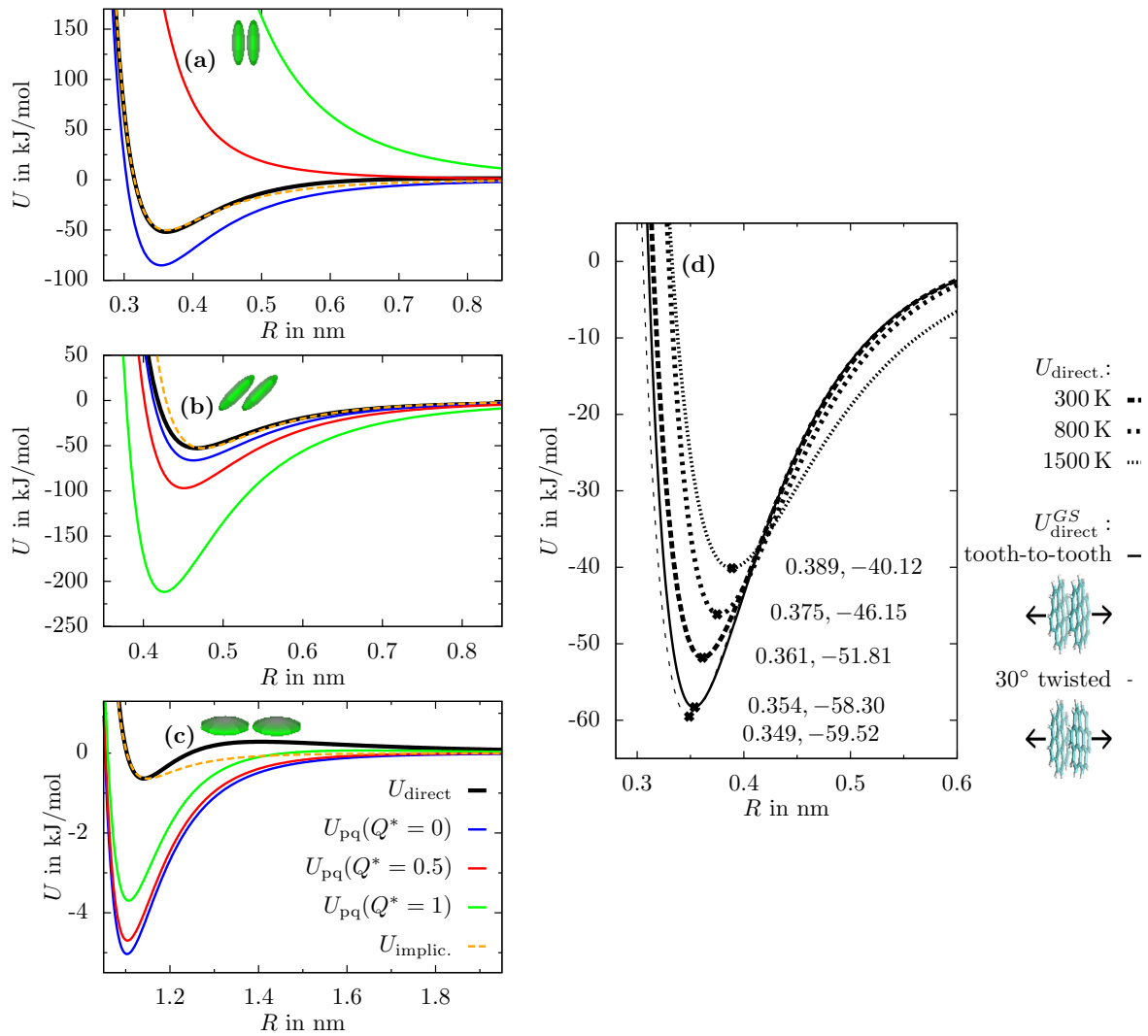


FIGURE 5.9: (a-c) Potential curves along the inter-molecular distance of the direct model, point quadrupole model (with reduced strengths: 0, 0.5, 1) and the implicit electrostatics model at 300 K for fixed configurations. The point quadrupole model with $Q^* = 0$ coincides per definition with our most precise van der Waals model (model M). (d) Potential curves for the face-face configuration using the direct model at 300 K, 800 K and 1500 K. In addition two ground state configurations are added.

As expected, these values are lower in magnitude than their ground state counterparts (see Sec. 5.4.5) but reveal the same characteristics. Regardless, when comparing potential curves for the implicit electrostatics model and the direct model at 300 K, we find a good agreement. This is because the implicit electrostatics model is designed to fit the direct model in close contact configurations. In Fig. 5.9 (c), the potential curves of the edge-edge configuration reveals a strong influence of the electrostatics at all distances. This becomes clear when comparing U_{direct} with the pair potential of the van der Waals model $U_{\text{mGB}}^{\text{vdW}} = U_{\text{pq}}(Q^* = 0)$.

Furthermore, the temperature dependence of the FF-configuration is shown in Fig. 5.9(d) for the direct model and the ground state direct model [see Eq. (5.25)] for two different configurations (tooth-to-tooth and 30°-twisted). We can observe that

the higher the temperature, the flatter the potential minimum and the larger the binding distance. The temperature dependence mainly stems from molecular bending modes as discussed in Sec. 5.2.3. Its dependence due to axial averaging is rather small, reflected by the small difference of both ground state potentials. It is also worthwhile to mention that there is no influence of temperature at around $R = 0.42$ nm, because at this point all potential curves intersect.

Chapter 6

Molecular bulk system of coronene molecules

6.1 Preface

The many-particle behavior for the models of the effective pair potentials from the previous chapter is now investigated. More specifically, we investigate structural equilibrium properties for the van der Waals models of coronene (M, K1, K2, S, and the atomic (A) reference model) at different densities in the limit of high temperatures (1500 K) in Sec. 6.2 and compare structural quantities of bulk crystals for the van der Waals models (M, K1, K2, A) at a broad range of temperatures (300–1500 K). We further perform a structure analysis of the bulk crystal formed by the full-electrostatic models (implic. elec. model, pq-model) in Sec. 6.3. The coarse-grained simulations are performed with molecular dynamics (MD) in the NVT or NPT ensemble (ensembles defined in Sec. 2.2). We have performed coarse-grained simulations with temperature (T) and pressure (P) control (if present) realized via a Berendsen thermostat (barostat) [17]. The translational and rotational equations of motion are solved according to Sec. 3.3.3 (the T-coupling in the atomistically detailed simulations of the columnar hexagonal nematic regime were performed using the method described in Sec. 3.4).

For all temperatures considered (300 K–1500 K), we have used the corresponding parametrized potentials introduced in Sec. 5.3 and 5.4 (the temperature-dependent parameters are presented in Tables A.1–A.4 in Appendix A.3). The moment of inertia entering the rotational equations of motion is set to $I = 14.76 \text{ u nm}^2$ corresponding to a coronene molecule in the ground state as depicted in Fig. 4.3. All simulations are performed using a force-shifted cutoff of 2.4 nm for the coarse-grained interactions. The time constant involved in T- or P-control is set to 2 ps. In case of pressure control we use a compressibility of $2.25 \cdot 10^{-4} \text{ bar}^{-1}$. However, an accurate choice for the value of the compressibility is not necessary since the quotient of the compressibility and the time constant of the pressure form the input parameter to the Berendsen pressure coupling. In all simulations, we used the speed-up techniques from Sec. 3.8 and a time step of 10 fs. All findings in this chapter build on our published articles corresponding to reference Nos. 78 and 79.

6.2 Van der Waals coronene

In the following sub-sections we discuss representative thermodynamic states pertaining to the isotropic and orientationally ordered regime for our effective van-der-Waals models, which we introduced in previous chapter.

6.2.1 Isotropic regime

The isotropic regime was explored by using an NVT ensemble (see Sec. 2.2.1) characterized by $N = 576$ particles, $T = 1500$ K, and $V_1 = (15 \text{ nm})^3$ or $V_2 = (8.3 \text{ nm})^3$. We assign a packing fraction to these systems by considering ellipsoidal particles whose axes are defined through the contact distances of U_{eff} for $T = 1500$ K. The corresponding packing fractions are $\eta_{(1)} \approx 0.04$ and $\eta_{(2)} \approx 0.21$, respectively.

Structural properties are extracted after an equilibration time of 2 ns. Structural investigations involving positional and orientational order are performed using the pair correlation functions $g^{000}(R)$, $g^{220}(R)$ and $g^{202}(R)$ as introduced in Sec. 2.7.1. Corresponding numerical results are shown in Fig. 6.1 while snapshots of the simulation system for the atomistic (A) model, model M and model S are shown in Fig. 6.2. Considering first the lower density [see Figs. 6.1(a)- 6.1(c)], we see that the angle-

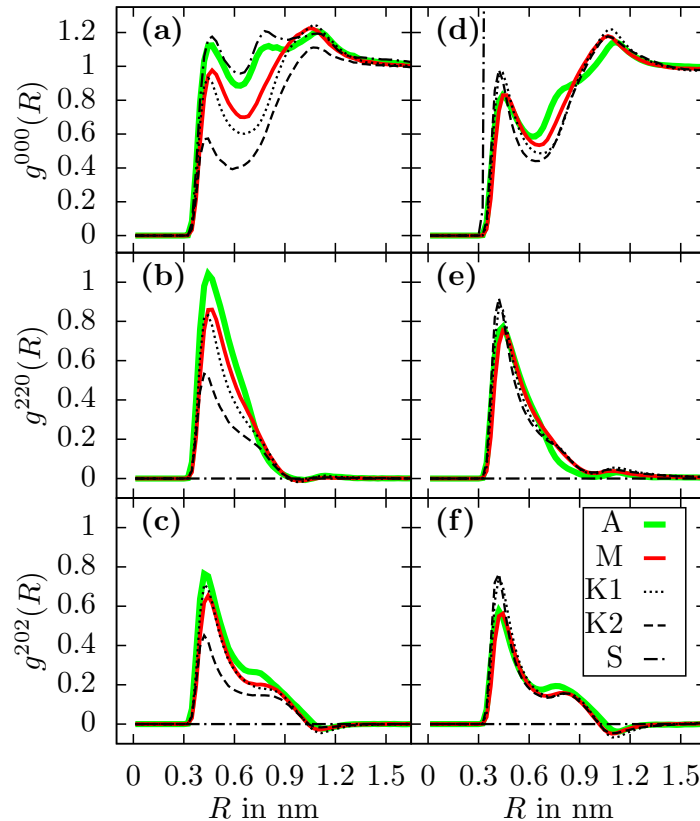


FIGURE 6.1: Coefficients of the pair correlation function at a low density [parts (a)-(c)] and a higher density [parts (d)-(f)] at $T = 1500$ K. Results are obtained using the models M, K1, K2, and the spherical model S. Included are data from atomic simulations (A).

averaged correlation of the atomic system is best reproduced by the data from the spherical model (S). Models M, K1, K2 underestimate the first peak in $g^{000}(R)$, with the largest error appearing from model K2. Regarding the non-spherical coefficients (for which the spherical model obviously cannot make predictions), we find that model M works best, while the largest deviation occurs again from model K2. This reflects the fact that also the angle dependence of the K2 potential is less pronounced than in M and K1 (see Fig. 5.5).

At the higher density, all the three models M, K1, K2 yield good results (as compared to the atomistic data) for the correlation functions considered [see Figs. 6.1(d)-6.1(f)]. The best accuracy is again provided by model M. A further interesting observation is that model S predicts a totally unphysical result for $g^{000}(R)$, which does not approach unity at large distances. This already indicates that systems characterized by this spherical potential are not in a stable equilibrium state. Rather the particles condense into a single large cluster, indicating a phase separation [see Fig. 6.2(f)]. Fur-

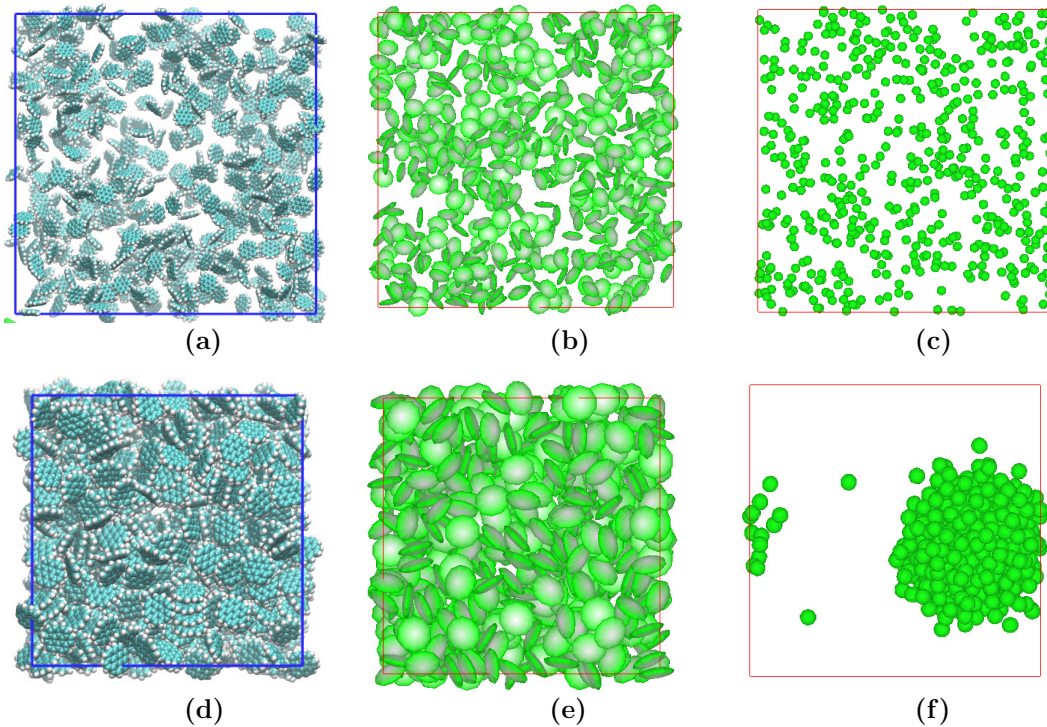


FIGURE 6.2: The atomistic system (a, d), the angle-resolved coarse-grained system (b, e) and the angle-averaged coarse-grained system (model M) (c, f) are shown at a packing fraction of $\eta_{(1)} \approx 0.04$ (top panels) as well as $\eta_{(2)} \approx 0.21$ (bottom panels).

thermore, we also investigate in Fig. 6.3 the structure via the pair correlation function

$$\mathcal{G}(\mathbf{R}, \hat{\mathbf{u}}_1, \hat{\mathbf{u}}_2) = g^{000}(R) \psi^{000} + g^{202}(R) \psi^{202}(\mathbf{R}, \hat{\mathbf{u}}_1, \hat{\mathbf{u}}_2) \quad (6.1)$$

involving g^{000} and g^{202} at both considered packing fractions. Investigating this quantity, we do not observe a significant difference between the models M and K1. However, model K2 slightly underestimates the structurization around a given particle when compared to the atomistic counterpart of \mathcal{G} . Returning to the condensation of model S, we also observe large values for the function \mathcal{G} in the high density system (i.e.

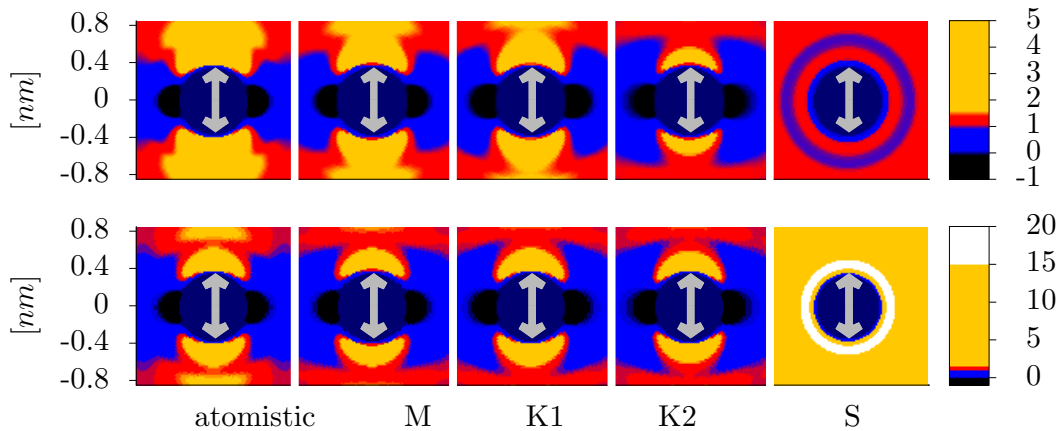


FIGURE 6.3: Pair correlation function \mathcal{G} , as defined in Eq. (6.1), is shown for the van der Waals models (M, K1, K2, S) of coronene at a packing fraction of $\eta_{(1)} \approx 0.04$ (top panels) and $\eta_{(2)} \approx 0.21$ (bottom panels). The reference particle is positioned in the center of each panel and oriented vertically.

$\eta = \eta_{(2)}$) and do not observe a decay towards unity (i.e. bulk density) in the range of interest.

This phenomenon, which is absent in the atomistic system, clearly indicates that modeling the system with an angle-averaged potential is not appropriate, at least not at intermediate and high densities. We take this failure as an a-posteriori justification for our effort to obtain angle-dependent potentials.

As a further test of our potentials, we have calculated the virial pressure [3] and the second virial coefficient, B_2 (see Sec. 2.3). The results are summarized in Table 6.1. At the lower density $\eta_{(1)}$, the pressure values predicted by the various models are fairly similar, and the second virial coefficient is rather small. This indicates that the pressure is dominated by its ideal-gas value. We also see that (at $\eta_{(1)}$) model S is closest to the atomistic value, consistent with the corresponding observation for $g^{000}(R)$ (see Fig. 6.1). At the larger density $\eta_{(2)}$ the differences in the pressure data are larger, as expected. The closest match of the atomistic value is given by model M [again consistent with our previous discussion of $g^{000}(R)$]. We also see that the pressure predicted by the spherical model is too small by two orders of magnitude. This is another manifestation of the above-mentioned failure of this model to predict a stable liquid phase. We note, however, that the corresponding value of B_2 matches per definition that of the atomic system, due to the fact that B_2 is solely a function of the two-particle (two-molecule) partition function, Z and the volume V according to [see Eq. (2.32) with $\alpha^6 = (C^D/S^{D-1})^2$]

$$B_2 = \frac{V}{2} - \frac{Z \alpha^6}{V}, \quad (6.2)$$

which are both fixed during coarse-graining (see Sec. 4.5).

TABLE 6.1: Atomic and coarse-grained simulation results for the pressure P and the pressure correction due to the second virial coefficient B_2 are shown for the two different system densities $\rho_{(1)} = 576/(15 \text{ nm})^3$ and $\rho_{(2)} = 576/(8.3 \text{ nm})^3$, respectively, at $T = 1500 \text{ K}$. The second virial coefficient of the atomic system matches per definition that of model S (see main text).

Model	$P_{(1)}$ [bar]	$B_2 \rho_{(1)}^2 / \beta$ [bar]	$P_{(2)}$ [bar]	$B_2 \rho_{(2)}^2 / \beta$ [bar]
atomic (A)	31.17	see S	200.21	see S
M	33.36	-0.74	246.29	-25.91
K1	34.01	0.07	260.03	2.40
K2	38.75	4.99	426.72	173.76
S	30.70	-0.84	1.71	-29.38
ideal gas	35.35	0	208.63	0

6.2.2 Columnar hexagonal nematic regime

At lower temperatures and sufficiently high densities the present van der Waals coronene system displays orientationally ordered phases at both the atomic and the coarse-grained level. One of these phases is a columnar phase characterized by a nematic ordering of the molecular symmetry axes and a hexagonal arrangement of the columns in the plane perpendicular to the column axes. The same type of phase also occurs in conventional GB systems consisting of discotic particles [48]. Moreover, columnar nematic phases have also been observed in systems of hexabenzocoronene derivatives [5]. In the following we investigate the stability of this high-density phase in both the atomic and the coarse-grained simulations. To this end we performed constant-pressure simulations using the NPT ensemble (see Sec. 2.2.2). In order to initialize the simulations, we first set up a perfect hexagonal columnar configuration, involving only face-face and edge-edge configurations with nearest-neighbor distances of 0.37 and 1.13 nm, and then applied a GROMACS energy minimization routine (steepest descent method [2]) [see Fig. 6.6(a)]. Simulations were then performed for temperatures ranging from 300 K to 1500 K in steps of 100 K, driving the system from the orientationally ordered into an isotropic regime. In all stages of these “melting” simulations, the pressure was fixed at 1 bar (with a compressibility five times larger than that of water), and the box shape (parallelepiped) was allowed to change its geometry (see Ref. 17). The equilibration time varied between 3 ns (ordered regime) and 95 ns (isotropic regime).

To evaluate the overall degree of ordering we calculated the nematic order parameter \bar{P}_2 as defined in Eq. (2.69)

$$\bar{P}_2 = \frac{1}{N} \left\langle \sum_i P_2(\hat{\mathbf{u}}_i \cdot \hat{\mathbf{n}}) \right\rangle, \quad (6.3)$$

where $\hat{\mathbf{n}}$ is a unit vector indicating the direction of the nematic director. The latter was taken to be the surface normal along which the columns are set up. To further investigate the order in the system, we measure the hexagonal bond order parameter (ψ_6), as defined in Eq. (2.70), which is suitable for columnar configurations. To calculate this quantity, we require the number of neighbors, Nb_j , for each particle j . Here,

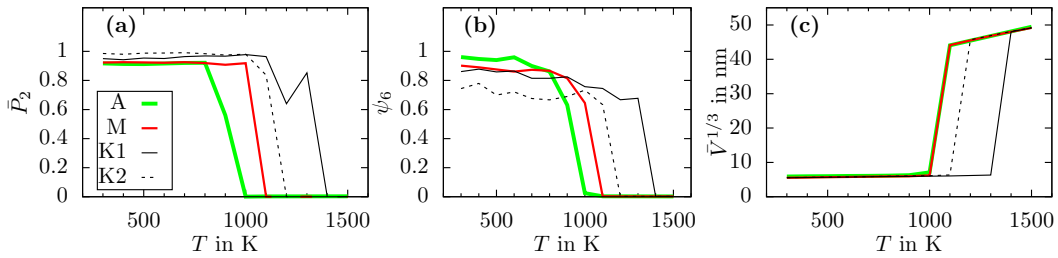


FIGURE 6.4: Order parameters [see Eqs. (2.69) and (2.70)] and characteristic length obtained from the average volume as functions of temperature and different models.

particles are considered neighbors if the projection of the connecting vector $\mathbf{R}_k - \mathbf{R}_j$ onto $\hat{\mathbf{n}}$ is smaller than 0.25 nm, while the projection perpendicular to $\hat{\mathbf{n}}$ is between 0.9 nm and 1.3 nm. The behavior of these two order parameters, as well as that of the calculated volume as functions of temperature is plotted in Fig. 6.4, where we have included results from the atomic system (A) and from the coarse-grained models M, K1, K2. At 300 K, the atomic system displays nearly perfect nematic and columnar ordering, that is both order parameters are close to unity. Upon increasing T , \bar{P}_2 (of the atomic system) exhibits a sudden decrease at $T \approx 900$ K, indicating the disappearance of nematic ordering. The parameter ψ_6 also decreases, but in a smoother way. This reflects the observation that the columns first somewhat rearrange before the columnar structure finally melts. As a consequence of melting, the volume of the system strongly increases, as indicated by the plot of the cube root of the average volume in Fig. 6.4(c). All of the coarse-grained models M, K1, K2 reproduce qualitatively the phase transition of the atomic system, although the predicted transition temperatures are clearly model-dependent. Taken all these parameters into account, model M provides the best representation of the atomic data. Although the drop of \bar{P}_2 upon heating occurs at somewhat too high temperature, the characteristic length provided by the third root of the volume is reproduced very accurately. Compared to M [and the atomic system (A)], we find that the first Kabadi model (K1) predicts the columnar melting at significantly larger temperatures ($T = 1300$ K – 1400 K). This can be explained by the fact that model K1 overestimates the attraction associated with the edge-edge configuration. Finally, the results of model K2 (which gives a correct edge-edge configuration), are between those of models M and K1.

In addition to the system-averaged order parameters discussed so far, we have also investigated the local structure in the columnar nematic phase. To this end we consider the correlation functions parallel and perpendicular to the nematic director $\hat{\mathbf{n}}$, g_{\parallel} and g_{\perp} . These functions are calculated based on expressions suggested in Ref. 5. However, here we consider normalized versions (where the correlation functions yield unity if no correlation is present) as defined in (2.61a) and (2.61b).

Numerical results for the correlation functions are plotted in Fig. 6.5, where we consider two temperatures within the nematic columnar regime. The atomic results for the function g_{\parallel} at 300 K [see Fig. 6.5(a)] clearly signal the preferred layer separation of 0.33 nm by sharp peaks. However, one also notices a secondary, weaker maximum at intermediate distances. These latter maxima indicate that a few columns are shifted along one another by half the thickness of a molecule. Considering the corresponding

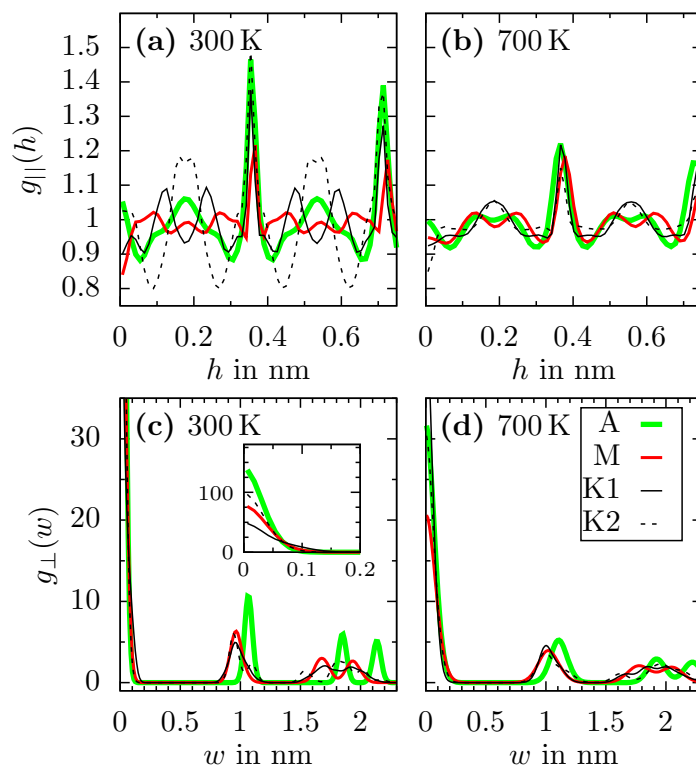


FIGURE 6.5: Pair distribution functions along the director (g_{\parallel}) and perpendicular to it (g_{\perp}) at $T = 300$ K and $T = 700$ K for the atomic (A) and the coarse-grained model systems (M, K1, K2).

coarse-grained results we see that model K2 reproduces not only the main peaks of g_{\parallel} at 300 K, but actually overestimates the intermediate ones. This results from the fact that K2 strongly favors face-face configurations relative to T- and V-like configurations. The other models (M, K1) generate a somewhat less rigid structure. At 700 K all coarse-grained models reproduce the features seen in the atomic data for g_{\parallel} [see Fig. 6.5(b)]. In particular, compared to 300 K, the data at 700 K reveal that the layer-to-layer distance has slightly increased.

Regarding the perpendicular correlations within the columnar phase, we find that model M yields the best reproduction of the hexagonal column arrangement in the atomic system; however, the lateral column separation is somewhat too small (as it is for models K1 and K2). This holds for both temperatures considered. The main temperature effect in both, g_{\parallel} and g_{\perp} , consists of a widening of peaks.

This is also indicated by direct inspection of the simulation snapshots presented in Figs. 6.6(b) and 6.6(c). At 300 K, the dominating structure is a face-face configuration in a tooth-to-tooth setup. On the contrary, at 700 K tooth-to-tooth-like configurations have essentially disappeared. The molecules appear to rotate freely around their symmetry axis.

6.2.3 Performance of the van der Waals models

We next summarize the performance of our van der Waals models. As expected Model M was found to be superior in most aspects, including the description of the

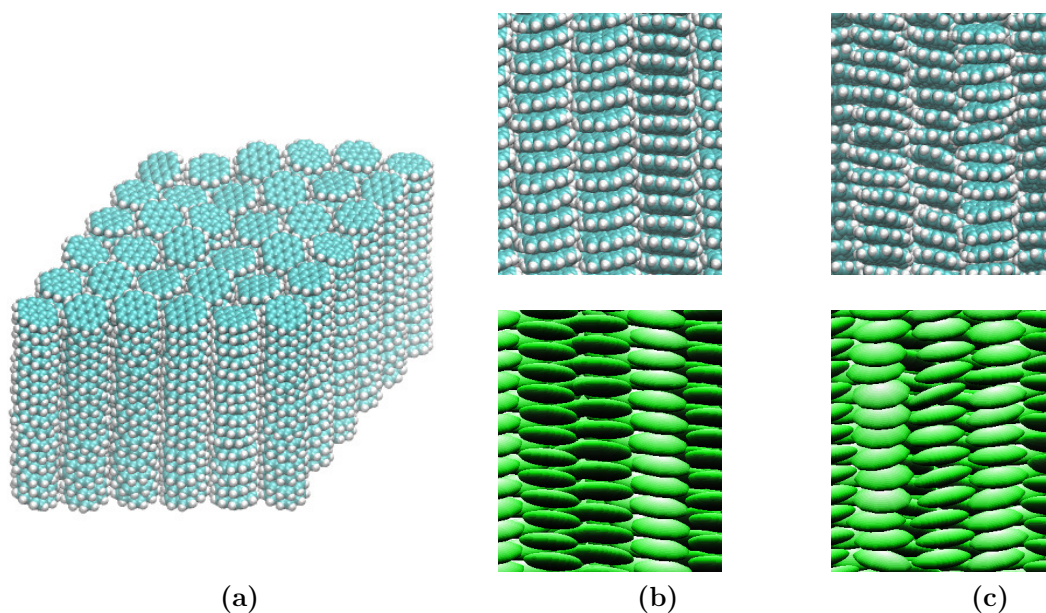


FIGURE 6.6: (a) Initial hexagonal columnar nematic state of the present system. (b) and (c): Snapshots of the hexagonal nematic regime after 3 ns at (b) 300 K and (c) 700 K within the atomic model and model M.

orientational phase transition occurring at high densities. However, it is also the most complex model in terms of the number of parameters involved. Indeed, the parametrization for the interaction strength involves four orientational dimer configurations, which have been chosen due to their relevance under strongly coupled conditions. The performance of the simpler Kabadi models, K1 and K2, (whose potential strength parametrizations are based on only two configurations) depends on the state considered. Specifically, K1 gives reliable results for the isotropic phase, while K2 works better with respect to the columnar-isotropic transition. Another important finding is that the most simple, spherical model (S) is useful only in the strongly diluted isotropic phase. Besides the obvious incapability of this model to predict orientationally ordered phases, already at intermediate densities, it falsely predicts a condensation transition, which is absent when using the angle-resolved (and atomistic) potentials. These findings clearly justify the additional effort in determining angle-resolved potentials. Moreover, to properly describe the various phases it turned out to be crucial to take into account the pronounced temperature dependence of the angle-dependent potential. An important example is the effective interaction in the face-face configuration, which is strongly affected by bending fluctuations stemming from the molecule's non-rigidity on the atomistic level.

We also note that, when comparing the computational time per core of the coarse-grained simulations (which are based on a self-written code) and the atomistic simulation time (based on the GROMACS package, version 4.5.5), we reached a speed-up of about a factor of 3 to 8. Part of this speed-up is likely due to the fact that we have represented the coronene molecules by a particularly simple shape, namely an uniaxial disc. The performance of other representations, e.g. a collection of fused rings [143] remains to be explored.

6.3 Coronene with electrostatics

In the current section we investigate a many-particle system of coronene molecules, modeled with electrostatic contributions, using MD simulations at constant temperature (T) and pressure (P) similar to previous section. First, we investigate in Sec. 6.3.1 the equilibrium structural properties of the crystalline unit cell at room temperature. Second, we analyze how certain structural parameters behave upon heating up the crystal until it melts in Sec. 6.3.2. Third, we summarize our electrostatics investigation in Sec. 6.3.3. Each simulation run starts from lattice-like initial conditions (described below) and leads to a relaxation of particle positions and box-vectors. To affect box lengths as well as box-angles we use anisotropic pressure coupling. In particular, the temperature and pressure coupling is realized with a modification of the Berendsen weak coupling scheme as described in Sec. 3.3.

The coronene molecules are modeled with either the point quadrupole model (see Sec. 5.4.3) or the implicit electrostatics model (see Sec. 5.4.4). Our many-particle system for all simulations consists of 576 molecules and is initialized with the following arrangement of unit cells in terms of box-vectors: $\mathbf{L}_1 = 4\mathbf{a}$, $\mathbf{L}_2 = 12\mathbf{b}$ and $\mathbf{L}_3 = 6\mathbf{c}$. Hereby \mathbf{a} , \mathbf{b} and \mathbf{c} denote the right-handed unit cell vectors, which together with the molecular arrangement and orientation in the unit cell are taken from Ref. 161. The molecules are aligned in a so-called herringbone pattern, which resembles tractor traces when seen from the side (see Fig. 6.7).

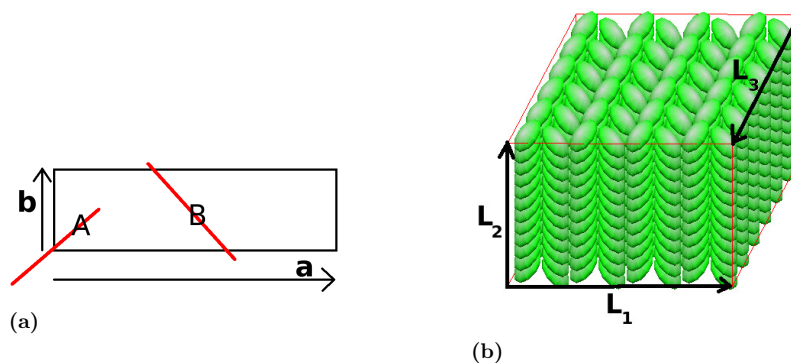


FIGURE 6.7: (a) Unit cell with molecules A and B (the red lines represent the side view of the discotic molecules). (b) Snapshot of a real crystalline configuration.

Just as in the non-electrostatic case, the pressure is set to 1 bar and the compressibility to $2.25 \cdot 10^{-4} \text{ bar}^{-1}$. The equilibration times range from 3.5 to 100 ns. To test the force-shifted cutoff (at 2.4 nm), we calculated the total electrostatic energy both with the cutoff and by using the full Ewald sum for quadrupoles (for the explicit expression, see Sec. 3.7.2.2 and Ref. 178). We found that the electrostatic energy from the cutoff procedure differs from the corresponding energy using the Ewald summation technique by only 0.04485% (in a perfect crystal). This justifies the simpler cut-off procedure.

6.3.1 Bulk crystal at room temperature

In the following, we investigate the equilibrium structure of the bulk crystal for the point quadrupole model (see Sec. 5.4.3; quadrupole strengths: $Q^* = 0, 0.5, 1, 1.5$) and the implicit electrostatics model (see Sec. 5.4.4) using trajectory data from the MD simulations. One important criteria to judge the performance of the different models are the unit cell parameters listed in Tab. 6.2.

TABLE 6.2: Variation of unit cell parameters for the different pair potentials at room temperature. The box lengths of the cell are denoted with a , b and c defined through the length of the unit cell vectors \mathbf{a} , \mathbf{b} and \mathbf{c} . The angles between the unit cell vectors are denoted with $\alpha = \sphericalangle(\mathbf{b}, \mathbf{c})$, $\beta = \sphericalangle(\mathbf{a}, \mathbf{c})$ and $\gamma = \sphericalangle(\mathbf{a}, \mathbf{b})$. The volume and the cohesion energy per particle are listed as well.

Model	a (Å)	b (Å)	c (Å)	α (°)	β (°)	γ (°)	V (Å ³)	E_{coh} (eV)
vdW model M	19.6444	3.6282	9.1430	90.02	117.74	89.98	576.78	1.5533
pq model ($Q^* = 0.5$)	17.0045	4.2382	9.2411	90.00	113.66	90.00	610.04	1.7153
pq model ($Q^* = 1$)	17.1237	4.0178	9.7228	90.00	116.52	90.00	598.53	2.9882
pq model ($Q^* = 1.5$)	17.7104	3.7246	9.9783	89.62	122.77	86.83	552.08	6.4402
impl. electr. model	17.6142	4.5524	9.5722	90.00	112.91	90.01	707.03	0.9457
experiment [47]	16.094(9)	4.690(3)	10.049(8)	90	110.79(2)	90	709.9(8)	/
experiment [160, 161]	16.119	4.702	10.102	90	110.9	90	717.1	1.39 – 1.54
database [56]	16.11	4.70	10.10	90	110.9	90	714.43	1.378-1.783

Inspecting the values for a , b , c , α , β , γ (for description see caption of Tab. 6.2), we find very good agreement of the implicit electrostatics model and the point quadrupole model for weak strength ($Q^* = 0.5$) with the corresponding experimental data. The remaining models ($Q^* \neq 0.5$) reveal slight deviations in a , b , c , and β . Nonetheless, the crystal structures are in all cases monoclinic ($\alpha = \gamma = 90^\circ$). Concerning the cohesion energy predicted by the point quadrupole models, we note a significant increase with the quadrupole strength. This stems from the overestimation of the binding energy for PD-configurations (see Fig. 5.9). The cohesion energy of the implicit electrostatics model is somewhat underestimated.

In order to further analyze the orientation of the corresponding molecules (named A and B) in the unit cell, we introduce the herringbone angle ϕ , which marks the angle between both molecular orientation axes that point “upwards” along \mathbf{b} (see Fig. 6.7), and is defined as follows

$$\phi = \arccos [\langle \text{sgn}(\hat{\mathbf{u}}_A \cdot \mathbf{b}) \hat{\mathbf{u}}_A \rangle \cdot \langle \text{sgn}(\hat{\mathbf{u}}_B \cdot \mathbf{b}) \hat{\mathbf{u}}_B \rangle]. \quad (6.4)$$

In Table 6.3 all molecular angles with respect to the body fixed unit cell are displayed. Specifically, we present the enclosed angles of the molecule A’s axis with each unit cell axis as performed in Ref. 161.

As expected, we observe a nematic phase for the van der Waals model (point quadrupole model with a zero quadrupole strength) reflected by a small value for the enclosed angle of the molecule A’s axis with the \mathbf{b} -axis, called ψ_N^A and a small herringbone angle ϕ . This finding is in accord with the van der Waals crystal investigated in Sec. 6.2.2. The alignment of the molecules with respect to all unit cell axes (χ_N^A , ψ_N^A , ω_N^A) for both the implicit electrostatics model and the point quadrupole model with

TABLE 6.3: The angles of molecule A with the \mathbf{a} , \mathbf{b} and its perpendicular axis $\mathbf{a} \times \mathbf{b}$ are denoted by χ_N^A , ψ_N^A and ω_N^A . The notation is taken from Ref. 161.

Model	χ_N^A (°)	ψ_N^A (°)	ω_N^A (°)	ϕ (°)
pq model ($Q^*=0$) / vdW model M	95.65	12.20	79.24	24.38
pq model ($Q^*=0.5$)	129.69	39.86	93.12	79.72
pq model ($Q^*=1$)	129.83	40.66	96.85	81.32
pq model ($Q^*=1.5$)	121.90	40.79	108.47	81.54
impl. electr. model	130.23	40.31	92.30	80.63
ideal crystal [160]	133.7	43.7	89.6	87.35

weak strength ($Q^* = 0.5$) is in good agreement with the experimental values. For all investigations (except for the nematic phase of the model without electrostatics), no significant change for the distance of neighboring columns was observed (corresponding distances are 8.7 Å and 9.8 Å).

6.3.2 Melting of the bulk crystal

We now turn to the investigation of structural changes of the reference bulk crystal [see Fig. 6.7(b)] upon heating the system. Hereby, we expect the crystal to melt. The temperature range considered covers $300 \text{ K} \leq T \leq 1500 \text{ K}$. After every 100 K a different isobaric-isothermal simulation run is performed.

We further investigate ϕ as a function of temperature for the different models as presented in Fig. 6.8(a). The melting from crystalline to isotropic phases is also reflected in Fig. 6.8(b) showing the cube root of the volume as a function of the temperature. When considering the reference temperatures of bulk coronene with respect to melting (710.5 K) [169] and boiling (798 K) [169], we recognize that coronene is liquid only in a narrow temperature band. In the implicit electrostatics model we observe a decay of the herringbone angle between 600 and 700 K towards zero indicating isotropic orientation. At 700 K the volume is significantly higher than at 600 K, and rises even faster with increasing temperature above 700K. We take these as indications of a liquid phase appearing at around 700 K and a gas phase at temperatures above 800 K. On the contrary in the implicit electrostatics model, the crystal structure for the point quadrupole model melts at significantly higher temperatures for all quadrupole strengths. It seems obvious that the melting temperature increases with the cohesion energy, as discussed earlier (see Sec. 6.3.1).

We next want to analyze the crystalline order parallel to the plane spanned by \mathbf{L}_1 and \mathbf{L}_3 with the correlation function g_{\parallel} which we defined in Eq. (2.61a). For the implicit electrostatics model, we observe a crystalline order [see Fig. 6.9(a)], that continuously vanishes with rising temperature. In contrast, the point quadrupole models do not exhibit this behavior [see Fig. 6.9(b)-(e)]. At a quadrupole strength of $Q^* = 1.5$ we no longer see positional order, while the orientational order still exists [see Fig. 6.8(a)]. To sum up, the transition temperature of the implicit electrostatics model can be suitably

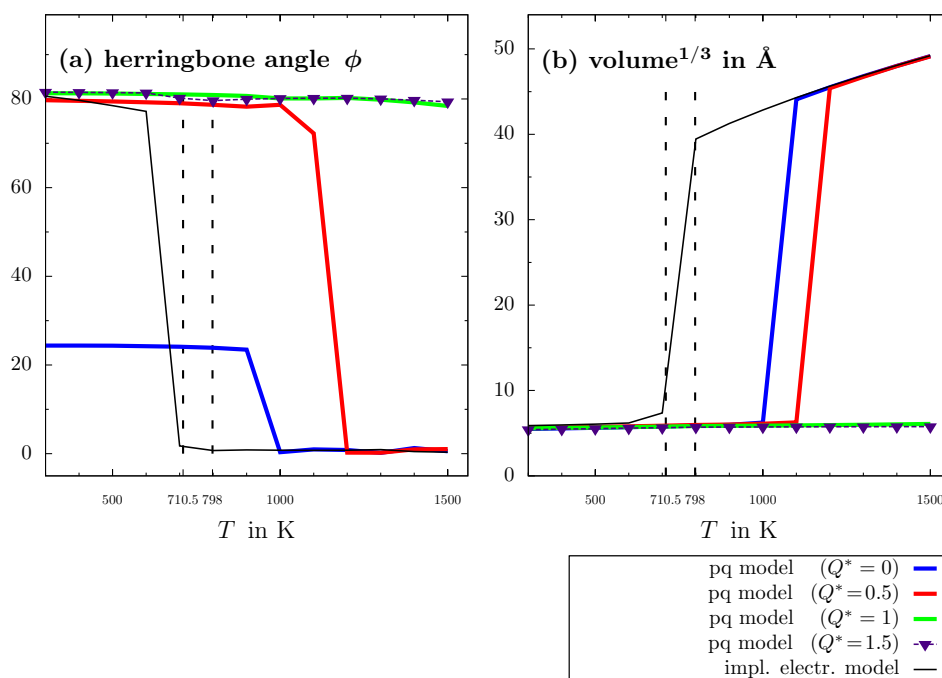


FIGURE 6.8: (a) Herringbone angle between neighboring discs and (b) volume as function of the temperature.

reproduced. Clearly it is not in full accordance with the experimental reference values. Nonetheless, this approach marks a way to treat the relevant electrostatics in a rather simple model eligible for large-scale computer simulations

6.3.3 Performance of the models with electrostatics

To assess the quality of modeling, unit cell parameters and structural quantities of the coronene bulk crystal, we calculated with constant pressure and temperature MD simulations. These results have been compared to their experimentally determined counterparts (see Sec. 6.3.1 and 6.3.2).

Based on our data, we can conclude that the simple point quadrupole approach, although yielding the correct long-range decay, gives unreliable results, even when the quadrupole strength is reduced to a value related to a reasonable cohesion energy.

Moreover, for all considered quadrupole strengths we observed melting temperatures far above the experimental values. Nevertheless, a small point quadrupole leads to a stabilization of the herringbone structure due to an energetic preference. In contrast, our second approach involving the implicit electrostatics model is able to stabilize the herringbone structure up to a melting point similar to experimental values. With this second model, we also encountered a liquid phase as observed in experiment. As a conclusion, the implicit electrostatics model seems superior in reproducing structure and melting. It is also more convenient from a computational perspective since it is simply a reparametrized Gay-Berne-like model (see Sec. 5.3.3). The crucial point for the success of the latter approach consists of choosing an extended charge distribution rather than a single point multipole. Hereby the characteristics of the electrostatic potential in the near field are reproduced in a great extent. Still, it would be interesting

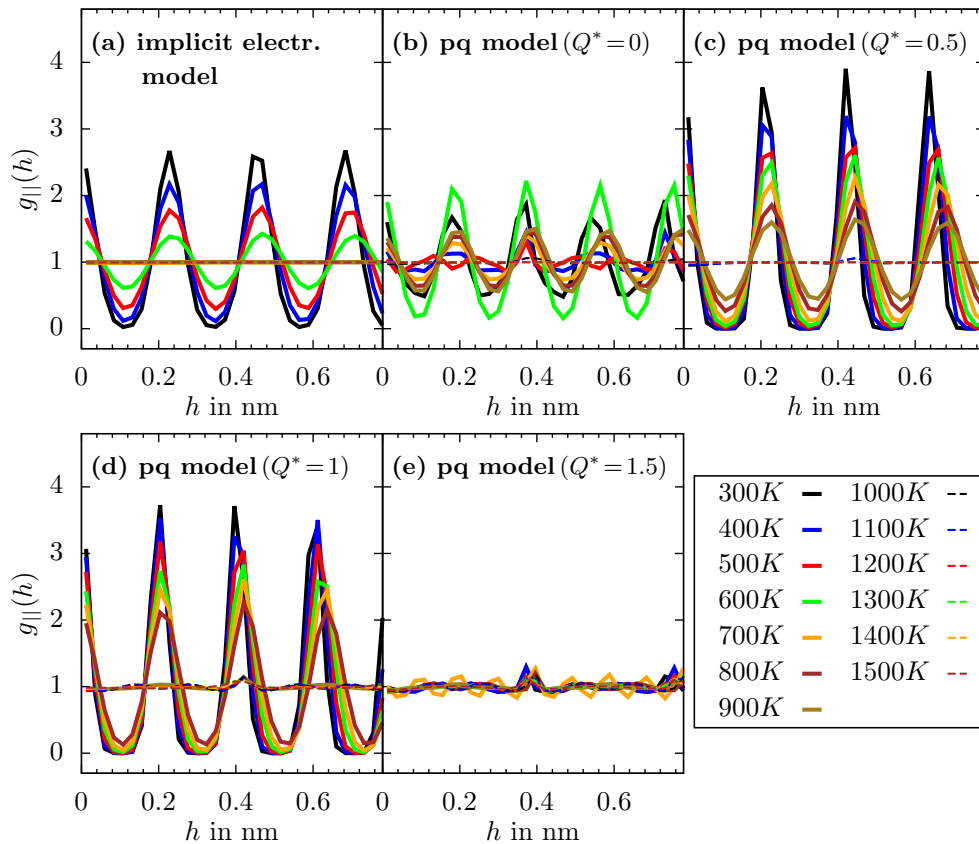


FIGURE 6.9: Temperature influence of the pair correlation function along the \mathbf{L}_1 - \mathbf{L}_3 -plane for the implicit electrostatics model and the point quadrupole model for various strengths.

to investigate the influence of an atomic point charge distribution on the structural and melting properties of the coronene crystal.

Besides the temperature-independent electrostatics and the ring-charge assumption, a further underlying assumption in our work is the pairwise additivity of the many-molecule interactions. The implications of this assumption were already investigated for crystalline benzene [53], which is similar to coronene. Further, it is worth mentioning that our temperature-dependent approach does not take into account formation and breaking of covalent bonds, which may be an important processes for very high temperatures and pressures [88].

For future work, it would be rather interesting to use ab-initio simulations to calculate effective pair potentials for coronene and compare them with our corresponding results for different temperatures. Finally, we propose applicability of our presented method to a similar class of discotic molecules, e.g. benzene or hexabenzocoronene.

Chapter 7

2D monolayer

7.1 Preface

In this chapter, we investigate the phase behavior of a two-dimensional system comprising one species of ellipse-shaped particles carrying a linear quadrupole moment in their center. These particles are designed to constitute a simple model for uncharged and non-polar conjugated organic molecules in terms of shape and electrostatics.

Our coarse-graining strategy so far (Chapter 4), can be characterized as a systematic transition from the atomistic level of detail towards a more abstract or coarse-grained level of detail. The resulting effective interactions are modeled in a fashion to reproduce pair potentials and structural quantities (Chapter 5 and 6). In this chapter, we on contrary do the opposite strategy. Since we do not have a certain molecular system in mind, it might be more promising to study first the phase behavior of this simple model and subsequently discuss further fields of application. This investigation enables a broader understanding of molecular as well as colloidal monolayer arrangements on a coarse-grained level. We are particularly interested in the alignment of conjugated organic molecules on inorganic surfaces. These so-called hybrid inorganic/organic systems (HIOS) form a rather new field of application in optoelectronics [21, 22, 46, 100, 167]. Experimental investigations of coronene (a conjugated organic molecule; see introduction) on germanium substrate (001) reveal two different observed structures [116] (depending on the packing fraction) parallel columns or compact herringbone-like configurations. Other flat molecules form complex and compact patterns [36, 37]. Moreover, colloidal patchy particles in a confined geometry [133, 144, 177] are examples for colloidal monolayer studies where a quadrupole is involved. More specifically, the simulation study of Bianchi *et al.* [20] as well as the experimental study of van Oostrum *et al.* [199] with particles described through similar models exhibit hexagonal and ring-like arrangements.

In this survey, we specifically study our quadrupolar-ellipse system at various aspect ratios and temperatures for a fixed pressure. The influence of the temperature on diverse ground states, which are calculated by Moritz Antlanger (TU Wien), is further scrutinized with molecular dynamics (MD) simulations in Sec. 7.3 for 840 particles. We find that ground state structures corresponding to particles with high eccentricity can withstand higher temperatures. The entire investigation, including the detailed ground state analysis, is based on our article listed in Ref. 77. With regard to linear

quadrupoles, we intuitively expect T-kind of configurations, especially when considering two isolated molecules. However, it turns out that the influence of the different aspect ratios and the underlying statistical ensemble (isobaric-isothermal; see Sec. 2.2.2) leads to a broad variety of phases besides the intuitive T-kind of configurations.

In the following, we introduce the model (Sec. 7.2) and later on provide results from the MD simulations (Sec. 7.3). Finally, we close this investigation by analyzing a crystalline melting line and a short investigation about the transferability of this results for other sets of parameters (Sec. 7.4).

7.2 Model

In this section, we introduce our coarse-grained interaction model, which is a direct composition of a short ranged soft-repulsive part, V_{sr} , and the electrostatic interaction between two linear point quadrupoles, V_{QQ} .

$$V = V_{\text{sr}} + V_{\text{QQ}} \quad (7.1)$$

As mentioned before, we investigate one component systems with ellipse-shaped particles of various aspect ratios. The latter is defined through the ratio between the ellipses main axes, i.e. $\kappa = \sigma_{\parallel}/\sigma_{\perp}$, where the axis with length σ_{\parallel} is parallel and those with σ_{\perp} is perpendicular to the later introduced linear quadrupole, which also lies in the two-dimensional plain. A schematic overview is depicted in Fig. 7.1(a). Throughout our investigation, we use particles with an equal surface area, i.e. $\sigma_{\perp} \cdot \sigma_{\parallel} = \sigma_0^2 = \text{const.}$ For the main axes thus follows

$$\sigma_{\parallel} = \sigma_0 \sqrt{\kappa} \quad \text{and} \quad \sigma_{\perp} = \frac{\sigma_0}{\sqrt{\kappa}}. \quad (7.2)$$

Concerning the shape of the molecules, we define a purely repulsive but rather hard inter-molecular pair potential that is based on the ellipse-like contact distance of Berne and Pechukas [19]. The variables, describing the dimer system, are introduced through Eqs. (4.16) or alternatively by Eqs. (4.17). The short range part

$$V_{\text{sr}}(R, a, b, c) = 4\epsilon_0 \left[\frac{\sigma(a, b, c)}{R} \right]^{18} \quad (7.3)$$

resembles the repulsive part of a Lennard-Jones interaction (here we use for the exponent a value of 18 instead of 6), while the contact distance σ (which marks the distance of vanishing pair potential) and defined as [19, 63]

$$\sigma(a, b, c) = \frac{\sigma_0}{\sqrt{\kappa}} \left\{ 1 - \frac{\chi}{2} \left[\frac{(a+b)^2}{1+\chi c} + \frac{(a-b)^2}{1-\chi c} \right] \right\}^{-1/2}, \quad (7.4)$$

with

$$\chi = \frac{\kappa^2 - 1}{\kappa^2 + 1}$$

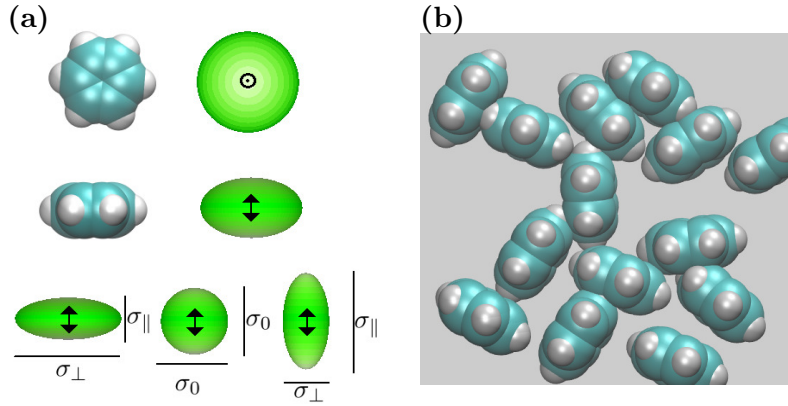


FIGURE 7.1: (a) Middle and top panels: top and side views of benzene together with our simple model. The axis of the linear point quadrupole (visualized by the double-arrow) is placed along the symmetry axis. Bottom panels: schematic view of our soft, anisometric particles carrying a linear quadrupole moment with $\kappa > 1$ (left panel), $\kappa = 1$ (center panel), and $\kappa < 1$ (right panel). (b) Exemplary monolayer system of benzene molecules.

being an anisotropy parameter. In its present form V_{sr} is similar to the interaction potential used in Ref. 165. The prefactor 4 is just a remnant of the Lennard-Jones potential without further purpose. We hereby restrict ourselves to rather hard particles to keep the system simple - and as we later see - this might reduce the parameter space. However, it is not infinitely hard and thus allows overlaps and a simple treatment for ground state and MD calculations. The interaction between two linear quadrupole moments with strength Q [defined in Eqs. (5.15) and (5.16)] can be written as [26, 68]

$$V_{\text{QQ}}(Q^2, R, a, b, c) = \frac{1}{4\pi\epsilon_{\text{pm}}} \frac{3Q^2}{4R^5} K(a, b, c), \quad (7.5)$$

where ϵ_{pm} marks the vacuum permittivity and $K(a, b, c)$ is defined in Eq. (5.10). Even though the interaction decays slower with the distance (i.e., $\sim 1/R^5$) than, e.g., van der Waals interactions ($\sim 1/R^6$) we can still calculate inter-particle energies with sufficient accuracy via a real-space lattice sum. We propose a cut-off radius of $R_{\text{cut}}/\sigma_0 = 6$ for both, electrostatic and repulsive interactions. In contrast, the ground state calculations were calculated at a cutoff radius $R_{\text{cut}}/\sigma_0 = 30$.

We next consider a dimer system and investigate depending on the aspect ratio the most attractive configuration for the particles. More specifically, we consider a system of two quadrupolar particles in contact, i.e. $R = \sigma(a, b, c)$ [see Eq. (7.4)] and only take the quadrupole-quadrupole interaction V_{QQ} into account. The corresponding ground state (minimal energy) configurations as function of the anisotropy parameter, κ , are illustrated in Fig. 7.2. It turns out that the T-configuration is only stable for values of κ close to unity. At large eccentricities ($\kappa < 0.75$ or $\kappa > 1.2$) the ground state dimer configuration is parallel displaced (PD).

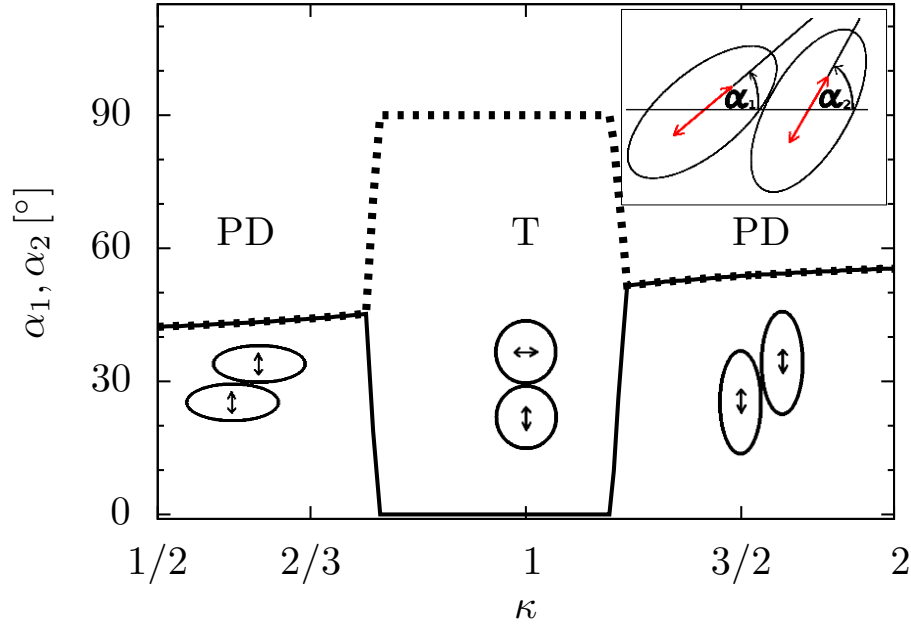


FIGURE 7.2: Minimum electrostatic energy configurations for ellipse-shaped particles with a central linear quadrupole along one axis (which is κ times the other axis) and a fixed area (for all κ). The corresponding orientation angles of the quadrupoles with respect to the particle connecting vector are shown as a function of the aspect ratio κ . Both angles can be interchanged due to the D_2 symmetry of the particles. The parallel displaced (PD) and T-configuration mark the two fundamental different minimum electrostatic energy configurations.

All our numerical calculations were performed in the NPT -ensemble (see Sec. 2.2.2), where the relevant thermodynamic potential is the free enthalpy, G , that is

$$G = E + P\langle S_0 \rangle - TS = H - TS. \quad (7.6)$$

E represents the internal energy, P is the pressure, and $\langle S_0 \rangle$ is the average area occupied by the system, T the temperature and S the entropy (for details see Sec. 2.2.2). For vanishing temperature, the free enthalpy G reduces to the enthalpy H . Based on the scales of length σ_0 , mass m_0 , and energy ϵ_0 , the quadrupole strength Q , the temperature T and the pressure P as well as the time t are expressed via their respective reduced units, i.e.

$$(Q^*)^2 = Q^2 / (4\pi\epsilon_{\text{pm}}\sigma_0^5\epsilon_0), \quad T^* = kT/\epsilon_0, \quad P^* = P\sigma_0^2/\epsilon_0, \quad t^* = t/\sqrt{\sigma_0^2 m_0/\epsilon_0}.$$

To start our investigation we require a proper setting for the $((Q^*)^2, P^*)$ pair. In this respect, we extract Q , σ_0 from a quadrupolar Gay-Berne model of benzene proposed by Golubkov *et al.* [65]. We introduce a quadrupole strength of $Q_{\text{benzene}} = -30.5812 \cdot 10^{-40} \text{Cm}^2$ and a spherical diameter (see Def. (7.2)) of $\sigma_0 \approx 0.307$ (when the Gay-Berne contact distance is used). Considering the surface tension of water defined in Ref. 200, $P_{\text{water}} = 71.99 \cdot 10^{-3} \text{Nm}^{-1}$ (value taken for 25°C), we arrive at the ratio

$$(Q_{\text{benzene}}^*)^2 / P_{\text{water}}^* = Q_{\text{benzene}}^2 / (4\pi\epsilon_{\text{pm}}\sigma_0^4 P_{\text{water}}) \approx 4.5.$$

We focus on this ratio because the (Q^2, P) parameter set effectively reduces to Q^2/P in the hard limit as we later discuss (see also Appendix A.5). Since the quadrupole is very pronounced in the near field, we consider in the MD simulations a reduced value of $(Q^*)^2/P^* = 2$. If $P^* = 1$ corresponds to P_{water} then for the energy scale ϵ_0 holds:

$$\epsilon_0 = P_{\text{water}} \cdot \sigma_0 / P^* = P_{\text{water}} \cdot \sigma_0^2 = 4.09 \text{kJ/mol.}$$

After all, we investigate the system for the parameter settings $((Q^*)^2, P^*) = (2, 1), (4, 2)$ in the MD simulations, where we provide a detailed structural investigation for $((Q^*)^2, P^*) = (2, 1)$ (at different temperatures). The ground state calculations (carried out by Moritz Antlanger) were performed at various parameter sets $((Q^*)^2, P^*) = (0.2, 0.1), (2, 1), (20, 10), (4, 2)$.

7.3 Results

For the parameter set $((Q^*)^2, P^*) = (2, 1)$, the ground state results are depicted in Fig. 7.3 (on page 108) and 7.4 (on page 109) on the left column each.

Depending on the aspect ratio considered, which is $\kappa = 0.4, \dots, 2.1$, we identify between 1 to 3 different orientations. Ground states, where particles show one orientation are observed for extreme κ -values (high eccentricity), i.e. $\kappa = 0.4$ or 2.1 . In this case, the particles form parallel columns where the particles' orientation vector is tilted with respect to the column vector. Two orientations revealing T- or herringbone kind of configurations are observed for most aspect ratios in-between ($\kappa = 0.48, 0.58, 0.8, 1, 1.38, 1.83$). Specifically, the T-configurations are observed for $\kappa \approx 1$ (here $\kappa = 0.8, 1, 1.38$). Another type of configuration showing two different orientations is found for $\kappa = 1.66$. As we see later, this kind of configuration is rather unstable and only found in a narrow κ -range. For $\kappa = 1.5$ we observe three orientations (which differ by multiples of an angle of 120°), where the particles' positions show a trihexagonal tiling.

Another interesting aspect appears when we compare the order parameter curves, defined in Sec. 2.7.2, for the parameter setting $((Q^*)^2, P^*) = (2, 1)$ shown in Fig. A.3 in Appendix A.4, with the respective curves obtained for the parameter setting $((Q^*)^2, P^*) = (0.2, 0.1)$ and $((Q^*)^2, P^*) = (20, 10)$ in the neighboring Figs. A.4 and A.5 (in Appendix A.4), respectively. These curves reveal a striking similarity, suggesting that an appropriate scaling of the quadrupole moment and the pressure yields the same (ground state) results. On the other other hand, the corresponding enthalpy curves are quite different in magnitude. We discuss these observations in more detail in the Appendix A.5. There we show, that there is indeed a parameter scaling relation for systems of hard particles (see Appendix A.5.1), yielding $P \propto Q^2$. However, here we consider particles with a soft core, even though this core is rather steep, (an exponent of $n = 18$ was used in this work for the short-range repulsion). Still, the softness seems to lead to a breakdown of the parameter scaling when analyzing the enthalpy. This is presumably due to the fact that a scaling of the input parameter also induces a small change of the density. We therefore suggest in Appendix A.6 an empirical scaling law for the ground state enthalpy of our system and provide numerical evidence for its justification. We can conclude that the empirical scaling law for the ground state

enthalpy seems applicable for κ around unity where the structures possess a 4-fold symmetry (T-configuration).

In the remaining part of this section, we analyze MD results for all considered aspect ratios κ and reduced temperatures T^* . Later on, we scrutinize the applicability of the finite temperature parameter scaling, that is $P \propto Q^2 \propto T$ in the hard limit (see Appendix A.5.2), for our “soft-core” model in Sec. 7.4. As previously mentioned, the ground state configurations for a variety of aspect ratios serve as initial conditions for the MD simulations.

All MD simulations were performed using the Berendsen weak coupling scheme as outlined in Sec. 3.3 for two dimensions. We hereby include also the speed-up techniques presented in Sec. 3.8. The MD simulations have been performed at several values of the reduced temperature $T^* = k_B T / \epsilon_0$, that is, $T^* = 0.1, 0.2, \dots, 1.6$. Throughout the investigation, we used a time increment of $\Delta t^* = 0.00136172$ (corresponding at a macroscopic level to $\Delta t \approx 2$ fs). An adequate choice of the time step is imposed by the mass of the particles, for which we have assumed the mass of benzene $m_0 = 78u$. Each simulation extends over 210 000 time steps. During the first 20 000 MD steps, the target temperature is gradually increased from $T^* = 0$ towards the respective target value. Structural quantities are then extracted only during the last 10 000 time steps of the simulation. The values for the temperature- and pressure-coupling constants τ_{trans} , τ_{rot} and τ_P were chosen to be 80 time steps. Of course, the actual volume change of the box is also influenced by the compressibility; its reduced, dimensionless counterpart, $K^* = K m_0^2 \sigma_0^2 / \epsilon_0$ is set to 0.01. We assume the mass distribution within the particles to be homogeneous and thus obtain for the dimensionless moment of inertia $I^* = 0.25 \cdot (\kappa + \frac{1}{\kappa})$. Concerning the pair forces \mathbf{F}_{ij} and torques \mathbf{M}_{ij} we perform a truncation at $R_{\text{cut}} = 6\sigma_0$, as mentioned, and shift them in order to make them vanish smoothly.

Corresponding snapshots for significant configurations after equilibrating are presented in Fig. 7.3 for $\kappa \leq 1$ and in Fig. 7.4 for $\kappa > 1$. The MD simulations reveal that the structures observed at zero temperature remain stable at low temperature. With increasing temperature, more and more defects start to form (see second column in Figs. 7.3 and 7.4). The most common of these is a slight wave-like modulation of previously straight lines. Finally, crystalline order is rapidly lost once the temperature is raised above a certain threshold value (see third column in Figs. 7.3 and 7.4); the related temperature depends strongly on κ . Configurations with $\kappa \approx 1$ (T_{sq}-configuration) and κ far from unity (PD-configuration) are the most stable ones, due to the fact that attractive quadrupole-quadrupole constellations can get very close (losing order for $T^* = 1.1$ and $T^* = 1.2$, respectively), while the configurations for $\kappa = 1.66$ melt even at a low temperature of $T^* = 0.5$. In order to investigate the transition from the ordered to the disordered regime, we focus on the average reduced potential energy $\langle E_{\text{pot}}^* \rangle$ and area $\langle S_0^* \rangle$. Figure 7.5 depicts $\langle E_{\text{pot}}^* \rangle$ and $\langle S_0^* \rangle$ as a function of the reduced temperature T^* for all considered aspect ratios κ . Upon increasing the temperature from zero, $\langle E_{\text{pot}}^* \rangle$ progressively decreases in magnitude and finally approaches zero, reflecting the diminishing role of particle interactions. At the same time, the area $\langle S_0^* \rangle$ increases. In fact, one would expect such an increase already in an ideal gas system where, at constant pressure, the ratio of temperature and area must be constant.

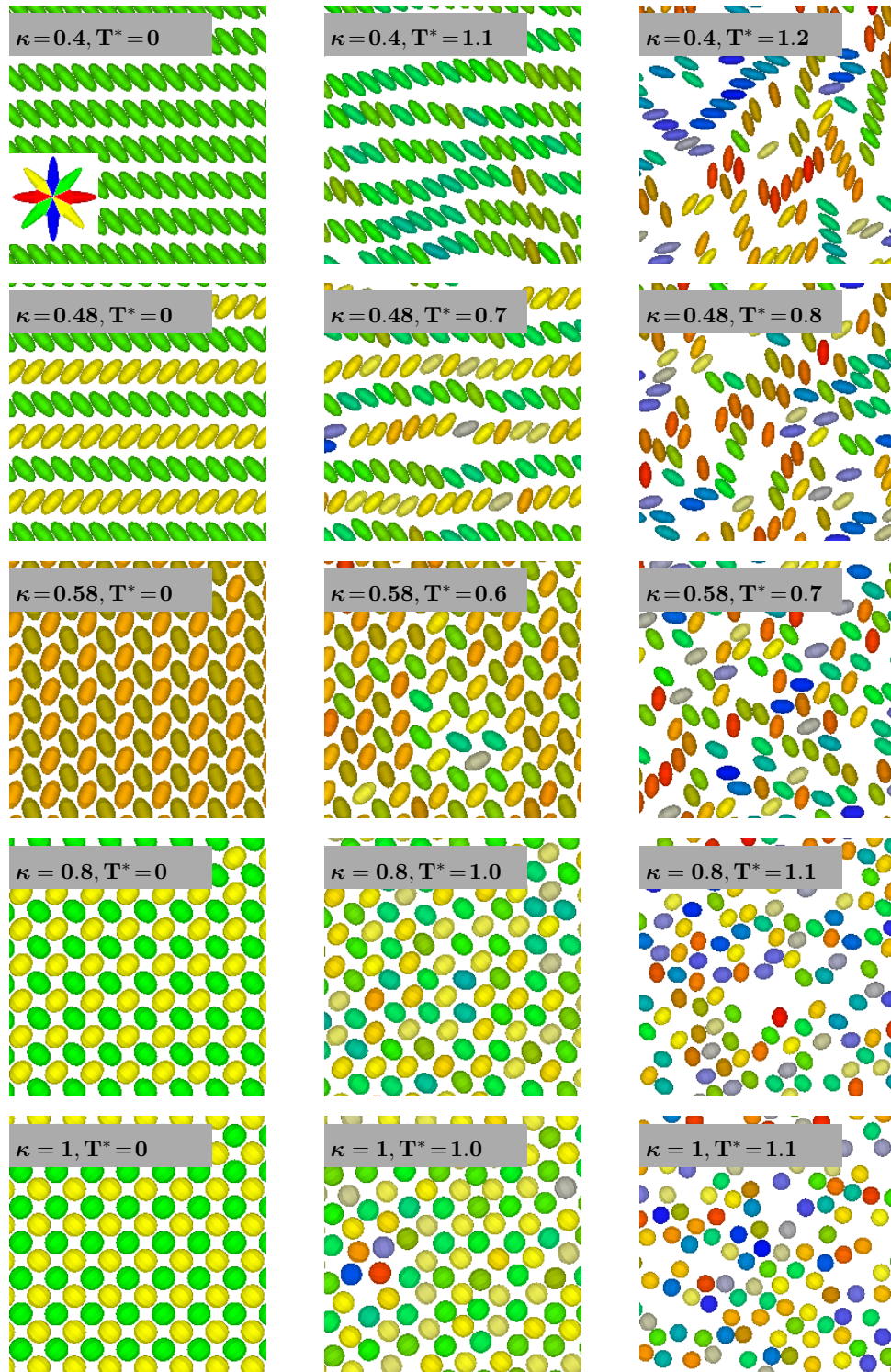


FIGURE 7.3: Snapshots of MD simulations for different values of $\kappa = \sigma_{\parallel}/\sigma_{\perp} \leq 1$ (as labeled) and $T^* = k_{\text{B}}T/\epsilon_0$ (as labeled). Different colors indicate different orientations of the linear quadrupole axis, which is orthogonal to the longest axis for $\kappa < 1$ (see inset in the top left panel). The ground states (left column) were calculated by Moritz Antlanger from the TU Wien using evolutionary algorithms.

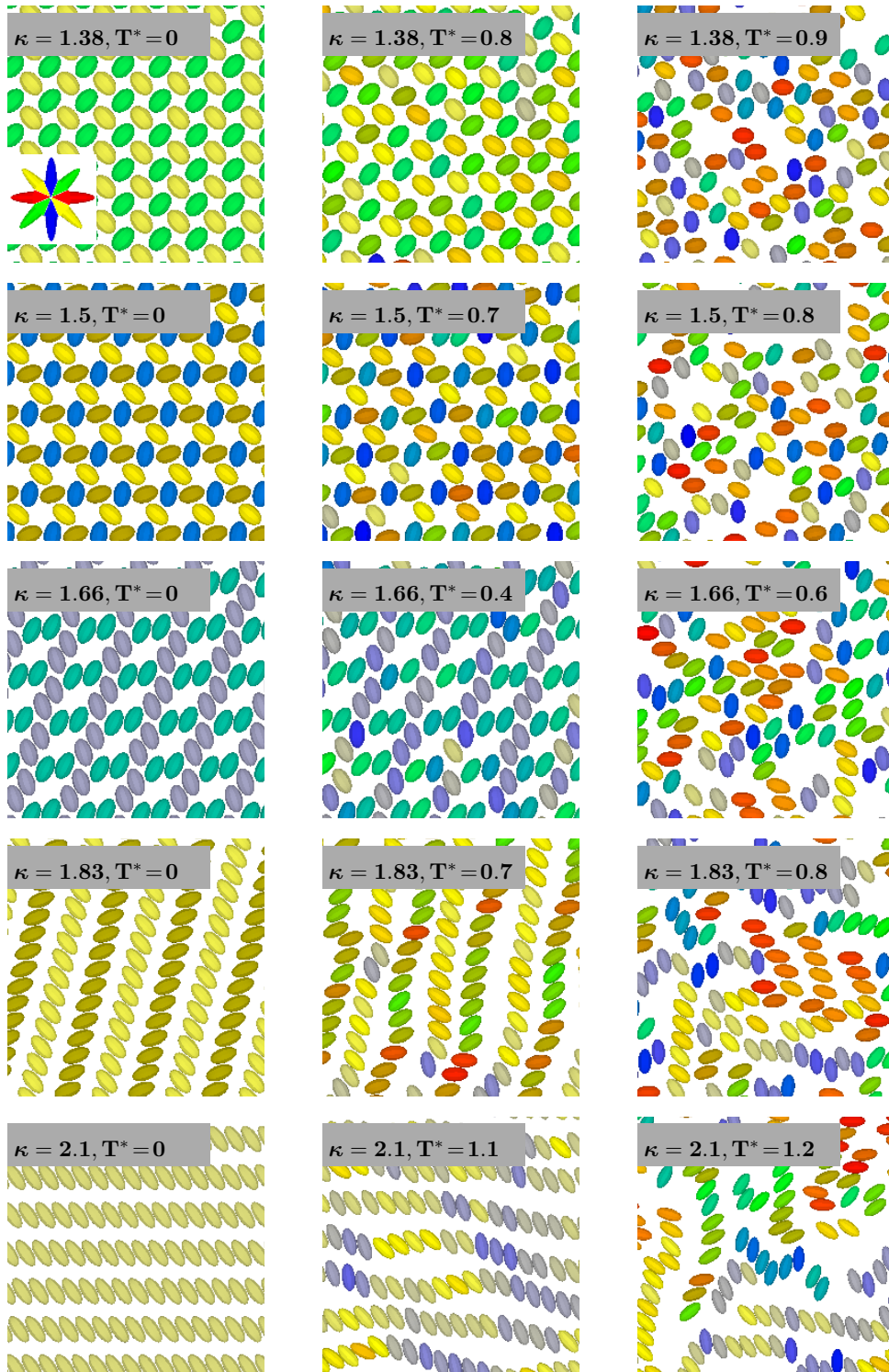


FIGURE 7.4: Snapshots of MD simulations for different values of $\kappa = \sigma_{\parallel}/\sigma_{\perp} > 1$ (as labeled) and $T^* = k_{\text{B}}T/\epsilon_0$ (as labeled). Different colors indicate different orientations of the linear quadrupole axis, which is parallel to the longest axis for $\kappa < 1$ (see inset in the top left panel). The ground states (left column) were calculated by Moritz Antlanger from the TU Wien using evolutionary algorithms.

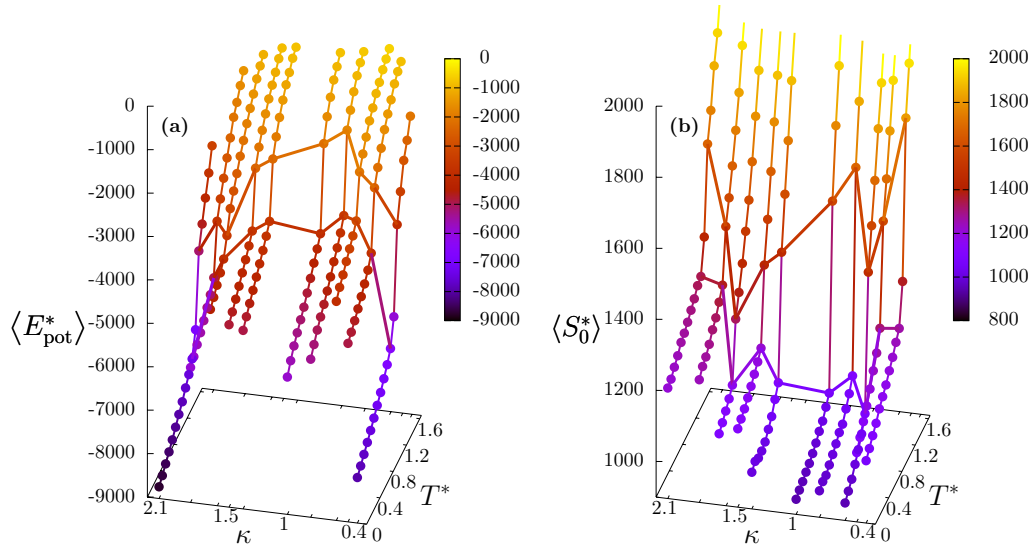


FIGURE 7.5: Potential energy $\langle E_{\text{pot}}^* \rangle$ and system area $\langle S_0^* \rangle$ as function of temperature T^* and aspect ratio κ . The color bars indicate the corresponding value. Each point represents one simulation run.

Interestingly, however, we observe for all values of κ a sudden change of the functions $\langle E_{\text{pot}}^*(T^*) \rangle$ and $\langle S_0^*(T^*) \rangle$ in a very small range of temperatures (with these changes occurring at the same T^* for the two quantities considered). We take this behavior as an indication of first order phase transitions; their positions are marked in Fig. 7.5 with a contour line along κ for the upper temperatures next to the discontinuities. With purpose we have not considered the corresponding susceptibility, c_P , since it is well established that energy fluctuations are not correctly reproduced with the Berendsen scheme [2, 3]. Only for $\kappa = 1.66$ we could not resolve any step discontinuity in the potential energy.

We now turn to Fig. 7.6 showing the investigation of the previously defined BOOPs Ψ_4 and Ψ_6 [see Eq. (2.62) on page 27]. For all our ground state configurations we find at least one of these two parameters being unequal zero. Moreover, considering the temperature dependence we observe for all κ an abrupt decay of Ψ_4 and Ψ_6 (if not zero at ground state) at the same temperatures where $\langle S_0^* \rangle$ abruptly increases. These step discontinuities seem to confirm the observations depicted in Figs. 7.3 and 7.4.

To further analyze the structure at finite temperatures we have calculated various coefficients of the pair distribution function $g^{l_1 l_2 l}$ in a rotationally invariant expansion as introduced in Sec. 2.7.1. Here we focus on the coefficients g^{000} , g^{220} and g^{202} .

In Fig. 7.7, we present numerical results for these three functions for $\kappa = 2.1$. Investigations for the other κ -values led to analogous conclusions concerning the later introduced melting curve. In all three correlation functions the first peak is located at around $0.8\sigma_0$. This position marks not exactly the face-to-face alignment (which is at around $0.69\sigma_0$) but a slightly shifted parallel configuration due to the quadrupole (see last row in Figs. 7.3 and 7.4). For $T^* = 1.2$, we detect a strong decay for $g^{000}(R)$ towards unity for large particle distances R . The crystalline order has completely vanished reflected by the missing peaks for larger R . Since for low temperatures all

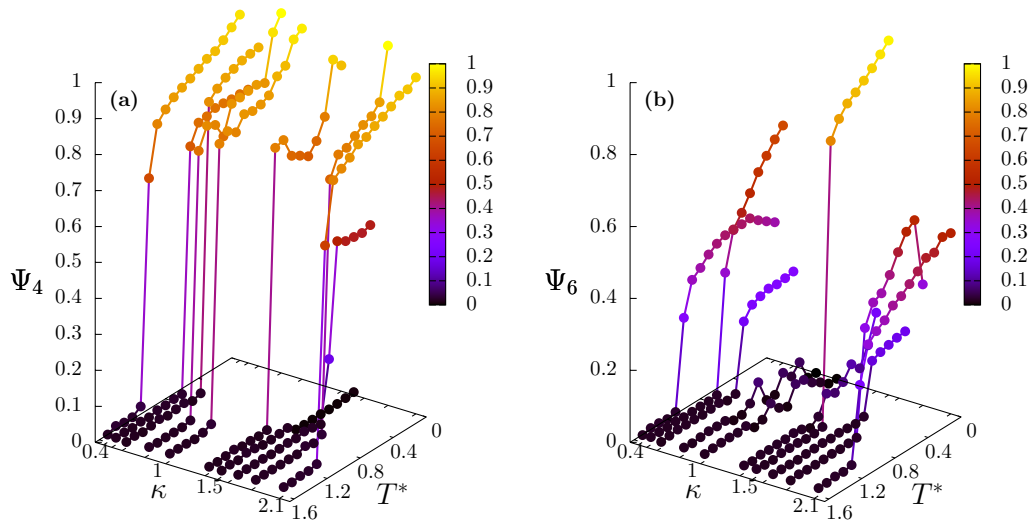


FIGURE 7.6: Bond orientational order parameters (a) Ψ_4 and (b) Ψ_6 as function of κ for different temperatures T^* . The color bars indicate the corresponding value.

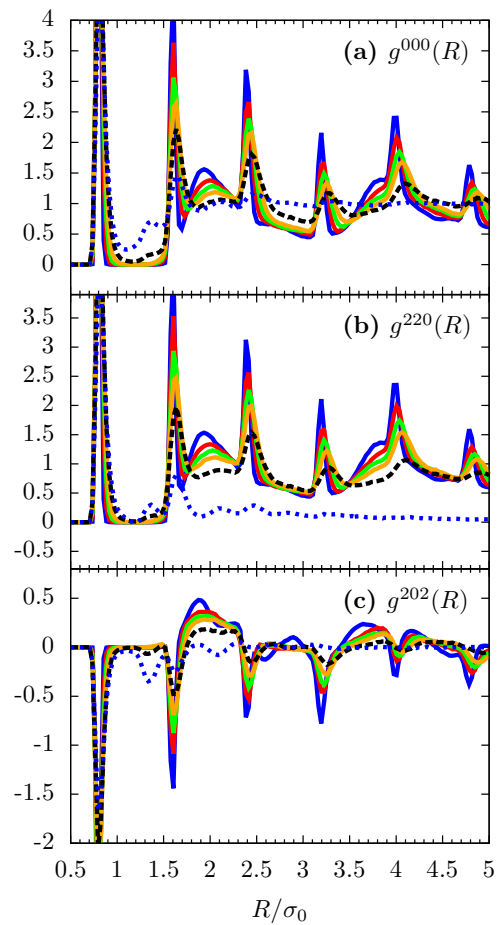


FIGURE 7.7: Correlation functions (a) g^{000} , (b) g^{220} and (c) g^{202} for $\kappa = 2.1$ and $T^* = 0.3, 0.5, \dots, 1.1, 1.2$.

particles point in the same direction, g^{220} is equivalent to g^{000} . However, when the temperature reaches $T^* = 1.2$, we observe no more orientational order for large R . This means, g^{220} goes to zero, whereas g^{202} oscillates around zero in the ordered phase for low temperatures ($T^* < 1.2$). It is due to the fact that g^{202} can per definition not contribute to the overall particle density. At $T^* = 1.2$, $g^{202}(R)$ completely vanishes for large R . As a consequence, there seems to be a loss of orientational order at $T^* = 1.2$ and beyond. The so-found melting temperatures are in coincidence with the temperatures corresponding to the step-like changes in the functions $\langle S_0^*(T^*) \rangle$, $\langle E_{\text{pot}}^*(T^*) \rangle$ (see Fig. 7.5) or the BOOPs (see Fig. 7.6).

This behavior leads us to define in the next section a corresponding line or *melting curve* that separates the ordered from the disordered phase when heating from the ordered phase.

7.4 Consequences of the Melting behavior

The melting curve, as announced above for $((Q^*)^2, P^*) = (2, 1)$, is presented in Fig. 7.8 for all considered aspect ratios κ . We point out that this line is just an estimate for the true, two-phase coexistence lines characterizing a first-order transition. For the latter, one would also expect the occurrence of hysteresis, that is, a delay in the phase transition depending on whether the system is heated up or cooled down from the low or high-temperature state. We further scrutinize this point in Appendix A.7.

Another interesting feature of the melting curve is that it exhibits some degree of symmetry in shape when exchanging κ and $1/\kappa$. Indeed, we would not expect full symmetry since the electrostatic properties in the cases κ and $1/\kappa$ are not equal [see bottom panels in Fig. 7.1(a)]. The curve further reflects that at large eccentricities the melting occurs at larger temperatures than for κ close to unity.

Given the large amount of numerical calculations required to construct the melting line in Fig. 7.8, which holds for one particular set of parameters $(P^*, (Q^*)^2)$, it would be clearly desirable to have a scaling relation which allows to easily obtain corresponding melting lines for other parameters. In Appendix A.5.2 we show that such a relation does indeed exist in the limit of *hard* particles. This relation states that the probability of a microscopic configuration of the many-particle system is invariant under the simultaneous transformations $Q^2 \rightarrow \mu \cdot Q^2$, $P \rightarrow \mu \cdot P$, $T \rightarrow \mu \cdot T$, with μ being a scaling factor. Here, we are considering soft particles [even though the repulsion exponent is rather large, see Eq. (7.3)].

We now discuss whether this rule can also be used, as an approximation, for the soft-core system. To test the scaling rule, we have repeated all simulations for the case $\mu = 2$, i.e. $((Q^*)^2, P^*) = (4, 2)$ with temperatures $T^* = 0.2, 0.4, \dots, 3.2$. The new melting curve for the latter parameter set is represented in Fig. 7.8 in the rescaled form as dashed line. We see that the new, rescaled melting curve is similar in shape but not in coincidence with the original curve. The new curve strictly lies above the reference curve which is an artefact of the stronger molecular overlaps leading to increased binding strength. Specifically, for all aspect ratios, we observe about three times higher cohesion energies for $((Q^*)^2, P^*) = (4, 2)$ at ground state. The factor 3 differs from the expected $\mu = 2$ value. In addition to the stronger overlaps, also the structural archetypes can differ at ground state. Especially at $\kappa = 1.38$, we

obtained a configuration exhibiting trihexagonal tiling at $((Q^*)^2, P^*) = (4, 2)$, whereas for $((Q^*)^2, P^*) = (2, 1)$ a T-configuration arises. That means the scaling law defined in Appendix A.5.2 does only give a rough approximation of the true result.

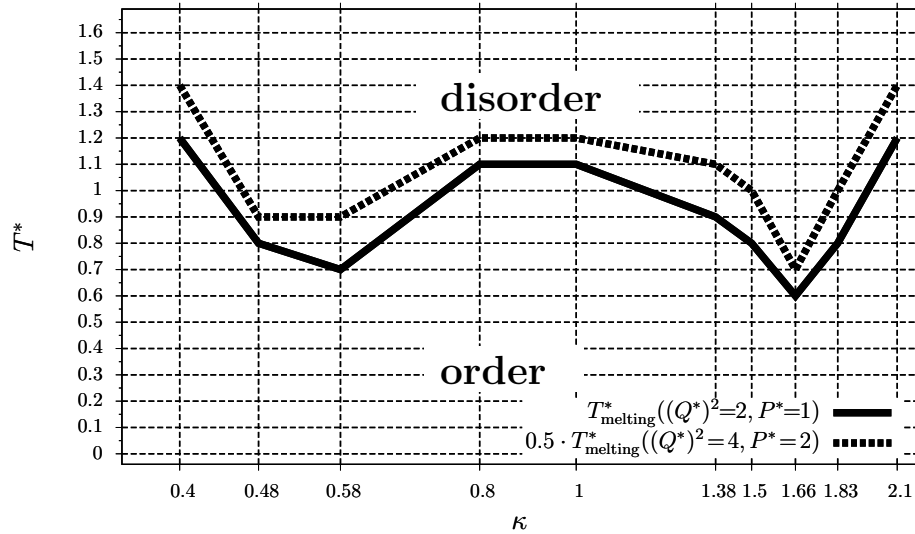


FIGURE 7.8: Melting curve $T^*_{\text{melting}}((Q^*)^2=2, P^*=1, \kappa)$ that separates the ordered phase (at low temperatures) from the disordered phase (at high temperatures) [solid line]. Additionally, a rescaled melting curve $0.5 \cdot T^*_{\text{melting}}((Q^*)^2=4, P^*=2, \kappa)$ is shown (dashed line). Points on the line are results that belong to the disordered regime.

Chapter 8

Conclusion and outlook

In this thesis, we have presented and discussed two main strategies to coarse-grain systems in equilibrium which comprise many molecules. We refer to them as bottom-up and top-down approach. These strategies were examined using a system of coronene molecules and a molecular monolayer system. We analyzed large amounts of data corresponding to the results from the coarse-graining approach, calculated through molecular dynamics simulations in various ensembles on the coarse-grained level of detail. Furthermore, we did detailed structural investigations on all levels of resolution. Our corresponding findings are published in [77–79].

The first major strategy - called bottom-up approach - deals with a systematic coarse-graining of an atomistic system composed of two coronene molecules as a prototype system. For this kind of system, we defined an effective pair potential and assumed pairwise additivity for the entire potential energy of the many-particle system. The fundamental principle of our coarse-graining method is based on a work of Kirkwood [98] from 1935 (see Sec. 4), who defined the potential of mean force. Here, we supplemented the standard coarse-graining procedure that is based on inter-molecular distances between the molecules [71, 111, 207, 210] with an additional angular dependence. We represent each molecule by its position and axial orientation, defined as the center of mass and the axis of the largest moment of inertia, respectively. The translational and rotational invariance of this dimer system further reduces the set of variables (Sec. 4.3.1). Coronene proved an ideal candidate for this study since its axially symmetric discotic shape, conserved over a rather large temperature range, can be approximated by uniaxial symmetry. For the underlying atomic interactions, we considered the generalized AMBER force field [208]. In order to qualitatively investigate the coarse-graining for a transparent set-up, we first neglected electrostatic interactions due to the complexity. The numerical interaction potential was then fitted to several interaction potentials based on the Berne-Pechukas [19] and Gay-Berne [63] potentials.

The probability of a coarse-grained configuration occurring in the canonical ensemble is related to the effective potential via a Boltzmann factor (see [176]). For the canonical sampling method, we used Langevin dynamics modified that enhanced the sampling rates for unlikely configurations where the molecules are largely separated. For this reason, we used the conventional umbrella sampling method (Sec. 4.4.2), where the bias potential is achieved through a spring acting between the molecules' centers of mass. We also calculated the effective pair potential using the steered dynamics

method (Sec. 4.4.4) and performed a qualitative comparison. All atomic simulations were performed by Karol Palczynki (Helmholtz-Zentrum Berlin) using GROMACS simulation packages [197]. We observed a strong temperature dependence for the pure distance-dependent effective potential. This was expected since the configuration space is still quite large, even for small inter-particle distances. So for high temperatures, non-attractive configurations become more likely (e.g., edge-edge configuration; see Table 5.1). By fixing the molecular degrees of freedom (i.e., centers of mass and the axial orientation), each molecule can only bend or the atomic positions smear out at high temperature. As expected, the temperature dependence is thus less pronounced. However, we still find a strong temperature dependence for planar configurations - which we interpret as due to the molecules' bending modes. In particular, higher temperatures lead to higher variances in the inter-molecular atom-atom distances. This means, that distances corresponding to a minimum in the Lennard-Jones potential between neighboring atoms of different molecules are less likely leading to an overall reduction in overall inter-molecular attraction.

In order to complete our investigation on the coronene molecule, we accounted for electrostatic interactions by using two different electrostatic approaches (see Sec. 5.4; [79]). One electrostatic approach is based on a linear point quadrupole [128], while the other is based on an extended charge distribution [143]. The latter takes into account effective interactions between ring-shaped charge distributions and is thus called the "charged-ring approach". The corresponding model is based on the same model potential as the one used for the van der Waals interaction (see Sec. 5.3.3; [78]). The only difference is in the parametrization. We dubbed this model the "implicit electrostatics model". In addition, in Chapter 6 we qualitatively compared both approaches using potential curves, unit cell parameters of the bulk crystal at room temperature and the temperature-driven crystal-isotropic phase transition. Based on our data, we can conclude that the simple point quadrupole approach (with various interaction strengths), despite yielding the correct long-range decay, gives unreliable results even when the quadrupole strength is reduced such that the corresponding bulk crystal has a reasonable cohesion energy. We observed melting temperatures in the herringbone-like crystal [160, 161] far above the experimental values at every tested quadrupole strength. Despite this drawback, a small point quadrupole stabilizes the herringbone structure due to an energetic preference. In contrast, the second electrostatic approach using the implicit electrostatics model can stabilize the herringbone structure up to a melting point similar to experimental values. With this second model, we also encountered a liquid phase as observed in the experiments. In conclusion, the implicit electrostatics model displays superior performance in reproducing structure and melting.

The next challenge was to include a surface for our system of organic molecules (see Chapter 7; [77]). Since this new system is quite complicated, especially due to the rather involved electrostatics introduced by the surface, we decided to propose a second strategy employing a top-down approach. Instead of defining effective potentials through systematic coarse-graining, we first introduced a simple model and scrutinized its phase behavior to see if it matched real systems. To keep the system simple, we only considered a monolayer of molecules with different aspect ratios, ranging from $\kappa = 0.4$ to $\kappa = 2.5$. The entire system was coupled to a pressure bath. The equilibrium

structures of this system were studied in their ground states and at finite temperatures. Each molecule is represented by an elliptical, purely-repulsive particle bearing a central, linear point quadrupole moment along one of the ellipse's main axis. The ground state structures, calculated by Dr. Moritz Antlanger (TU Wien), show parallel stacks of molecules and many different herringbone patterns, hexagonal, and quadratic T-configurations and even patterns with hexagonal tiling. The trend in the ground state structures for higher eccentricities seems to be to form row-like structures when the other parameters are held fixed. These ground state structures were used for finite temperature simulations at various temperatures, including the temperatures of the isotropic phase. During these finite temperature simulations, we observed no plastic phase during melting.

To sum up, these strategies seem promising and provide interesting insights into the performance of these fairly new methodologies. A major challenge in this work was generating a coarse-graining, MD simulation, and data evaluation package (with graphical output in real time) for all the ensembles and interactions considered for the sake of completeness.

We next want to propose possible topics for further research in this field of coarse-graining. Thus far, we have focused on two biased sampling modifications for the two-molecule simulations to overcome potential barriers: umbrella sampling [188, 189] and steered dynamics [83, 134]. In the following, we present several improvements for these methods. For both methods the inter-molecular orientation vector - defined through the connecting vector between the center of mass positions - was only constrained by length. Fixing the direction of this vector, however, would reduce the number of redundant configurations that result from simple rotations of the entire two-molecule system. In this context, one might also modify the umbrella sampling method, which in the current form suffers from needing a strong overlap in the umbrella windows (see Chapter 5.2.3). The best choice for a bias potential can be made if the effective potential is known. Adaptive umbrella sampling [127], where the underlying bias potential is iteratively changed in a single histogram method, is an improvement on this technique. The steered dynamics method can also be improved. We used a quasi-static steered dynamics method, i.e., one in which the molecules are pulled apart very slowly; however, this non-equilibrium sampling method can be expanded to calculate angle- and distance dependent effective pair potentials at higher pulling speeds, as shown by Park *et al.* [148], for pure distance-dependent problems. Returning to our effective potential, we have to account for its temperature dependence, as shown in Sec. 4.5. Using the underlying methodology for its calculation (see Chapter 4), it is possible to extend it towards a pressure-dependent potential as well. This would lead to more consistent results between atomic and coarse-grained models, but would introduce the pressure as an additional parameter for the effective potential.

Another field of further research would be to address the level of detail of the microscopic system from which we started our coarse-graining investigation. More specifically, in this study we coarse-grain atomic two-molecule systems based on atomic trajectory data. A further improvement could be achieved by using ab-initio [30, 120] simulation data directly. This technique, which combines molecular dynamics with

density functional theory, would avoid inaccuracies due to the mapping of the sub-atomic level of detail onto the atomic level of detail, from which we started our investigation (using atomic force-fields). Since this kind of simulations is rather slow, an advanced method for biasing the simulations should be used, as mentioned above. However, the improvement in coarse-grained simulations achieved through this extension might be less promising than taking into account interactions of three- or more molecules (see [53] for an estimate of energetic three-molecule contributions). Taking into account coarse-grained potentials involving three or more molecules may significantly improve the results, since a pairwise additive decomposition of the potential energy underestimates the many-particle (molecule) effect caused by molecular bending modes or polarization effects. In this work, much effort was spent finding and parametrizing interaction models which sufficiently described the numerically developed effective pair potentials from our systematic coarse-graining procedure. However, it might be interesting as well to use the numerical potentials (or its derivatives) directly, i.e. a tabularized effective pair potential. Future research could also investigate the way we treat interactions. In most cases, interactions are given in a functional form or in terms of tables. When considering higher-order molecule interactions, i.e., interactions of three or more molecules, our modeling strategy might be very challenging or even fail, because appropriate models for three- or more-molecule interactions have to be established or alternatively the tables describing the interactions get quite large. A coarse-grained solution for this challenge might be given through neural-network potentials [14, 74].

Other issues worth considering in more detail include ground states or minimal energy configurations of molecular clusters of various size at the atomic level of detail (for coronene, see [57]). A cluster analysis at finite temperature with replica exchange methods [183, 185] may provide more insights into models resembling real systems. Performing the same investigation for a coarse-grained system will additionally assess the quality of coarse-graining. As well as future investigations into cluster formation, bulk crystallization might provide an interesting avenue. The challenge here lies in the computational methods, so we recommend replica-exchange methods as well. For this kind of investigation, we suggest starting with small but periodic systems and using lattice sum rather than full Ewald-summation techniques [178] for the long-range interactions to minimize the computational and programming time when calculating initial results.

Returning to our monolayer study, where the particles can only rotate in the plane, the model could be extended to the case where the molecules' rotation is not restricted to a plane, in order to study colloidal layers swimming at a liquid-liquid or liquid-gas interface. A preliminary result is depicted in Fig. 8.1(a). In this context, the influence of external electric fields, especially time-dependent ones like rotating fields, may eventually switch between standing and lying states of the molecules.

Throughout our survey, we considered one-component systems. A next step might be to consider mixtures of molecules with different shapes or different electrostatic interactions. An initial suggestion would be to include particles with an inverted quadrupole which represent the same molecules but with different chemical functionalization. As the electrostatic interaction potential between equal particles does not depend on the sign of the quadrupole strength, interesting structural effects might

be detected when clusters of different species come into close contact. A preliminary survey involving a symmetric binary mixture is depicted and described in Fig. 8.1(b).

Including a static external electric field with a stripe-like pattern that couples to the linear point quadrupole, as proposed by Della-Sala *et al.* [43], may account for different surface profiles. A preliminary result for a pure 2D system is depicted in Fig. 8.1(c). We note that for this surface field, a Monte Carlo investigation for a para-sexiphenyl

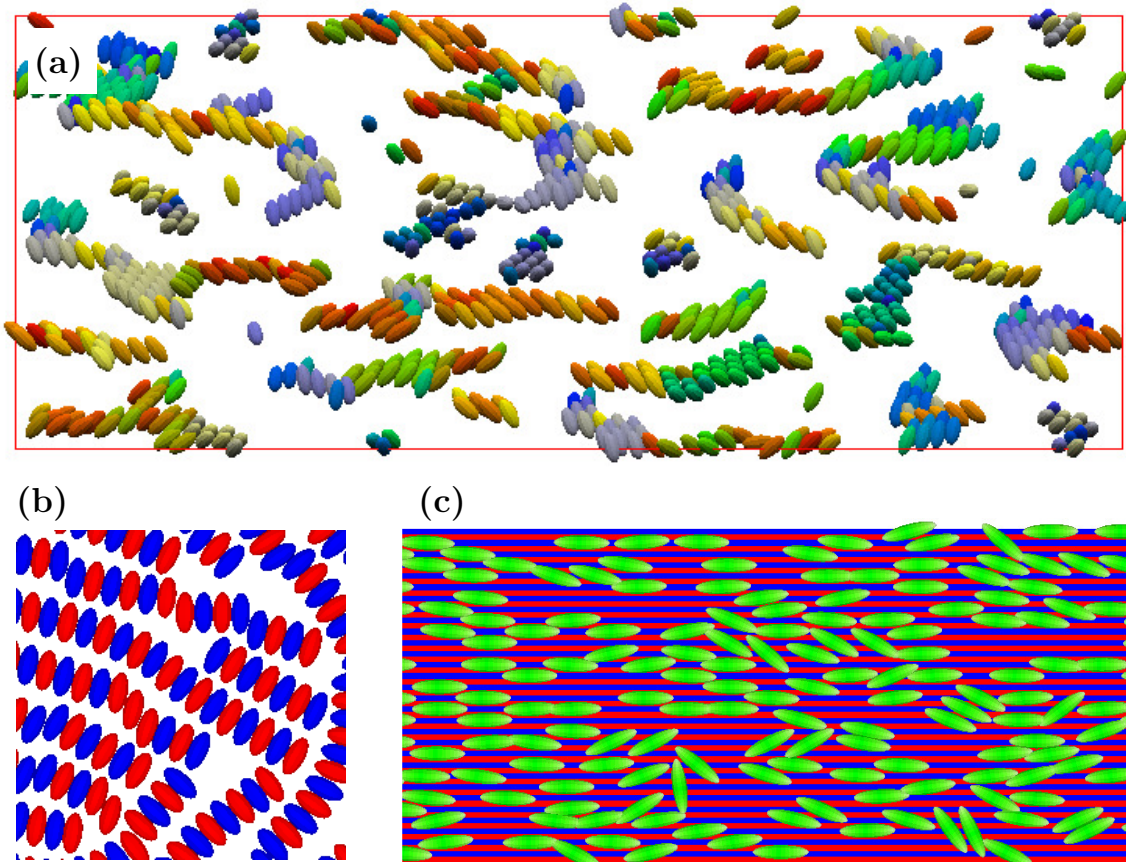


FIGURE 8.1: Annealing simulation results using the same setup and parameters as described in Chapter 7.3 (a) with full rotational degrees of freedom (forming a Langmuir-Blodgett film of rods with central linear quadrupole along the particle axis); (b) instead of single-component, a mixture of 50% of $Q^* = \sqrt{2}$ and 50% of $Q^* = -\sqrt{2}$. (c) Elongated soft ellipsoids with longitudinal linear quadrupole on an alternating electrostatic charged surface inspired by a study by Della Sala *et al.* [43].

model (incorporating a linear point quadrupole and free rotations) on a lattice has already been performed [99]. It is important to emphasize that we have focused on a special type of quadrupoles for the entire monolayer study, namely a linear quadrupole. Another fundamentally different and interesting quadrupole geometry is given by the square quadrupole, as investigated in [129] for three dimensional systems.

One reason to develop effective interactions is to possibly create phase diagrams at less computational cost. Alternatively, one could first investigate the phase diagram of small molecular systems composed of a few molecules at atomic detail. Using the phase behavior of these structures, it might then be interesting to focus on free energy

perturbation theories to systematically describe the phase diagram from a coarser perspective, i.e., with fewer parameters.

As mentioned earlier, one very interesting field of application for our equilibrium structures is optoelectronics. Understanding the alignment of organic molecules on inorganic surfaces that form hybrid inorganic/organic systems (HIOS) can help in the manufacture of efficient devices in this scientific field. In particular, organic solar cells [6, 69, 73, 137, 171, 174], organic field effect transistors (OFETs) [184, 190] or organic light emitting devices (OLEDs) [24, 38, 204] are promising fields of application. Calculating important features like charge-, hole-, or exciton-transfer from coarse-grained simulation data would greatly help optimize and tune these optoelectronic devices.

So far, all the mentioned applications involve quite small objects. However, our strategies could also be used to define effective interactions between cosmic objects like star clusters or even galaxies, provided relativistic effects are considered.

To summarize, our coarse-graining methods are quite important in order to understand and simulate macroscopic systems with only a few parameters. We think the strategies presented here can improve the current understanding of molecular ordering in 3D bulk systems and 2D monolayers. These findings are particularly important for new achievements in optoelectronics and colloidal science. These strategies and corresponding methodologies also contribute to the field of statistical and computational physics.

Appendices

A.1 Continuous phase transition

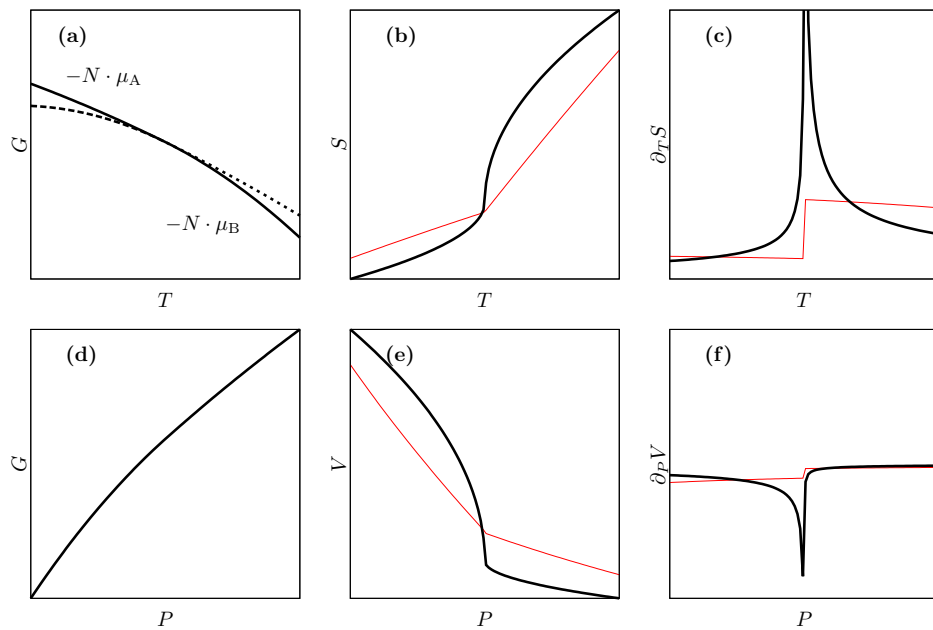


FIGURE A.2: Second order phase transition shown by means of (a) the free enthalpy G and (b) entropy S as a function of the temperature as well as (d) G and (e) the volume V as a function of the pressure. In (c) and (f) the second derivatives of the free enthalpy G with respect to temperature and pressure are shown. The red curves represent alternative characteristics.

A.2 First derivatives

We next provide explicit expressions for the pair force and torque for the modified Gay-Berne (mGB) (Sec. 5.3.3), linear quadrupole-quadrupole interaction (Sec. 5.4.3) and soft-repulsive ellipse interaction (Sec. 7.2). The Kabadi interaction (Sec. 5.3.2) is recovered from the mGB interaction when choosing $\theta = 0$ and $\xi = 0$ and can also be found in Ref. 65.

A.2.1 Modified Gay-Berne (mGB) interaction

Force pulling on particle A from particle B:

$$\mathbf{F}_{AB} = \nabla_{\mathbf{R}} U_{\text{mGB}} = 4(\nabla_{\mathbf{R}} \epsilon) \left[\left(\frac{1}{R^*} \right)^{12} - \left(\frac{1}{R^*} \right)^6 \right] + 4\epsilon \left[12 \left(\frac{1}{R^*} \right)^{11} - 6 \left(\frac{1}{R^*} \right)^5 \right] \nabla_{\mathbf{R}} \left(\frac{1}{R^*} \right) \quad (\text{A.1})$$

with

$$\nabla_{\mathbf{R}} \epsilon = \mu \epsilon_0 \epsilon_{\text{BP}}^{\nu} (\epsilon')^{\mu-1} \nabla_{\mathbf{R}} \epsilon' \quad (\text{A.2a})$$

$$\nabla_{\mathbf{R}} \epsilon' = -\frac{\chi'}{2} (\nabla_{\mathbf{R}} A'^+ \nabla_{\mathbf{R}} A'^-) + \theta \gamma' (A'^+ A'^-)^{\gamma'-1} \nabla_{\mathbf{R}} (A'^+ A'^-) \quad (\text{A.2b})$$

$$\nabla_{\mathbf{R}} A'^{\pm} = 2 \frac{\hat{\mathbf{u}}_A \hat{\mathbf{R}} \pm \hat{\mathbf{u}}_B \hat{\mathbf{R}}}{1 \pm \chi' \hat{\mathbf{u}}_A \hat{\mathbf{u}}_B} (\nabla_{\mathbf{R}}(\hat{\mathbf{u}}_A \hat{\mathbf{R}}) \pm \nabla_{\mathbf{R}}(\hat{\mathbf{u}}_B \hat{\mathbf{R}})) \quad (\text{A.2c})$$

$$\nabla_{\mathbf{R}}(\hat{\mathbf{u}}_{A/B} \hat{\mathbf{R}}) = \frac{1}{R} (\hat{\mathbf{u}}_{A/B} - (\hat{\mathbf{u}}_{A/B} \hat{\mathbf{R}}) \hat{\mathbf{R}}) \quad (\text{A.2d})$$

$$\nabla_{\mathbf{R}} \left(\frac{1}{R^*} \right) = \frac{d_w \sigma_0}{(R - \sigma + d_w \sigma_0)^2} (\nabla_{\mathbf{R}} \sigma - \hat{\mathbf{R}}) \quad (\text{A.2e})$$

$$\nabla_{\mathbf{R}} \sigma = -\frac{\sigma^3}{2\sigma_0^2} \left(-\frac{\chi}{2} (\nabla_{\mathbf{R}} A'^+ \nabla_{\mathbf{R}} A'^-) + \xi \mu (A^+ A^-)^{\mu-1} \nabla_{\mathbf{R}} (A^+ A^-) \right) \quad (\text{A.2f})$$

$$\nabla_{\mathbf{R}} A^{\pm} = 2 \frac{\hat{\mathbf{u}}_A \hat{\mathbf{R}} \pm \hat{\mathbf{u}}_B \hat{\mathbf{R}}}{1 \pm \chi \hat{\mathbf{u}}_A \hat{\mathbf{u}}_B} (\nabla_{\mathbf{R}}(\hat{\mathbf{u}}_A \hat{\mathbf{R}}) \pm \nabla_{\mathbf{R}}(\hat{\mathbf{u}}_B \hat{\mathbf{R}})) \quad (\text{A.2g})$$

Torque on particle A from particle B:

$$\mathbf{M} = -\hat{\mathbf{u}}_A \times \nabla_{\hat{\mathbf{u}}_A} U$$

$$\nabla_{\hat{\mathbf{u}}_A} U = 4(\nabla_{\hat{\mathbf{u}}_A} \epsilon) \left[\left(\frac{1}{R^*} \right)^{12} - \left(\frac{1}{R^*} \right)^6 \right] + 4\epsilon \left[12 \left(\frac{1}{R^*} \right)^{11} - 6 \left(\frac{1}{R^*} \right)^5 \right] \nabla_{\hat{\mathbf{u}}_A} \left(\frac{1}{R^*} \right) \quad (\text{A.3})$$

with

$$\nabla_{\hat{\mathbf{u}}_A} \epsilon = \epsilon_0 \left[\nu \epsilon_{\text{BP}}^{\nu-1} (\nabla_{\hat{\mathbf{u}}_A} \epsilon_{\text{BP}}) (\epsilon')^{\nu} + \mu \epsilon_{\text{BP}}^{\nu} (\epsilon')^{\mu-1} (\nabla_{\hat{\mathbf{u}}_A} \epsilon_{\text{BP}}) \right] \quad (\text{A.4a})$$

$$\nabla_{\hat{\mathbf{u}}_A} \epsilon' = -\frac{\chi'}{2} (\nabla_{\hat{\mathbf{u}}_A} A'^+ + \nabla_{\hat{\mathbf{u}}_A} A'^-) + \theta \gamma' (A'^+ A'^-)^{\gamma'-1} \nabla_{\hat{\mathbf{u}}_A} (A'^+ A'^-) + \xi \nabla_{\hat{\mathbf{u}}_A} K \quad (\text{A.4b})$$

$$\nabla_{\hat{\mathbf{u}}_A} A'^{\pm} = 2 \frac{\hat{\mathbf{u}}_A \hat{\mathbf{R}} \pm \hat{\mathbf{u}}_B \hat{\mathbf{R}}}{1 \pm \chi' \hat{\mathbf{u}}_A \hat{\mathbf{u}}_B} \hat{\mathbf{R}} \mp \left(\frac{\hat{\mathbf{u}}_A \hat{\mathbf{R}} \pm \hat{\mathbf{u}}_B \hat{\mathbf{R}}}{1 \pm \chi' \hat{\mathbf{u}}_A \hat{\mathbf{u}}_B} \right)^2 \chi' \hat{\mathbf{u}}_B \quad (\text{A.4c})$$

$$\nabla_{\hat{\mathbf{u}}_A} \epsilon_{\text{BP}} = \epsilon_{\text{BP}}^3 \chi^2 (\hat{\mathbf{u}}_A \hat{\mathbf{u}}_B) \hat{\mathbf{u}}_B \quad (\text{A.4d})$$

$$\begin{aligned} \nabla_{\hat{\mathbf{u}}_A} K &= -10(\hat{\mathbf{u}}_A \hat{\mathbf{R}}) (1 + 3(\hat{\mathbf{u}}_B \hat{\mathbf{R}})^2) \hat{\mathbf{R}} \\ &\quad + 4 \left((\hat{\mathbf{u}}_A \hat{\mathbf{u}}_B) - 5(\hat{\mathbf{u}}_A \hat{\mathbf{R}})(\hat{\mathbf{u}}_B \hat{\mathbf{R}}) \right) (\hat{\mathbf{u}}_B - 5(\hat{\mathbf{u}}_B \hat{\mathbf{R}}) \hat{\mathbf{R}}) \end{aligned} \quad (\text{A.4e})$$

$$\nabla \left(\frac{1}{R^*} \right) = \frac{d_w \sigma_0}{(R - \sigma + d_w \sigma_0)^2} \nabla_{\hat{\mathbf{u}}_A} \sigma \quad (\text{A.4f})$$

$$\nabla \sigma = -\frac{\sigma^3}{2\sigma_0^2} \left(-\frac{\chi}{2} (\nabla_{\hat{\mathbf{u}}_A} A^+ + \nabla_{\hat{\mathbf{u}}_A} A^-) + \xi \gamma (A^+ A^-)^{\gamma-1} \nabla_{\hat{\mathbf{u}}_A} (A^+ A^-) \right) \quad (\text{A.4g})$$

$$\nabla_{\hat{\mathbf{u}}_A} A^{\pm} = 2 \frac{\hat{\mathbf{u}}_A \hat{\mathbf{R}} \pm \hat{\mathbf{u}}_B \hat{\mathbf{R}}}{1 \pm \chi \hat{\mathbf{u}}_A \hat{\mathbf{u}}_B} \hat{\mathbf{R}} \mp \left(\frac{\hat{\mathbf{u}}_A \hat{\mathbf{R}} \pm \hat{\mathbf{u}}_B \hat{\mathbf{R}}}{1 \pm \chi \hat{\mathbf{u}}_A \hat{\mathbf{u}}_B} \right)^2 \chi \hat{\mathbf{u}}_B \quad (\text{A.4h})$$

A.2.2 Linear quadrupole-quadrupole (QQ) interaction

Force pulling on particle A from particle B:

$$\begin{aligned} \mathbf{F}_{\text{AB}} &= -\frac{15 Q^2}{4\pi R^6} K - \frac{3}{4\pi \epsilon_0 R^5} \left(10(\hat{\mathbf{u}}_A \hat{\mathbf{R}}) \nabla_{\mathbf{R}}(\hat{\mathbf{u}}_A \hat{\mathbf{R}}) + 10(\hat{\mathbf{u}}_B \hat{\mathbf{R}}) \nabla_{\mathbf{R}}(\hat{\mathbf{u}}_B \hat{\mathbf{R}}) \right) \\ &\quad - \frac{3}{4\pi \epsilon_0 R^5} \left((20(\hat{\mathbf{u}}_A \hat{\mathbf{u}}_B) - 70(\hat{\mathbf{u}}_A \hat{\mathbf{R}})(\hat{\mathbf{u}}_B \hat{\mathbf{R}})) \nabla_{\mathbf{R}}((\hat{\mathbf{u}}_A \hat{\mathbf{R}})(\hat{\mathbf{u}}_B \hat{\mathbf{R}})) \right) \end{aligned} \quad (\text{A.5})$$

with

$$\nabla_{\mathbf{R}}((\hat{\mathbf{u}}_A \hat{\mathbf{R}})(\hat{\mathbf{u}}_B \hat{\mathbf{R}})) = (\hat{\mathbf{u}}_A \hat{\mathbf{R}}) \nabla_{\mathbf{R}}(\hat{\mathbf{u}}_B \nabla_{\mathbf{R}} \hat{\mathbf{R}}) + (\hat{\mathbf{u}}_A \hat{\mathbf{R}}) (\hat{\mathbf{u}}_B \hat{\mathbf{R}}), \quad (\text{A.6})$$

where the remaining derivatives are determined through Eq. (A.2d). This leads to $\mathbf{F}_{\text{AB}} \propto \frac{1}{R^6}$.

Torque on particle A from particle B:

$$\mathbf{M}_{\text{AB}} = -\hat{\mathbf{u}}_A \times \frac{Q^2}{4\pi \epsilon_0 R^5} \nabla_{\hat{\mathbf{u}}_A} K \quad (\text{A.7})$$

The expression $\nabla_{\hat{\mathbf{u}}_A} K$ is given defined in Eq. (A.4e).

A.2.3 Soft repulsive ellipse interaction

Force pulling on particle A from particle B:

$$\mathbf{F}_{\text{AB}} = \nabla_{\mathbf{R}} U_{\text{sr}} = 4\epsilon \left[18 \left(\frac{1}{R^*} \right)^{17} \right] \nabla_{\mathbf{R}} \left(\frac{1}{R^*} \right) \quad (\text{A.8})$$

The expression $\nabla_{\mathbf{R}} \left(\frac{1}{R^*} \right)$ can be taken from Eqs. (A.2e)–(A.2g) when choosing $\epsilon = 0$.

Torque on particle A from particle B:

$$\begin{aligned} \mathbf{M} &= -\hat{\mathbf{u}}_A \times \nabla_{\hat{\mathbf{u}}_A} U_{\text{sr}} \\ \nabla_{\hat{\mathbf{u}}_A} U &= 4\epsilon \left[18 \left(\frac{1}{R^*} \right)^{17} \right] \nabla_{\hat{\mathbf{u}}_A} \left(\frac{1}{R^*} \right) \end{aligned} \quad (\text{A.9})$$

The expression $\nabla_{\hat{\mathbf{u}}_A} \left(\frac{1}{R^*} \right)$ can be taken from Eqs. (A.4f)–(A.4h) when choosing $\epsilon = 0$.

A.3 Parametrizations

The following tables summarize the parameters used to fit the effective potentials according to models K1, K2, M and the implicit electrostatic model for different temperatures T . The fit parameters stem from SD and US simulation results, as described in Sec. 5.3, for 300 K, 800 K, and 1500 K. For the temperatures in-between we interpolated potential minima and contact distances to receive the fit parameters.

TABLE A.1: Model K1

T (K)	κ	κ'	μ	ν	σ_0 (nm)	ϵ_0 (kJ/mol)	d_w
300	0.2885	0.1554	1	1	1.0529	7.7633	0.3884
400	0.2892	0.1462	1	1	1.0603	7.1782	0.3869
500	0.2899	0.1372	1	1	1.0678	6.6170	0.3854
600	0.2905	0.1284	1	1	1.0752	6.0790	0.3839
700	0.2912	0.1197	1	1	1.0826	5.5635	0.3825
800	0.2919	0.1112	1	1	1.0900	5.0699	0.3811
900	0.2916	0.1116	1	1	1.0906	5.0081	0.3901
1000	0.2914	0.1121	1	1	1.0912	4.9462	0.3992
1100	0.2911	0.1125	1	1	1.0918	4.8843	0.4082
1200	0.2909	0.1130	1	1	1.0925	4.8225	0.4172
1300	0.2907	0.1135	1	1	1.0931	4.7608	0.4262
1400	0.2904	0.1140	1	1	1.0937	4.6990	0.4352
1500	0.2902	0.1145	1	1	1.0943	4.6373	0.4442

TABLE A.2: Model K2

T (K)	κ	κ'	μ	ν	σ_0 (nm)	ϵ_0 (kJ/mol)	d_w
300	0.2885	0.0530	1	1	1.0529	2.6836	0.3884
400	0.2892	0.0518	1	1	1.0603	2.5722	0.3869
500	0.2899	0.0504	1	1	1.0678	2.4602	0.3854
600	0.2905	0.0491	1	1	1.0752	2.3476	0.3839
700	0.2912	0.0476	1	1	1.0826	2.2345	0.3825
800	0.2919	0.0461	1	1	1.0900	2.1209	0.3811
900	0.2916	0.0459	1	1	1.0906	2.0748	0.3901
1000	0.2914	0.0456	1	1	1.0912	2.0288	0.3992
1100	0.2911	0.0453	1	1	1.0918	1.9828	0.4082
1200	0.2909	0.0450	1	1	1.0925	1.9369	0.4172
1300	0.2907	0.0447	1	1	1.0931	1.8911	0.4262
1400	0.2904	0.0444	1	1	1.0937	1.8453	0.4352
1500	0.2902	0.0440	1	1	1.0943	1.7996	0.4442

TABLE A.3: Model M

T (K)	κ	χ'	μ	ν	σ_0 (nm)	ϵ_0 (kJ/mol)	d_w	γ	γ'	θ	ξ
300	0.2885	-0.7895	1	1	1.0529	6.5481	0.3884	4	4	0.1592	-0.1967
400	0.2892	-0.7916	1	1	1.0603	6.3553	0.3869	4	4	0.2019	-0.1984
500	0.2899	-0.7939	1	1	1.0678	6.1614	0.3854	4	4	0.2478	-0.2002
600	0.2905	-0.7962	1	1	1.0752	5.9666	0.3839	4	4	0.2971	-0.2022
700	0.2912	-0.7986	1	1	1.0826	5.7707	0.3825	4	4	0.3503	-0.2043
800	0.2919	-0.8012	1	1	1.0900	5.5739	0.3811	4	4	0.4078	-0.2065
900	0.2916	-0.8024	1	1	1.0906	5.4425	0.3901	4	4	0.4426	-0.2063
1000	0.2914	-0.8037	1	1	1.0912	5.3113	0.3992	4	4	0.4790	-0.2060
1100	0.2911	-0.8051	1	1	1.0918	5.1802	0.4082	4	4	0.5171	-0.2057
1200	0.2909	-0.8064	1	1	1.0925	5.0494	0.4172	4	4	0.5571	-0.2055
1300	0.2907	-0.8079	1	1	1.0931	4.9187	0.4262	4	4	0.5991	-0.2052
1400	0.2904	-0.8094	1	1	1.0937	4.7882	0.4352	4	4	0.6434	-0.2049
1500	0.2902	-0.8109	1	1	1.0943	4.6579	0.4442	4	4	0.6900	-0.2046

TABLE A.4: Implicit electrostatics model

$T(\text{K})$	κ	χ'	μ	ν	$\sigma_0(\text{nm})$	$\epsilon_0(\text{kJ/mol})$	d_w	γ	γ'	θ	ξ
300	0.2856	-0.7639	1	1	1.1026	5.3125	0.3440	4	4	1.4825	-0.3123
400	0.2867	-0.7635	1	1	1.1088	5.2244	0.3406	4	4	1.5003	0.3120
500	0.2877	-0.7631	1	1	1.1149	5.1354	0.3373	4	4	1.5196	-0.3117
600	0.2888	-0.7627	1	1	1.1211	5.0456	0.3340	4	4	1.5403	-0.3114
700	0.2898	-0.7623	1	1	1.1273	4.9548	0.3307	4	4	1.5626	-0.3111
800	0.2909	-0.7618	1	1	1.1335	4.8633	0.3275	4	4	1.5865	-0.3107
900	0.2905	-0.7622	1	1	1.1362	4.7541	0.3378	4	4	1.6406	-0.3111
1000	0.2902	-0.7626	1	1	1.1390	4.6452	0.3480	4	4	1.6969	-0.3115
1100	0.2899	-0.7631	1	1	1.1418	4.5365	0.3582	4	4	1.7558	-0.3119
1200	0.2896	-0.7635	1	1	1.1446	4.4280	0.3683	4	4	1.8173	-0.3123
1300	0.2892	-0.7639	1	1	1.1474	4.3197	0.3784	4	4	1.8816	-0.3127
1400	0.2889	-0.7644	1	1	1.1501	4.2117	0.3885	4	4	1.9491	-0.3132
1500	0.2886	-0.7649	1	1	1.1529	4.1038	0.3984	4	4	2.0198	-0.3137

A.4 Enthalpy and order parameter curves for the monolayer system at ground state

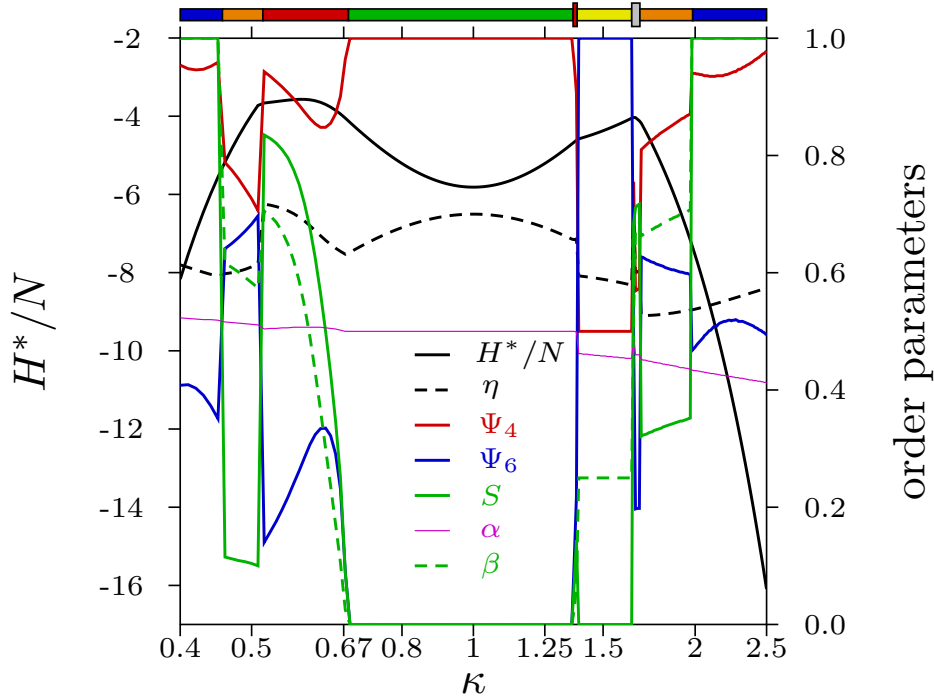


FIGURE A.3: Reduced enthalpy per particle (H^*/N ; left vertical axis) as well as filling fraction η and different order parameters (for their definitions see Sec. 2.7.2) of the observed ground state configurations (right vertical axis) as functions of κ (as labeled) for $(Q^*)^2 = 2$ and $P^* = 1$. Note the logarithmic scale along the κ -axis. The horizontal bar above the panel specifies the κ -range where the respective ordered structural archetype is the energetically most favorable one via the following color code: T-configurations with quadratic bond order (green), closed herringbone pattern (red), loose packed herringbone pattern (orange), parallel displaced configurations (blue), pattern with trihexagonal tiling (yellow), branched configurations (gray). Corresponding snapshots can be found in the first column of Fig. 7.3 and 7.4. The curves were determined by Moritz Antlinger (TU Wien).

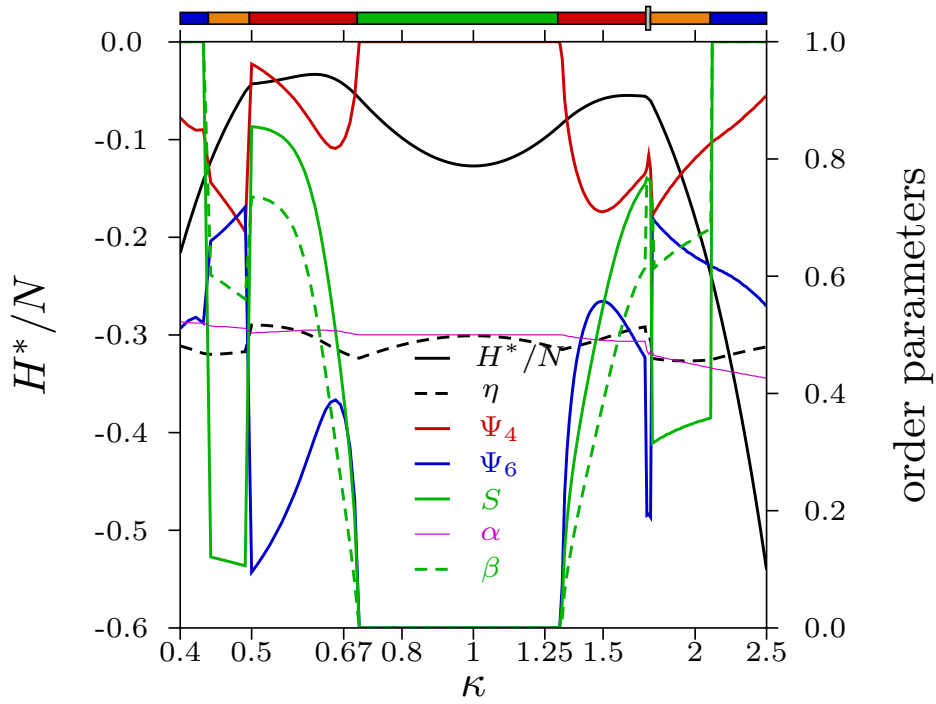


FIGURE A.4: Same as Figure A.3, now for $(Q^*)^2 = 0.2$ and $P^* = 0.1$.

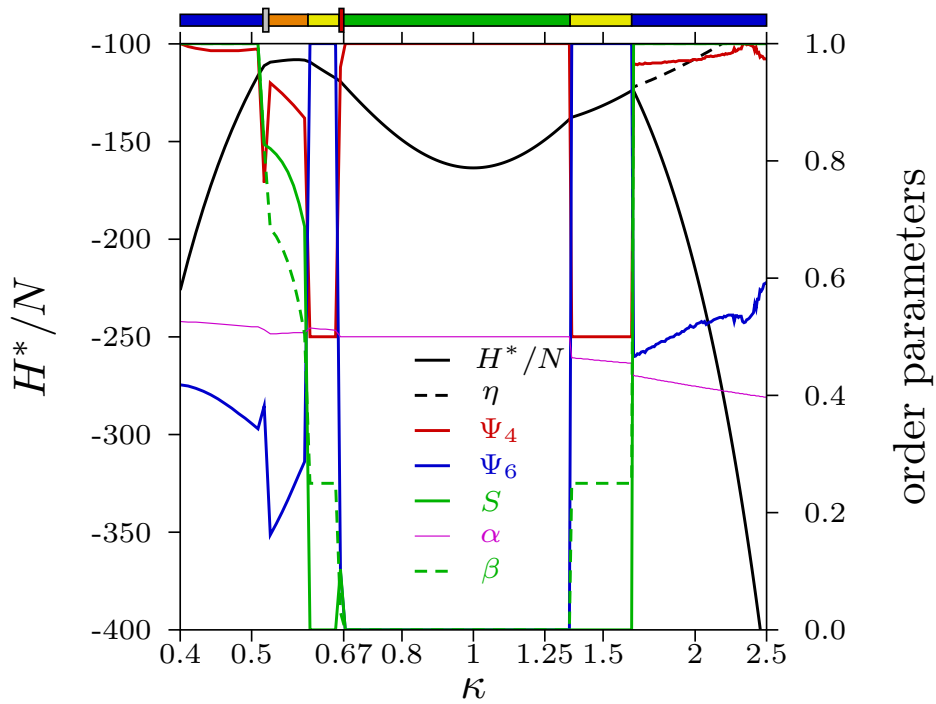


FIGURE A.5: Same as Figure A.3, now for $(Q^*)^2 = 20$ and $P^* = 10$.

A.5 Reduction of parameter space for hard particles

The goal of the present section is to derive scaling relations for the system presented in Chapter 7 with its system parameters Q^2 (quadrupole moment) and P (pressure) such that the equilibrium configuration of the many-particle system remains unchanged. To this end we here present a simplified version of our interaction potential, that is, the *quadrupolar hard-ellipse* (QHE) model defined by

$$V_{\text{QHE}}(Q^2, \mathbf{r}_{ij}, \hat{\mathbf{u}}_i, \hat{\mathbf{u}}_j) = \begin{cases} V_{\text{r}}(Q^2, \mathbf{r}_{ij}, \hat{\mathbf{u}}_i, \hat{\mathbf{u}}_j) & , \mathbf{r}_{ij} > \sigma(\mathbf{r}_{ij}, \hat{\mathbf{u}}_i, \hat{\mathbf{u}}_j) \\ \infty & , \text{else.} \end{cases} \quad (\text{A.10})$$

Contrary to our original model [see Sec. 7.2], the QHE model consists of infinitely hard ellipsoidal particles, whereas the quadrupole part of the interaction, Eq. (7.5), is identical to our original model. The potential energy E_{pot} of a specific configuration within the QHE model is defined through

$$E_{\text{pot}}(Q^2, \mathbf{r}_{ij}, \hat{\mathbf{u}}_i, \hat{\mathbf{u}}_j) = \sum_{i < j} V_{\text{QHE}}(Q^2, \mathbf{r}^N, \hat{\mathbf{u}}^N), \quad (\text{A.11})$$

where $\mathbf{r}^N = (\mathbf{r}_1, \dots, \mathbf{r}_N)$ and $\hat{\mathbf{u}}^N = (\hat{\mathbf{u}}_1, \dots, \hat{\mathbf{u}}_N)$ specify the microscopic configuration.

A.5.1 Ground state

In a non-degenerate ground state, the particles are positioned and oriented such that the enthalpy, H , is minimal, that is

$$H = \min_{S_0, \mathbf{r}^N, \hat{\mathbf{u}}^N} (E_{\text{pot}}(Q^2, \mathbf{r}^N, \hat{\mathbf{u}}^N) + P S_0). \quad (\text{A.12})$$

The scaling of the interaction potential Eq. (A.10) with the quadrupole strength Q^2 results in a scaling of the entire potential energy, Eq. (A.11), i.e. $E_{\text{pot}}(\mu \cdot Q^2) = \mu \cdot E_{\text{pot}}(Q^2)$. We also note that the enthalpy H is a linear combination of E_{pot} and P . Therefore, when replacing Q^2 by $\mu \cdot Q^2$, Eq. (A.12) yields the same ground state only if the pressure is scaled with μ as well. We can thus conclude that the ground state configuration $(S_0^{\text{GS}}, \mathbf{r}_{\text{GS}}^N, \hat{\mathbf{u}}_{\text{GS}}^N)$ is invariant under the transformations $P \rightarrow \mu \cdot P$ and $Q^2 \rightarrow \mu \cdot Q^2$ for hard particles.

A.5.2 Finite temperatures

We next consider the QHE system at $T > 0$. The probability of a microscopic configuration in the (N, P, T) ensemble is given by

$$\rho(S_0, \mathbf{r}^N, \hat{\mathbf{u}}^N) dS_0 d\mathbf{r}^N d\hat{\mathbf{u}}^N = \frac{e^{-(k_{\text{B}}T)^{-1}(E_{\text{pot}}(Q^2, \mathbf{r}^N, \hat{\mathbf{u}}^N) + P \cdot S_0)}}{Z_{\text{conf}}} dS_0 d\mathbf{r}^N d\hat{\mathbf{u}}^N, \quad (\text{A.13})$$

where Z_{conf} is the corresponding configuration integral. It is obvious that Eq. (A.13) is invariant under the transformations $E_{\text{pot}} \rightarrow \mu \cdot E_{\text{pot}}$, $P \rightarrow \mu \cdot P$, and $T \rightarrow \mu T$. From Eq. (7.5) and (A.11) we know that the potential energy for non-overlapping particles

in the hard-body limit is proportional to Q^2 , i.e.,

$$E_{\text{pot}} = \sum_{i < j} V_{\text{QHE}}(\mathbf{r}_{ij}, \hat{\mathbf{u}}_i, \hat{\mathbf{u}}_j) \propto Q^2. \quad (\text{A.14})$$

Thus we have the simple law: $Q^2 \rightarrow \mu \cdot Q^2$, $P \rightarrow \mu \cdot P$, $T \rightarrow \mu \cdot T$.

In particular, given the size of the molecule σ_{new} , its aspect ratio κ and the quadrupole strength Q_{new}^2 , it is thus possible to estimate the order-disorder transition temperature for a monolayer system. Therefore, we first calculate the reduced quadrupole strength

$$(Q_{\text{new}}^*)^2 = Q_{\text{new}}^2 / (4\pi\epsilon_{\text{pm}} \cdot \sigma_{\text{new}}^5 \epsilon_0).$$

The proportionality factor

$$\mu = (Q_{\text{new}}^*/Q^*)^2 \xrightarrow{(Q^*)^2=2} 0.5 \cdot (Q_{\text{new}}^*)^2$$

then determines the order-disorder temperature according to $T_{\text{melting,new}}^* = \mu \cdot T_{\text{melting}}^*$ at a pressure $P_{\text{new}}^* = \mu \cdot P^* \xrightarrow{P^*=1} \mu$.

A.6 Applicability of parameter scaling for non-hard particles at ground state

We now explore to which extent we can apply the parameter scaling relations derived for the QHE system in Appendix A.5 to the actual, soft-particle system investigated in the main part of this work (see Sec. 7.2).

The total potential energy for a specific configuration of soft quadrupolar ellipsoids is defined through

$$E_{\text{pot}}(Q^2, \mathbf{r}^N, \hat{\mathbf{u}}^N) = \sum_{i < j} V_{\text{sr}}(\mathbf{r}_{ij}, \hat{\mathbf{u}}_i, \hat{\mathbf{u}}_j) + V_{\text{lr}}(\mathbf{r}_{ij}, \hat{\mathbf{u}}_i, \hat{\mathbf{u}}_j). \quad (\text{A.15})$$

As pointed out in the discussion of the ground states (see Sec. 7.3), the order parameters as functions of κ reveal strong similarities when one compares the parameter sets $((Q^*)^2, P^*) = (0.2, 0.1)$ and $((Q^*)^2, P^*) = (20, 10)$. This suggests that the soft-particle system fulfills, at $T = 0$, a similar scaling relation as the QHE system. However, the corresponding enthalpy curves match only in terms of shape, not in terms of magnitude. We thus introduce a phenomenological correction to the simple scaling of the enthalpy as described in Appendix A.5.1. Specifically, we assume that a scaling of P and Q^2 with a factor μ results in a small rescaling of the ground state coordinates, i.e. $\mathbf{r}_i \rightarrow \gamma \mathbf{r}_i$, where the rescaling factor γ is close to unity. We further assume that, when going from one ground state with parameters (Q^2, P) to a new ground state with $(\mu \cdot Q^2, \mu \cdot P)$, the rescaling factor γ is related to the change in density according to

$$\gamma = \sqrt{\frac{\eta}{\eta_{\text{new}}}}. \quad (\text{A.16})$$

Accordingly, the ground state cell volume is scaled with γ^2 . Regarding the total potential energy, we assume that its scaling with respect to Q^2 and the positions is the same as in the QHE system [see Eqs. (A.11), (A.10) and (7.5)], yielding

$$E_{\text{pot,new}}^{\text{GS}}(\mu \cdot Q^2, \gamma \cdot \mathbf{r}_{ij}, \hat{\mathbf{u}}_i, \hat{\mathbf{u}}_j) \approx \frac{\mu}{\gamma^5} E_{\text{pot}}^{\text{GS}}(Q^2, \mathbf{r}_{ij}, \hat{\mathbf{u}}_i, \hat{\mathbf{u}}_j). \quad (\text{A.17})$$

Taken altogether we obtain the following approximation for the enthalpy:

$$H_{\text{new}} \approx \frac{\mu}{\gamma^5} E_{\text{pot}}^{\text{GS}}(Q^2) + \mu \cdot P \gamma^2 S_0^{\text{GS}} = \frac{\mu}{\gamma^5} H + \mu \cdot \left[\gamma^2 - \frac{1}{\gamma^5} \right] \cdot P S_0^{\text{GS}}. \quad (\text{A.18})$$

To check this phenomenological scaling rule we calculate, as an example, new enthalpies from the enthalpies obtained at $(Q^*)^2 = 0.2$, $P^* = 0.1$ and $(Q^*)^2 = 20$, $P^* = 10$. Corresponding curves are presented in Fig. A.6. We can conclude that Eq. (A.18)

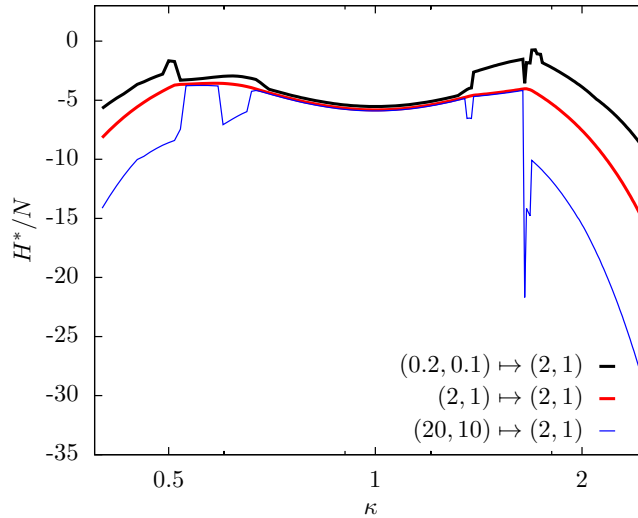


FIGURE A.6: Enthalpy curves mapped to the enthalpy with parameters $((Q^*)^2, P^*) = (2, 1)$ according to Eq. (A.18).

seems applicable for κ around unity where the structures possess a 4-fold symmetry (T-configuration). Larger deviations of the mapped enthalpies with the reference values occur for particles with high eccentricity.

A.7 Annealing results for the monolayer system

Finally and for the sake of completeness, we now turn to the investigation of the phase transition in the opposite direction in our monolayer system. The question is whether the ground state structures can at least locally be reproduced with molecular dynamics simulations starting from larger temperatures. To check this, we performed cooling simulations for each κ -value where the systems are initialized with random particle positions and orientations. The initial pressure and temperature are set to $P^* = 10$ and $T^* = 5$, respectively. The initial box-shape is quadratic with a side length of $50\sigma_0$. Within the first 200 000 steps we linearly decrease pressure and temperature down

to $P^* = 1$ and $T^* = 0.1$, respectively. The total number of steps is set to 410 000. Remaining simulation parameters are adopted from Sec. 7.3.

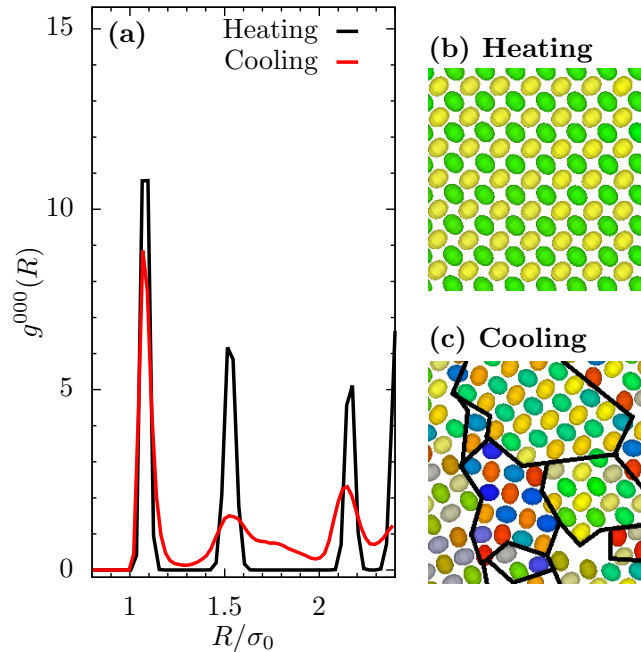


FIGURE A.7: (a) Radial distribution function for a system with $\kappa = 0.8$ at temperature $T^* = 0.1$ after a (b) melting and (c) cooling procedure. For the color code of the snapshots see Figs. 7.3 and 7.4.

It turned out that obtaining the calculated ground state configurations via simulated annealing is successful only for very few parameter points. In general, the calculations are plagued by frustration effects, especially for κ far from unity, where particles have difficulties to rotate. As an example we consider the radial distribution function g^{000} for $\kappa = 0.8$ (i.e., κ is close to unity) as depicted in Fig. A.7(a). We observe a coincidence in the peak positions of g^{000} , but not in their heights. We interpret this deviation as an artefact of the crystallite structure appearing after cooling (see Fig. A.7(b) and (c)). This might be a consequence of the lack of long-range order in 2D systems.

Bibliography

- [1] Atomic position data was provided by Karol Palczynski, who performed all atomistically-resolved simulations.
- [2] *Gromacs 4.5.4 Manual*: <http://www.gromacs.org/Documentation/Manual>.
- [3] M. P. Allen and D. J. Tildesley. *Computer Simulation of Liquids (Oxford Science Publications)*. Oxford science publications. Oxford University Press, reprint edition, 1989.
- [4] R. Anandakrishnan, C. Baker, S. Izadi, and A. V. Onufriev. Point charges optimally placed to represent the multipole expansion of charge distributions. *PLoS ONE*, 8(7):e67715, 2013.
- [5] D. Andrienko, V. Marcon, and K. Kremer. Atomistic simulation of structure and dynamics of columnar phases of hexabenzocoronene derivatives. *J. Chem. Phys.*, 125(12):124902, 2006.
- [6] A. Arias, J. MacKenzie, R. Stevenson, J. Halls, M. Inbasekaran, E. Woo, D. Richards, and R. Friend. Photovoltaic performance and morphology of polyfluorene blends: a combined microscopic and photovoltaic investigation. *Macromolecules*, 34(17):6005–6013, 2001.
- [7] M. Babadi, R. Everaers, and M. R. Ejtehadi. Coarse-grained interaction potentials for anisotropic molecules. *J. Chem. Phys.*, 124(17):174708, 2006.
- [8] T. Baştuğ, P.-C. Chen, S. M. Patra, and S. Kuyucak. Potential of mean force calculations of ligand binding to ion channels from Jarzynski’s equality and umbrella sampling. *J. Chem. Phys.*, 128(15):–, 2008.
- [9] J. Baschnagel, K. Binder, W. Paul, M. Laso, U. W. Suter, I. Batoulis, W. Jilge, and T. Bürger. On the construction of coarse-grained models for linear flexible polymer chains: Distribution functions for groups of consecutive monomers. *J. Chem. Phys.*, 95(8):6014–6025, 1991.
- [10] M. A. Bates and D. Frenkel. Phase behavior of two-dimensional hard rod fluids. *J. Chem. Phys.*, 112(22):10034–10041, 2000.
- [11] M. A. Bates and G. R. Luckhurst. Computer simulation studies of anisotropic systems xxix. quadrupolar gay-berne discs and chemically induced liquid crystal phases. *Liq. Cryst.*, 24(2):229–241, 1998.

- [12] G. Bautista-Carbajal and G. Odriozola. Phase diagram of two-dimensional hard ellipses. *J. Chem. Phys.*, 140(20):204502, 2014.
- [13] A. D. Becke. Density-functional exchange-energy approximation with correct asymptotic behavior. *Phys. Rev., A*, 38(6):3098–3100, 1988.
- [14] J. Behler. Neural network potential-energy surfaces in chemistry: a tool for large-scale simulations. *Phys. Chem. Chem. Phys.*, 13:17930–17955, 2011.
- [15] W. F. D. Bennett, J. L. MacCallum, M. J. Hinner, S. J. Marrink, and D. P. Tieleman. Molecular view of cholesterol flip-flop and chemical potential in different membrane environments. *J. Am. Chem. Soc.*, 131(35):12714–12720, 2009.
- [16] S. V. Bennun, M. I. Hoopes, C. Xing, and R. Faller. Coarse-grained modeling of lipids. *Chem. Phys. Lipids*, 159(2):59–66, 2009.
- [17] H. J. C. Berendsen, J. P. M. Postma, W. F. van Gunsteren, A. DiNola, and J. R. Haak. Molecular dynamics with coupling to an external bath. *J. Chem. Phys.*, 81(8):3684–3690, 1984.
- [18] M. Bernabei, P. Bacova, A. J. Moreno, A. Narros, and C. N. Likos. Fluids of semiflexible ring polymers: effective potentials and clustering. *Soft Matter*, 9:1287–1300, 2013.
- [19] B. J. Berne and P. Pechukas. Gaussian model potentials for molecular interactions. *J. Chem. Phys.*, 56(8):4213–4216, 1972.
- [20] E. Bianchi, C. N. Likos, and G. Kahl. Self-assembly of heterogeneously charged particles under confinement. *ACS Nano*, 7(5):4657–4667, 2013.
- [21] S. Blumstengel, H. Glowatzki, S. Sadofev, N. Koch, S. Kowarik, J. P. Rabe, and F. Henneberger. Band-offset engineering in organic/inorganic semiconductor hybrid structures. *Phys. Chem. Chem. Phys.*, 12(37):11642–11646, 2010.
- [22] S. Blumstengel, S. Sadofev, and F. Henneberger. Electronic coupling of optical excitations in organic/inorganic semiconductor hybrid structures. *New J. Phys.*, 10(6):065010, 2008.
- [23] E. M. Boczko and C. L. Brooks. Constant-temperature free energy surfaces for physical and chemical processes. *J. Phys. Chem.*, 97(17):4509–4513, 1993.
- [24] P. Boher, T. Leroux, V. Collomb-Patton, and T. Bignon. Optical characterization of oled displays. *J. Soc. Inf. Disp.*, 2015. <http://dx.doi.org/10.1002/jsid.369>.
- [25] M. Born and R. Oppenheimer. Zur Quantentheorie der Molekeln. *Ann. Phys. (Berlin)*, 389(20):457–484, 1927.
- [26] T. Boublik. Perturbation theory of pure quadrupolar hard gaussian overlap fluids. *Mol. Phys.*, 69(3):497–505, 1990.

- [27] D. Brown and J. Clarke. A loose-coupling, constant-pressure, molecular dynamics algorithm for use in the modelling of polymer materials. *Comput. Phys. Commun.*, 62(2):360–369, 1991.
- [28] N.-V. Buchete, J. E. Straub, and D. Thirumalai. Orientational potentials extracted from protein structures improve native fold recognition. *Protein Sci.*, 13(4):862–874, 2004.
- [29] G. Bussi, D. Donadio, and M. Parrinello. Canonical sampling through velocity rescaling. *J. Chem. Phys.*, 126(1):014101, 2007.
- [30] R. Car and M. Parrinello. Unified approach for molecular dynamics and density-functional theory. *Phys. Rev. Lett.*, 55:2471–2474, 1985.
- [31] E. Carter, G. Ciccotti, J. T. Hynes, and R. Kapral. Constrained reaction coordinate dynamics for the simulation of rare events. *Chem. Phys. Lett.*, 156(5):472–477, 1989.
- [32] A. Cheng and K. M. Merz. The pressure and pressure tensor for macromolecular systems. *J. Phys. Chem.*, 100(2):905–908, 1996.
- [33] J. D. Chodera, W. C. Swope, J. W. Pitera, C. Seok, and K. A. Dill. Use of the weighted histogram analysis method for the analysis of simulated and parallel tempering simulations. *J. Chem. Theory Comput.*, 3(1):26–41, 2007.
- [34] J. A. Cuesta and D. Frenkel. Monte Carlo simulation of two-dimensional hard ellipses. *Phys. Rev., A*, 42(4):2126–2136, 1990.
- [35] J. A. Cuesta, C. F. Tejero, and M. Baus. Isotropic-nematic transition of hard ellipses. *Phys. Rev., A*, 39(12):6498–6506, 1989.
- [36] K. Cui, O. Ivasenko, K. S. Mali, D. Wu, X. Feng, K. Mullen, S. De Feyter, and S. F. L. Mertens. Potential-driven molecular tiling of a charged polycyclic aromatic compound. *Chem. Commun.*, 50:10376–10378, 2014.
- [37] K. Cui, K. S. Mali, O. Ivasenko, D. Wu, X. Feng, M. Walter, K. Müllen, S. De Feyter, and S. F. L. Mertens. Squeezing, then stacking: From breathing pores to three-dimensional ionic self-assembly under electrochemical control. *Angew. Chem. Int. Ed.*, 53(47):12951–12954, 2014.
- [38] B. D’Andrade and S. Forrest. White organic light-emitting devices for solid-state lighting. *Adv. Mater.*, 16(18):1585–1595, 2004.
- [39] L. X. Dang and B. M. Pettitt. Chloride ion pairs in water. *J. Am. Chem. Soc.*, 109(18):5531–5532, 1987.
- [40] E. Darve and A. Pohorille. Calculating free energies using average force. *J. Chem. Phys.*, 115(20):9169–9183, 2001.
- [41] J. Dautenhahn and C. K. Hall. Monte carlo simulation of off-lattice polymer chains: effective pair potentials in dilute solution. *Macromolecules*, 27(19):5399–5412, 1994.

- [42] F. de J. Guevara-Rodríguez and G. Odriozola. Hard ellipsoids: Analytically approaching the exact overlap distance. *J. Chem. Phys.*, 135(8):084508, 2011.
- [43] F. Della Sala, S. Blumstengel, and F. Henneberger. Electrostatic-Field-Driven Alignment of Organic Oligomers on ZnO Surfaces. *Phys. Rev. Lett.*, 107(14):146401, 2011.
- [44] P. Derreumaux and N. Mousseau. Coarse-grained protein molecular dynamics simulations. *J. Chem. Phys.*, 126(2):025101, 2007.
- [45] M. Dijkstra, J. P. Hansen, and P. Madden. Gelation of a clay colloid suspension. *Phys. Rev. Lett.*, 75:2236–2239, 1995.
- [46] C. Draxl, D. Nabok, and K. Hannewald. Organic/inorganic hybrid materials: Challenges for ab initio methodology. *Acc. Chem. Res.*, 47(11):3225–3232, 2014.
- [47] T. Echigo, M. Kimata, and T. Maruoka. Crystal-chemical and carbon-isotopic characteristics of karpatite (C₂₄H₁₂) from the Picacho Peak Area, San Benito County, California: Evidences for the hydrothermal formation. *Am. Mineral.*, 92(8-9):1262–1269, 2007.
- [48] A. Emerson, G. Luckhurst, and S. Whatling. Computer simulation studies of anisotropic systems: XXIII. The Gay-Berne discogen† Presented at the European Liquid Crystal Conference, Flims, Switzerland, 8–12 March 1993. *Mol. Phys.*, 82(1):113–124, 1994.
- [49] O. Engin, A. Villa, M. Sayar, and B. Hess. Driving forces for adsorption of amphiphilic peptides to the air-water interface. *J. Phys. Chem. B*, 114(34):11093–11101, 2010.
- [50] R. Eppenga and D. Frenkel. Monte carlo study of the isotropic and nematic phases of infinitely thin hard platelets. *Mol. Phys.*, 52(6):1303–1334, 1984.
- [51] F. Ercolessi and J. B. Adams. Interatomic potentials from first-principles calculations: The force-matching method. *Europhys. Lett.*, 26(8):583–588, 1994.
- [52] P. Español, M. Serrano, and I. Zuñiga. Coarse-graining of a fluid and its relation with dissipative particle dynamics and smoothed particle dynamic. *Int. J. Mod. Phys. C*, 8(04):899–908, 1997.
- [53] D. Evans and R. Watts. Interactions between benzene molecules. *Mol. Phys.*, 31(1):83–96, 1976.
- [54] D. J. Evans and B. L. Holian. The nose–hoover thermostat. *J. Chem. Phys.*, 83(8):4069–4074, 1985.
- [55] R. Everaers and M. R. Ejtehadi. Interaction potentials for soft and hard ellipsoids. *Phys. Rev. E*, 67:041710, 2003.
- [56] J. K. Fawcett and J. Trotter. The crystal and molecular structure of coronene. *R. Soc. Lond. Proc. Ser. A Math. Phys. Eng. Sci.*, 289(1418):366–376, 1966.

- [57] I. Fedorov, Y. Zhuravlev, and V. Berven. Properties of crystalline coronene: Dispersion forces leading to a larger van der waals radius for carbon. *Phys. Status Solidi B*, 249(7):1438–1444, 2012.
- [58] S. E. Feller, Y. Zhang, R. W. Pastor, and B. R. Brooks. Constant pressure molecular dynamics simulation: the langevin piston method. *J. Chem. Phys.*, 103(11):4613–4621, 1995.
- [59] D. Fincham. Leapfrog rotational algorithms for linear molecules. *Mol. Simul.*, 11(1):79–89, 1993.
- [60] T. Fließbach. *Statistische Physik: Lehrbuch zur Theoretischen Physik IV*, volume 4. Springer-Verlag, 2010.
- [61] M. M. Francl, C. Carey, L. E. Chirlian, and D. M. Gange. Charges fit to electrostatic potentials. 11. can atomic charges be unambiguously fit to electrostatic potentials? *J. Comput. Chem.*, 17(3):367–383, 1996.
- [62] R. A. Friedman and M. Mezei. The potentials of mean force of sodium chloride and sodium dimethylphosphate in water: An application of adaptive umbrella sampling. *J. Chem. Phys.*, 102(1):419–426, 1995.
- [63] J. G. Gay and B. J. Berne. Modification of the overlap potential to mimic a linear site–site potential. *J. Chem. Phys.*, 74(6):3316–3319, 1981.
- [64] M. K. Ghosh, N. Uddin, and C. H. Choi. Hydrophobic and hydrophilic associations of a methanol pair in aqueous solution. *J. Phys. Chem. B*, 116(49):14254–14260, 2012.
- [65] P. A. Golubkov and P. Ren. Generalized coarse-grained model based on point multipole and Gay-Berne potentials. *J. Chem. Phys.*, 125(6):64103, 2006.
- [66] P. A. Golubkov, J. C. Wu, and P. Ren. A transferable coarse-grained model for hydrogen-bonding liquids. *Phys. Chem. Chem. Phys.*, 10(15):2050–2057, 2008.
- [67] A. Gramada and P. E. Bourne. Coarse-graining the electrostatic potential via distributed multipole expansions. *Comput. Phys. Commun.*, 182(7):1455–1462, 2011.
- [68] C. Gray and K. Gubbins. *Theory of Molecular Fluids. Volume 1: Fundamentals, volume 9 of International Series on Monographs on Chemistry*. Clarendon Press, Oxford University Press, New York, 1984.
- [69] M. A. Green, K. Emery, Y. Hishikawa, W. Warta, and E. D. Dunlop. Solar cell efficiency tables (version 45). *Prog. Photovolt: Res. App.*, 23(1):1–9, 2015.
- [70] H. Grubmüller, B. Heymann, and P. Tavan. Ligand binding: Molecular mechanics calculation of the streptavidin-biotin rupture force. *Science*, 271(5251):997–999, 1996.

- [71] E. Guardia, R. Rey, and J. Padró. Potential of mean force by constrained molecular dynamics: a sodium chloride ion-pair in water. *Chem. Phys.*, 155(2):187–195, 1991.
- [72] J. R. Gullingsrud, R. Braun, and K. Schulten. Reconstructing potentials of mean force through time series analysis of steered molecular dynamics simulations. *J. Comput. Phys.*, 151(1):190–211, 1999.
- [73] J. J. Halls, A. C. Arias, J. D. MacKenzie, W. Wu, M. Inbasekaran, E. Woo, and R. Friend. Photodiodes based on polyfluorene composites: influence of morphology. *Adv. Mater.*, 12(7):498–502, 2000.
- [74] C. M. Handley and P. L. A. Popelier. Potential energy surfaces fitted by artificial neural networks. *J. Phys. Chem. A*, 114(10):3371–3383, 2010.
- [75] J.-P. Hansen and I. R. McDonald. *Theory of Simple Liquids: With Applications to Soft Matter*. Academic Press, 2013.
- [76] C. Haydock, J. C. Sharp, and F. G. Prendergast. Tryptophan-47 rotational isomerization in variant-3 scorpion neurotoxin. A combination thermodynamic perturbation and umbrella sampling study. *Biophys. J.*, 57(6):1269–1279, 1990.
- [77] T. Heinemann, M. Antlanger, M. Mazars, S. H. L. Klapp, and G. Kahl. Equilibrium structures of anisometric, quadrupolar particles confined to a monolayer. *J. Chem. Phys.*, 144(7), 2016.
- [78] T. Heinemann, K. Palczynski, J. Dzubiella, and S. H. L. Klapp. Angle-resolved effective potentials for disk-shaped molecules. *J. Chem. Phys.*, 141(21):214110, 2014.
- [79] T. Heinemann, K. Palczynski, J. Dzubiella, and S. H. L. Klapp. Coarse-grained electrostatic interactions of coronene: Towards the crystalline phase. *J. Chem. Phys.*, 143(17):174110, 2015.
- [80] P. Hohenberg and W. Kohn. Inhomogeneous electron gas. *Phys. Rev.*, 136:B864–B871, 1964.
- [81] W. G. Hoover. Generalization of Nosé’s isothermal molecular dynamics: Non-Hamiltonian dynamics for the canonical ensemble. *Phys. Rev., A*, 40(5):2814–2815, 1989.
- [82] C. A. Hunter and J. K. M. Sanders. The nature of pi-pi interactions. *J. Am. Chem. Soc.*, 112(14):5525–5534, 1990.
- [83] S. Izrailev, S. Stepaniants, B. Isralewitz, D. Kosztin, H. Lu, F. Molnar, W. Wriggers, and K. Schulten. Steered molecular dynamics. In P. Deuffhard, J. Hermans, B. Leimkuhler, A. Mark, S. Reich, and R. Skeel, editors, *Computational Molecular Dynamics: Challenges, Methods, Ideas*, volume 4 of *Lecture Notes in Computational Science and Engineering*, pages 39–65. Springer Berlin Heidelberg, 1999.

- [84] S. Izvekov, M. Parrinello, C. J. Burnham, and G. A. Voth. Effective force fields for condensed phase systems from ab initio molecular dynamics simulation: A new method for force-matching. *J. Chem. Phys.*, 120(23):10896–10913, 2004.
- [85] S. Izvekov and G. A. Voth. A multiscale coarse-graining method for biomolecular systems. *J. Phys. Chem. B*, 109(7):2469–2473, 2005.
- [86] A. F. Jakobsen. Constant-pressure and constant-surface tension simulations in dissipative particle dynamics. *J. Chem. Phys.*, 122(12):124901, 2005.
- [87] C. Jarzynski. Nonequilibrium equality for free energy differences. *Phys. Rev. Lett.*, 78(14):2690–2693, 1997.
- [88] E. Jennings, W. Montgomery, and P. Lerch. Stability of coronene at high temperature and pressure. *J. Phys. Chem. B*, 114(48):15753–15758, 2010.
- [89] W. Jiang, Y. Luo, L. Maragliano, and B. Roux. Calculation of free energy landscape in multi-dimensions with hamiltonian-exchange umbrella sampling on petascale supercomputer. *J. Chem. Theory Comput.*, 8(11):4672–4680, 2012.
- [90] W. L. Jorgensen. Optimized intermolecular potential functions for liquid alcohols. *J. Phys. Chem.*, 90(7):1276–1284, 1986.
- [91] W. L. Jorgensen, J. D. Madura, and C. J. Swenson. Optimized intermolecular potential functions for liquid hydrocarbons. *J. Am. Chem. Soc.*, 106(22):6638–6646, 1984.
- [92] V. N. Kabadi. Molecular Dynamics of Fluids: The Gaussian Overlap Model II. *Ber. Bunsenges. Phys. Chem.*, 90(4):327–332, 1986.
- [93] V. M. Kaganer and E. B. Loginov. Crystallization phase transitions and phase diagram of Langmuir monolayers. *Phys. Rev. Lett.*, 71(16):2599–2602, 1993.
- [94] V. M. Kaganer, H. Möhwald, and P. Dutta. Structure and phase transitions in Langmuir monolayers. *Rev. Mod. Phys.*, 71(3):779–819, 1999.
- [95] V. M. Kaganer and M. A. Osipov. Molecular model for the simultaneous orientational and translational ordering in a two-dimensional liquid. *J. Chem. Phys.*, 109(7):2600–2603, 1998.
- [96] I. Kalcher, J. C. F. Schulz, and J. Dzubiella. Ion-specific excluded-volume correlations and solvation forces. *Phys. Rev. Lett.*, 104(9):097802, 2010.
- [97] K. Kim and K. Jordan. Comparison of density functional and MP2 calculations on the water monomer and dimer. *J. Phys. Chem.*, 98(40):10089–10094, 1994.
- [98] J. G. Kirkwood. Statistical mechanics of fluid mixtures. *J. Chem. Phys.*, 3(5):300–313, 1935.
- [99] N. Kleppmann and S. H. L. Klapp. A scale-bridging modeling approach for anisotropic organic molecules at patterned semiconductor surfaces. *J. Chem. Phys.*, 142(6):064701, 2015.

- [100] R. Koch, J. J. Finnerty, and T. Bruhn. Theoretical study on the nonlinear optical properties of phenylenes and influencing factors. *J. Phys. Org. Chem.*, 21(11):954–962, 2008.
- [101] M. Kocman, M. Pykal, and P. Jurecka. Electric quadrupole moment of graphene and its effect on intermolecular interactions. *Phys. Chem. Chem. Phys.*, 16:3144–3152, 2014.
- [102] W. Kohn and L. J. Sham. Self-consistent equations including exchange and correlation effects. *Phys. Rev.*, 140(4A):A1133–A1138, 1965.
- [103] E. A. Koopman and C. P. Lowe. Advantages of a Lowe-Andersen thermostat in molecular dynamics simulations. *J. Chem. Phys.*, 124(20):204103, 2006.
- [104] S. Kumar, J. M. Rosenberg, D. Bouzida, R. H. Swendsen, and P. A. Kollman. The weighted histogram analysis method for free-energy calculations on biomolecules. I. The method. *J. Comput. Chem.*, 13(8):1011–1021, 1992.
- [105] S. Kumar, J. M. Rosenberg, D. Bouzida, R. H. Swendsen, and P. A. Kollman. Multidimensional free-energy calculations using the weighted histogram analysis method. *J. Comput. Chem.*, 16(11):1339–1350, 1995.
- [106] C. Lee, W. Yang, and R. G. Parr. Development of the Colle-Salvetti correlation-energy formula into a functional of the electron density. *Phys. Rev. B: Condens. Matter*, 37(2):785–789, 1988.
- [107] B. Leimkuhler, E. Noorizadeh, and O. Penrose. Comparing the efficiencies of stochastic isothermal molecular dynamics methods. *J. Stat. Phys.*, 143(5):921–942, 2011.
- [108] B. Leimkuhler, E. Noorizadeh, and F. Theil. A gentle stochastic thermostat for molecular dynamics. *J. Stat. Phys.*, 135(2):261–277, 2009.
- [109] T. Lelièvre, M. Rousset, and G. Stoltz. Computation of free energy differences through nonequilibrium stochastic dynamics: The reaction coordinate case. *J. Comput. Phys.*, 222(2):624–643, 2007.
- [110] L. Li, L. Harnau, S. Rosenfeldt, and M. Ballauff. Effective interaction of charged platelets in aqueous solution: Investigations of colloid laponite suspensions by static light scattering and small-angle x-ray scattering. *Phys. Rev. E*, 72:051504, 2005.
- [111] C. N. Likos. Effective interactions in soft condensed matter physics. *Physics Reports*, 348(4–5):267–439, 2001.
- [112] H. J. Limbach and K. Kremer. Multi-scale modelling of polymers: perspectives for food materials. *Trends Food Sci. Technol.*, 17(5):215–219, 2006.
- [113] H. Lu and K. Schulten. Steered molecular dynamics simulation of conformational changes of immunoglobulin domain I27 interpret atomic force microscopy observations. *Chem. Phys.*, 247(1):141–153, 1999.

- [114] H. Löwen and G. Krampposthuber. Optimal effective pair potential for charged colloids. *Europhys. Lett.*, 23(9):673–678, 1993.
- [115] S. J. Marrink, H. J. Risselada, S. Yefimov, D. P. Tieleman, and A. H. de Vries. The martini force field: coarse grained model for biomolecular simulations. *J. Phys. Chem. B*, 111(27):7812–7824, 2007.
- [116] J. Martínez-Blanco, A. Mascaraque, Y. S. Dedkov, and K. Horn. Ge(001) as a template for long-range assembly of π -stacked coronene rows. *Langmuir*, 28(8):3840–3844, 2012.
- [117] Y. Martínez-Ratón and E. Velasco. Enhanced stability of the tetratic phase due to clustering. *Phys. Rev. E*, 79(1):011711, 2009.
- [118] G. J. Martyna, M. L. Klein, and M. Tuckerman. Nosé–hoover chains: the canonical ensemble via continuous dynamics. *J. Chem. Phys.*, 97(4):2635–2643, 1992.
- [119] G. J. Martyna, D. J. Tobias, and M. L. Klein. Constant pressure molecular dynamics algorithms. *J. Chem. Phys.*, 101(5):4177–4189, 1994.
- [120] D. Marx and J. Hutter. Ab initio molecular dynamics: Theory and implementation. *Modern methods and algorithms of quantum chemistry*, 1:301–449, 2000.
- [121] A. Masunov and T. Lazaridis. Potentials of mean force between ionizable amino acid side chains in water. *J. Am. Chem. Soc.*, 125(7):1722–1730, 2003.
- [122] M. Mazars. Long ranged interactions in computer simulations and for quasi-2D systems. *Phys. Rep.*, 500(2):43–116, 2011.
- [123] C. McBride and M. R. Wilson. Molecular dynamics simulations of a flexible liquid crystal. *Mol. Phys.*, 97(4):511–522, 1999.
- [124] R. L. McGreevy and L. Pusztai. Reverse monte carlo simulation: A new technique for the determination of disordered structures. *Mol. Simul.*, 1(6):359–367, 1988.
- [125] L. Mederos, E. Velasco, and Y. Martínez-Ratón. Hard-body models of bulk liquid crystals. *J. Phys.: Condens. Matter*, 26(46):463101, 2014.
- [126] S. Melchionna, G. Ciccotti, and B. Lee Holian. Hoover NPT dynamics for systems varying in shape and size. *Mol. Phys.*, 78(3):533–544, 1993.
- [127] M. Mezei. Adaptive umbrella sampling: self-consistent determination of the non-boltzmann bias. *J. Comput. Phys.*, 68(1):237–248, 1987.
- [128] J. H. Miller, W. G. Mallard, and K. C. Smyth. Intermolecular potential calculations for polycyclic aromatic hydrocarbons. *J. Phys. Chem.*, 88(21):4963–4970, 1984.
- [129] M. A. Miller, J. J. Shepherd, and D. J. Wales. Structural trends in clusters of quadrupolar spheres. *Mol. Phys.*, 106(12-13):1655–1664, 2008.

- [130] B. M. Mognetti, L. Yelash, P. Virnau, W. Paul, K. Binder, M. Müller, and L. G. MacDowell. Efficient prediction of thermodynamic properties of quadrupolar fluids from simulation of a coarse-grained model: The case of carbon dioxide. *J. Chem. Phys.*, 128(10):–, 2008.
- [131] A. Morriss-Andrews, J. Rottler, and S. S. Plotkin. A systematically coarse-grained model for DNA and its predictions for persistence length, stacking, twist, and chirality. *J. Chem. Phys.*, 132(3):035105, 2010.
- [132] H. A. Morriss-Andrews. *Coarse-Grained Molecular Dynamics Simulations of DNA Representing Bases as Ellipsoids*. PhD thesis, UNIVERSITY OF BRITISH COLUMBIA (Vancouver), 2009.
- [133] I. Muševič, M. Škarabot, U. Tkalec, M. Ravnik, and S. Žumer. Two-dimensional nematic colloidal crystals self-assembled by topological defects. *Science*, 313(5789):954–958, 2006.
- [134] T. Mülders, P. Krüger, W. Swegat, and J. Schlitter. Free energy as the potential of mean constraint force. *J. Chem. Phys.*, 104(12):4869–4870, 1996.
- [135] M. P. Neal and A. J. Parker. Computer simulations using a quadrupolar Gay-Berne model. *Mol. Cryst. Liq. Cryst. A*, 330(1):565–572, 1999.
- [136] M. P. Neal and A. J. Parker. Molecular dynamics study of mesophase formation using a transverse quadrupolar Gay-Berne model. *Phys. Rev. E*, 63:011706, 2000.
- [137] J. Nelson. Solar cells by self-assembly? *Science*, 293(5532):1059–1060, 2001.
- [138] R. M. Neumann. Entropic approach to brownian movement. *Am. J. Phys.*, 48(5):354–357, 1980.
- [139] S. O. Nielsen, C. F. Lopez, G. Srinivas, and M. L. Klein. A coarse grain model for n-alkanes parameterized from surface tension data. *J. Chem. Phys.*, 119(14):7043–7049, 2003.
- [140] J. Norberg and L. Nilsson. Stacking free energy profiles for all 16 natural ribodinucleoside monophosphates in aqueous solution. *J. Am. Chem. Soc.*, 117(44):10832–10840, 1995.
- [141] S. Nosé. A unified formulation of the constant temperature molecular dynamics methods. *J. Chem. Phys.*, 81(1):511–519, 1984.
- [142] S. Nose. Constant-temperature molecular dynamics. *J. Phys.: Condens. Matter*, 2(S):SA115, 1990.
- [143] O. I. Obolensky, V. V. Semenikhina, A. V. Solov'yov, and W. Greiner. Interplay of electrostatic and van der waals forces in coronene dimer. *Int. J. Quant. Chem.*, 107(6):1335–1343, 2007.
- [144] U. Ognysta, A. Nych, V. Nazarenko, M. Skarabot, and I. Musevic. Design of 2D binary colloidal crystals in a nematic liquid crystal. *Langmuir*, 25(20):12092–12100, 2009.

- [145] Y. Olivier, L. Muccioli, and C. Zannoni. Quinquephenyl: The simplest rigid-rod-like nematic liquid crystal, or is it? An atomistic simulation. *ChemPhysChem*, 15(7):1345–1355, 2014.
- [146] S. Orlandi, L. Muccioli, M. Ricci, R. Berardi, and C. Zannoni. Core charge distribution and self assembly of columnar phases: The case of triphenylenes and azatriphenylenes. *Chem. Cent. J.*, 1:15, 2007.
- [147] K. Palczynski, G. Heimel, J. Heyda, and J. Dzubiella. Growth and characterization of molecular crystals of para-sexiphenyl by all-atom computer simulations. *Cryst. Growth Des.*, 14(8):3791–3799, 2014.
- [148] S. Park, F. Khalili-Araghi, E. Tajkhorshid, and K. Schulten. Free energy calculation from steered molecular dynamics simulations using jarzynski’s equality. *J. Chem. Phys.*, 119(6):3559–3566, 2003.
- [149] M. Parrinello and A. Rahman. Polymorphic transitions in single crystals: A new molecular dynamics method. *J. Appl. Phys.*, 52(12):7182–7190, 1981.
- [150] J. P. Perdew, K. Burke, and M. Ernzerhof. Generalized gradient approximation made simple. *Phys. Rev. Lett.*, 77(18):3865–3868, 1996.
- [151] I. Pettersson and T. Liljefors. Benzene-benzene (phenyl-phenyl) interactions in MM2/MMP2 molecular mechanics calculations. *J. Comput. Chem.*, 8(8):1139–1145, 1987.
- [152] I. V. Pivkin and G. E. Karniadakis. Accurate coarse-grained modeling of red blood cells. *Phys. Rev. Lett.*, 101(11):118105, 2008.
- [153] P. Poier, C. N. Likos, A. J. Moreno, and R. Blaak. An Anisotropic Effective Model for the Simulation of Semiflexible Ring Polymers. *Macromolecules*, 48(14):4983–4997, 2015.
- [154] M. Praprotnik, L. D. Site, and K. Kremer. Adaptive resolution molecular-dynamics simulation: Changing the degrees of freedom on the fly. *J. Chem. Phys.*, 123(22):224106, 2005.
- [155] S. L. Price and A. J. Stone. The electrostatic interactions in van der Waals complexes involving aromatic molecules. *J. Chem. Phys.*, 86(5):2859–2868, 1987.
- [156] D. Quigley and M. I. J. Probert. Langevin dynamics in constant pressure extended systems. *J. Chem. Phys.*, 120(24):11432–11441, 2004.
- [157] M. Rapacioli, F. Calvo, F. Spiegelman, C. Joblin, and D. J. Wales. Stacked clusters of polycyclic aromatic hydrocarbon molecules. *J. Phys. Chem. A*, 109(11):2487–2497, 2005.
- [158] S. W. Rick and B. Berne. Free energy of the hydrophobic interaction from molecular dynamics simulations: the effects of solute and solvent polarizability. *J. Phys. Chem. B*, 101(49):10488–10493, 1997.

- [159] J. M. Robertson et al. 248. Crystal-structure studies of polynuclear hydrocarbons. Part VI. 1, 12: 2, 3: 4, 5: 6, 7: 8, 9: 10, 11-hexabenzocoronene. *J. Chem. Soc. (Resumed)*, pages 1280–1284, 1961.
- [160] J. M. Robertson and J. White. Crystal structure of coronene. *Nature*, 154:605–606, 1944.
- [161] J. M. Robertson and J. G. White. 164. The crystal structure of coronene: a quantitative X-ray investigation. *J. Chem. Soc.*, pages 607–617, 1945.
- [162] L. Rosso, J. B. Abrams, and M. E. Tuckerman. Mapping the backbone dihedral free-energy surfaces in small peptides in solution using adiabatic free-energy dynamics. *J. Phys. Chem. B*, 109(9):4162–4167, 2005.
- [163] B. Roux. The calculation of the potential of mean force using computer simulations. *Comput. Phys. Commun.*, 91(1–3):275–282, 1995.
- [164] A. A. Samoletov, C. P. Dettmann, and M. A. Chaplain. Thermostats for “slow” configurational modes. *J. Stat. Phys.*, 128(6):1321–1336, 2007.
- [165] S. Sarman. Biaxial nematic liquid crystal phases of a soft ellipsoid-string fluid. *Phys. Chem. Chem. Phys.*, 2(17):3831–3839, 2000.
- [166] B. Schatschneider, S. Monaco, J.-J. Liang, and A. Tkatchenko. High-throughput investigation of the geometry and electronic structures of gas-phase and crystalline polycyclic aromatic hydrocarbons. *J. Phys. Chem. C*, 118(34):19964–19974, 2014.
- [167] R. Schlesinger, F. Bianchi, S. Blumstengel, C. Christodoulou, R. Ovsyannikov, B. Kobin, K. Moudgil, S. Barlow, S. Hecht, S. Marder, et al. Efficient light emission from inorganic and organic semiconductor hybrid structures by energy-level tuning. *Nat. Commun.*, 6, 2015.
- [168] H. Schmidle. *Computer simulations of complex fluids in two dimensions*. PhD thesis, Technische Universität Berlin, Fakultät II - Mathematik und Naturwissenschaften, 2012.
- [169] M. Schmidt, A. Masson, and C. Bréchnignac. Coronene cluster experiments: Stability and thermodynamics. *Int. J. Mass Spectrom.*, 252(2):173–179, 2006. Special Issue on Cluster Cooling.
- [170] R. Schmidt, B. Teo, and J. Brady. Use of umbrella sampling in the calculation of the potential of mean force for maltose in vacuum from molecular dynamics simulations. *J. Phys. Chem.*, 99(29):11339–11343, 1995.
- [171] L. Schmidt-Mende, A. Fechtenkötter, K. Müllen, E. Moons, R. H. Friend, and J. D. MacKenzie. Self-organized discotic liquid crystals for high-efficiency organic photovoltaics. *Science*, 293(5532):1119–1122, 2001.
- [172] J. W. Schroer and P. A. Monson. Phase equilibrium in a quadrupolar hard sphere interaction site model of benzene. *J. Chem. Phys.*, 114(9):4124–4130, 2001.

- [173] F. Schwabl. *Statistische Mechanik*. Springer-Verlag, 2006.
- [174] S. E. Shaheen, C. J. Brabec, N. S. Sariciftci, F. Padinger, T. Fromherz, and J. C. Hummelen. 2.5% efficient organic plastic solar cells. *Appl. Phys. Lett.*, 78(6):841–843, 2001.
- [175] H. Shen, Y. Li, P. Ren, D. Zhang, and G. Li. Anisotropic Coarse-Grained Model for Proteins Based On Gay–Berne and Electric Multipole Potentials. *J. Chem. Theory Comput.*, 10(2):731–750, 2014.
- [176] M. J. Sippl. Calculation of conformational ensembles from potentials of mean force: an approach to the knowledge-based prediction of local structures in globular proteins. *J. Mol. Biol.*, 213(4):859–883, 1990.
- [177] M. Škarabot, M. Ravnik, S. Žumer, U. Tkalec, I. Poberaj, D. Babič, N. Osterman, and I. Muševič. Interactions of quadrupolar nematic colloids. *Phys. Rev. E*, 77(3):031705, 2008.
- [178] W. Smith. Point multipoles in the Ewald summation (revisited). *CCP5 Newsletter No. 15*, pages 15–25, 1998.
- [179] R. Sokolovskii and E. E. Burnell. Orientational order of near D3h solutes in nematic liquid crystals. II. Description via Gay–Berne model with embedded quadrupoles. *J. Chem. Phys.*, 130(15):154507, 2009.
- [180] M. Souaille and B. Roux. Extension to the weighted histogram analysis method: combining umbrella sampling with free energy calculations. *Comput. Phys. Commun.*, 135(1):40–57, 2001.
- [181] A. Stone. The description of bimolecular potentials, forces and torques: the s and v function expansions. *Mol. Phys.*, 36(1):241–256, 1978.
- [182] T. Straatsma, M. Zacharias, and J. McCammon. Holonomic constraint contributions to free energy differences from thermodynamic integration molecular dynamics simulations. *Chem. Phys. Lett.*, 196(3):297–302, 1992.
- [183] Y. Sugita and Y. Okamoto. Replica-exchange molecular dynamics method for protein folding. *Chem. Phys. Lett.*, 314(1–2):141–151, 1999.
- [184] Y. Sun, Y. Liu, and D. Zhu. Advances in organic field-effect transistors. *J. Mater. Chem.*, 15(1):53–65, 2005.
- [185] R. H. Swendsen and J.-S. Wang. Replica monte carlo simulation of spin-glasses. *Phys. Rev. Lett.*, 57:2607–2609, 1986.
- [186] T. Taylor, M. Schmollngruber, C. Schröder, and O. Steinhauser. The effect of Thole functions on the simulation of ionic liquids with point induced dipoles at various densities. *J. Chem. Phys.*, 138(20):204119, 2013.
- [187] B. Thole. Molecular polarizabilities calculated with a modified dipole interaction. *Chem. Phys.*, 59(3):341–350, 1981.

- [188] G. Torrie and J. Valleau. Nonphysical sampling distributions in Monte Carlo free-energy estimation: Umbrella sampling. *J. Comput. Phys.*, 23(2):187–199, 1977.
- [189] G. M. Torrie and J. P. Valleau. Monte Carlo free energy estimates using non-Boltzmann sampling: Application to the sub-critical Lennard-Jones fluid. *Chem. Phys. Lett.*, 28(4):578–581, 1974.
- [190] L. Torsi, M. Magliulo, K. Manoli, and G. Palazzo. Organic field-effect transistor sensors: a tutorial review. *Chem. Soc. Rev.*, 42:8612–8628, 2013.
- [191] G. A. Tritsarlis and A. G. Vanakaras. Two-dimensional ordered porous patterns by molecular design. *Langmuir*, 26(11):7808–7812, 2010.
- [192] E. Trizac, L. Bocquet, R. Agra, J.-J. Weis, and M. Aubouy. Effective interactions and phase behaviour for a model clay suspension in an electrolyte. *J. Phys.: Condens. Matter*, 14(40):9339–9352, 2002.
- [193] W. Tschöp, K. Kremer, J. Batoulis, T. Bürger, and O. Hahn. Simulation of polymer melts. I. Coarse-graining procedure for polycarbonates. *Acta Polym.*, 49(2-3):61–74, 1998.
- [194] W. Tschöp, K. Kremer, O. Hahn, J. Batoulis, and T. Bürger. Simulation of polymer melts. II. From coarse-grained models back to atomistic description. *Acta Polym.*, 49(2-3):75–79, 1998.
- [195] S. Tsuzuki. Interactions with aromatic rings. In D. Wales, editor, *Intermolecular forces and clusters I*, volume 115 of *Structure and Bonding*, pages 149–193. Springer Berlin Heidelberg, 2005.
- [196] S. Tsuzuki, K. Honda, T. Uchimaru, M. Mikami, and K. Tanabe. Origin of Attraction and Directionality of the π/π Interaction: Model Chemistry Calculations of Benzene Dimer Interaction. *J. Am. Chem. Soc.*, 124(1):104–112, 2002.
- [197] D. Van Der Spoel, E. Lindahl, B. Hess, G. Groenhof, A. E. Mark, and H. J. C. Berendsen. Gromacs: Fast, flexible, and free. *J. Comput. Chem.*, 26(16):1701–1718, 2005.
- [198] B. P. van Eijck, R. W. Hoofst, and J. Kroon. Molecular dynamics study of conformational and anomeric equilibria in aqueous d-glucose. *J. Phys. Chem.*, 97(46):12093–12099, 1993.
- [199] P. D. J. van Oostrum, M. Hejazifar, C. Niedermayer, and E. Reimhult. Simple method for the synthesis of inverse patchy colloids. *J. Phys.: Condens. Matter*, 27(23):234105, 2015.
- [200] N. B. Vargaftik, B. N. Volkov, and L. D. Voljak. International tables of the surface tension of water. *J. Phys. Chem. Ref. Data*, 12(3):817–820, 1983.
- [201] C. Vega. A perturbation theory of hard quadrupolar fluids. *Mol. Phys.*, 75(2):427–442, 1992.

- [202] J. Vieillard-Baron. Phase transitions of the classical hard-ellipse system. *J. Chem. Phys.*, 56(10):4729–4744, 1972.
- [203] E. Villa, A. Balaeff, L. Mahadevan, and K. Schulten. Multiscale method for simulating Protein-DNA complexes. *Multiscale Model Sim.*, 2(4):527–553, 2004.
- [204] P. Vincett, W. Barlow, R. Hann, and G. Roberts. Electrical conduction and low voltage blue electroluminescence in vacuum-deposited organic films. *Thin Solid Films*, 94(2):171–183, 1982.
- [205] O. A. von Lilienfeld and D. Andrienko. Coarse-grained interaction potentials for polyaromatic hydrocarbons. *J. Chem. Phys.*, 124(5):054307, 2006.
- [206] G. Voth. *Coarse-Graining of Condensed Phase and Biomolecular Systems*. CRC Press, 2008.
- [207] H. Wang, C. Junghans, and K. Kremer. Comparative atomistic and coarse-grained study of water: What do we lose by coarse-graining? *Eur. Phys. J. E Soft Matter*, 28(2):221–229, 2009.
- [208] J. Wang, R. M. Wolf, J. W. Caldwell, P. A. Kollman, and D. A. Case. Development and testing of a general amber force field. *J. Comput. Chem.*, 25(9):1157–1174, 2004.
- [209] M. R. Wilson. Molecular dynamics simulations of flexible liquid crystal molecules using a Gay-Berne/Lennard-Jones model. *J. Chem. Phys.*, 107(20):8654–8663, 1997.
- [210] Z. Wu, Q. Cui, and A. Yethiraj. A new coarse-grained model for water: The importance of electrostatic interactions. *J. Phys. Chem. B*, 114(32):10524–10529, 2010.
- [211] P. Xu, H. Shen, L. Yang, Y. Ding, B. Li, Y. Shao, Y. Mao, and G. Li. Coarse-grained simulations for organic molecular liquids based on Gay-Berne and electric multipole potentials. *J. Mol. Model.*, 19(2):551–558, 2013.
- [212] W. S. Young and C. L. Brooks III. A reexamination of the hydrophobic effect: Exploring the role of the solvent model in computing the methane–methane potential of mean force. *J. Chem. Phys.*, 106(22):9265–9269, 1997.
- [213] Y. Zhao and D. G. Truhlar. A prototype for graphene material simulation: structures and interaction potentials of coronene dimers. *J. Phys. Chem. C*, 112(11):4061–4067, 2008.

Danksagung

Ich bedanke mich an dieser Stelle bei allen, die mich während meiner Promotionsphase unterstützten und mir hilfreich zur Seite standen.

Speziell möchte ich meine Betreuerin Prof. Sabine Klapp hervorheben, die mir meine Promotion ermöglicht und mich darüber hinaus durch viele konstruktive Gespräche und Kritiken betreut hat.

Weiterhin danke ich Karol Palczynski, Prof. Joachim Dzubiella, Prof. Martial Mazars, Prof. Gerhard Kahl, Dr. Moritz Antlanger und Dr. Carlos Alvarez für die Zusammenarbeit. Durch Prof. Sabine Klapp, Prof. Martial Mazars und Prof. Gerhard Kahl bekam ich auch die Möglichkeit, Forschungsaufenthalte in Paris und Wien wahrzunehmen.

Außerdem danke ich Prof. Christos Likos für die sofortige Zusage als Zweitgutachter sowie Prof. Mario Dähne für den Prüfungsvorsitz.

Eine angenehme Arbeitsatmosphäre verbreiteten in unserem Büro Helge Neitsch, Dr. Tarlan Vezirov, Alexander Kraft und Benjamin von Lospichl.

Für das Korrekturlesen bin ich Dr. Stavros Peroukidis, Dr. Alice von der Heydt, David Rudkowski, Arzu Yener, Alexander Kraft, Benjamin von Lospichl, Henning Reinken, Sarah Loos, Rodrigo Lugo-Frias und Dr. Christian Heinemann dankbar.

Erwähnenswert sind für mich auch die fachlichen Diskussionen mit den Mitgliedern des Sonderforschungsbereiches 951 Karol Palczynski, Prof. Joachim Dzubiella und Dr. Honghui Shang sowie mit den internen Kollegen Sascha Gerloff, Dr. Robert Gernert, Dr. Nicola Kleppmann, Dr. Florian Kogler und Thomas Martyneec.

Des Weiteren geht mein Dank an die Sekretärin unseres Instituts Norma Rettich.

Schlussendlich möchte ich mich bei meinen Eltern Elisabeth und Wolfgang Heinemann bedanken, die mich zeitlebens unterstützt haben.